Direct Numerical Simulation of Multi-phase Flow in Complex Media

Mohammad Reza Hashemi

Ph.D. thesis in Civil Engineering

Universitat Politècnica de Catalunya

Departament d'Enginyeria Civil i Ambiental

Supervisors: Dr. Pavel Ryzhakov

Prof. Riccardo Rossi

Barcelona, November 2021

To my beloved family.

Abstract

In numerous applications, two–phase liquid–gas transport at sub–millimeter length scales plays a substantial role in the determination of the behavior of the system at hand. As its main application, the present work focuses on the polymer electrolyte membrane (PEM) fuel cells. Desirable performance and operational life–time of this class of high–throughput energy conversion devices requires an effective water management, which *per se* relies on proper prediction of the water–air transport mechanisms. Such two–phase flow involves interfacial forces and phenomena, like hysteresis, that are associated with the physicochemical properties the liquid, gas, and if present, the solid substrate. In this context, numerical modeling is a viable means to obtain valuable predictive understanding of the transport mechanisms, specially for cases that experimental analyses are complicated and/or prohibitively expensive.

In this work, an efficient finite element/level–set framework is developed for three–dimensional simulation of two–phase flow. In order to achieve a robust solver for practical applications, the physical complexities are consistently included and the involved numerical issues are properly tackled; the pressure discontinuity at the liquid-gas interface is consistently captured by utilizing an enriched finite element space. The method is stabilized within the framework of variational multiscale stabilization technique. A novel treatment is further proposed for the small–cut instability problem. It is shown that the proposed model can provide accurate results minimizing the spurious currents. A robust technique is also developed in order to filter out the possible noises in the level–set field. It is shown that it is a key to prevent irregularities caused by the persistent remnant of the spurious currents. It is shown how the well-established contact–line models can be incorporated into the variational formulation. The importance of the inclusion of the sub–elemental hydrodynamics is also elaborated. The results presented

in the present work rely on the combination of the linearized molecular kinetic and the hydrodynamic theories. Recalling the realistic behavior of liquids in contact with solid substrates, the contact–angle hysteresis phenomenon is taken into account by imposing a consistent pinning/unpinning mechanism developed within the framework of the level–set method. Aside from the main developments, a novel technique is also proposed to significantly improve the accuracy and minimize the the loss in the geometrical features of the interface during the level–set convection based on the back and forth error compensation correction (BFECC) algorithm.

Within the context of this thesis, the numerical model is validated for various cases of gas bubble in a liquid and liquid droplets in a gas. For the latter scenario, besides free droplets, the accuracy of the proposed numerical method is assessed for capturing the dynamics droplets spreading on solid substrates. The performance of the model is then analyzed for the capturing the configuration of a water droplet on an inclined substrate in the presence the contact–angle hysteresis. The proposed method is finally employed to simulate the dynamics of a water droplet confined in a gas channel and exposed to air-flow.

Acknowledgements

First, I gratefully acknowledge the financial support I received from the International Center for Numerical Methods in Engineering (CIMNE) and the Spanish Ministry of Science, Innovation and Universities (Ministerio de Ciencia, Innovación y Universidades) to carry out this research.

I specially thank Dr. Pavel Ryzhakov and Prof. Riccardo Rossi for offering me the opportunity to join their team. Pavel and Riccardo, without your guidance, this work could not be performed. I deeply appreciate your generous support.

Contents

List of Figures

Chapter 1

Introduction

1.1 Application: Water Transport in Polymer Electrolyte Membrane Fuel Cell

Modeling of two-phase flow of immiscible fluids has a large range of engineering applications, among others, water-oil flow in a reservoir [88], cavitation [40, 107], various microfluidic applications [137], and liquid-gas flow in micro-channels [9, 41, 113, 126] as well as porous [29] and fibrous [129] media. One of the recent applications where accurate modeling of the two-phase flow is essential is the polymer electrolyte membrane (PEM) fuel cell (also known as proton exchange membrane fuel cells) [4, 67, 156].

PEM fuel cells are modern energy conversion devices, known for their high efficiency and eco-friendliness [8]. The by-product of PEM fuel cells fueled with hydrogen is water and their efficiency is up to three times higher than that of high-temperature combustion devices [86]. By producing hydrogen using water electrolysis, which utilizes excess renewable energy, an emission-free transportation may be achieved. Nevertheless, high cost and limited durability hinder the large-scale commercialization of PEM fuel cells. In a PEM fuel cell, as depicted in Fig. 1.1, fuel (hydrogen) and oxidant (oxygen or air) are fed in the gaseous state through the Gas Channels (GC). The chemical reaction takes place and electrical current is produced once the fuel and oxidant molecules reach the platinum Catalyst Layer (CL), where a chemical reaction takes place. Polymer Electrolyte/Proton Exchange Membrane (PEM) ensures the conductivity of hydrogen protons, while it is practically impermeable to the electrons [91]. Despite the promising potential of PEM fuel cells to become one of the main sources of clean energy for

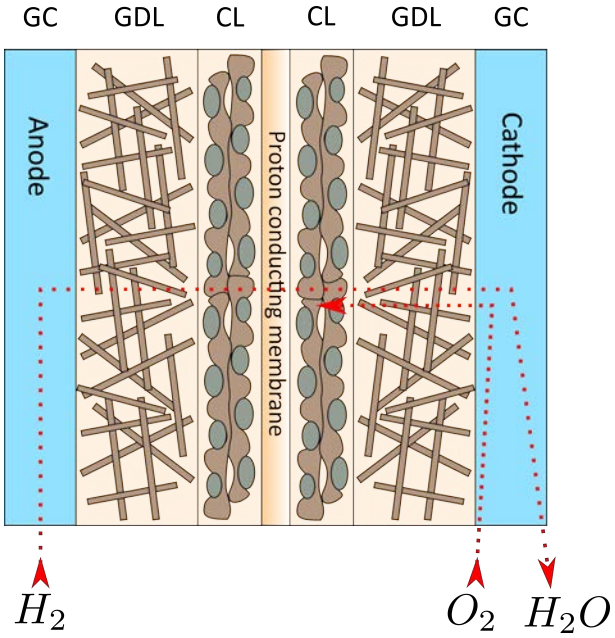

Figure 1.1: Schematic of a PEM fuel cell.

transportation purposes [25], their usage is still hindered by their durability [44].

The performance of a fuel cell is usually measured in term of voltage losses; at low and moderate currents, kinetic and ohmic losses dominate. On the other hand, at high currents, the main factor in reducing efficiency is the so-called mass transport loss that is due to the accumulation of by-product water. This trapped water blocks the access of air to the reaction site [135]. Therefore, the so-called "water management" [53, 87] is among the challenging issues that directly affect the performance and durability of PEM fuel cells.

Efficient water management requires the evacuation of the water droplets that breakthrough the outer face of the gas diffusion layer (GDL) into the gas channel (GC) [85] (see Fig. 1.2). This evacuation is mediated by the air flowing in the GC at the cathode. Thus, particular attention should be paid to the prediction of the droplet detachment conditions, which, in turn, lead to insights regarding the efficiency of water evacuation for a given operation regime. In this context, the analysis of the dynamics of water droplets confined in the GC is of main importance [139], which requires the incorporation of the complex wettability characteristics of the outer face of the GDL [69, 156]. In such analyses, besides the experimental investigations and deliberate measurements and/or visualizations, numerical modelling can be acquired as a viable means to provide

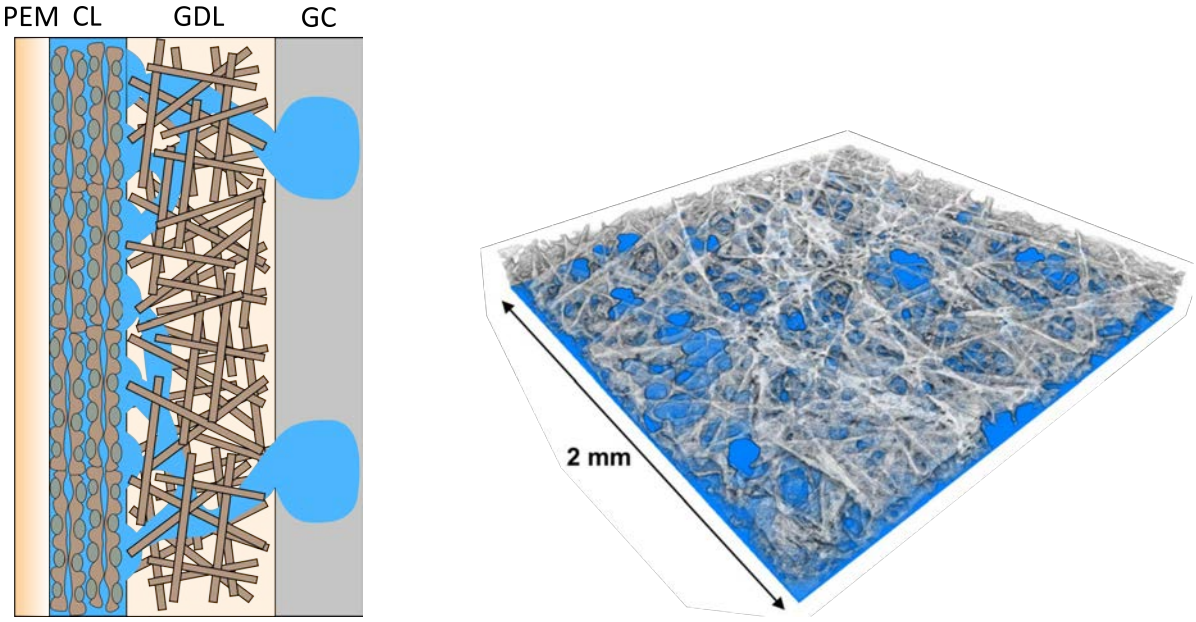

(a) (b)

Figure 1.2: a) Schematic of water transport in the cathode of PEM fuel cell. b) Distribution of liquid water in a GDL [19].

fundamental understanding of the phenomena.

In order to obtain desirably accurate results using a numerical method, however, one needs to suitably treat the jump in the material properties at the liquid-gas interface and incorporate the capillary forces. Moreover, once the liquid-gas interface contacts a solid substrate, special treatments are necessary to adequately address the contact–line dynamics. These challenging issues are further elaborated in the following.

1.2 Challenges

1.2.1 Surface tension

In the modeling of surface tension dominated multi-phase flows, the accuracy, robustness, and efficiency of the numerical methods are adversely affected by the principal role of the surface tension [68]. In this context, the main challenge is to consistently represent the strong pressure discontinuity (jump) across the interface as well as the weak discontinuity (in the pressure gradient) that is associated with the jump in density. Moreover, accurate representation of these discontinuities are affecting the shape and

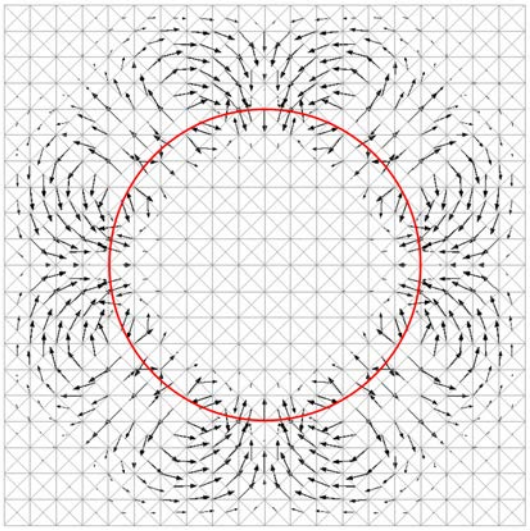

Figure 1.3: Spurious currents around a neutrally buoyant droplet at equilibrium [58].

position of the liquid-gas interface and vice versa. These aspects are particularly challenging since the mesh-based numerical methods are conventionally developed to model continuous fields inside a computational cell. Any inconsistency between the modeled surface tension and the pressure jump leads to large non-physical spurious (parasitic) currents [46, 94] as shown in Fig. 1.3.

1.2.2 Contact–line Dynamics

In the modeling of phenomena associated with the multi-phase flow in the presence of a solid substrate, one of the major challenges is to deal with the moving boundary of the three-phase (gas/liquid/solid) interface, the so–called "contact–line", using an appropriate condition [13, 112, 115]. Upon the disturbance of the equilibrium condition of a droplet laying on a solid substrate, unbalanced interfacial forces actively move the contact–line until a new equilibrium is achieved. During this transition, the wetting (dewetting) process is defined as the spreading (contraction) of the contact–line. Wetting, or generally the dynamics of the contact–line [110], cannot be adequately described using Young's relation [56, 147] since its usage is limited to the static equilibrium condition. Figure 1.4 presents a graphical description of the contact–line dynamics for a spreading droplet (see [112] for the detailed description of the phenomena).

Theoretical investigations of the movement of the contact-line [37, 63] imply that the classical continuum-level hydrodynamics along with the conventional no-slip condition at

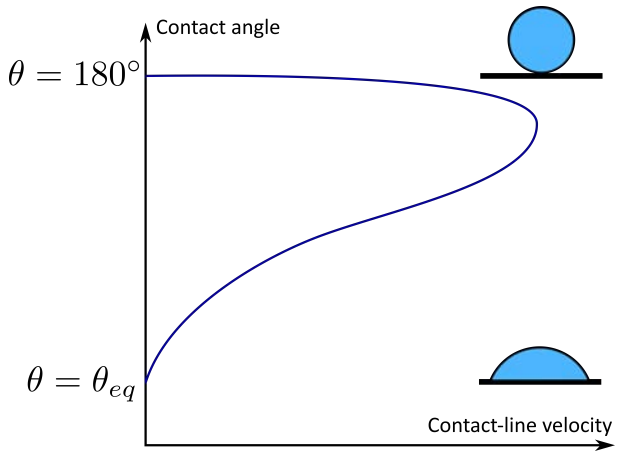

Figure 1.4: Qualitative description of the contact–line dynamics during droplet spreading.

the solid surface lead to an unbounded velocity gradient and consequently a singularity in the stress at the contact-line. The conventional approach to alleviate this singularity is to take into account a slip condition in the vicinity of the contact-line [61, 62], for which there is also some evidence from molecular dynamics [96, 97, 130].

Employing the slip condition in the context of the continuum hydrodynamics [73] allows for a theoretical solution for the viscous bending phenomenon and leads to the well-established Cox's relation [27], which gives a correlation between the apparent macroscopic contact-angle and the microscopic contact-angle. More recently, it was shown that alleviating the stress singularity can result in a complement to the hydrodynamic theory; Zhang and Mohseni [152] explored the possibility of integrating the singular stress in the close vicinity of the contact-line in order to obtain a model for the dynamic microscopic contact-angle. Moreover, one can acquire the rolling motion of the liquid instead of the slippage, thus, obtaining the interface formation theory [111].

Besides the hydrodynamic theory that focuses on the phenomena at the continuum level, molecular kinetic theory [12, 155] has also been acquired to derive a model for the moving contact-line. It was shown that the resulting model is consistent with the results of the molecular dynamic simulations [11, 31]. Both the Cox's relation and the molecular kinetic model have been examined by fitting the experimentally observed correlation between the contact-angle and the contact-line velocity [10, 89, 110].

It had been revealed that depending on the features of the set of experiments, one model or another provides a better match [33, 82, 101]. This can be explained as a result of the fact that the hydrodynamic theory accounts for the viscous dissipation while the

molecular kinetic theory focuses on the energy dissipation in a very close vicinity of the contact-line [110]. Thus, depending on the flow configuration and the velocity of the contact-line, either of these mechanisms is dominant and the behavior can be better characterized with the respective model. So far, due to the ambiguity in determining the underlying physics and the lack of a systematic approach to determine constitutive parameters [103, 152], it is not a straightforward task to decide which theory (and the resulting) model is generally superior. Therefore, in order to exploit the pros of both the theories, combined models were proposed [16, 32, 34, 90, 92], in which the frictional contact-line slip is taken into account as well as the viscous dissipation. Moreover, recent studies [42, 71] have revealed that without such a combination, the modeling would be deficient.

Realistic Solid Contact

One of the major complexities associated with the modeling of droplet spreading in real–life applications, is the contact–angle hysteresis [38]. Specifically for the analysis of droplet dynamics in GC of PEM fuel cells, it is essential to incorporate a dynamic (non–static) contact–angle [5, 128] along with the prerequisites of the hysteresis phenomenon [153]. This requirement particularly arises from the physicochemical properties of the fibrous substrate formed by the face of GDL [48].

Hysteresis is associated with the pinning of the contact–line [30] and characterized by receding and advancing contact–angles [47], which are linked to the dewetting and wetting processes, respectively. This phenomenon is basically caused by the chemical properties [39], or more accurately by the heterogeneity [15, 59] in the properties of the solid substrate that comes into contact with the gas and liquid phases. Surface roughness is also a determining factor causing a dramatic variation in the contact–angle hysteresis [99].

In order to successfully perform numerical simulation of droplets in contact with solid substrates, the above–mentioned phenomena should be consistently incorporated in the computational model of the two–phase flow.

1.3 State of the Art Techniques

In the following, the numerical techniques that are so far developed for modeling the droplet dynamics are briefly reviewed.

1.3.1 Simplified Models

The so-called "force balance" models [74] constitute the simplest approach for the analysis of the droplet configuration. With the aim of estimating the detachment condition in terms of the size of the droplet, the net force equilibrium is analytically computed [153]. Although the associated computational cost of such extremely simplified models is low, they are only suitable for the qualitative study of detachment of an isolated droplet in GC.

Simplified approaches have also been developed for the qualitative analysis of liquid transport in porous (or fibrous) media; the class of pore-network models [51, 52, 114] can be utilized to predict the spread of the liquid phase merely at the equilibrium conditions. These approaches rely on the correlation between the pressure difference and the flow rate in micro-throats [100, 154]. Besides the basic formulation, the simplifications can also be imposed to the geometrical complexities [120] and/or the transient nature of the transport mechanisms [84].

Nonetheless, in the present work, neither of such simplifications is utilized and a computational fluid dynamics (CFD) model is developed that solves the Navier-Stokes equations for two-phase flow allowing the accurate capturing of the involved physical phenomena. Another notable approach to performed a detailed simulation in the context of multi–phase flow, but out of the scope of the present work, is the Lattice–Boltzmann method [145].

1.3.2 Lagrangian Interface Tracking

In order to develop a numerical model for multi–phase flows, it is necessary to integrate a mechanism to capture the interface between immiscible phases. Several approaches have been developed that track the interface in the Lagrangian manner, *i.e.* relying on a constantly deforming and/or moving computational mesh fitted to the evolving interface. These class of methods include fully Lagrangian frameworks [80] and arbitrary Lagrangian Eulerian (ALE) methods [132]. A embedded Lagrangian Eulerian approach [105, 106] has also been recently developed and successfully applied to water–air multi–phase flow inside GC [69, 77]. This method is based on a Lagrangian fluid flow solver for the liquid phase (droplets), while the interacting gas flow is treated in the Eulerian framework and solved on a fixed mesh.

The major difficulty with these methods crops up when one should deal with large

and complex mesh deformations. In these cases, it is highly probable that the quality of the computational mesh is deteriorated to an extent that the remeshing process becomes necessary. Therefore, generally, the Lagrangian interface tracking is associated with the computationally highly expensive remeshing techniques. Besides the cost, such approaches lack a systematic methodology for taking into account the topological changes in the interface. In other words, in order to recognize the interface once droplet breakup and merging occur as well as during the movement of their contact–line with a solid substrate, joining and/or separating the mesh nodes should be performed according to some ad-hoc geometrical criteria. These difficulties hinders the usage of this class of approaches for three–dimensional simulation of multi–phase transport phenomena in complex geometrical configurations, which would require frequent costly remeshing and dealing with ambiguities in the re-identification of the liquid–gas interface.

1.3.3 Fully Eulerian Approaches

Dropping the need for mesh deformation, and consequently the remeshing, fully Eulerian methods are more efficient than the above mentioned approaches for un–simplified, namely “direct", numerical modeling. For capturing the evolution of the liquid–gas interface on a fixed computational mesh, different techniques have so far been developed [127], However, the most robust and widely used techniques are the volume of fluid method [60] and the Level-set method [123].

Due to its remarkable mass conservation property, the Volume-of-fluid (VOF) technique [60] has widely been used for CFD applications in the field of liquid–gas transport problems [5, 41, 43, 72]. Nonetheless, by just providing the volume to volume ratio of the phases in each computational cell, it is hardly possible to introduce a generic methodology for efficient reproduction of the phase boundaries [50, 79]. Accurate representation of the geometry of the liquid–gas interface is essential for the reliable calculation of the interfacial forces. In this sense, the VOF technique is not a robust option for a detailed analysis of the phenomena associated with the multi-phase transport in complex media.

The level-set method [123] is a viable alternative for the VOF technique in the context of multi-phase flow simulation. This technique has also been widely utilized [3, 83, 119, 151] to capture the phase boundaries in the liquid–gas flows. Instead of the volume ratio, the level–set method translates the geometrical configuration of the interface into a continuous function, and therefore, greatly facilitates the calculation of the corresponding geometrical data. Nonetheless, generally, the level–set method does not guarantee the

mass conservation (keep phase volume constant in case of incompressible fluids) and requires the implementation of an additional procedure to compensate for the mass loss [49, 116, 146]. In some works, the VOF technique and the level–set method are combined together [121, 122] in order to benefit from their specific properties. However, there is always the risk of incompatibility between the outcome of these two different techniques [93].

Here, it is also worth to mention the phase–field methods [65, 66] that are not classified among the so–called "sharp–interface" capturing techniques. Although the phase–field methods can be a means to circumvent difficulties associated with choosing the adequate model for contact–line dynamics [148], they require an extremely refined mesh in the vicinity of the liquid-gas interface. This leads to prohibitively high computational costs especially in three–dimensional simulations. Nevertheless, this class of methods is out of the scope of the current work and would not be further discussed here.

Surface Tension Treatment

Solving the momentum equation on a fixed computational mesh, one of the main difficulties in the fully Eulerian methods is associated with the imposition of the interfacial conditions, *e.g.* surface tension; the computational cells that form the discretized domain are cut by the phase interface at arbitrary locations, while the flow field is generally continuous inside each cell.

The most common approach to tackle this difficulty is the so-called “continuum surface force” model [14], which is based on the substitution of the interfacial condition by its numerical approximation as a smoothed body force [21, 125, 133]. In other words, the physically localized surface tension is represented by a body force smoothed over a support domain spread across several computational cells and constitute the transition from the liquid to the gas phase. Therefore, the numerical error can be minimized by narrowing this support domain, which requires utilizing a highly refined mesh adjacent to the interface. Especially for three-dimensional simulations or in cases that involve geometrical complexities, such adaptive mesh refinement leads to a high computational cost. Some *ad hoc* techniques have also been proposed to circumvent this issue, such as the ghost fluid method [70, 75] and the sharp interface method [124].

More important than the smoothing error, however, is that the continuum surface force model is incapable of providing a consistent balance between the implemented surface tension and the pressure gradient, or jump in physically consistent model. This issue

leads to significantly large non-physical parasitic velocities called "spurious currents" [94]. In order to resolve this shortcoming, different approaches has so far been proposed such as the cut finite element method [57] and the balanced force approach [1, 45, 140]. These techniques can effectively suppress the spurious currents.

The above–mentioned issues can also be resolved using the class of finite element based techniques that tackle the discontinuities via enriching the generally continuous space [7, 22, 54, 81]. These methods can robustly capture the weak (jump in the gradient) and/or strong (jump in the variable) discontinuities that are internal to the computational elements. If the enrichment is done locally at the level of the (cut) elements, the method is called the enriched finite element method [64]. On the other hand, in the so-called "extended finite element" methods [22], the enrichment is associated with the nodes. One of the main advantages of utilizing the enriched finite element method is that it lets one perform a static condensation step to avoid adding new degrees of freedoms and thus, minimize the computational costs associated with the enriched approximation of the discontinuous variable at the cut.

In the context of two–phase flows, Coppola-Owen and Codina [26] proposed an enriched finite element method for an accurate capturing of the weak pressure discontinuity, *i.e.* a jump in the pressure gradient. They showed that such enrichment effectively resolves the spurious currents that are typically observed in the presence of gravity, due to the jump in the density at the phase interface. More recently, an enriched finite element space was proposed by Ausas *et al.* [6] that is capable of capturing the strong pressure discontinuity (jump) across the interface. This enriched finite element space has already been successfully employed for the numerical simulation of surface–tension dominated two–phase flows [17].

Contact–line Dynamics

The commonly used approach for the numerical modeling of the contact–line dynamics is the so–called "generalized Navier–slip condition" [95, 98], which combines the Navier–slip condition on the solid substrate with a friction force proportional to the velocity of the contact–line. Its thermodynamic consistency [103, 104] and agreement with the molecular dynamic simulation of the wetting dynamics [102] has already been shown. Being utilized in various numerical techniques [55, 78, 142, 143, 151], it comprises the state–of–the–art in the numerical modeling of the moving contact–line. Alternatively, one can impose the standard Navier–slip condition and directly employ a friction force

at the contact–line [77].

Nevertheless, The majority of the numerical models that are developed for addressing the dynamics of the contact–line suffer from severe mesh–dependence of the results [108, 136]. This issue is rooted in two defects of the conventional approaches. Using the meshes of a finite size, which is comparable to the macroscopic length–scale of the problem, it is impossible to fully resolve the hydrodynamics in the "small–scale" vicinity of the contact–line. Even though this unresolved length–scale is far larger than the molecular length–scale, it is still non-resolvable using the common computational meshes [35, 118]. This can however be solved by incorporation of the hydrodynamic theory [2, 76, 144]. The second defect is the representation of the interfacial forces as a smoothed body force [141, 151], which is an essential ingredient of the commonly utilized continuum force approach. In this way, one needs to do excessive mesh refinements in the vicinity of the interface to minimize its "artificial thickness", which is usually supported by a few layers of computational cells.

Another class of methods were also developed that rely on the diffusive, in contrast to the convective, movement of the contact–line [150]. Notable methods in this class are the diffuse interface methods [66, 117, 149]. No further details about this class of methods will be presented here since these methods are out of the scope of the present work.

1.4 Outline of Present Work

In this work, the weak and strong pressure discontinuities across the phase interface are captured using a new enriched finite element space and in order to deal with small–cut instabilities, a specific stabilization term is introduced besides those corresponding to the variational multiscale stabilization [24]. Within the framework of the proposed numerical method, the perfectly sharp interface is treated as a zero–thickness surface. The evolution of the phase interface is captured using the level–set method and the noises are are filtered out by solving an artificial diffusion equation [131] complemented by a correction [134] step. The consistency of this noise filtering technique, especially for cases with a solid contact, is maintained by introduction of the appropriate boundary conditions.

In order to capture the contact–line dynamics, the molecular kinetic model is incorporated into the variational formulation [18] of the method. The sub–elemental variation

in the contact–angle is also taken into account via the simplified form of Cox's relation [27]. The stress singularity is circumvented by employing the Navier–slip condition on the solid substrate. Similar to the phase interface, the contact–line is represented by a (zero–thickness) curve. Finally, the proposed numerical method is further developed by implementing a contact–line pinning mechanism, which underlies the contact–angle hysteresis phenomenon.

In the following, Chapter 2 encloses the elaboration of the proposed enriched finite element method, its stabilization, and the essential requirements of the level–set method, *e.g.* the noise filtering technique. In Chapter 3, the basics of the incorporation of the contact–line dynamics are presented along with the validation tests. Chapter 4 is dedicated to the incorporation of the contact–angle hysteresis. In Appendix A, a side achievements of the present work is presented; namely, an accurate method for the level–set convection. This latter ingredient is beneficial for a significantly more accurate capturing of the evolution of the phase interface.

Chapter 2

Enriched Finite Element/Level–set Framework

2.1 Introduction

As the first step to reach the goal of the present work, in this chapter, the creation of the enriched finite element space, based on the shape functions of the standard finite element space, is described. The proposed method is stabilized within the framework of the variational multiscale approach [24]. Moreover, in order to tackle the small–cut instabilities, the condition of the enrichment matrix, whose inverse is involved in the static condensation procedure, is improved. Besides the enriched finite element method, the level–set method is described in this chapter as a means to capture the evolution of the phase interface. A specific noise reduction technique is further proposed to regularize the level–set function in cases of a dominant surface tension. The above–mentioned aspects of the present work are enclosed in the following publication.

2.2 Article data

Title: An enriched finite element/level-set method for simulating two-phase incompressible fluid flows with surface tension
Authors: M.R. Hashemi, P.B. Ryzhakov and R. Rossi
Journal: Computer Methods in Applied Mechanics and Engineering, Volume 370, 1 October 2020, 113277

Received: April 2020, Revised: June 2020, Accepted: July 2020
DOI: 10.1016/j.cma.2020.113277

An Enriched Finite Element/Level-Set Method For Simulating Two-Phase Incompressible Fluid Flows With Surface Tension

Mohammad R. Hashemi[a,b,*], Pavel B. Ryzhakov[a,b], Riccardo Rossi[a,b]

[a] *Centre Internacional de Mètodes Numèrics en Enginyeria (CIMNE), 08034 Barcelona, Spain*

[b] *Universitat Politècnica de Catalunya (UPC), 08034 Barcelona, Spain*

Abstract

A finite element method is introduced to simulate surface tension dominated flow of two immiscible fluids featuring an enriched space for capturing both strong and weak pressure discontinuities. The proposed enriched finite element space is created utilizing the standard finite element shape functions. Discontinuities are captured by adding merely one additional degree of freedom per each node of the elements cut by the interface. Being local to the cut elements, these additional degrees of freedom are eliminated before assembling the global system of equations following a condensation procedure. The method is stabilized introducing a procedure for improving the conditioning of the enriched pressure contribution to the stiffness matrix in small-cut situations. An improved smoothing strategy based on an artificial diffusion equation is proposed to enhance the performance of the method on rather coarse meshes. A series of three-dimensional two-phase fluid flow benchmarks are solved to assess the performance of the method. Particular attention is paid to surface tension dominated cases. The method is verified by showing its accuracy in capturing strong pressure discontinuity at the interface of a spherical droplet as well as its capability in handling large pressure gradient discontinuity in a hydrostatic liquid-gas container. The method is further validated by simulating oscillations of a slightly disturbed

*Corresponding author.

Email addresses: mhashemi@cimne.upc.edu (Mohammad R. Hashemi), pryzhakov@cimne.upc.edu (Pavel B. Ryzhakov), rrossi@cimne.upc.edu (Riccardo Rossi)

spherical droplet. The mass conservation property of the method and the effect of the smoothing procedure on the result is assessed by simulating the oscillations of a prolate droplet. Ultimately, the method is tested in a more challenging setting by simulating the rising gas bubble inside a liquid domain.

Keywords: Two-phase flow, Surface tension, Stabilized enriched FEM, Strong and weak Pressure discontinuities, Microfluidics, Droplets

1. Introduction

Numerical simulation of two-phase flow of immiscible fluids has become an attractive research topic due to the large range of engineering applications that involve this phenomenon. Among others, these include *e.g.* water-oil flow in a reservoir [1], cavitation [2, 3], various microfluidic applications [4] and liquid-gas flow in micro-channels [5, 6]. One of the recent applications where accurate modeling of the two-phase flow is essential is the polymer electrolyte membrane (PEM) fuel cell, an efficient eco-friendly energy conversion device [7]; developing a numerical tool capable of accurately predicting the excessive liquid water evacuation through the diffusion layer and eventually gas channels of PEM fuel cells can be seen as a basic prerequisite to making an important technological advancement, since inadequate evacuation of liquid water strongly limits the efficiency and durability of the cells [8].

In the above-mentioned applications however, the accuracy, robustness, and efficiency of the numerical methods are adversely affected by the principal role of the surface tension [9]. Unfortunately, the existing commercial and open-source general purpose computational fluid dynamics solvers rarely offer a ready-to-use option to simulate surface tension dominated multi-phase flows.

In the numerical simulation of surface tension dominated flows, the main challenge is to consistently represent the strong pressure discontinuity (jump) across the interface as well as the weak discontinuity in the pressure gradient that is associated with the jump in density. Moreover, accurate representation of these discontinuities are affecting the shape and position of the liquid-gas interface and vice versa. These aspects are particularly challenging since the mesh-based numerical methods are conventionally developed to model continuous fields inside a computational cell. In order to overcome this shortcoming, several approaches, in which the interface is defined by the moving computational mesh were developed. These include a fully

Lagrangian approach [10], an Arbitrary Lagrangian Eulerian method [11], and the Embedded Lagrangian Eulerian method [12]. However, when dealing with large complex interface deformations, the computationally costly remeshing process is unavoidable. Moreover, in such frameworks there exist no general criteria for the re-identification of the interface once a topological change takes place, *i.e.* ad-hoc geometrical criteria are required to join or separate nodes during the breakup and merging of the phase domains as well as the contact with a solid surface.

On the other hand, fixed-mesh Eulerian methods are more efficient in the sense that remeshing is unnecessary. Moreover, the mesh quality is always maintained. However, since the interface generally cuts the computational cells in arbitrary locations, one needs to develop special strategies for dealing with the surface tension.

Within the framework of Eulerian methods, the most commonly used approach is the so-called "continuum surface force" model [13], which relies on representing surface tension as a smoothed body force. In order to minimize the smoothing error in this approach, the support domain that is generally chosen to be several cells long should be as narrow as possible. Evidently, this technique, needs a highly refined mesh in the vicinity of the interface. Moreover, this technique results in an inconsistency between the modeled surface tension and the pressure jump that in turn leads to large non-physical spurious (parasitic) currents [14]. These issues have been addressed in various publications. The ghost fluid method [15, 16], and the sharp interface method [17] were introduced to resolve the smoothing error while the balanced force approach [18, 19, 20] was proposed to suppress the spurious currents. The manipulated finite element space proposed by Ausas *et al.* [21] and the cut finite element method [22] are also among the alternative approaches.

Besides the above-mentioned methods, there is a class of techniques aiming at capturing intra-element discontinuities through enriching the approximation of variables within the framework of the finite element method [23, 24, 25]. This enrichment can either be associated with nodes resulting in the so-called "extended finite element method" [24] or be local to the elements cut by the interface. This latter option is the basis of the so-called "enriched finite element method" [26]. In the enriched finite element method, one can utilize a static condensation to eliminate the additional (enriched) degrees of freedom and consequently enhance the efficiency of the computations. Coppola-Owen and Codina [27] introduced an enriched finite element

method for two-phase flows with a density jump at the interface and consequently a weak pressure (gradient) discontinuity due to the jump in the gravitational forces. They reported that using the enriched finite element space to represent the discontinuity in the pressure gradient, the spurious currents are significantly reduced. Later, Ausas *et al.* [28] proposed another enriched finite element space to capture the strong pressure discontinuity across the interface. This enriched pressure space was being successfully applied to the simulation of two-phase liquid-gas capillary flow [29].

In the present work, a new enriched finite element space is introduced that can capture both the strong and weak pressure discontinuities. This enriched space is created based on the shape functions of the standard finite element space. Moreover, the proposed enriched finite element method is stabilized within the framework of variational multiscale approach [30]. A stabilization procedure is also introduced to maintain the stiffness matrix well-conditioned during the condensation process.

In addition to the challenge in the implementation of the surface tension effect, unlike the Lagrangian methods, a robust interface capturing technique is also an essential need for a fixed-mesh Eulerian method. There are a number of approaches for this aim [31]; among them the volume of fluid method [32] and the Level-set method [33] are the most established ones. The level-set method is the natural choice to be used in conjunction with the finite element method since it produces a smooth function representing the interface, which can be directly employed to calculate the curvature. Nevertheless, a rather large surface tension can disturb this notable feature by introducing noise. This can be cured by either increasing the temporal and spatial resolutions [34] or using a smoothing procedure [35, 36]. In the present work, the artificial diffusion equation proposed by Tornberg and Engquist [36] is used. However, this process is known to result in spurious shrinkage, *i.e.* a non-physical volume-loss, in case the level-set function is substituted by the smoothed function. In order to alleviate this issue in the present work, this smoothing technique is improved borrowing the idea originally proposed for the Laplacian surface smoothing [37].

In the following sections, first, the pressure enriched finite element space and the stabilization technique is discussed. The implemented interface capturing technique, i.e. the level-set method along with the smoothing procedure, is then presented. In section 3, verification and validation test-cases are reported. The paper ends with a summary and several concluding remarks.

2. Numerical Method

2.1. Governing Equations

Complying with the continuum condition, fluid flow is governed by momentum conservation equation,

$$\rho\left(\frac{\partial \mathbf{u}}{\partial t}+\mathbf{u}\cdot\nabla\mathbf{u}\right)=\rho\mathbf{b}+\nabla\cdot\boldsymbol{\sigma}\quad\text{in }\Omega, \tag{1}$$

and the mass conservation equation,

$$\frac{\partial \rho}{\partial t}+\nabla\cdot(\rho\mathbf{u})=\frac{\partial \rho}{\partial t}+\mathbf{u}\cdot\nabla\rho+\rho\nabla\cdot\mathbf{u}=0\quad\text{in }\Omega, \tag{2}$$

where ρ is density, $\mathbf{b}$ is the body force, and $\mathbf{u}$ denotes velocity vector. It should be noted that for an incompressible homogeneous single-fluid, Eq. (2) reduces to $\nabla\cdot\mathbf{u}=0$. Fluid domain $\Omega\subset\mathbb{R}^d$ is bounded by $\partial\Omega\subset\mathbb{R}^{d-1}$. For a Newtonian fluid total stress tensor is obtained as

$$\boldsymbol{\sigma}=-p\mathbb{I}+\mu\left(\nabla\mathbf{u}+\nabla\mathbf{u}^T\right), \tag{3}$$

where μ is viscosity, p is pressure, and $\mathbb{I}$ denotes the identity tensor. Equations (1) and (2) are subject to initial condition

$$\mathbf{u}(\mathbf{x},0)=\mathbf{u}_0\quad\text{in }\Omega, \tag{4}$$

as well as Dirichlet

$$\mathbf{u}(\mathbf{x},t)=\mathbf{u}_D\quad\text{on }\partial\Omega_D, \tag{5}$$

and Neumann

$$\mathbf{t}(\mathbf{x},t)=\mathbf{t}_N\quad\text{on }\partial\Omega_N, \tag{6}$$

boundary conditions with the initial velocity field $\mathbf{u}_0$ and traction vector $\mathbf{t}=\mathbf{n}\cdot\boldsymbol{\sigma}$, where $\mathbf{n}$ denotes the outward normal vector to $\partial\Omega$.

2.1.1. Two-phase Flow

The aim of the present work is to develop a numerical method to simulate two-phase (more specifically liquid-gas) flow. Considering two immiscible fluids, one can distinguish subdomains Ω_1 and Ω_2, which are occupied by fluid 1 and fluid 2, respectively, with $\Omega=\Omega_1\cup\Omega_2$ and $\Omega_1\cap\Omega_2=\varnothing$. These

two domains are recognized by specific properties of the occupying fluid, (ρ_1, μ_1) and (ρ_2, μ_2). At the fluids interface $\Gamma = \partial\Omega_1 \cap \partial\Omega_2$,

$$[\![\mathbf{u}(\mathbf{x}, t)]\!] = 0 \quad \text{on } \Gamma \tag{7}$$

ensures the velocity continuity. Surface tension is included as

$$[\![\mathbf{t}(\mathbf{x}, t)]\!] = -\gamma\kappa\mathbf{n} \quad \text{on } \Gamma, \tag{8}$$

with surface tension coefficient γ, interface curvature κ, and $\mathbf{n}$ on Γ being the outward unit normal to $\partial\Omega_1$.

2.2. Variational Formulation

Considering test functions $\mathbf{w} \in \boldsymbol{\mathcal{V}}(\Omega)$ vanishing at $\partial\Omega_D$ and $q \in \mathcal{Q}(\Omega)$ for the momentum and continuity equations, respectively, one obtains the variational form of Eqs. (1) and (2) as

$$\int_\Omega \rho \left(\frac{\partial \mathbf{u}}{\partial t} + \mathbf{u} \cdot \nabla \mathbf{u} \right) \cdot \mathbf{w} d\Omega = \int_\Omega \rho \mathbf{b} \cdot \mathbf{w} d\Omega + \int_\Omega (\nabla \cdot \boldsymbol{\sigma}) \cdot \mathbf{w} d\Omega \tag{9}$$

and

$$\int_\Omega q\rho \left(\nabla \cdot \mathbf{u} \right) d\Omega = 0, \tag{10}$$

where $\boldsymbol{\mathcal{V}}(\Omega) \subset [\mathcal{H}^1(\Omega)]^d$, $\mathcal{Q}(\Omega) \subset \mathcal{L}^2(\Omega)$. Rewriting Eq. (9) using integration by parts for the stress term, one obtains

$$\begin{aligned} \int_\Omega \rho \left(\frac{\partial \mathbf{u}}{\partial t} + \mathbf{u} \cdot \nabla \mathbf{u} \right) \cdot \mathbf{w} d\Omega = \int_\Omega \rho \mathbf{b} \cdot \mathbf{w} d\Omega \quad &+ \quad \int_\Omega \nabla \cdot (\boldsymbol{\sigma} \cdot \mathbf{w}) \, d\Omega \\ &- \quad \int_\Omega \boldsymbol{\sigma} : \nabla \mathbf{w} d\Omega \end{aligned} \tag{11}$$

Expanding stress for a Newtonian fluid (Eq. (3)), on obtains

$$\begin{aligned} \int_\Omega \rho \left(\frac{\partial \mathbf{u}}{\partial t} + \mathbf{u} \cdot \nabla \mathbf{u} \right) \cdot \mathbf{w} d\Omega = \int_\Omega \rho \mathbf{b} \cdot \mathbf{w} d\Omega + \int_\Omega p \nabla \cdot \mathbf{w} d\Omega \\ - \int_\Omega \mu \left(\nabla \mathbf{u} + \nabla \mathbf{u}^T \right) : \nabla \mathbf{w} d\Omega + \int_{\partial\Omega} \mathbf{t} \cdot \mathbf{w} d(\partial\Omega). \end{aligned} \tag{12}$$

Using the finite element method (FEM), equation set (12) is discretized on each element Ω^e, and then summed up over the entire computational

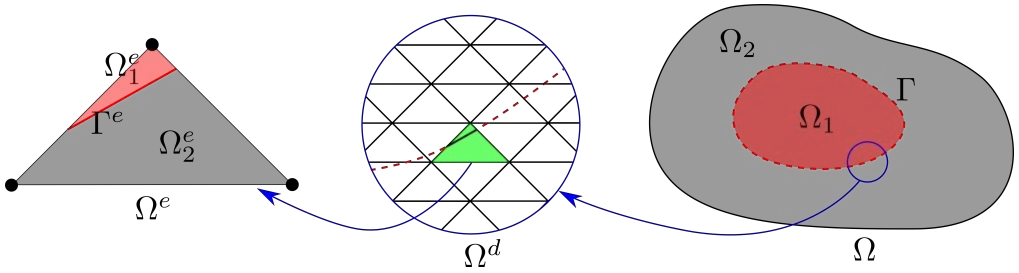

Figure 1: Schematic of two-fluid discretized domain, Ω_1^e, Ω_2^e, and Γ^e. Continuum domains are marked by Ω_1 and Ω_2.

(discretized) fluid domain Ω^d in order to obtain an assembled system of equations. The schematic of the domains is illustrated in Fig. 1. It is evident that by using linear elements, discretized interface Γ^d is constructed by line segment Γ^e in 2D (flat surface Γ^e in 3D). In the following, subscript d is omitted and the same notation is used for both the continuum and discretized domains.

For internal elements that are not cut by the interface, the surface integral on the right-hand side of Eq. (12) is canceled out by assembling the equations over the set of neighboring elements. Nevertheless, this integral must be calculated on $\partial\Omega_N$ and Γ to give

$$\int_\Omega \rho\left(\frac{\partial \mathbf{u}}{\partial t} + \mathbf{u}\cdot\nabla\mathbf{u}\right)\cdot\mathbf{w}d\Omega = \int_\Omega \rho\mathbf{b}\cdot\mathbf{w}d\Omega - \int_\Omega \mu\left(\nabla\mathbf{u}+\nabla\mathbf{u}^T\right):\nabla\mathbf{w}d\Omega$$
$$+\int_\Omega p\nabla\cdot\mathbf{w}d\Omega + \int_{\partial\Omega}\mathbf{t}_N\cdot\mathbf{w}d(\partial\Omega_N) - \int_\Gamma -\gamma\kappa\mathbf{n}\cdot\mathbf{w}d\Gamma. \tag{13}$$

In this work, cut elements Ω_c^e are split into $\Omega_1^e = \Omega_c^e \cap \Omega_1$ and $\Omega_2^e = \Omega_c^e \cap \Omega_2$ as schematically shown in Fig. 2 for a possible case and therefore, the last term on the right-hand-side of Eq. (13) is directly calculated on $\Gamma^e = \Omega_c^e \cap \Gamma$. In this way, unlike the conventional continuum surface force approach [13], no smoothing error is introduced. It must be noted that this splitting is performed merely to facilitate the calculation of the integral terms in Eq. (13). In other words, variables are stored only at the nodes of the base element, Ω_c^e, while pressure enrichment as described in section 2.2.1 is the key to handle the discontinuity across the interface.

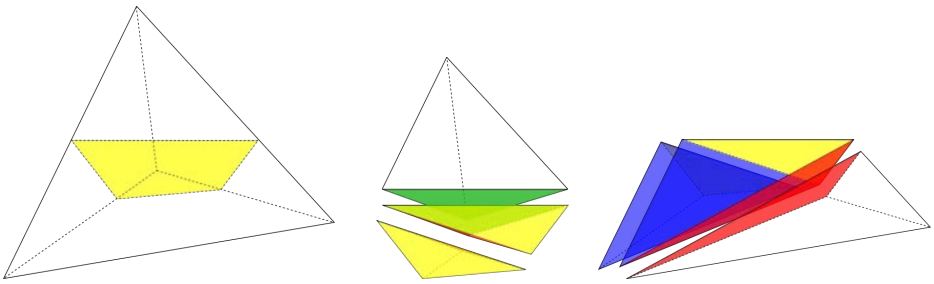

(a) Ω_c^e with Γ^e shaded (b) Ω_1^e (c) Ω_2^e

Figure 2: Schematic of a possible cut in a tetrahedral element. Matching faces are marked with the same color.

2.2.1. Enriched Finite Element Space

Using the standard finite element approximation of variables, $[\mathbf{u}_h, p_h] \in \boldsymbol{\mathcal{V}}_h \times \mathcal{Q}_h$, which is essentially continuous over the solution domain, the consistent representation of the discontinuity condition (8) is unfeasible. Precisely, the standard finite element space represents the discontinuity as a continuous variation with a sharp gradient in the vicinity of the cut. This shortcoming leads to severe spurious (parasitic) currents whenever $\gamma \neq 0$ is taken. In the present work, this issue is resolved by utilizing an enriched finite element space, $\mathcal{Q} = \mathcal{Q}_h \oplus \mathcal{Q}^{enr}$, for pressure. Denoting the standard finite element approximation by subscript h, for $\mathbf{x}$ inside a cut element, the approximated variables read

$$\bar{\mathbf{u}}(\mathbf{x}, t) = \mathbf{u}_h(\mathbf{x}, t), \tag{14}$$

and

$$\bar{p}(\mathbf{x}, t) = p_h(\mathbf{x}, t) + p_{enr}(\mathbf{x}, t), \tag{15}$$

where

$$p_h(\mathbf{x}, t) = \sum_{I \in \mathcal{N}_c^e} N_I(\mathbf{x}) p_I(t), \tag{16}$$

and

$$p_{enr}(\mathbf{x}, t) = \sum_{I \in \mathcal{N}_c^e} N_I^{enr}(\mathbf{x}) p_I^{enr}(t). \tag{17}$$

For the sake of simplicity in the rest of this paper, the over-bar is omitted; *i.e.* $\mathbf{u}$ and p denote the approximated velocity and pressure, respectively. Here, $\mathcal{N}_c^e$ is the set of all nodes of the cut element Ω_c^e and $N_I(\mathbf{x})$ is the finite

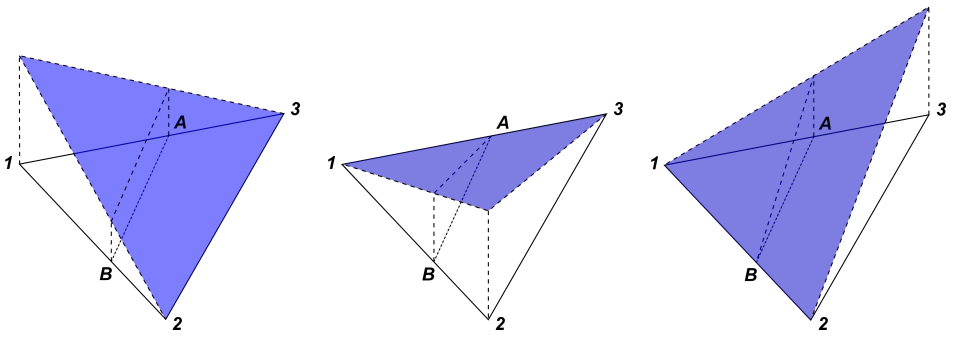

(a) N_1 (b) N_2 (c) N_3

Figure 3: Finite element shape functions. The interface is represented by line AB.

element shape function associated to node I. In this work, enriched shape function N_I^{enr} is defined as

$$N_I^{enr}(\mathbf{x},t) = \frac{1}{2}H(\mathbf{x},t)\left(H(\mathbf{x},t) - H(\mathbf{x}_I,t)\right)N_I(\mathbf{x}), \tag{18}$$

where $H(\mathbf{x},t)$ is defined as

$$H(\mathbf{x},t) = \begin{cases} 1 & if\ \phi(\mathbf{x},t) > 0 \\ -1 & if\ \phi(\mathbf{x},t) \leq 0 \end{cases} \tag{19}$$

The standard and enriched shape functions are illustrated in Figs. 3 and 4, respectively. For more simplicity in these illustrations, a 2D linear triangular element is presented. It is easy to show that using these enriched shape functions, $p(\mathbf{x}_I,t) = p_h(\mathbf{x}_I,t)$. The proposed choice of N^{enr} allows using the existing standard shape functions to construct the discontinuous enriched space. Another beneficial feature is that the jump in the pressure field and the difference in the pressure gradient across the interface are efficiently represented by introducing three (four in case of 3D tetrahedral element) additional degrees of freedom, p_I^{enr}, for each element cut by the interface. In this way, p^{enr} and $q^{enr} \in \mathcal{Q}^{enr}$ can be introduced to complement p_h and $q_h \in \mathcal{Q}_h$, respectively. Theses additional degrees of freedoms, p_I^{enr}, are local and hence can be eliminated from the system of equations following the condensation procedure elaborated in section 2.2.3. It is also worth to note that for incompressible Newtonian two-phase systems, *e.g.* water-air flow, pressure dominates the normal stress force, $\mathbf{t}\cdot\mathbf{n}$, acting on the interface. In

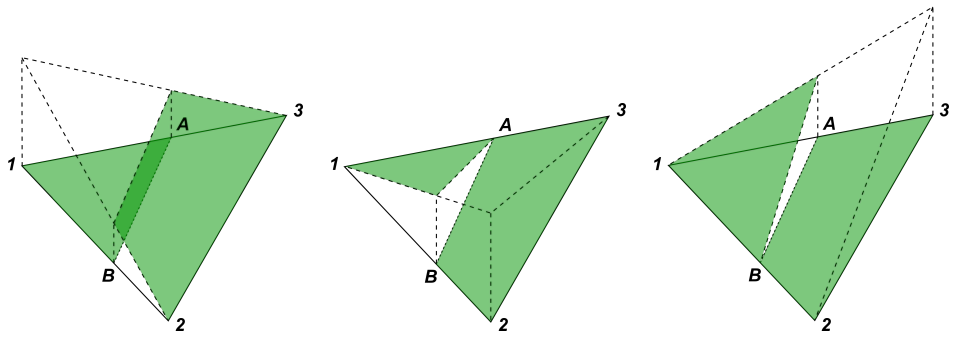

(a) N_1^{enr} (b) N_2^{enr} (c) N_3^{enr}

Figure 4: Enriched shape functions. The interface is represented by line AB.

this sense, satisfactory results can be obtained without acquiring an enriched velocity field.

2.2.2. Stabilization

In the present work, $P1 - P1$ elements are utilized and the numerical method is stabilized within the Variational Multi-Scale (VMS) framework [30]. Approximating $[\mathbf{u}, p]$ using elements of a finite size, the numerical method is unable to resolve the physics at the spatial scale smaller than the element-size. The idea of VMS is to include the unresolved contributions known as "sub-scales" in the variational formulation [38]. Denoting these sub-scale by subscript s, one can write

$$\mathbf{u} = \mathbf{u}_h + \mathbf{u}_s, \tag{20}$$

and

$$p = p_h + p^{enr} + p_s. \tag{21}$$

Substituting the complemented velocity (2.2.2) and pressure (21) into Eq. (13) and summing up the variational form of continuity equation (10) give

$$
\begin{aligned}
&-\int_{\Omega}\rho\left(\frac{\partial \mathbf{u}_h}{\partial t}+\mathbf{u}\cdot\nabla\mathbf{u}_h\right)\cdot\mathbf{w}d\Omega-\int_{\Omega}\rho\left(\frac{\partial \mathbf{u}_s}{\partial t}+\mathbf{u}\cdot\nabla\mathbf{u}_s\right)\cdot\mathbf{w}d\Omega\\
&+\int_{\Omega}\rho\mathbf{b}\cdot\mathbf{w}d\Omega+\int_{\Omega}\left(p_h+p_s+p^{enr}\right)\nabla\cdot\mathbf{w}d\Omega-\int_{\Gamma}-\gamma\kappa\mathbf{n}\cdot\mathbf{w}d\Gamma\\
&-\int_{\Omega}\mu\left(\nabla\mathbf{u}_h+\nabla\mathbf{u}_h^T\right):\nabla\mathbf{w}d\Omega-\int_{\Omega}\mu\left(\nabla\mathbf{u}_s+\nabla\mathbf{u}_s^T\right):\nabla\mathbf{w}d\Omega\\
&+\int_{\partial\Omega}\mathbf{t}_N\cdot\mathbf{w}d(\partial\Omega_N)+\int_{\Omega}\left(q+q^{enr}\right)\rho\left[\nabla\cdot\left(\mathbf{u}_h+\mathbf{u}_s\right)\right]d\Omega=0
\end{aligned}
\tag{22}
$$

It is worth to note that $\mathbf{u}_s$ and p_s are zero on boundary $\partial\Omega$ and thus, the corresponding surface integral terms are omitted. Noting that

$$
\begin{aligned}
\int_{\Omega}\rho\left(\mathbf{u}\cdot\nabla\mathbf{u}_s\right)\cdot\mathbf{w}d\Omega \quad &= \int_{\Omega}\rho\nabla\cdot\left[\mathbf{u}\left(\mathbf{u}_s\cdot\mathbf{w}\right)\right]d\Omega-\int_{\Omega}\rho\mathbf{u}\cdot\left(\nabla\mathbf{w}\cdot\mathbf{u}_s\right)d\Omega\\
&-\int_{\Omega}\rho\left(\nabla\cdot\mathbf{u}\right)\cdot\left(\mathbf{w}\cdot\mathbf{u}_s\right)d\Omega,
\end{aligned}
\tag{23}
$$

and the fact that $\mathbf{u}_s$ can be considered a static variable ($\partial\mathbf{u}_s/\partial t\approx 0$), the following form of Eq. (22) is obtained.

$$
\begin{aligned}
&-\int_{\Omega}\rho\left(\frac{\partial \mathbf{u}_h}{\partial t}+\mathbf{u}\cdot\nabla\mathbf{u}_h\right)\cdot\mathbf{w}d\Omega+\int_{\Omega}\rho\mathbf{u}\cdot\left(\nabla\mathbf{w}\cdot\mathbf{u}_s\right)d\Omega+\int_{\Omega}\rho\left(\nabla\cdot\mathbf{u}\right)\cdot\left(\mathbf{w}\cdot\mathbf{u}_s\right)d\Omega\\
&+\int_{\Omega}\rho\mathbf{b}\cdot\mathbf{w}d\Omega+\int_{\Omega}\left(p_h+p_s+p^{enr}\right)\nabla\cdot\mathbf{w}d\Omega-\int_{\Gamma}-\gamma\kappa\mathbf{n}\cdot\mathbf{w}d\Gamma\\
&-\int_{\Omega}\mu\left(\nabla\mathbf{u}_h+\nabla\mathbf{u}_h^T\right):\nabla\mathbf{w}d\Omega-\int_{\Omega}\mu\left(\nabla\mathbf{u}_s+\nabla\mathbf{u}_s^T\right):\nabla\mathbf{w}d\Omega\\
&+\int_{\partial\Omega}\mathbf{t}_N\cdot\mathbf{w}d(\partial\Omega_N)+\int_{\Omega}\left(q+q^{enr}\right)\rho\left[\nabla\cdot\left(\mathbf{u}_h+\mathbf{u}_s\right)\right]d\Omega=0
\end{aligned}
\tag{24}
$$

In the present work, the algebraic sub-grid scale technique [39, 40] is chosen to model the sub-scales $\mathbf{u}_s$ and p_s as

$$
\mathbf{u}_s(\mathbf{u}_h,p_h,p^{enr})=\tau_1\mathbf{r}^m(\mathbf{u}_h,p_h,p^{enr}),
\tag{25}
$$

and

$$
p_s(\mathbf{u}_h)=\tau_2 r^c(\mathbf{u}_h),
\tag{26}
$$

where residuals of the momentum and continuity equations are

$$\begin{aligned}\mathbf{r}^m(\mathbf{u}_h, p_h, p^{enr}) \quad &= \rho\mathbf{b} - \rho\left(\frac{\partial \mathbf{u}_h}{\partial t} + \mathbf{u}\cdot\nabla\mathbf{u}_h\right) + \nabla p_h \\ &+\nabla p^{enr} - \nabla\cdot\left[\mu\left(\nabla\mathbf{u}_h + \nabla\mathbf{u}_h^T\right)\right], \end{aligned} \tag{27}$$

and

$$r^c(\mathbf{u}_h) = -\rho\nabla\cdot\mathbf{u}_h, \tag{28}$$

respectively. In Eqs. (25) and (26),

$$\tau_1 = \left(\frac{\rho}{\Delta t} + \frac{c_1\mu}{h_e^2} + \frac{c_2\rho\|\mathbf{u}\|}{h_e}\right)^{-1} \tag{29}$$

and

$$\tau_2 = \frac{h_e^2}{c_1\tau_1} \tag{30}$$

are constant stabilization coefficients with h_e denoting an average element size, $c_1 = 4$, and $c_2 = 2$. For a linear element, the viscous stress term on the right-hand-side of Eq. (27) vanishes. Using integration by parts and taking into account that $\mathbf{u}_s$ is essentially zero on the boundary, one can write

$$\int_\Omega \left(q + q^{enr}\right)\rho\left(\nabla\cdot\mathbf{u}_s\right)d\Omega = -\int_\Omega \nabla\left(q + q^{enr}\right)\cdot\left(\rho\mathbf{u}_s\right)d\Omega \tag{31}$$

Using Eqs. (25) and (26) in Eq. (24), the residual of the variational formulation is

$$\begin{aligned}&\boldsymbol{\mathcal{R}}(\mathbf{u}_h, \mathbf{w}, p_h, q, p^{enr}, q^{enr}) = -\int_\Omega \rho\left(\frac{\partial \mathbf{u}_h}{\partial t} + \mathbf{u}\cdot\nabla\mathbf{u}_h\right)\cdot\mathbf{w}d\Omega \\ &+\int_\Omega \rho\mathbf{u}\cdot\left(\nabla\mathbf{w}\cdot\mathbf{u}_s\right)d\Omega + \int_\Omega \rho\left(\nabla\cdot\mathbf{u}\right)\cdot\left(\mathbf{w}\cdot\mathbf{u}_s\right)d\Omega \\ &+\int_\Omega \rho\mathbf{b}\cdot\mathbf{w}d\Omega + \int_\Omega \left(p_h + p_s + p^{enr}\right)\nabla\cdot\mathbf{w}d\Omega - \int_\Gamma -\gamma\kappa\mathbf{n}\cdot\mathbf{w}d\Gamma \\ &-\int_\Omega \mu\left(\nabla\mathbf{u}_h + \nabla\mathbf{u}_h^T\right):\nabla\mathbf{w}d\Omega - \int_\Omega \mu\left(\nabla\mathbf{u}_s + \nabla\mathbf{u}_s^T\right):\nabla\mathbf{w}d\Omega + \int_{\partial\Omega} \mathbf{t}_N\cdot\mathbf{w}d(\partial\Omega_N) \\ &+\int_\Omega \left(q + q^{enr}\right)\rho\left(\nabla\cdot\mathbf{u}_h\right)d\Omega - \int_\Omega \nabla\left(q + q^{enr}\right)\cdot\left(\rho\mathbf{u}_s\right)d\Omega \end{aligned} \tag{32}$$

2.2.3. Condensation of Additional Degrees of Freedom

The discretized system of equations for each element can be derived by applying the generalized Newton-Raphson method to the residual of the variational formulation as

$$\sum_{J\in\mathcal{N}^e}\left[\frac{\partial}{\partial(\mathbf{u}_J,p_J,p_J^{enr})}\left(\frac{\partial\boldsymbol{\mathcal{R}}(\mathbf{u}_h,\mathbf{w},p_h,q,p^{enr},q^{enr})}{\partial(\mathbf{w}_I,q_I,q_I^{enr})}\right)\right](\delta\mathbf{u}_J,\delta p_J,\delta p_J^{enr}) = \frac{\partial\boldsymbol{\mathcal{R}}(\mathbf{u}_h,\mathbf{w},p_h,q,p^{enr},q^{enr})}{\partial(\mathbf{w}_I,q_I,q_I^{enr})} \quad \forall\, I\in\mathcal{N}^e \tag{33}$$

where $I,J\in\mathcal{N}^e$ and $\mathcal{N}^e$ denotes all nodes of element e and δ denotes the increment of a variable. It should be noted that p_I^{enr} and q_I^{enr} are defined only for elements cut by the interface. Equation (33) can be split into standard and enriched parts as

$$\begin{aligned}\sum_{J\in\mathcal{N}^e}\left[\frac{\partial}{\partial(\mathbf{u}_J,p_J)}\left(\frac{\partial\mathbf{R}(\mathbf{u}_h,\mathbf{w},p_h,q,p^{enr},q^{enr})}{\partial(\mathbf{w}_I,q_I)}\right)\right](\delta\mathbf{u}_J,\delta p_J) + \\ \sum_{J\in\mathcal{N}^e}\left[\frac{\partial}{\partial(p_J^{enr})}\left(\frac{\partial\mathbf{R}(\mathbf{u}_h,\mathbf{w},p_h,q,p^{enr},q^{enr})}{\partial(\mathbf{w}_I,q_I)}\right)\right](\delta p_J^{enr}) = \\ \frac{\partial\mathbf{R}(\mathbf{u}_h,\mathbf{w},p_h,q,p^{enr},q^{enr})}{\partial(\mathbf{w}_I,q_I)} \quad \forall\, I\in\mathcal{N}^e\end{aligned} \tag{34}$$

and

$$\begin{aligned}\sum_{J\in\mathcal{N}^e}\left[\frac{\partial}{\partial(\mathbf{u}_J,p_J)}\left(\frac{\partial\mathbf{R}(\mathbf{u}_h,\mathbf{w},p_h,q,p^{enr},q^{enr})}{\partial(q_I^{enr})}\right)\right](\delta\mathbf{u}_J,\delta p_J) + \\ \sum_{J\in\mathcal{N}^e}\left[\frac{\partial}{\partial(p_J^{enr})}\left(\frac{\partial\mathbf{R}(\mathbf{u}_h,\mathbf{w},p_h,q,p^{enr},q^{enr})}{\partial(q_I^{enr})}\right)\right](\delta p_J^{enr}) = \\ \frac{\partial\mathbf{R}(\mathbf{u}_h,\mathbf{w},p_h,q,p^{enr},q^{enr})}{\partial(q_I^{enr})} \quad \forall\, I\in\mathcal{N}^e.\end{aligned} \tag{35}$$

Rewriting these equations in matrix form, one obtains

$$\mathbf{KU}+\mathbf{VP}_{enr}=\mathbf{F} \tag{36}$$

and

$$\mathbf{HU}+\mathbf{K}_{enr}\mathbf{P}_{enr}=\mathbf{F}_{enr}. \tag{37}$$

Here, $\mathbf{U} = (\delta\mathbf{u}, \delta p)$ contains all the nodal unknowns (sixteen in case of a tetrahedral element), while $\mathbf{P}_{enr}$ contains the unknowns associated with enriched pressures (four in case of a tetrahedral element). Note that $\mathbf{K}_{enr}$ is a local matrix for each cut element (with the size of 4 x 4 for a linear tetrahedron).

Condensation implies deriving an equation for δp^{enr} using Eq. (35) and substituting it in Eq. (34). This results in

$$\left[\mathbf{K} - \mathbf{V}\mathbf{K}_{enr}^{-1}\mathbf{H}\right]\mathbf{U} = \mathbf{F} - \mathbf{V}\mathbf{K}_{enr}^{-1}\mathbf{F}_{enr} \tag{38}$$

2.2.4. Remedy for Small-cut Elements

Generally, the numerical methods that are developed to simulate multiphase flows on a fixed mesh are prone to severe instabilities when small-cut elements are present in the computational domain, *i.e.* volume ratio of Ω_1^e/Ω_2^e is either extremely large or infinitesimally small comparing to the numerical accuracy of the computing system. For the present method, one of the main causes for such instabilities is the failure of the condensation procedure due to the poor condition of $\mathbf{K}_{enr}$ preventing the calculation of its inverse. In this work, this issue is resolved by penalizing the elemental system of equations as

$$\int_\Gamma \alpha[\![\nabla p - \mathcal{G}]\!] \cdot [\![\nabla q]\!] d\Gamma = 0. \tag{39}$$

Here, $[\![\mathcal{G}]\!]$ represents an approximation of the jump in the pressure gradient that is evaluated in each cut element from a nodal approximation of $\mathbf{G} = \nabla p_h$ as

$$[\![\mathcal{G}]\!]^e \approx \sum_{I\in\mathcal{N}_-^e} \mathbf{G}_I N_I / \sum_{I\in\mathcal{N}_-^e} N_I - \sum_{I\in\mathcal{N}_+^e} \mathbf{G}_I N_I / \sum_{I\in\mathcal{N}_+^e} N_I, \tag{40}$$

where $\mathcal{N}_-^e = \mathcal{N}^e \cap \Omega_1$ and $\mathcal{N}_+^e = \mathcal{N}^e \cap \Omega_2$. Considering the role of enriched pressures in the elements cut by the interface, for more simplicity, the contribution of cut elements in the calculation of $\mathbf{G}$ is neglected. It is also worth noting that due to the continuity of the basic finite element space, $[\![\nabla p_h]\!] = [\![\nabla a_h]\!] = 0$ and consequently,

$$[\![\nabla p]\!] = [\![\nabla p_h]\!] + [\![\nabla p_{enr}]\!] = [\![\nabla p_{enr}]\!], \tag{41}$$

and

$$[\![\nabla q]\!] = [\![\nabla q_h]\!] + [\![\nabla q_{enr}]\!] = [\![\nabla q_{enr}]\!]. \tag{42}$$

Therefore, the penalty equation is equivalent to

$$\int_\Gamma \alpha[\![\nabla p_{enr}]\!] \cdot [\![\nabla q_{enr}]\!] d\Gamma = \int_\Gamma \alpha[\![\mathcal{G}]\!] \cdot [\![\nabla q_{enr}]\!] d\Gamma. \tag{43}$$

The penalty coefficient, α, is estimated by analyzing the order of terms appearing in $\mathbf{K}_{enr}$, which consists of

$$\int_\Omega \rho\tau_1 \left(\nabla q_{enr} \cdot \nabla p_{enr}\right) d\Omega. \tag{44}$$

Therefore,

$$\alpha = \rho \left(\frac{\rho}{\Delta t} + \frac{c_1 \mu}{h_e^2} + \frac{c_2 \rho \|\mathbf{u}\|}{h_e} \right)^{-1} \left(\frac{V_{element}}{A_{cut}} \right). \tag{45}$$

The ratio of the volume of the element to the area of the cut interface, $V_{element}/A_{cut}$, scales α with the size of the cut and consequently ensures that $\mathbf{K}_{enr}$ maintains its good condition in severe cases of a small-cut.

2.3. Level Set Method

In the previous sections, the position of the interface was considered to be known a priori at each time-step. In this sense, it is necessary to follow the evolution of the interface during the time-marching procedure. Since, an Eulerian approach is employed in this work, it is not a straightforward task to track the interface. Therefore, the level-set method [33] is utilized as a means to determine Γ, and consequently the evolution of Ω_1 and Ω_2 in time. The basic idea is to introduce continuous function ϕ, which determines the extent of fluid domains, Ω_1 and Ω_2, as well as the interface Γ in the following manner;

$$\phi(\mathbf{x}, t) = \begin{cases} < 0 & \text{if } \mathbf{x} \in \Omega_1 \\ 0 & \text{if } \mathbf{x} \in \Gamma \\ > 0 & \text{if } \mathbf{x} \in \Omega_2 \end{cases} \tag{46}$$

This property of ϕ is maintained by taking into account its convection in accordance to the velocity field as

$$\frac{\partial \phi}{\partial t} + \mathbf{u} \cdot \nabla \phi = 0 \quad \text{in } \Omega. \tag{47}$$

This equation, which is derived from the mass conservation Eq. (2) is subject to the initial condition

$$\phi(\mathbf{x}, 0) = \phi_0(\mathbf{x}) \quad \text{in } \Omega, \tag{48}$$

and inflow boundary condition

$$\phi(\mathbf{x},t) = \phi_{in} \quad \text{on } \partial\Omega_{in}. \tag{49}$$

Here, transport equation (47) along with its boundary condition (49) is solved using a semi-Lagrangian scheme benefiting from an error compensation step [41]. The scheme can be summarized in the following four steps:

1. finding $\hat{\phi}(\mathbf{x}_I, t_{n+1}) = \phi(\hat{\mathbf{x}}_I, t_n)$, where $\hat{\mathbf{x}}_I = \mathbf{x}_I - \mathbf{u}(\mathbf{x}_I, t_{n+1})(t_{n+1} - t_n)$.
2. finding $\check{\phi}(\mathbf{x}_I, t_n) = \hat{\phi}(\check{\mathbf{x}}_I, t_{n+1})$, where $\check{\mathbf{x}}_I = \mathbf{x}_I + \mathbf{u}(\mathbf{x}_I, t_{n+1})(t_{n+1} - t_n)$.
3. calculating $\bar{\phi}(\mathbf{x}_I, t_n) = \phi(\mathbf{x}_I, t_n) + \frac{1}{2}[\phi(\mathbf{x}_I, t_n) - \check{\phi}(\mathbf{x}_I, t_n)]$.
4. finding $\phi(\mathbf{x}_I, t_{n+1}) = \bar{\phi}(\hat{\mathbf{x}}_I, t_n)$.

One should note that in the implemented scheme, no actual particle is added to the computational domain for tracing the backward and forward movements. Instead, only the corresponding coordinates ($\hat{\mathbf{x}}$ and $\check{\mathbf{x}}$) are computed and field variables are interpolated at these "fictitious positions" of node I.

The basic feature of the level set method is to easily deduce geometrical parameters from the well-defined level-set function;

$$\mathbf{n} = \frac{\nabla\phi}{\|\nabla\phi\|}, \tag{50}$$

and

$$\kappa = \nabla \cdot \mathbf{n}. \tag{51}$$

Equations (50) and (51) imply that one needs the level-set function to possess at least C1-continuity. However, representing ϕ as a finite element variable, it possess only C0-continuity. Therefore, the described approach requires recovery of $\mathbf{n}$ (or equivalently $\mathbf{G} = \nabla\phi$) as a C0-continuous nodal value. This is done by solving

$$\int_\Omega (\mathbf{G} - \nabla\phi)\, d\Omega = 0. \tag{52}$$

Numerical experiences show that the robustness of the method can be improved by also introducing a nodal curvature by solving

$$\int_\Omega \left[\kappa - \nabla \cdot \left(\frac{\mathbf{G}}{\|\mathbf{G}\|}\right)\right] d\Omega = 0. \tag{53}$$

This improves the estimation of the curvature and consequently, lessens the non-physical parasitic currents in the vicinity of the interface.

However, advection of the level set function with the velocity field according to Eq. (47) can result in distortions in the ϕ-field and consequently affect the accuracy in the geometrical parameters of interest ($\mathbf{n}$ and κ). In this work, the so-called "back and forth error compensation and correction" method [42, 41] is used to minimize the error introduced as a result of irregularities in the gradient of the level-set function. Moreover, as proposed by Tornberg and Engquist [36], solving the following diffusion equation for $\tilde{\phi}$ helps filtering the nonphysical oscillations in the zero level-set distance function, *i.e.* the interface.

$$\tilde{\phi} - \varepsilon \nabla^2 \tilde{\phi} = \phi \tag{54}$$

Diffusion coefficient $\varepsilon \sim 10^{-1} h_e^2$ is small enough not to significantly affect the interface. Nevertheless, it is well-known that the method is prone to "mass-loss", understood as the non-physical shrinkage of domain Ω_1. Due to this issue, as a conventional rule, smoothed function $\tilde{\phi}$ is only used during the calculation of the curvature of the interface while ϕ is used to define the domains [34]. However, in the present work, the intention is to substitute the level-set function ϕ by $\tilde{\phi}$ in order to improve the results obtained for rather coarse meshes. To this end, the shrinkage is alleviated by adapting the idea [37] proposed in the context of Laplacian surface smoothing. Based on this idea, the shrinkage is compensated by reverting the distance function for node i according to

$$\phi_i = \tilde{\phi}_i - d\phi_{avg,i}, \tag{55}$$

where

$$d\phi_{avg,i} = \frac{1}{N_i} \sum_{j}^{N_i} \left(\tilde{\phi}_j - \phi_j \right), \tag{56}$$

and N_i denotes the number of nodes j connected to node i.

Nonetheless, ϕ-field can still be endlessly stretched or expanded by a non-zero strain-rate [43] and therefore, $\nabla\phi$ can become indefinitely large or extremely small. As a direct result of this issue, the accuracy of the curvature calculation procedure and consequently, the solution of the momentum equation are severely disturbed. The more important and indirect consequence of the issue is failure of the method to retain the regularity of the interface [44], which ruins the solution. In this work, the re-initialization procedure proposed in [45] is utilized to keep the level-set function as close as possible to a

distance function, *i.e.* $\|\nabla\phi\| \approx 1$. In order to anchor the interface in place, *i.e.* keep the zero level-set function intact, all nodes of the elements cut by the interface are neglected in the re-initialization procedure. It is also worth to note that in this work, the level-set re-initialization is performed for the whole computational domain.

The proposed numerical method is summarized in Algorithm 1. Here, (superscript) n counts the number of marched time-steps, n_{rd} determines the frequency of ϕ-reinitialization procedure ($n_{rd} = 50$ in the present work), and $\mathcal{N}$ and $\mathcal{E}$ denote the sets of all nodes and elements in the discretized domain, respectively.

Algorithm 1: The proposed numerical method

Input: $\mathbf{u}_0$, $\mathbf{u}_D$, $\mathbf{t}_N$, ϕ_0, and ϕ_{in}
Output: $\mathbf{u}_I$, p_I, and ϕ_I; $I \in \mathcal{N}$

$n = 1$
$t = 0$
while $t <$ *run-time* **do**
  solve Eq. (47) for ϕ_I^n
  if $n = in_{rd}$; $i = \{1, 2, 3, \ldots\}$ **then**
    reinitialize ϕ
  do smoothing according to Eqs. (54) and (55)
  solve Eqs. (52) and (53) for κ_I
  for *all* $e \in \mathcal{E}$ **do**
    if $e \cap \Gamma \neq \varnothing$ **then**
      do element spliting
    create elemental system of equations (33)
    if $e \cap \Gamma \neq \varnothing$ **then**
      do introducing the penalty term (39)
      do condensation (38)
  do assembling the Linear System of Equations (LSE)
  solve LSE for $[\mathbf{u}_I, p_I]$
  update $n = n + 1$
  update $t = n\Delta t$

3. Numerical examples

The present model is implemented by the authors within Kratos MultiPhysics code [46, 47], a high performance computing (HPC) open-source software. The non-linear system of equations is linearized using the generalized Newton's method and solved with the convergence relative tolerance of 10^{-6} for both velocity and pressure fields. It must be noted that a fully implicit monolithic approach is used to obtain unknown velocities and pressures at the same time while the time integration is performed using the second order backward difference method (BDF2). For solving the linearized system of equations, the algebraic multigrid solver from AMGCL library [48] is applied; the GMRES(m) method with restart parameter $m = 40$, Gauss-Seidel smoother, and the convergence tolerance of 10^{-9} is utilized.

It should be noted that in the following simulations, mass conservation of the level-set method is enhanced following the procedure presented in [49, 50]. It consists of slightly modifying the level-set function by $\delta\phi$ computed as

$$\delta\phi = -\frac{V_1^0 - V_1}{A}, \tag{57}$$

where superscript 0 specifies the initial state, $V_1 = \int_{\Omega_1} d\Omega$ is the volume of the liquid phase (Ω_1), and $A = \int_\Gamma d\Gamma$ denotes the area of the interface.

3.1. Spherical Droplet at Equilibrium

The aim of this test-case is to investigate the capability and accuracy of the present numerical method in capturing the strong discontinuity in the pressure field ("pressure jump") caused by the surface tension.

Here, a liquid-gas system consisting of a spherical liquid droplet surrounded by gas is simulated. The configuration is at equilibrium in the absence of gravity. Surface tension at the liquid-gas interface depends exclusively on the local curvature and thus, on the coordinates $(x_{int}, y_{int}, z_{int})$ that define the interface position. The two-phase system is confined in a box with dimensions $L = W = H = 0.01m$, and the interface initially obeys $(x_{int}-x_c)^2+(y_{int}-y_c)^2+(z_{int}-z_c)^2-a^2 = 0$ with $a = 0.003m$, where (x_c, y_c, z_c) denotes the center of the box. Material properties of the two fluids are chosen as: dynamic viscosity $\mu_l = \mu_g = 0.001N \cdot s/m^2$, density $\rho_l = 1000kg/m^3$ and $\rho_g = 1kg/m^3$, and surface tension coefficient $\gamma = 0.1N/m$.

Figure 5 shows the the pressure distribution on a cut surface passing through the center of the spherical droplet. One can see that the standard

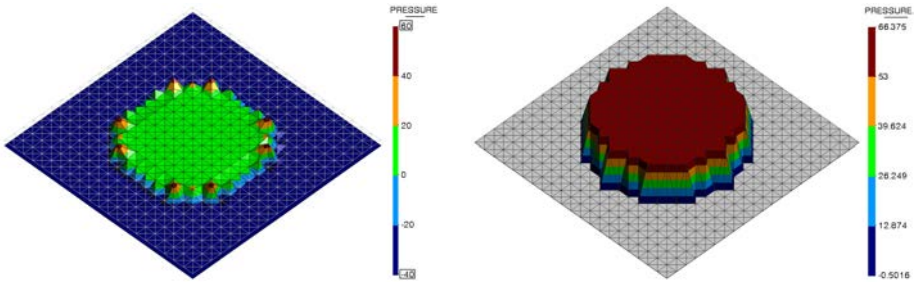

(a) Standard FEM (b) Enriched FEM

Figure 5: Calculated pressure field for the spherical droplet at equilibrium. Results are presented for a cut surface passing through the center of the sphere.

(non-enriched) finite element method is incapable of representing the pressure jump caused by the surface tension and consequently, multiple peaks and valleys appear in the vicinity of the interface (see Fig. 5(a)). On the other hand, as illustrated in Fig. 5(b), the proposed enriched finite element method accurately captures the pressure jump at the interface as well as the expected uniform pressure fields for the individual sub-domains.

In order to further analyze the benefits of using the proposed method, pressure distribution is plotted along the center-line of the cube for two different mesh resolutions, $a/h_e \approx 4.2$ (with $\sim 25K$ elements) and $a/h_e \approx 8.6$ (with $\sim 200K$ elements). Figure 6(a) shows a slight decrease in the liquid pressure at the interface for $a/h_e \approx 4.2$, when using $a/h_e \approx 8.6$, pressure distribution matches the analytic solution.

Next, we test the method with respect to its ability of suppressing the spurious "parasitic" currents, typically manifesting in numerical multiphase simulations in the vicinity of the material interfaces. Ideally, as long as the droplet maintains its equilibrium spherical configuration and the pressure field is in balance with the surface tension, velocity in the entire domain including the interface should be exactly zero. However, it is well-known that in the numerical simulations, spurious velocities arise in the vicinity of the interface. The robustness of the method can be estimated in terms of its ability to suppress and/or control these "parasitic" currents. Large values and uncontrolled time evolution of the parasitic currents can be considered as a sign of a serious flaw in the method.

The parasitic currents are illustrated in Fig. 7 for both the standard and enriched finite element methods. For the sake of clarity in Fig. 7(a), velocity

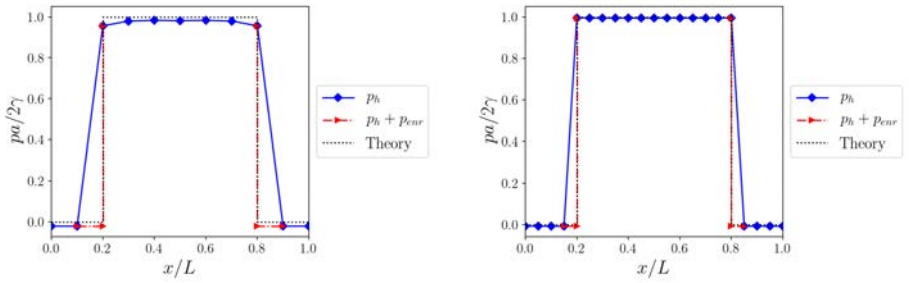

(a) $a/h_e \approx 4.2$ (b) $a/h_e \approx 8.6$

Figure 6: Pressure distribution along a line-segment passing through the center of the spherical droplet at equilibrium.

vectors are plotted using a scale factor of 0.005 for the non-enriched case ($|\mathbf{u}|_{max}^{spurious} \sim 10^{-1} m/s$). A unit scaling factor is used for the enriched one ($|\mathbf{u}|_{max}^{spurious} \sim 10^{-3} m/s$) shown in Fig. 7(b). One can see that the proposed enriched finite element method is successful in significantly suppressing the spurious velocities, which are reduced by two orders of magnitude comparing to the standard method.

In order to get an insight of the computational efficiency of the method, the cost of different steps is estimated. In Table 1, CPU-times associated with the enriched and non-enriched FEM flow solvers, as well as the level-set convection, smoothing, and distance re-initialization operations are reported for a single time-step. For distance re-initialization, since this process is not called in every time-step, the reported value reflects the portion of its computational cost associated with a single time-step. The resolution is set to $a/h_e \approx 12.7$ and the computational domain consists of $\sim 700K$ elements. The code is run using eight threads (four cores) on a PC with Intel® Core™ i7-4790 CPU. It is observed that by introducing the enrichment, CPU-time is increased by almost 30% for a single iteration of the non-linear solver. Nonetheless, this additional cost is perfectly compensated by the improved convergence, which even leads to around 30% smaller overall CPU-time. In other words, for the present test, the enriched solver obtains a convergent solution for the non-linear system of equations by performing three iterations, while the non-enriched solver needs six iterations.

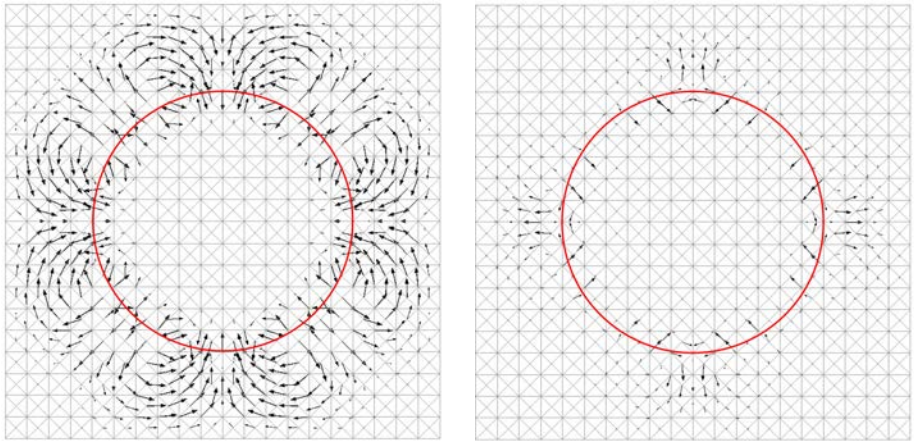

(a) Standard FEM, scale factor = $\frac{1}{20}$ (b) Enriched FEM, scale factor = 1.0

Figure 7: Spurious (parasitic) velocity vectors for the spherical droplet at equilibrium. Results are presented for a cut surface passing through the center of the sphere.

Table 1: CPU time associated with the main solver with and without enrichment as well as the level-set convection, smoothing, and re-initialization operations. These times are reported in seconds and measured for a single time-step.

Enriched flow solver	Non-enriched flow solver	Level-set convection	Smoothing process	Distance re-initialization	Total time per step
One iteration: 3.43s Until convergence (3 iterations): 10.3s	One iteration: 2.59s Until convergence (6 iterations): 15.5s	0.47s	1.02s	1.19s	Enriched method: 13.0s Non-enriched method: 18.2s

3.1.1. Smoothing

It is well-known that without an appropriately designed smoothing strategy, numerical simulation of a surface-tension dominated multi-phase flow leads to non-regularities in the level-set function [34]. This issue becomes particularly severe in lengthy simulations. In this section, the effectiveness of the smoothing procedure proposed in the present work is assessed using the previous test-case, namely for the spherical droplet at equilibrium. Figure 8 illustrates the liquid-gas interface at different instances obtained without applying a smoothing scheme along with the result obtained utilizing smoothing. These results are presented for $a/h_e \approx 6.4$ (with $\sim 90K$ elements). The proposed smoothing algorithm clearly enhances the robustness of the numerical method by almost completely removing the noise in the zero level-set function. One can see that in case of applying smoothing, the simulation reaches $t = 1000\ \Delta t$ without any pronounced sign of the spurious shapes, while the non-smoothed method leads to severe shape alterations already at early stages of the simulations. We note that such an irregularity in the interface may also be alleviated by using mesh refinement in the vicinity of the interface. However, this latter option would result in a higher computational cost of the simulation, particularly in the transient problems.

3.2. Two-phase Hydrostatic Pressure

Besides the accurate capturing of the pressure discontinuity in a surface tension dominated problems shown in section 3.1, the proposed pressure-enriched finite element method is capable of capturing the weak pressure discontinuity at the interface. This feature is assessed by simulating a liquid-gas container at the hydrostatic equilibrium. Physical properties of the liquid and the gas phases are taken from the previous test-case. Geometry is as follows: a cubic unitary domain is filled with liquid up to $z = 0.493L$. The rest of the domain is filled with gas. No surface tension is considered and gravity is applied with $g = -10m/s^2$ in the z-direction. A large discontinuity in the pressure gradient is expected due to the jump in density at the interface (considered density ratio equals 1/1000). The test is run for a mesh of $L/h_e \approx 14.1$ (with $\sim 25K$ elements).

Figure 9 shows the pressure distribution along the z-axis. Simulation results are shown for both the standard and the enriched FEM model. Although the nodal pressure is well approximated by both models, the enriched one leads to a slightly more accurate pressure approximation in the vicinity

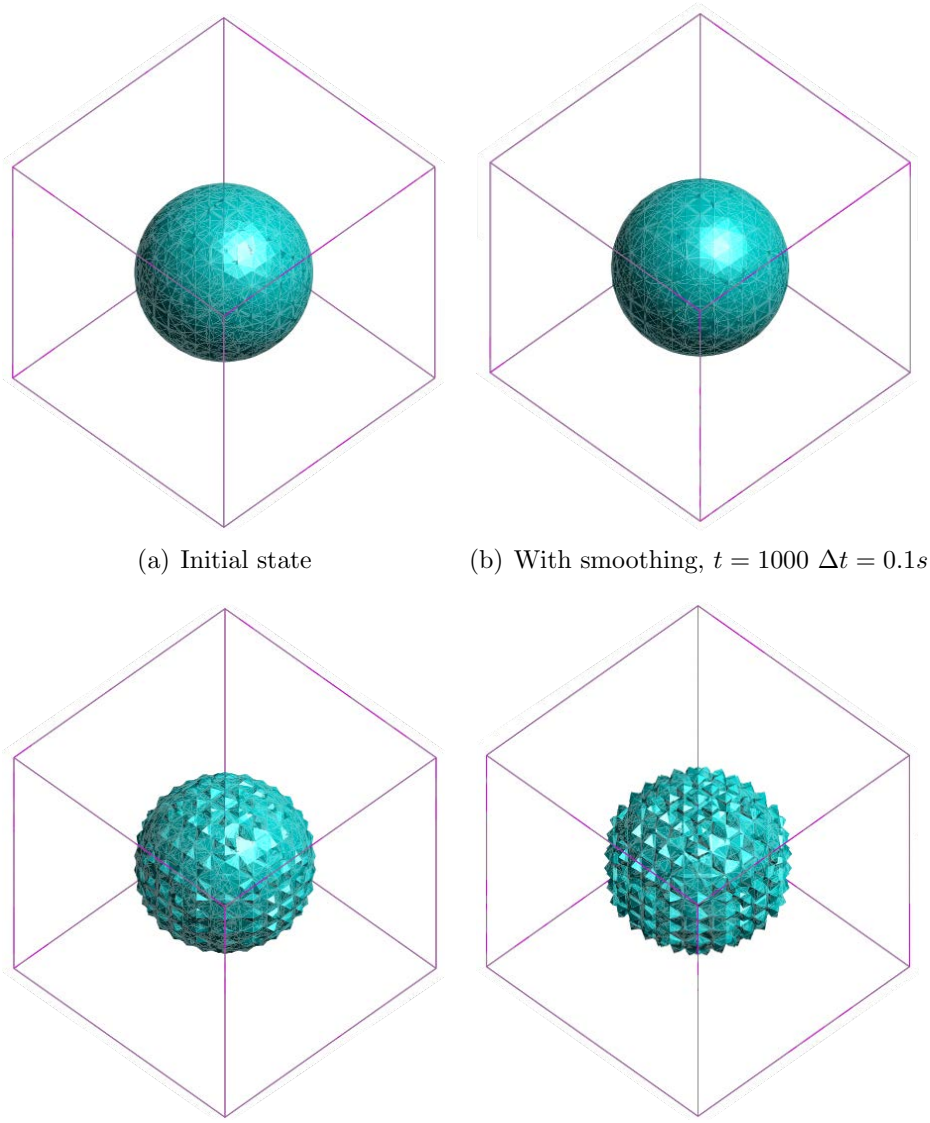

(a) Initial state

(b) With smoothing, $t = 1000$ $\Delta t = 0.1s$

(c) Without smoothing, $t = 0.05s$

(d) Without smoothing, $t = 0.1s$

Figure 8: Snapshots of the liquid-gas interface of the spherical droplet at equilibrium (b) with and (c,d) without smoothing procedure.

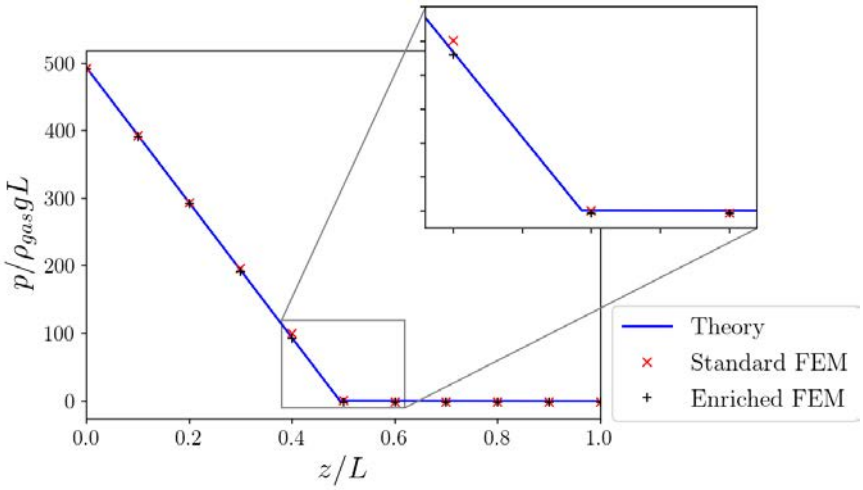

Figure 9: Hydrostatic pressure distribution at $t = 100$ $\Delta t = 0.01s$.

of the interface as observed in the inset of Fig. 9. Nonetheless, the distinctive capability of the proposed enrichment in handling the weak pressure discontinuity is revealed by assessing its ability to provide a balance between the gravitational force and the pressure gradient within the elements cut by the interface. This can be figured out by analyzing the spurious currents; the smaller the parasitic currents the higher is the exactitude in satisfying the force balance. In the previous section, it was observed that the balancing between the surface tension and the pressure jump led to smaller parasitic currents in the vicinity of the liquid-gas interface. Time evolution of the maximum (spurious) velocity is illustrated in Fig. 10. It is evident that the standard finite element method is incapable of handling the weak pressure discontinuity while, the proposed pressure enriched finite element space is the key to suppress the spurious currents. Figure 11 shows these spurious currents at the tenth time step ($t = 0.001s$).

3.3. Oscillating Droplet

The next test aims at studying the performance of the method applied to the simulation of transient behavior of a liquid-gas system.

The benchmark is obtained by considering the geometry and the material properties used in the previous example, but perturbing the interface at the initial state. In this case, the liquid-gas interface is expected to oscillate

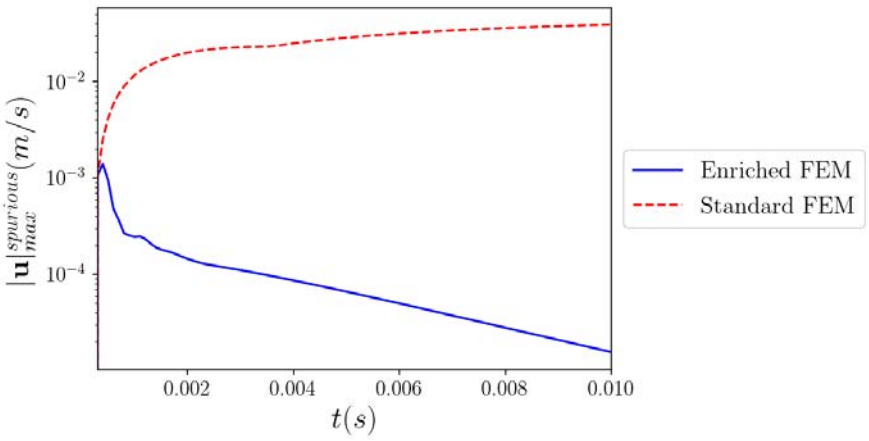

Figure 10: Time-evolution of the parasitic current for the hydrostatic liquid-gas container.

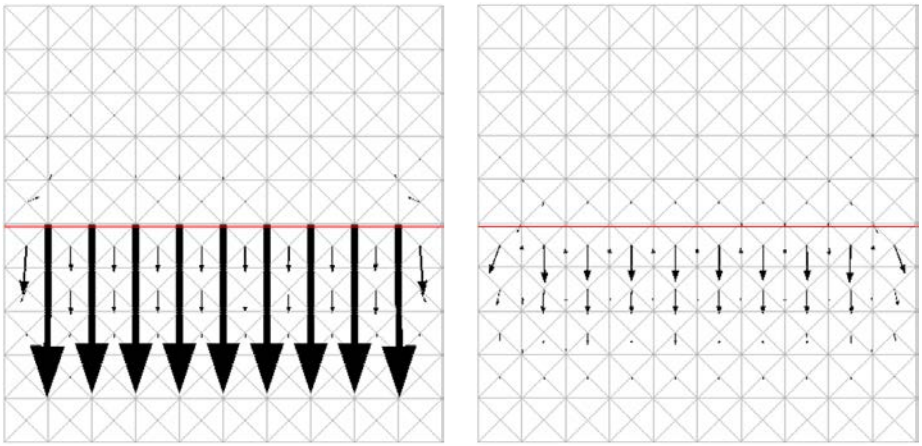

(a) Standard FEM, scale factor = $\frac{1}{2}$ (b) Enriched FEM, scale factor = 5.0

Figure 11: Spurious (parasitic) velocity vectors for the hydrostatic liquid-gas container at $t = 10\ \Delta t = 0.001s$. Results are presented for a vertical cross-section passing through the center of the cubic container perpendicular to the interface.

with a gradually decreasing oscillation amplitude until the spherical shape is regained.

Two different cases are analyzed. In the first one, the spherical droplet is disturbed only slightly. This enables comparison with the analytic solution (known for nearly spherical shapes) in terms of oscillation frequency. In the second case, a prolate droplet is used to investigate the performance of the method for a configuration that is far from equilibrium. Since the interface is subject to large reciprocating deformations in this case, it gives a particularly good insight regarding the performance of the implemented interface capturing technique.

3.3.1. Slightly Disturbed Spherical Droplet

In this section, the spherical shape of the interface (obeying $(x_{int} - x_c)^2/a^2 + (y_{int} - y_c)^2/b^2 + (z_{int} - z_c)^2/c^2 - 1 = 0$ with $a = b = c = 0.003$) is slightly disturbed ($b = 0.00315m$) and its motion is compared to the theory presented in [51]. As already mentioned, physical properties are set to the same values chosen in section 3.1. In Fig. 12, time evolution of maximum vertical coordinate y_{int} is plotted for various mesh resolutions. Theoretical value of the decaying amplitude of the oscillations is also calculated based on the theory presented in [51] and illustrated in Fig. 12 for comparison. This theoretical amplitude is calculated based on the formula obtained by Lamb (Article 355 in [51]) as $Y \propto \exp(-t/\tau)$. Here, Y is the amplitude of oscillations and

$$\tau = \frac{\rho a^2}{5\mu}, \tag{58}$$

for the most significant (second) mode of oscillations. One can see that for mesh resolutions of $a/h_e \geq 6.4$, the numerical simulation provides a good match with the theoretical result in terms of oscillations' dissipation.

Frequency of the oscillation is calculated applying Fast Fourier Transform (FFT) to the time evolution of the maximum y_{int}. Error in frequency is presented in Fig. 13. This error is calculated with respect to the theoretical prediction of the frequency of the second mode of oscillations according to the formula presented in article 275 of [51]

$$\omega^2 = \frac{24\gamma}{(3\rho_1 + 2\rho_2)a^3}. \tag{59}$$

The convergence rate is seen to be practically of second-order and the relative error is about 1% for the finest mesh with $a/h_e \approx 12.7$ (with $\sim 660K$

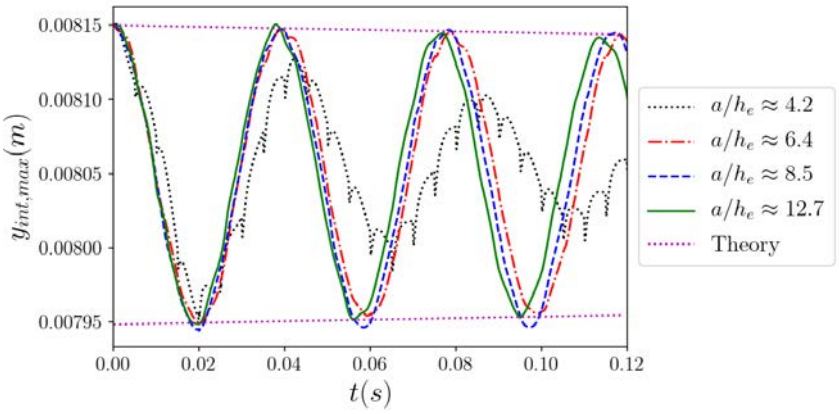

Figure 12: Oscillation of a slightly disturbed spherical droplet; decay in the amplitude in comparison with theory [51].

elements).

3.3.2. Prolate Spheroid Droplet

In this case, the spherical droplet is further disturbed, obtaining a prolate initial shape with $a = c = 0.002m$ and $b = 0.0035m$. Radius of the spherical shape at equilibrium is $R = (abc)^{1/3}$. In order to reach the equilibrium quickly, dynamic viscosity is increased to $\mu_l = \mu_g = 0.01N \cdot s/m^2$ while all other properties are unchanged. Time-evolution of maximum vertical coordinate of the liquid-gas interface $y_{int,max}$ is plotted in Fig. 14 for different mesh resolutions. Results show that the solution becomes convergent for $R/h_e \geq 6.8$. It must also be noted that without applying the small-cut treatment presented in section 2.2.4, the simulation terminates prematurely due to inability to converge. The solver failure occurs as soon as the interface approaches a node, *i.e.* when the liquid to gas volume ratio becomes extremely large or negligibly small in a cut element, making the condensation of the enriched pressure impossible.

Another important property a numerical multiphase flow model must possess is the ability to preserve volume of each phase. This conservation property is known to be affected by errors in the advection of the level-set function as well as the distance re-initialization and smoothing procedures.

In Fig. 15, time-evolution of the ratio of the numerically calculated liquid

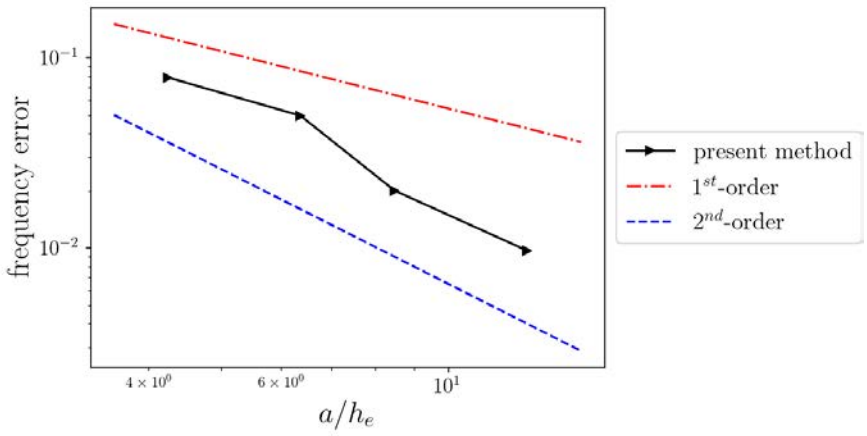

Figure 13: Oscillation of a slightly disturbed spherical droplet; error in the calculated frequency.

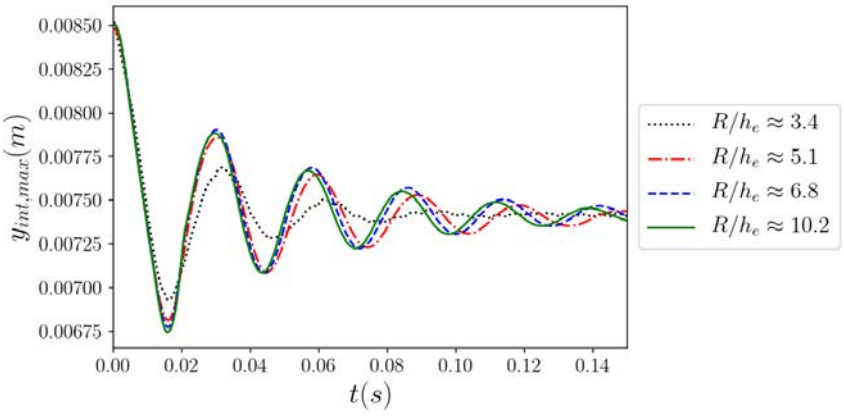

Figure 14: Oscillation of a spheroid droplet; time evolution of maximum y_{int} for different mesh resolutions.

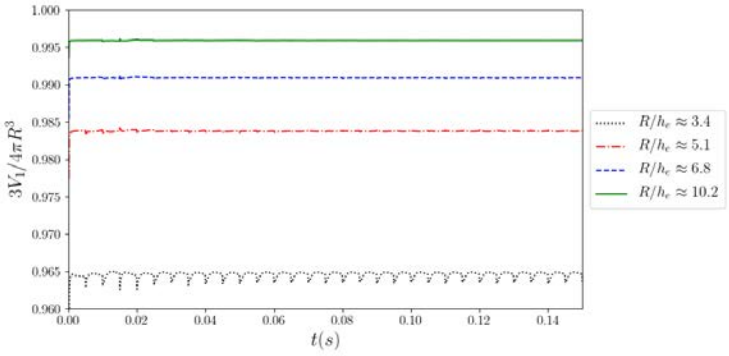

Figure 15: Oscillation of a spheroid droplet; time evolution of droplet volume ratio for different mesh resolutions.

volume to the expected value of $4\pi R^3/3$ is shown for different mesh resolutions. One can see that the relative volume loss is smaller than 3.5% for the coarsest mesh with $R/h_e \approx 3.4$. The volume loss decreases as the mesh is refined reaching a value of 0.5% for the finest mesh used in this test ($R/h_e \approx 10.2$ with $\sim 660K$ elements). The perfectly horizontal trend of the graphs in Fig. 15 reveals the important fact that the volume loss is not accumulative and volume fluctuations are negligibly small for the present method.

Long-time evolution of the maximum vertical coordinate of the interface $y_{int,max}$ is illustrated in Fig. 16 for $R/h_e \approx 6.8$. Droplet eventually reaches its equilibrium shape at around $t = 0.35s$, when the amplitude of the oscillation is negligibly small. By applying FFT to the data presented in Fig. 16, the frequency of the most dominant mode of oscillations is $220Rad/s$. This is in agreement with $\omega = 239Rad/s$ obtained from Eq. (59) by substituting a with R in the formula. The calculated frequency becomes $226Rad/s$ by applying FFT to data obtained for $t \geq 1.5s$.

Figure 17 presents snapshots of the interface at different onsets. It is observed that the ultimate spherical shape, which represents the theoretically expected equilibrium state of the droplet is reached in Fig. 17(d) after undergoing a series of oscillatory deformations.

One of the major ingredients of the present method is the proposed smoothing procedure (Eqs. (54) and (55)). This technique facilitates ob-

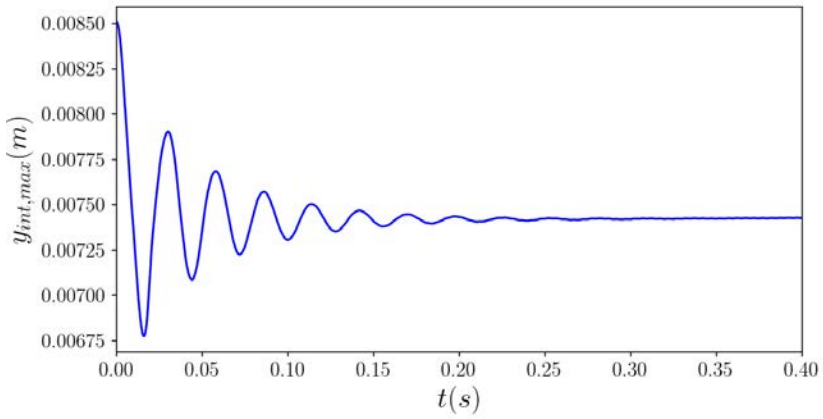

Figure 16: Oscillation of a spheroid droplet; long-time evolution of maximum y_{int}.

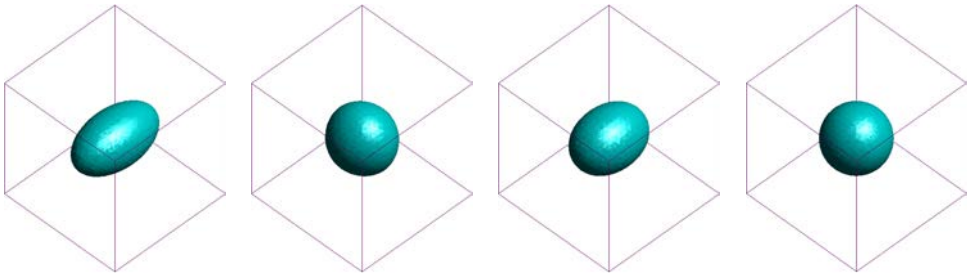

(a) Initial state (b) $t = 0.01s$ (c) $t = 0.03s$ (d) $t = 0.4s$

Figure 17: Snapshots of the interface for the oscillating spheroid droplet.

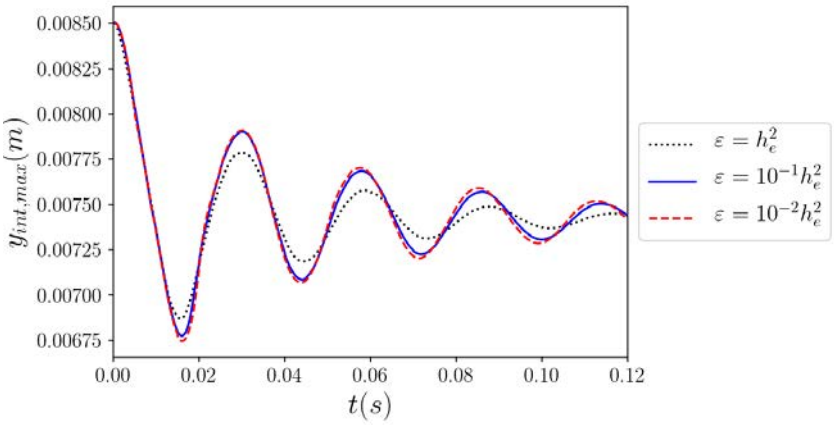

Figure 18: Oscillation of a spheroid droplet; time evolution of maximum y_{int} for different values of smoothing diffusion coefficients (ε).

taining desirable results on a rather coarse mesh without performing costly refinement in the vicinity of the interface that is required otherwise.

In Fig. 18, time evolution of maximum y_{int} is shown for three different smoothing diffusion coefficients. The result is almost unaffected for $\varepsilon \leq 10^{-1}h_e^2$ while choosing $\varepsilon = h_e^2$ evidently adds to the numerical dissipation.

Time evolution of the volume ratio for three different ε is presented in Fig. 19. The effect of an excessive smoothing manifests in a nonphysical droplet shrinkage, which is subsequently corrected by the distance modification procedure used in the proposed numerical method (Eq. (57)). The effect of this combination (shrinkage and correction) along with the distance re-initialization procedure result in a high-frequency oscillations in the volume ratio as seen in Fig. 19.

Since the numerical experiments show that using $\varepsilon = 10^{-1}h_e^2$ leads to a better convergence for different test-cases, this smoothing diffusion constant is chosen as the default value used throughout this work.

3.4. Three-dimensional Bubble Rise

The experiment conducted by Hnat and Buckmaster [52] has become a benchmark for two-phase liquid-gas flow solvers [53, 54, 55]. In this test-case, the rising of an initially spherical gas ($\rho_g = 1.0kg/m^3$ and $\mu_g = 0.001kg/m{\cdot}s$)

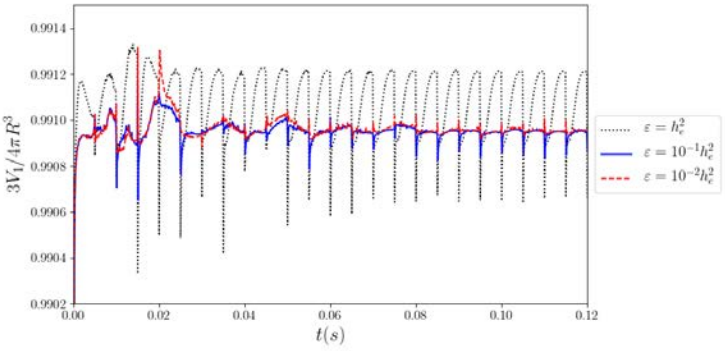

Figure 19: Oscillation of a spheroid droplet; time evolution of droplet volume ratio for different ε.

bubble of radius $a = 0.0061m$ is simulated. This benchmark is used here to study the capabilities of the proposed method in simulating a considerably complex two-phase flow problem using a rather coarse mesh. Here, the bubble rises inside a rectangular container (width and length of $W = L = 0.054m$, and height of $H = 0.072m$) filled with a still liquid ($\rho_l = 875.5kg/m^3$ and $\mu_l = 0.118kg/m \cdot s$). Gravity ($g = 9.8m/s^2$) and surface tension of $\gamma = 0.0322N/m$ are considered.

Figure 20, presents sequential snapshots of the interface and bubble cross-section taken at equal time intervals (0.03 s). The terminal shape of the bubble at $t = 0.21s$ closely matches with the previous experimental and numerical results [52, 54]. The terminal velocity of the bubble is approximated as $u_b = 0.191m/s$, which is also in an acceptable agreement with the experimental value of $0.215m/s$. Nevertheless, this result is obtained using a uniform coarse mesh ($a/h_e \approx 4.8$ with $\sim 900K$ elements) and a more accurate solution can be obtained by further refining the mesh. To the best of authors' knowledge, reasonably accurate solutions in the literature are reported for $a/h_e \geq 15$, while very coarse meshes ($a/h_e \sim 5$) led to an unacceptable solution [56]. On the other hand, the results obtained in the present work show that the proposed method is robust enough to obtain an acceptable solution for a challenging problem associated with complex interface deformations and non-uniform velocity distributions using a rather coarse mesh. In this test, the change in the volume of the bubble is less than 0.75%, which

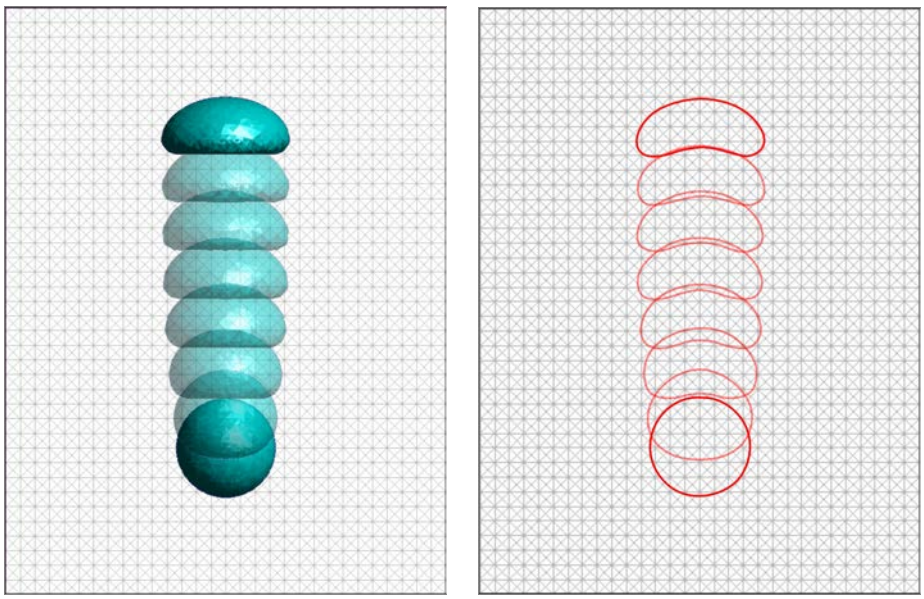

(a) (b)

Figure 20: Snapshots of the rising bubble with time intervals of $0.03s$. (a) Three-dimensional view of the bubble air-liquid interface, and (b) cross-section of the bubble.

asserts the volume conservation property of the proposed numerical method.

It is also worth to note that in this test, as well as many other complex two-phase flows where large interface motions manifest, it is common to encounter either small or large gas-to-liquid volume ratio in a cut element. In such situations, if no small-cut treatment is implemented, the enriched pressure condensation step introduces large errors, which consequently hinders achieving a convergent solution for the non-linear system of equations. Particularly, in the present bubble-rise test case, if no small-cut treatment is applied, the number of non-linear solver iterations increases from 2-3 to 6-8 iterations per step as soon as the volume ratio of sub-elements becomes large. However, the small-cut treatment allows maintaining the Newton-Raphson solver convergence at the level of 2-3 iterations per step. Needless to say, at the moment of crossing the node, *i.e.* when the true small-cut threshold is exceeded, the solver terminates. Therefore, not only the proposed small-cut treatment is obligatory in severe small-cut situations, it is also beneficial for maintaining the convergence of the numerical method in less severe cases.

4. Summary and conclusions

A pressure enriched finite element method was proposed to simulate surface tension dominated two-phase flows. The proposed enriched finite element space was capable of handling both the weak and strong discontinuity in a variable by duplicating the number of corresponding degrees of freedom (e.g. four additional degrees of freedom are needed for pressure enrichment with 3D tetrahedral mesh) merely for the cut elements. The method was stabilized within the framework of the variational multiscale approach. A stabilization procedure was also proposed to enhance the condensation process in the severe "small-cut" situations. The level-set method was implemented to capture the evolution of the interface while a smoothing procedure was proposed to improve the result obtain on a coarse mesh. The proposed method was validated by simulating a series of test-cases including an oscillating droplet and a rising bubble.

It was verified that the method is capable of accurate capturing a sharp pressure jump as well as a large discontinuity in the pressure gradient at the liquid-gas interface and results in a dramatic reduction in the spurious currents. Obtained results showed the solid performance of the proposed method on relatively rough meshes. It is worth to note that robust performance of the proposed enriched FEM-level set method depends on careful application

of smoothing procedure and the proposed small-cut treatment strategy. The present work defines the first step in establishing a computational framework for analyzing two-phase microfluidic flows particularly aiming at studying the two-phase transport in the PEM fuel cells.

5. Acknowledgment

This work was performed within the framework of AMADEUS project ("Advanced Multi-scAle moDEling of coupled mass transport for improving water management in fUel cellS", reference number PGC2018-101655-B-I00) supported by the *Ministerio de Ciencia, Innovacion e Universidades* of Spain.

Conflict of interest

The authors declare that they have no conflict of interest.

References

[1] H. Patel, S. Das, J. Kuipers, J. Padding, E. Peters, A coupled volume of fluid and immersed boundary method for simulating 3d multiphase flows with contact line dynamics in complex geometries, Chemical Engineering Science 166 (2017) 28–41.

[2] E. Samiei, M. Shams, R. Ebrahimi, A novel numerical scheme for the investigation of surface tension effects on growth and collapse stages of cavitation bubbles, European Journal of Mechanics-B/Fluids 30 (2011) 41–50.

[3] G. Falcucci, E. Jannelli, S. Ubertini, S. Succi, Direct numerical evidence of stress-induced cavitation, Journal of Fluid Mechanics 728 (2013) 362–375.

[4] M. Wörner, Numerical modeling of multiphase flows in microfluidics and micro process engineering: a review of methods and applications, Microfluidics and nanofluidics 12 (2012) 841–886.

[5] C. Fang, C. Hidrovo, F.-m. Wang, J. Eaton, K. Goodson, 3-d numerical simulation of contact angle hysteresis for microscale two phase flow, International Journal of Multiphase Flow 34 (2008) 690–705.

[6] V. Talimi, Y. Muzychka, S. Kocabiyik, Numerical simulation of the pressure drop and heat transfer of two phase slug flows in microtubes using moving frame of reference technique, International Journal of Heat and Mass Transfer 55 (2012) 6463–6472.

[7] A. Jarauta, P. Ryzhakov, Challenges in computational modeling of two-phase transport in polymer electrolyte fuel cells flow channels: a review, Archives of Computational Methods in Engineering 25 (2018) 1027–1057.

[8] A. Weber, R. Borup, R. Darling, P. Das, T. Dursch, W. Gu, D. Harvey, A. Kusoglu, S. Litster, M. Mench, et al., A critical review of modeling transport phenomena in polymer-electrolyte fuel cells, Journal of the Electrochemical Society 161 (2014) F1254–F1299.

[9] A. Jarauta, P. Ryzhakov, J. Pons-Prats, M. Secanell, An implicit surface tension model for the analysis of droplet dynamics, Journal of Computational Physics 374 (2018) 1196–1218.

[10] M. d. Mier-Torrecilla, S. Idelsohn, E. Oñate, Advances in the simulation of multi-fluid flows with the particle finite element method. application to bubble dynamics, International journal for numerical methods in fluids 67 (2011) 1516–1539.

[11] Ž. Tuković, H. Jasak, A moving mesh finite volume interface tracking method for surface tension dominated interfacial fluid flow, Computers & fluids 55 (2012) 70–84.

[12] P. B. Ryzhakov, A. Jarauta, An embedded approach for immiscible multi-fluid problems, International Journal for Numerical Methods in Fluids 81 (2016) 357–376.

[13] J. U. Brackbill, D. B. Kothe, C. Zemach, A continuum method for modeling surface tension, Journal of computational physics 100 (1992) 335–354.

[14] S. Popinet, S. Zaleski, A front-tracking algorithm for accurate representation of surface tension, International Journal for Numerical Methods in Fluids 30 (1999) 775–793.

[15] M. Kang, R. P. Fedkiw, X.-D. Liu, A boundary condition capturing method for multiphase incompressible flow, Journal of Scientific Computing 15 (2000) 323–360.

[16] H. Liu, S. Krishnan, S. Marella, H. Udaykumar, Sharp interface cartesian grid method ii: A technique for simulating droplet interactions with surfaces of arbitrary shape, Journal of Computational Physics 210 (2005) 32–54.

[17] M. Sussman, K. M. Smith, M. Y. Hussaini, M. Ohta, R. Zhi-Wei, A sharp interface method for incompressible two-phase flows, Journal of computational physics 221 (2007) 469–505.

[18] M. M. Francois, S. J. Cummins, E. D. Dendy, D. B. Kothe, J. M. Sicilian, M. W. Williams, A balanced-force algorithm for continuous and sharp interfacial surface tension models within a volume tracking framework, Journal of Computational Physics 213 (2006) 141–173.

[19] M. O. Abu-Al-Saud, S. Popinet, H. A. Tchelepi, A conservative and well-balanced surface tension model, Journal of Computational Physics 371 (2018) 896–913.

[20] B. Xie, P. Jin, Y. Du, S. Liao, A consistent and balanced-force model for incompressible multiphase flows on polyhedral unstructured grids, International Journal of Multiphase Flow 122 (2020) 103125.

[21] R. F. Ausas, F. S. Sousa, G. C. Buscaglia, An improved finite element space for discontinuous pressures, Computer Methods in Applied Mechanics and Engineering 199 (2010) 1019–1031.

[22] P. Hansbo, M. G. Larson, S. Zahedi, A cut finite element method for a stokes interface problem, Applied Numerical Mathematics 85 (2014) 90–114.

[23] P. Minev, T. Chen, K. Nandakumar, A finite element technique for multifluid incompressible flow using eulerian grids, Journal of Computational Physics 187 (2003) 255–273.

[24] J. Chessa, T. Belytschko, An enriched finite element method and level sets for axisymmetric two-phase flow with surface tension, International Journal for Numerical Methods in Engineering 58 (2003) 2041–2064.

[25] S. Groß, A. Reusken, An extended pressure finite element space for two-phase incompressible flows with surface tension, Journal of Computational Physics 224 (2007) 40–58.

[26] S. R. Idelsohn, J. M. Gimenez, J. Marti, N. M. Nigro, Elemental enriched spaces for the treatment of weak and strong discontinuous fields, Computer Methods in Applied Mechanics and Engineering 313 (2017) 535–559.

[27] A. Coppola-Owen, R. Codina, Improving eulerian two-phase flow finite element approximation with discontinuous gradient pressure shape functions, International journal for numerical methods in fluids 49 (2005) 1287–1304.

[28] R. F. Ausas, G. C. Buscaglia, S. R. Idelsohn, A new enrichment space for the treatment of discontinuous pressures in multi-fluid flows, International Journal for Numerical Methods in Fluids 70 (2012) 829–850.

[29] J. Bruchon, Y. Liu, N. Moulin, Finite element setting for fluid flow simulations with natural enforcement of the triple junction equilibrium, Computers & Fluids 171 (2018) 103–121.

[30] R. Codina, S. Badia, J. Baiges, J. Principe, Variational multiscale methods in computational fluid dynamics, Encyclopedia of Computational Mechanics Second Edition (2018) 1–28.

[31] T. E. Tezduyar, Interface-tracking and interface-capturing techniques for finite element computation of moving boundaries and interfaces, Computer Methods in Applied Mechanics and Engineering 195 (2006) 2983–3000.

[32] C. W. Hirt, B. D. Nichols, Volume of fluid (vof) method for the dynamics of free boundaries, Journal of computational physics 39 (1981) 201–225.

[33] M. Sussman, P. Smereka, S. Osher, A level set approach for computing solutions to incompressible two-phase flow, Journal of Computational physics 114 (1994) 146–159.

[34] S. Groß, V. Reichelt, A. Reusken, A finite element based level set method for two-phase incompressible flows, Computing and visualization in science 9 (2006) 239–257.

[35] R. Codina, O. Soto, A numerical model to track two-fluid interfaces based on a stabilized finite element method and the level set technique, International Journal for Numerical Methods in Fluids 40 (2002) 293–301.

[36] A.-K. Tornberg, B. Engquist, A finite element based level-set method for multiphase flow applications, Computing and Visualization in Science 3 (2000) 93–101.

[37] J. Vollmer, R. Mencl, H. Mueller, Improved laplacian smoothing of noisy surface meshes, in: Computer graphics forum, volume 18, Wiley Online Library, 1999, pp. 131–138.

[38] T. J. Hughes, G. R. Feijóo, L. Mazzei, J.-B. Quincy, The variational multiscale method—a paradigm for computational mechanics, Computer methods in applied mechanics and engineering 166 (1998) 3–24.

[39] R. Codina, A stabilized finite element method for generalized stationary incompressible flows, Computer Methods in Applied Mechanics and Engineering 190 (2001) 2681–2706.

[40] R. Codina, J. Principe, Dynamic subscales in the finite element approximation of thermally coupled incompressible flows, International journal for numerical methods in fluids 54 (2007) 707–730.

[41] T. F. Dupont, Y. Liu, Back and forth error compensation and correction methods for semi-lagrangian schemes with application to level set interface computations, Mathematics of Computation (2007) 647–668.

[42] T. F. Dupont, Y. Liu, Back and forth error compensation and correction methods for removing errors induced by uneven gradients of the level set function, Journal of Computational Physics 190 (2003) 311–324.

[43] M. F. Trujillo, L. Anumolu, D. Ryddner, The distortion of the level set gradient under advection, Journal of Computational Physics 334 (2017) 81–101.

[44] C. Min, On reinitializing level set functions, Journal of computational physics 229 (2010) 2764–2772.

[45] R. N. Elias, M. A. Martins, A. L. Coutinho, Simple finite element-based computation of distance functions in unstructured grids, International journal for numerical methods in engineering 72 (2007) 1095–1110.

[46] Kratos Multiphysics on GitHub, https://github.com/KratosMultiphysics/Kratos, 2020. Accessed: 2020-01-03.

[47] P. Dadvand, R. Rossi, E. Oñate, An object-oriented environment for developing finite element codes for multi-disciplinary applications, Archieves of Computational Methods in Engineering 17/3 (2010) 253–297.

[48] D. Demidov, Amgcl: an efficient, flexible, and extensible algebraic multigrid implementation, Lobachevskii Journal of Mathematics 40 (2019) 535–546.

[49] R. Löhner, C. Yang, E. Oñate, On the simulation of flows with violent free surface motion, Computer Methods in Applied Mechanics and Engineering 195 (2006) 5597–5620.

[50] R. N. Elias, A. L. Coutinho, Stabilized edge-based finite element simulation of free-surface flows, International Journal for Numerical Methods in Fluids 54 (2007) 965–993.

[51] H. Lamb, Hydrodynamics, Cambridge University Press, 1932.

[52] J. Hnat, J. Buckmaster, Spherical cap bubbles and skirt formation, The Physics of Fluids 19 (1976) 182–194.

[53] D. Gueyffier, J. Li, A. Nadim, R. Scardovelli, S. Zaleski, Volume-of-fluid interface tracking with smoothed surface stress methods for three-dimensional flows, Journal of Computational physics 152 (1999) 423–456.

[54] Y. Wang, S. Simakhina, M. Sussman, A hybrid level set-volume constraint method for incompressible two-phase flow, Journal of Computational Physics 231 (2012) 6438–6471.

[55] B. Xie, P. Jin, H. Nakayama, S. Liao, F. Xiao, A conservative solver for surface-tension-driven multiphase flows on collocated unstructured grids, Journal of Computational Physics 401 (2020) 109025.

[56] S. Ii, K. Sugiyama, S. Takeuchi, S. Takagi, Y. Matsumoto, F. Xiao, An interface capturing method with a continuous function: The thinc method with multi-dimensional reconstruction, Journal of Computational Physics 231 (2012) 2328–2358.

Chapter 3

Droplet Spreading on Solid Substrates: Contact–line Dynamics

3.1 Introduction

In this chapter, the pressure–enriched finite element/level–set method, which was introduced in the previous chapter, is further advanced by implementing the requirements for the modeling of the contact–line dynamics. The molecular kinetic model and the Navier-slip condition as well as the incorporation of the sub-elemental hydrodynamics are discussed in this chapter. Here, the proposed method is verified by comparing the result with the theoretical model developed for droplets of the spherical–cap shape [138]. The validation is further performed by reproducing the experimental data *et al.* [110] related to the spreading of liquid squalane on a solid silica substrate. It is shown that the proposed method provides satisfactory results using rather coarse meshes. This makes it a suitable choice for three–dimensional liquid–gas transport problems as those encountered in studying the water management in PEM fuel cells. The following publication comprises the content of the present chapter.

3.2 Article data

Title: Three dimensional modeling of liquid droplet spreading on solid surface: An enriched finite element/level-set approach
Authors: M.R. Hashemi, P.B. Ryzhakov and R. Rossi

Journal: Journal of Computational Physics, Volume 442, 1 October 2021, 110480
Available online: June 2021
DOI: 10.1016/j.jcp.2021.110480

Three Dimensional Modeling of Liquid Droplet Spreading on Solid Surface: an Enriched Finite Element/Level-set Approach

Mohammad R. Hashemi[a,b,*], Pavel B. Ryzhakov[a,b], Riccardo Rossi[a,b]

[a] *Centre Internacional de Mètodes Numèrics en Enginyeria (CIMNE), 08034 Barcelona, Spain*

[b] *Universitat Politècnica de Catalunya (UPC), 08034 Barcelona, Spain*

Abstract

A physically consistent approach is introduced to simulate dynamics of droplets in contact with solid substrates. The numerical method is developed by introducing the molecular–kinetic model within the framework of the level-set/enriched finite element method and including the theoretically resolved sub-elemental hydrodynamics. The level-set method is customized to comply fully with the model acquired for the moving contact-line. The consistency of the proposed method is verified by comparing the simulation results with the theoretical predictions. In order to further validate the method, the spreading of a droplet is numerically modeled and compared rigorously with the experimental data reported in the literature. The proposed method is also employed to capture the evolution of a droplet trapped in a conical pore. All test-cases are simulated on three-dimensional computational domains.

Keywords: Two-phase flow, Surface tension, Wetting, Microfluidics, Droplets, Contact-line

*Corresponding author.

Email addresses: mhashemi@cimne.upc.edu (Mohammad R. Hashemi), pryzhakov@cimne.upc.edu (Pavel B. Ryzhakov), rrossi@cimne.upc.edu (Riccardo Rossi)

1. Introduction

Accurate modeling of liquid spreading on a solid surface [1] is of a fundamental importance in the analysis of multi-phase flows in micro-channels [2, 3] as well as porous [4] and fibrous [5] media, which are encountered in a wide range of industrial applications. One such application, that motivated the developments of the present work, is the water-air transport in the gas channels and fibrous diffusion layer of polymer electrolyte membrane fuel cells (PEMFCs) [6, 7] that is an essential factor in the determination of the performance of the cell [8, 9].

In the modeling of phenomena associated with the multi-phase flow in the presence of a solid substrate, one of the major challenges is to deal with the moving boundary of the three-phase (gas/liquid/solid) interface, the so-called contact-line, using an appropriate condition [10, 11]. Theoretical investigations of the movement of the contact-line [12, 13] imply that the classical continuum-level hydrodynamics along with the conventional no-slip condition at the solid surface lead to an unbounded velocity gradient and consequently a singularity in the stress at the contact-line. The conventional approach to alleviate this singularity is to take into account a slip condition in the vicinity of the contact-line [14, 15], for which there is also some evidence from molecular dynamics simulations [16, 17, 18].

Employing the slip condition in the context of the continuum hydrodynamics allows for a theoretical solution for the viscous bending phenomenon and leads to the well-established Cox's relation [19], which gives a correlation between the apparent macroscopic contact-angle and the microscopic contact-angle. More recently, it was shown that alleviating the stress singularity can result in a complement to the hydrodynamic theory; Zhang and Mohseni [20] explored the possibility of integrating the singular stress in the close vicinity of the contact-line in order to obtain a model for the dynamic microscopic contact-angle.

Besides the hydrodynamic theory that focuses on the phenomena at the continuum level, molecular–kinetic theory [21] has also been acquired to derive a model for the moving contact-line. It was shown that the resulting model is consistent with the results of the molecular dynamics simulations [22, 23]. Both the Cox's relation and the molecular–kinetic model have been examined by fitting the experimentally observed correlation between the contact-angle and the contact-line velocity [24, 25, 26].

It had been revealed that depending on the features of the set of experi-

ments, one model or another provides a better match [27, 28, 29]. This can be explained as a result of the fact that the hydrodynamic theory accounts for the viscous dissipation while the molecular–kinetic theory focuses on the energy dissipation in a very close vicinity of the contact-line [26]. Thus, depending on the flow configuration and the velocity of the contact-line, either of these mechanisms is dominant and the behavior can be better characterized with the respective model. Based on the experimental results, due to the ambiguity in determining the underlying physics and the lack of a systematic approach to determine constitutive parameters [30, 20], it is not a straightforward task to decide which theory (and the resulting) model should be employed. Therefore, in order to exploit the pros of both the theories, combined models were proposed [31, 32, 33, 34, 35], in which the frictional contact-line slip is taken into account as well as the viscous dissipation. Recently, utilizing a series of molecular dynamics simulations, Fernández-Toledano *et al.* [36] stated that the hydrodynamic theory is a reliable means for correlating the apparent (experimentally measurable) contact–angle and the microscopic contact–angle, while the molecular–kinetic theory governs the dynamic microscopic contact–angle. This confirms the rationale of developing combined models like the one proposed by Petrov and Petrov [31].

In the context of the numerical modeling of the dynamics of the contact-line, the utilization of the generalized Navier-slip condition [37, 38, 39] is a viable choice [40]. Being based on the combination of the Navier-slip condition on the solid substrate and the frictional movement of the contact-line due to the unbalanced Young stress, it is consistent with the molecular dynamics simulations [37, 39] and the thermodynamic principles [30, 41] for modeling the wetting phenomena. The generalized Navier-slip condition has so far been applied in the numerical simulation of various cases involving moving contact-line [42, 43, 44, 45]. A numerically different, but fundamentally similar approach is the direct imposition of a friction force at the contact-line along with the standard Navier-slip condition [46]. In the numerical modeling, it is also possible to impose the no-slip condition on the solid surface while the force singularity is circumvented by modifying the conventional formulation [39]; as a notable choice, diffusion can be introduced as the mechanism underlying the contact-line movement [47] similar to the diffuse interface methods [48, 49, 50]. Nevertheless, this approach is out of the scope of the present paper and will not be further discussed here.

Besides the utilized slip condition, one of the fundamental issues with the computational methods applied to the moving contact-line problem is

the mesh-dependence of the results [51, 52]. A physical and a numerical factor, at least partially, responsible for this issue are the unresolved sub-grid hydrodynamics and the interfacial force smoothing, respectively. In the vicinity of the contact-line, hydrodynamic mechanisms act at a small length-scale which, even being far beyond the molecular–scale, cannot be adequately resolved unless a prohibitive refinement of the computational mesh is performed [53]. The hydrodynamic theory is a means to circumvent the need for such refinement [54] and helps improving the mesh-independence of the numerical results [55, 56, 57]. On the other hand, conventional numerical methods typically utilize a numerically smooth representation of the physically localized surface tension [58, 59, 60] following the so-called "continuum force approach" [61]. In the presence of the moving contact-line, the unbalanced Young stress is also smoothed out to act similar to a body force centralized at the contact-line [62, 45]. This approach is associated with an artificial thickness of the interface, which is usually set equal to the length of a few computational cells for the best performance. Therefore, fixing the ratio of this smoothing length to the cell size [45], a highly refined mesh is necessary in the vicinity of the interface and the contact-line in order to minimize the error. A remedy to this issue is to utilize a computational mesh that is fitted to the liquid-gas interface, *e.g.* [63, 64, 46]. However, such an approach may result in severely deformed meshes and requires a frequent remeshing, which dramatically increases the computational costs, particularly in 3D. Moreover, in case of a severe topological change in the liquid phase, this class of approaches may lead to ambiguities in the recognition of the liquid boundary.

In this work, a numerical method is presented that by alleviating the above mentioned issues, provides reasonably accurate results on rather coarse meshes. The previously introduced pressure-enriched finite element/level-set model for the two-phase flows [65] is further developed by incorporating the requirements of the moving contact-line problems. The simplified form of the molecular–kinetic model is implemented along with the Navier-slip condition that acts on the solid substrate. Following the methodology presented by Buscaglia and Ausas [66], the implementation of the moving contact line condition is done by revising the variational formulation of the method. In order to make the overall numerical algorithm consistent, the level-set smoothing procedure [65] is also modified by introducing a boundary condition that is compatible with the contact line condition. To account for the sub-elemental hydrodynamics, the simplified form of Cox's relation [19] is used under the

condition of a small capillary number. In addition, this relation is applied only once the contact angle reaches the value within a threshold of the equilibrium contact angle. This ensures that the contact line velocity is limited and consequently, the Reynolds number is small. Nevertheless, in order to remove these limitations, a more general hydrodynamic model [67, 54] should be acquired that is a subject of future developments. In this work, an element splitting procedure [65] is performed at each step, which enables representing interface with zero-thickness. Consequently, the terms associated with the moving contact-line model are integrated along the curve representing the contact-line while the surface tension acts locally at the interface. It must be noted that such domain splitting is fully exploited by incorporating an enriched finite element space, which enables pressure (gradient) discontinuity within an element.

In the following section, the governing equations including the contact-line condition are first discussed and then implemented in the variational form. Then, the customized version of the level-set method is briefly described and the additional boundary condition required for the smoothing procedure is introduced. The performance of the present method is verified by comparing the result with the theoretical relation between the footprint radius and the contact angle of a droplet spreading with a spherical-cap shape [68] at a small Bond number [69]. The results are further validated against the experimental data published by Seveno *et al.* [26] for a droplet of liquid squalane that is spreading on a solid silica substrate. The degree of mesh-(in)dependence of the results is shown for both test-cases. All simulations presented in this work are conducted for three-dimensional computation domains.

2. Numerical Method

The momentum and mass conservation equations for a fluid system can be written as

$$\rho\left(\frac{\partial \mathbf{u}}{\partial t} + \mathbf{u}\cdot\nabla\mathbf{u}\right) = \rho\mathbf{b} + \nabla\cdot\boldsymbol{\sigma} \quad \text{in } \Omega, \tag{1}$$

and

$$\frac{\partial \rho}{\partial t} + \nabla\cdot(\rho\mathbf{u}) = 0 \quad \text{in } \Omega, \tag{2}$$

respectively. It should be noted that in this work, the homogeneous fluid domains (liquid and gas) are considered to be incompressible and consequently,

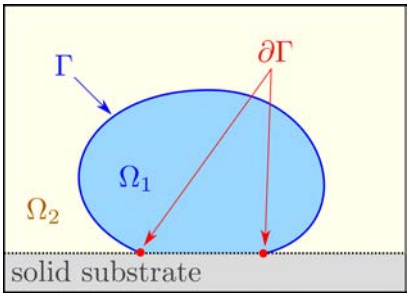

Figure 1: Schematic of the fluid domain $\Omega = \Omega_1 \cup \Omega_2$.

Eq. (2) reduces to $\nabla \cdot \mathbf{u} = 0$ in each phase. The fluid domain, $\Omega \subset \mathbb{R}^d$, is bounded by boundary $\partial\Omega \subset \mathbb{R}^{d-1}$, where d defines the number of spatial dimensions. This set of equations is subject to the initial condition

$$\mathbf{u}(\mathbf{x}, 0) = \mathbf{u}_0 \quad \text{in } \Omega, \tag{3}$$

Dirichlet

$$\mathbf{u}(\mathbf{x}, t) = \mathbf{u}_D \quad \text{on } \partial\Omega_D, \tag{4}$$

and Neumann

$$\mathbf{T}(\mathbf{x}, t) = \mathbf{T}_N \quad \text{on } \partial\Omega_N, \tag{5}$$

boundary conditions. The traction vector is calculated as $\mathbf{T} = \mathbf{n} \cdot \boldsymbol{\sigma}$ with the total stress tensor, $\boldsymbol{\sigma}$, being obtained from the Newtonian constitutive equation

$$\boldsymbol{\sigma} = -p\mathbb{I} + \mu\left(\nabla\mathbf{u} + \nabla\mathbf{u}^T\right). \tag{6}$$

Here, $\mathbf{n}$ is a unit vector normal to $\partial\Omega$ and pointing to the outside of Ω.

2.1. Multi-phase flow

Let us consider a system consisting of two immiscible fluids and a solid substrate (see Fig. 1). Then, the domain Ω can be separated into Ω_1 and Ω_2 with $\Gamma = (\Omega_1 \cap \Omega_2)$ and $\Omega = (\Omega_1 \cup \Omega_2)$. The separating interface Γ is a constituent part of both $\partial\Omega_1$ and $\partial\Omega_2$, while it coincides with the solid substrate only at the contact-line $\partial\Gamma = (\partial\Omega \cap \Gamma)$, where the three phases (both fluids 1 and 2 along with the solid substrate) come into contact and three surface tensions, γ, γ_{1s}, and γ_{2s}, act simultaneously on the fluid 1-fluid 2, fluid 1-solid, and fluid 2-solid interfaces, respectively (see Fig. 2).

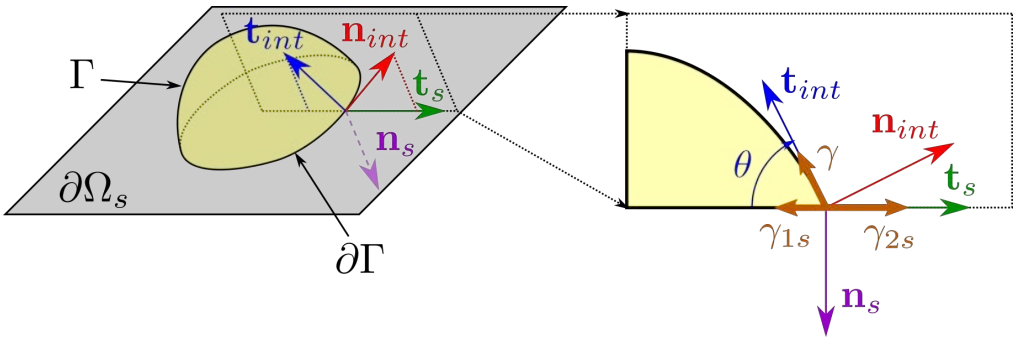

Figure 2: Schematic of a droplet contacting a solid surface. Liquid-gas, liquid-solid, and gas-solid surface tensions with respective coefficients of γ, γ_{1s}, and γ_{2s} are depicted in this figure.

Being internal to the fluid domain Ω, the interfacial conditions can be interpreted as a jump in the traction due to the surface tension

$$[\![\mathbf{T}(\mathbf{x},t)]\!] = -\gamma\kappa\mathbf{n}_{int} \quad \text{on } \Gamma, \tag{7}$$

and continuity of the velocity field

$$[\![\mathbf{u}(\mathbf{x},t)]\!] = 0 \quad \text{on } \Gamma, \tag{8}$$

where $\mathbf{n}_{int}$ is the normal to the interface, Γ, and for any variable A the jump operator reads $[\![A]\!] = A_1 - A_2$ with subscripts 1 and 2 denoting the value in the corresponding phase domains.

At the contact–line for the equilibrium state [70] ($\theta = \theta_Y$), Young's relation [71] states that [10, 72]

$$\gamma\cos(\theta_Y) + \gamma_{1s} = \gamma_{2s}. \tag{9}$$

Therefore, one can simply write $\cos(\theta_Y) = (\gamma_{2s} - \gamma_{1s})/\gamma$. In case the configuration deviates from the equilibrium, the unbalanced Young stress (force per unit length) is defined as [32, 50]

$$\tau_Y = \gamma\left[\cos(\theta_Y) - \cos(\theta)\right]. \tag{10}$$

Here, τ_Y can be interpreted as the net (effective) tension that acts parallel to the solid substrate at the contact-line and is responsible for its movement. Based on the molecular–kinetic theory [21], the movement of the contact-line

is associated with an energy dissipation that is usually referred to as a friction force acting on a moving contact-line [33, 39, 50]. Denoting the slip–velocity associated with the movement of the contact–line with u_{slip}, this underlying mechanism can be represented by [25, 36]

$$u_{slip} = 2k^0\lambda \sinh\left(\frac{\lambda^2\tau_Y}{2k_BT}\right) \quad \text{on } \partial\Gamma, \tag{11}$$

where parameters k^0 and λ are the characteristic frequency and the average distance of the (random thermal) molecular displacements in the vicinity of the contact–line, respectively. In Eq. (11), k_B is the Boltzmann constant and T denotes the absolute temperature. In its simplest form, if the argument of sinh in Eq. (11) is small, the formula of the molecular–kinetic theory reads

$$\tau_Y = \zeta u_{slip} \quad \text{on } \partial\Gamma, \tag{12}$$

with $\zeta = k_BT/k^0\lambda^3$ representing the coefficient of friction at the contact–line [26]. Furthermore, in order to avoid the singularity in the vicinity of the contact-line [73], the no-slip condition on the solid substrate is substituted by the Navier-slip boundary condition that can be formulated as [39, 66, 74]

$$\mathbf{n}_s \cdot \mathbf{u} = 0 \quad \text{on } \partial\Omega_s, \tag{13}$$

and

$$\mathbb{I}_s \cdot \mathbf{T} = -\beta\mathbb{I}_s \cdot \mathbf{u} = -\beta\mathbf{u} \quad \text{on } \partial\Omega_s, \tag{14}$$

where $\mathbf{n}_s$ is the normal to solid substrate $\partial\Omega_s$, and $\mathbb{I}_s = (\mathbb{I} - \mathbf{n}_s \otimes \mathbf{n}_s)$ denotes the surface unit tensor with $\mathbb{I}$ being the identity tensor. In this work, the slip condition (13) is implemented using the local rotation of the unknown velocities at solid surface $\partial\Omega_s$ as discussed in [75].

It is worth mentioning that the combination of (12) and (14) is essentially equivalent to the so-called "generalized Navier boundary condition" [39]. Another important point to mention is that so far, no systematic approach has been introduced for *a priori* determination of parameters β and ζ to be used in a numerical simulation [45]. In section 3.2, it is shown that for the present method, ζ can be set according to the corresponding parameter obtained by fitting the experimental data by a comparable model (*e.g.* see [26]).

2.1.1. Sub-element Hydrodynamics

Considering the practical difficulties in computationally resolving the hydrodynamics in the vicinity of the contact-line with micrometer length-scales [76, 53, 77], the well-established hydrodynamic theory is utilized to

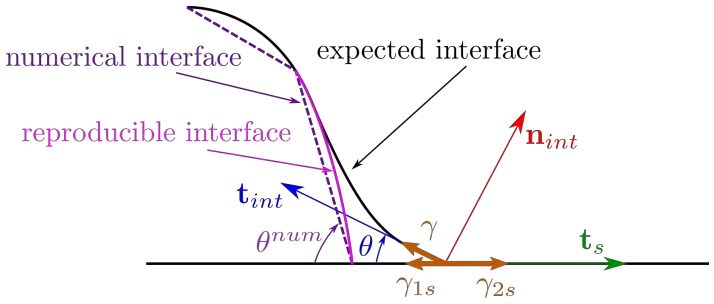

Figure 3: Schematic of the computationally reproduced and the physically expected interface.

incorporate the sub-element variation of the contact angle that occurs due to the so-called "viscous bending" phenomenon [25, 1] (see Fig. 3). In this work, the formulation is based on the simplified linear form [68] of the asymptotic solution to the hydrodynamic theory [19] as

$$\theta^3 = (\theta^{num})^3 - 9\mathrm{Ca}\ln(\frac{h_e}{l_{micro}}), \tag{15}$$

where the capillary number is defined as $Ca = u_{cl}\mu/\gamma$ and l_{micro} is the microscopic slip length-scale. If h_e is considered to be equal to the length-scale associated with the conventional experimental measurements of the contact-angle, $\ln(h_e/l_{micro}) \sim 10$ would be expected [25, 68]. It is worth noting that the simultaneous incorporation of Eqs. (12) and (15) leads to the simplified form of the combined molecular–kinetic/hydrodynamic model proposed by Petrov and Petrov [31, 26].

The original Cox's relation [19] is valid for $Ca \ll 1$ and small Reynolds number while its simplified form in Eq. (15) can be utilized in cases of a small contact angle, $\theta < 3\pi/4$, with a vanishing viscosity ratio, $\mu_2/\mu_1 \ll 1$ (considering μ_2 for the surrounding fluid Ω_2) [68]. For the test-cases solved in this paper, Eq. (15) is applied only for $Ca < 0.3$ and $\theta^{num} - \theta_Y < 2\pi/10$. The latter condition prevents the application of Eq. (15) in situations that a large difference between the dynamic contact-angle and θ_Y leads to a rather large contact-line velocity and consequently, a fairly large Reynolds number. In order to alleviate this condition, one can follow the approach presented in [67]; however, in order to keep the simplicity of the formulation, it is not implemented in this work.

Although it is known that the microscopic length-scale l_{micro} is in the

order of one nanometer, it is generally obtained by performing a proper data-fitting [26, 68]. In this sense, l_{micro} is added to the list of unknown model parameters [35] along with β and ζ. For the cases considered in this work, microscopic length-scale is set to $l_{micro} = 10^{-9}m$ that gives $\ln(h_e/l_{micro}) \sim 10$ for the employed computational meshes. Numerical simulations also shows that slight variation of l_{micro} does not lead to any significant changes in the results. Combining Eq. (15) with the generalized Navier condition, Yamamoto *et al.* has also reported that $l_{micro} \sim 10^{-9}m$ led to the most satisfactory results in their capillary rise simulations [56].

2.2. Variational formulation

The variational form of the momentum equation (1) can be written for the whole fluid domain as [65]

$$\int_\Omega \rho \left(\frac{\partial \mathbf{u}}{\partial t} + \mathbf{u} \cdot \nabla \mathbf{u} \right) \cdot \mathbf{w} d\Omega = \int_\Omega \rho \mathbf{b} \cdot \mathbf{w} d\Omega + \int_\Omega p \nabla \cdot \mathbf{w} d\Omega - \int_\Omega \mu \left(\nabla \mathbf{u} + \nabla \mathbf{u}^T \right) : \nabla \mathbf{w} d\Omega + \int_{\partial\Omega} \mathbf{T} \cdot \mathbf{w} d(\partial\Omega), \tag{16}$$

where $\mathbf{w}$ is a test function in $[\mathcal{H}^1(\Omega)]^d$ that vanishes at the Dirichlet boundary conditions. For separate incompressible fluid domains, Ω_1 and Ω_2, the variational form of the continuity equation (2) becomes

$$\int_\Omega q\rho \left(\nabla \cdot \mathbf{u} \right) d\Omega = 0, \tag{17}$$

with q being a test-function in $\mathcal{L}^2(\Omega)$. The boundary integral term $\int_{\partial\Omega} \mathbf{T} \cdot \mathbf{w} d(\partial\Omega)$ on the right–hand–side of eq. (16) essentially includes the Neumann boundary (5), interfacial (7), and Navier-slip (14) conditions as well as the surface tension along with the molecular–kinetic model (11) acting at the contact line. Considering unit vectors $\mathbf{t}_{int}$ and $\mathbf{t}_s$ being tangential to the interface and the solid substrate, respectively (as shown in Fig. 2), one has $\mathbb{I}_s \cdot \mathbf{t}_{int} = -\cos(\theta)\mathbf{t}_s$ and consequently, the molecular–kinetic model (11) can be rewritten as

$$(\gamma_{2s} - \gamma_{1s})\mathbf{t}_s + \gamma \mathbb{I}_s \cdot \mathbf{t}_{int} - \frac{2k_B T}{\lambda^2} \sinh^{-1}\left(\frac{u_{slip}}{2k^0 \lambda} \right) \mathbf{t}_s = 0 \quad \text{on } \partial\Gamma. \tag{18}$$

Substituting the corresponding relations into Eq. (16), one obtains

$$\begin{aligned}\int_\Omega \rho\left(\frac{\partial \mathbf{u}}{\partial t}+\mathbf{u}\cdot\nabla\mathbf{u}\right)\cdot\mathbf{w}d\Omega &= \int_\Omega \rho\mathbf{b}\cdot\mathbf{w}d\Omega+\int_\Omega p\nabla\cdot\mathbf{w}d\Omega\\ &-\int_\Omega \mu\left(\nabla\mathbf{u}+\nabla\mathbf{u}^T\right):\nabla\mathbf{w}d\Omega+\int_{\partial\Omega_N}\mathbf{T}_N\cdot\mathbf{w}d(\partial\Omega)\\ &-\int_{\partial\Omega_s}\beta\mathbf{u}\cdot\mathbf{w}d(\partial\Omega)-\int_\Gamma\gamma\kappa\mathbf{n}_{int}\cdot\mathbf{w}d\Gamma\\ &+\int_{\partial\Gamma}\Big[(\gamma_{2s}-\gamma_{1s})\mathbf{t}_s+\gamma\mathbb{I}_s\cdot\mathbf{t}_{int}\\ &-\frac{2k_BT}{\lambda^2}\sinh^{-1}\left(\frac{u_{slip}}{2k^0\lambda}\right)\mathbf{t}_s\Big]\cdot\mathbf{w}d(\partial\Gamma).\end{aligned}\tag{19}$$

Here, the slip–velocity at the contact–line reads $u_{slip}=\mathbf{t}_s\cdot\mathbf{u}$. Simplifying the molecular–kinetic model (11) to its linear form (12), one obtains

$$\int_{\partial\Gamma}\frac{2k_BT}{\lambda^2}\sinh^{-1}\left(\frac{u_{slip}}{2k^0\lambda}\right)\mathbf{t}_s\cdot\mathbf{w}d(\partial\Gamma)=\int_{\partial\Gamma}\zeta(\mathbf{t}_s\cdot\mathbf{u})\mathbf{t}_s\cdot\mathbf{w}d(\partial\Gamma).\tag{20}$$

For the sake of simplicity and in order to facilitate comparisons with the references chosen in the present work (where ζ is provided), the linear approximation (Eq. (20)) is used if not mentioned otherwise.

It must be noted that a similar variational formulation for the contact line dynamics has been derived by Buscaglia and Ausas [66] using the principle of virtual work. Conventionally, the variational formulation is derived by smoothing the surface tensions based on the continuum force approach (see [42] for example).

In this work, the accurate integration of the terms appearing in the variational formulation (19) is done by splitting of the cut elements. In Fig. 4, this procedure is schematically shown for a sample element cut by the interface. Elemental integration domains $\Omega_1^{e,cut}$ and $\Omega_2^{e,cut}$ are split into tetrahedra to facilitate the integration. The integration of the terms associated with the elemental interface (Γ^e), contact-line ($\partial\Gamma^e$), and solid substrate ($\partial\Omega_s^e$) are performed by utilizing the quadrature points as schematically illustrated in Fig. 5. By employing a high–order (two points for line-segments, three points for triangles, and four points for tetrahedra) Gaussian quadrature, one can assure that the integration procedure does not introduce further error to the solution (*i.e.* the number of Gauss points is sufficient for the integration of

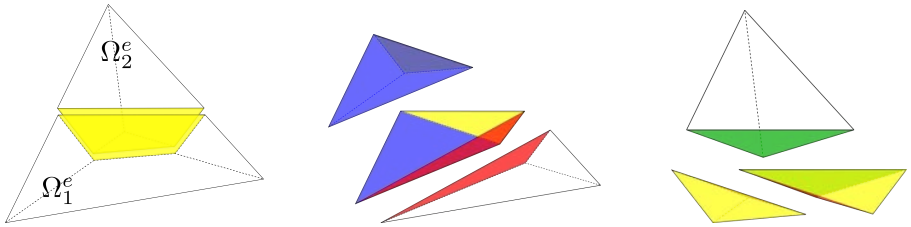

(a) $\Omega^{e,cut}$ (b) $\Omega_1^{e,cut}$ (c) $\Omega_2^{e,cut}$

Figure 4: Schematic of a possible cut in a tetrahedral element. The interface, Γ^e, is shaded by yellow and the matching faces are marked with the same color.

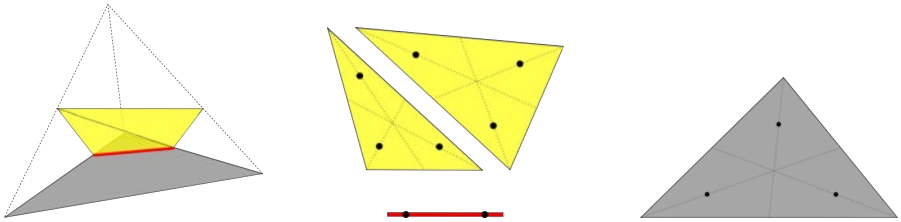

(a) $\Omega^{e,cut}$ (b) Γ^e and $\partial\Gamma^e$ (c) $\partial\Omega_s^{e,cut}$

Figure 5: Schematic of a possible cut in a tetrahedral element contacting the solid surface. $\partial\Gamma^e$ is marked with a red solid line and quadrature points are represented by black dots.

functions up to third–order). The conventional alternative to the element splitting procedure is the incorporation of a smoothed numerical approximation of the delta function; in the continuum force approach, this is essentially needed to formulate the surface tension and the contact–line model. In the present approach, due to the employment of the splitting methodology, such an approximation is not required and the associated errors are alleviated.

The presented formulation is implemented withing the framework of the stabilized pressure enriched finite element method proposed in [65]. Within element e, the standard finite element approximation of the flow variables reads

$$\mathbf{u}(\mathbf{x},t) = \sum_{I\in\mathcal{N}^e} \mathbf{u}_I(t) N_I^e(\mathbf{x}), \tag{21}$$

and

$$p(\mathbf{x},t) = \sum_{I\in\mathcal{N}^e} p_I(t) N_I^e(\mathbf{x}), \tag{22}$$

where $\mathcal{N}^e$ denotes the set of associated nodes and N_I^e is the shape function

corresponding to node I. However, using the standard finite element approximation, it is impossible to capture the intra-element discontinuity in the presence of material interfaces; in the context of multi-phase flows [65], this is the source of the so-called "spurious currents". In order to resolve this issue, the pressure approximation within an element cut by the interface can be enriched by accounting for a "jump" as

$$p(\mathbf{x},t) = \sum_{I \in \mathcal{N}^{e,cut}} p_I(t) N_I^{e,cut}(\mathbf{x}) + \sum_{I \in \mathcal{N}^{e,cut}} p_{I,enr}^{e,cut}(t) N_{I,enr}^{e,cut}(\mathbf{x}), \tag{23}$$

with enriched nodal pressure $p_{I,enr}^{e,cut}$ being local to the cut element.

In this work, enriched shape function $N_{I,enr}$ is constructed based on standard continuous shape function N_I as

$$N_{I,enr}(\mathbf{x}) = \begin{cases} N_I(\mathbf{x}) & \textbf{if } (\mathbf{x}_I \in \Omega_1 \textbf{ and } \mathbf{x} \in \Omega_2) \textbf{ or } (\mathbf{x}_I \in \Omega_2 \textbf{ and } \mathbf{x} \in \Omega_1) \\ 0 & \textbf{else} \end{cases} \tag{24}$$

Using this set of enriched shape functions, both the jump in the pressure and discontinuity in its gradient can be captured within a cut element. After introducing the enrichment terms, the variational multiscale methodology with the well–established algebraic sub-grid scale stabilization [78] along with a special small–cut treatment approach is utilized to stabilize the method as proposed in [65]. The momentum equation is then linearized using the generalized Newton's method and solved along with the mass conservation equation in a fully implicit monolithic manner. One of the remarkable features of this enrichment procedure is that upon the creation of the local elemental system of equations, pressure condensation procedure [65] is performed at the elemental level, thus, omitting the introduction of the additional enriched pressure degrees of freedom. Therefore, the degrees of freedom, and consequently, the size of the assembled global system of equations is the same as that of the standard finite element method.

2.3. Level-set

In the present method, the evolution of the interface is captured using the level-set method [79], which is based on the introduction of the continuous function ϕ that represents the signed distance to the interface. The level-set function is convected according to the velocity field by solving

$$\frac{\partial \phi}{\partial t} + \mathbf{u} \cdot \nabla \phi = 0 \quad \text{in } \Omega. \tag{25}$$

In the present work, this pure convection equation is stabilized following the methodology proposed by Codina [80]. The level-set function gradually loses its regularity due to its deviation from a distance function [81] and high frequency noise (oscillatory interface) [82]. The first problem can be resolved by frequent reinitialization of the level-set function in a way that $\|\nabla\phi\| \approx 1$ is satisfied [83]. Due to the hyperbolic nature of the conventional level-set reinitialization formulation, it is necessary to take into account the so-called "blind-spot region" in the vicinity of the solid surface [84]. Nonetheless, in the present work, the marching level-set reinitialization procedure proposed by Elias *et al.* [85] is performed for the whole domain once in every 50 time-steps.

Following the idea presented in [86], the high frequency oscillations can be effectively cured by solving a diffusion equation for the level-set function as

$$\tilde{\phi} - \varepsilon\nabla^2\tilde{\phi} = \phi \quad \text{in } \Omega, \tag{26}$$

where $\tilde{\phi}$ and ϕ are the smoothed (non-oscillatory) and original level-set functions, respectively. Here, $\varepsilon = 5 \times 10^3 \Delta t h_e^2$, with Δt being the size of the time-step and h_e the element size. In the absence of contact with a solid, Eq. (26) can be solved without introducing any specific boundary condition [86, 82, 65]. In the present method, a Neumann boundary condition is implemented on the solid substrate as

$$\mathbf{n}_s \cdot \nabla\tilde{\phi} = \mathbf{n}_s \cdot \nabla\phi \quad \text{on } \partial\Omega_s. \tag{27}$$

Combining Eqs. (10), (12), and (15),

$$\theta^{num} = \left\{ \left(\cos^{-1}\left[\frac{\zeta}{\gamma} u_{slip} + \cos(\theta_Y) \right] \right)^3 + 9\mathrm{Ca}\ln\left(\frac{h_e}{l_{micro}}\right) \right\}^{1/3}, \tag{28}$$

at the cut elements, boundary condition (27) is substituted by

$$\mathbf{n}_s \cdot \nabla\tilde{\phi} = -\|\nabla\phi\| \cos(\theta^{num}) \quad \text{on } \partial\Omega_s^{e,cut}. \tag{29}$$

It should be noted that in case of the application of the full form of the molecular–kinetic model, Eq. (28) should be rewritten incorporating Eq. (11).

The main shortcoming of the presented level-set smoothing scheme is the probability of a slight droplet shrinkage. As proposed in [65], this issue can

be resolved by performing a correction step as

$$\phi_I = \tilde{\phi}_I - \frac{1}{\mathcal{N}_I} \sum_{J}^{\mathcal{N}_I} \left(\tilde{\phi}_J - \phi_J \right), \tag{30}$$

where $\mathcal{N}_I$ is the number of nodes J that are connected to node I. In this work, in order not to perturb the contact angle, a modified correction procedure is proposed by separating the set of nodes interior to the fluid domain from those that lie on the solid substrate, *i.e.*

$$J \in \begin{cases} \Omega \setminus \partial\Omega_s & \text{if } I \in (\Omega \setminus \partial\Omega_s) \\ \partial\Omega_s & \text{if } I \in \partial\Omega_s \end{cases} \tag{31}$$

Above, all the ingredients of the proposed method are detailed. The summary of the overall strategy is presented in Algorithm 1.

3. Results

The proposed numerical method is implemented within KRATOS Multi-physics [87] an open-source framework for multi-physics computations. The second order backward difference (BDF2) time integration is applied to the flow equations and the Crank–Nicolson scheme is used for time-marching of the level-set convection equation. Algebraic multigrid library (AMGCL [88]) was used to solve the linear system of equations using the GMRES(m) method (with restart parameter $m = 40$). The convergence tolerance of the linear solver is set to 10^{-9}, while a relative tolerance of 10^{-5} is considered to check the convergence of velocity and pressure.

In the following, the performance of proposed numerical method is first verified by comparing the simulation results with the theoretical relation obtained for the footprint radius of a liquid droplet spreading on a solid substrate at small Bond numbers. The method is further validated against the experimental data published in the literature for a millimeter-sized squalane droplet spreading on a substrate of silicone wafer. In the end, the capability of the method is assessed by simulating a droplet trapped inside conical pores. In all cases solved in this paper, gravity $g = 9.8m/s^2$ acts in the negative z–direction, and Ω_2 is composed of air with $\rho = 1.0kg/m^3$ and $\mu = 1.0 \times 10^{-5} Pa.s$. For the sake of convenience, the contact-angle is reported in degrees in the rest of this paper.

Algorithm 1: Summary of the proposed method

Input: $\mathbf{u}_0$, $\mathbf{u}_D$, $\mathbf{T}_N$, and ϕ_0
Output: $\mathbf{u}_I$, p_I, and ϕ_I; node $I \in \Omega$

$n = 1$
$t = 0$
while $t <$ *run-time* **do**
  solve Eq. (25) for $\phi_I^{(n+1/2)}$ with ***half*** time-step
  if $n = \{50, 100, 150, \ldots\}$ **then**
    reinitialize ϕ
  do smoothing according to Eqs. (26) and (30) with conditions (27) and (29)
  calculate curvature
  for *all elements* e **do**
    if $e \cap \Gamma \neq \varnothing$ **then**
      do element spliting
      calculate contact angle
    create elemental system of equations
  do assembling the Linear System of Equations (LSE)
  solve LSE for $\left[\mathbf{u}_I^{(n+1)}, p_I^{(n+1)}\right]$
  solve Eq. (25) for $\phi_I^{(n+1)}$ with ***half*** time-step
  update $n = n + 1$
  update $t = n\Delta t$

Remark

Before assessing the results of the proposed method, it is worth to provide an insight of the computational costs associated with its application: using a mesh with $\sim 500K$ elements, the total run–time per time–step is around $62s$, of which almost 80% corresponds to the two-phase flow solver, 4% to the level–set convection, 8% to the level–set smoothing procedure, and about 8% is consumed for the level–set re-initialization procedure.

3.1. Verification with theory

If a droplet retains its spherical-cap shape during spreading on a solid surface, one can write a correlation between the footprint radius and the instantaneous contact-angle based on the mass conservation of an incompressible liquid. The resulting correlation reads as $r(t) = f\left(\theta(t)\right)$ with [33]

$$f\left(\theta\right) = \left\{ \frac{3V}{\pi} \frac{\left[1+\cos(\theta)\right]\sin(\theta)}{\left[1-\cos(\theta)\right]\left[2+\cos(\theta)\right]} \right\}^{1/3}. \tag{32}$$

Starting from $\theta(0) = \pi/2$, the ratio of the terminal radius r_Y to the initial radius of the droplet R_0 is

$$\frac{r_Y}{R_0} = \left\{ \frac{2\left[1+\cos(\theta_Y)\right]\sin(\theta_Y)}{\left[1-\cos(\theta_Y)\right]\left[2+\cos(\theta_Y)\right]} \right\}^{1/3}. \tag{33}$$

The basic assumption of a spherical-cap droplet is valid if the Bond number ($Bo = \rho_1 g R_0^2/\gamma$) is small or equivalently the height of the droplet is smaller than the capillary length-scale ($l_c \sim \sqrt{\gamma/\rho_1 g}$) [69, 33, 68]. This condition indicates that gravity is dominated by the capillary force and therefore, has a negligible effect on the droplet dynamics. Note that this assumption is questionable for fluids with large viscosity, *e.g.* for polymeric liquids [33].

Here, a liquid droplet with an initially hemispherical shape (initial contact-angle of $\theta_0 = 90^\circ$) and an initial radius of $R_0 = 1.5mm$ is spreading on a solid substrate. The system is confined in a box filled by air with no-slip lateral and top boundaries. The schematic of the whole system is shown in Fig. 6. The dimensions are $L = W = 8mm$ and $H = 3mm$, liquid viscosity is $\mu_1 = 1.0 \times 10^{-3} Pa.s$, density is $\rho_1 = 920 kg/m^3$, and the liquid-air surface tension is $\gamma = 4.26 \times 10^{-2} N/m$. This gives a $Bo = 0.48$ or equivalently a capillary length-scale of $l_c = 2.2mm$. The equilibrium contact-angle is set to $\theta_Y = 58^\circ$ and the results are obtained using $\beta = 10^3 Pa.s/m$ and $\zeta = 1.0 Pa.s$,

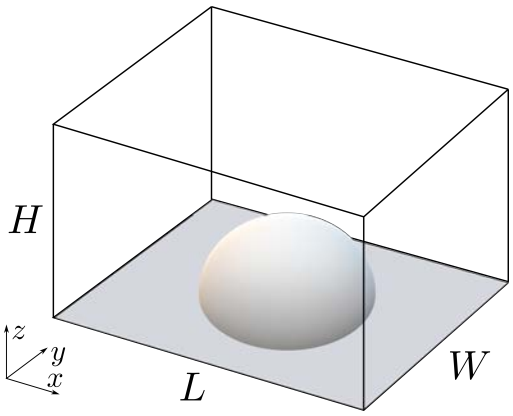

Figure 6: Schematic of the initial configuration of the liquid droplet inside a solid box.

noting that this example does not intent to reproduce any real-world experiment.

This problem is solved for four different (structured) meshes of $R_0/h_e \approx 7.8$, 11.3, 15.3, and 19.1, composed of tetrahedral elements with the size of $h_e = (1/6V_e)^{1/3}$, where V_e is the volume of a single element. The time evolution of the contact angle and the footprint (base) radius of the droplet is shown in Figs. 7 and 8, respectively. In this work, the contact-angle is calculated as the average of θ obtained for all cut elements with $\Omega^e \cap \partial\Gamma \neq \varnothing$. The reported radius is also the average distance of the center of the solid substrate, located at $(x, y, z) = (L/2, W/2, 0)$, to the center of all $\partial\Gamma^e = \Omega^e \cap \partial\Gamma$. In the mentioned figures, the theoretical values of θ_Y and r_Y obtained from Eq. (33) are shown for comparison. In addition, since the Bond number is finite, the corrected equilibrium footprint radius, in the presence of gravity is calculated based on the theory developed in [69] and denoted by $r_{Y,g}$ in the following figures.

As seen in Figs. 7 and 8, numerically obtained droplet configuration at equilibrium, *i.e.* (θ_{eq}, r_{eq}) shows a good consistency with the theoretical prediction $(\theta_Y, r_{Y,g})$; while the error in θ_{eq} is around 3.1% and 2.4% for $R_0/h_e \approx 7.8$ and 11.3, respectively, it is reduced to below 0.5% for two finer meshes of $R_0/h_e \approx 15.3$ and 19.1. The corresponding errors in the footprint radius at equilibrium in comparison with $r_{Y,g}$ are around 5.0%, 1.1%, 0.6%, and 0.3% for $R_0/h_e \approx 7.8$, 11.3, 15.3, and 19.1, respectively.

For all the employed meshes, the largest deviation from the theoretical value in terms of the dynamic contact-angle and the evolving footprint radius

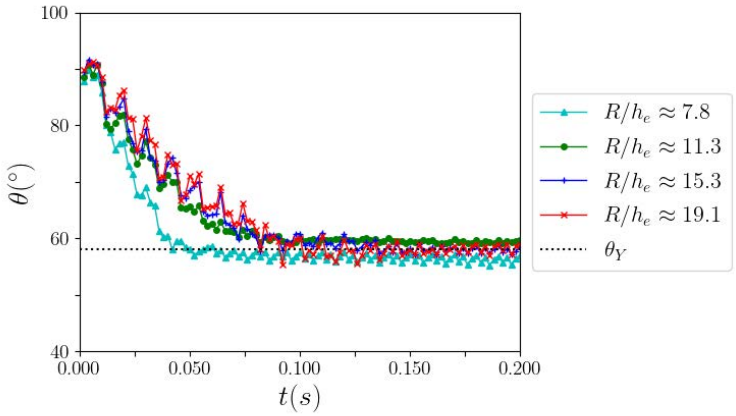

Figure 7: The effect of the mesh resolution on the time-evolution of the contact angle for a droplet spreading with $Bo = 0.48$ and $\theta_Y = 58°$.

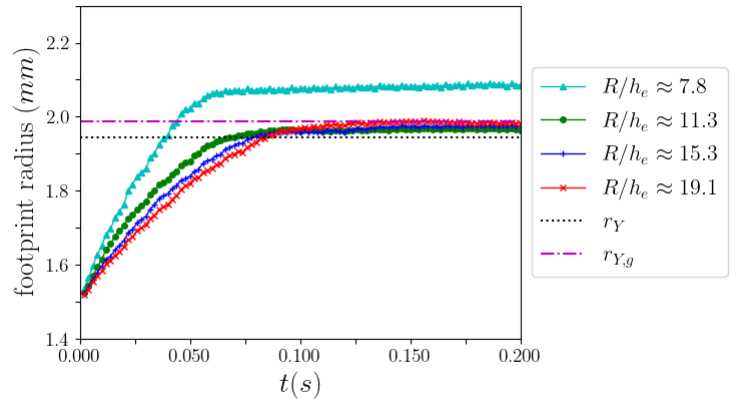

Figure 8: The effect of the mesh resolution on the time-evolution of the footprint radius of a droplet spreading with $Bo = 0.48$ and $\theta_Y = 58°$.

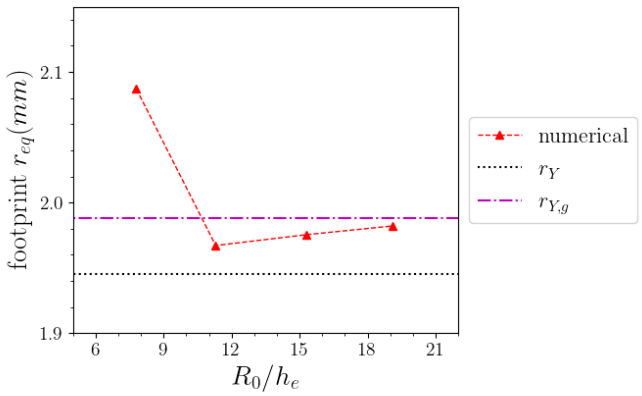

Figure 9: Mesh convergence of the footprint radius of a droplet spreading with $Bo = 0.48$ and $\theta_Y = 58°$. The theoretical value of r_{eq} is shown by dotted-line.

of the droplet, is observed in the middle stages of the spreading. The mesh-convergence of r_{eq} is shown in Fig. 9. The equilibrium configuration of the droplet is obviously converging by increasing the mesh resolution. In the present test-case, the settings lead to a very small capillary number and therefore, the difference between θ and θ^{num} is fairly small.

Considering the initial configuration of the droplet and fact that the height of the droplet, and consequently the effect of gravity is constantly decreasing during the spreading, it is expected that the spherical-cap assumption and consequently, Eq. (32) can also be applied to the evolution of the radius of the droplet. It is shown in Fig. 10, where the numerically obtained footprint radius of the droplet for $R_0/h_e \approx 15.3$ is compared to Eq. (32); the agreement is clearly seen. However, specially for the initial stages of the spreading, the slight deviation is expected as a result of a finite gravity and the effect of inertia.

It should be noted that releasing the droplet from rest with its center-of-gravity initially located above the solid substrate, triggers a series of oscillations in the contact-angle (see Fig. 7, it is also directly reflected in Fig. 10 for $r = f(\theta)$ curve). These are physically expected inertial oscillations with an origin similar to what was theoretically formulated in [89] (art. 275); any disturbance in the shape of a droplet in the simultaneous presence of the surface tension and inertia, results in an oscillatory behavior. Since

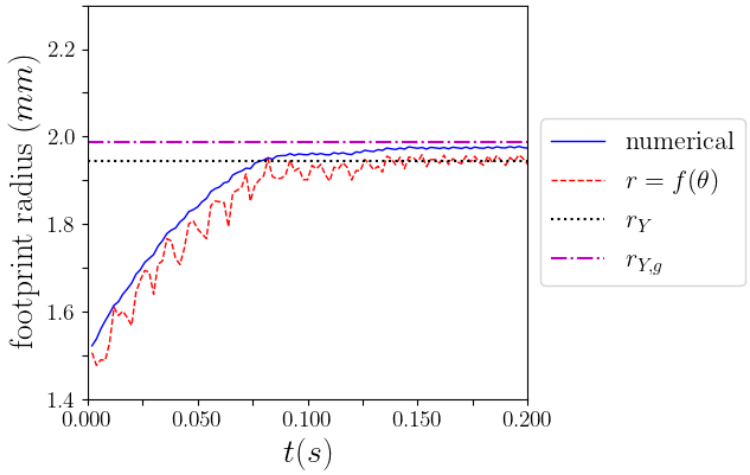

Figure 10: Time-evolution of the footprint radius of a droplet spreading with $Bo = 0.48$ and $\theta_Y = 58°$, in comparison with $r = f(\theta)$.

the initial triggering disturbance is of a spontaneous nature, these oscillation are eventually damped due to viscous dissipation. On the other hand, the persistent high-frequency oscillations of insignificant amplitude in the contact-angle (particularly evident near the steady-state) occur due to the intermittent level-set re-initialization (performed every 50 time–steps in the present work).

3.1.1. Obtuse Contact–angle

In order to further analyze the performance of the proposed method for an obtuse equilibrium contact–angle, the same test–case of the droplet spreading is simulated here with $\theta_0 = 159°$ and $\theta_Y = 105°$. Time–evolution of the contact–angle as well as the footprint radius is shown in Fig. 11. Here, despite being characterized by the same Bond number ($Bo = 0.48$), which corresponds to the initial radius of the droplet, the significantly larger height suggests a pronounced effect of gravity on the equilibrium shape of the droplet. This explains the rather large difference between $r_Y = 1.30mm$ and $r_{Y,g} = 1.77mm$. In addition, releasing the droplet with its center–of–gravity being initially positioned farther from the solid substrate (at $z_0 = 1.4mm$) triggers more profound inertial oscillations.

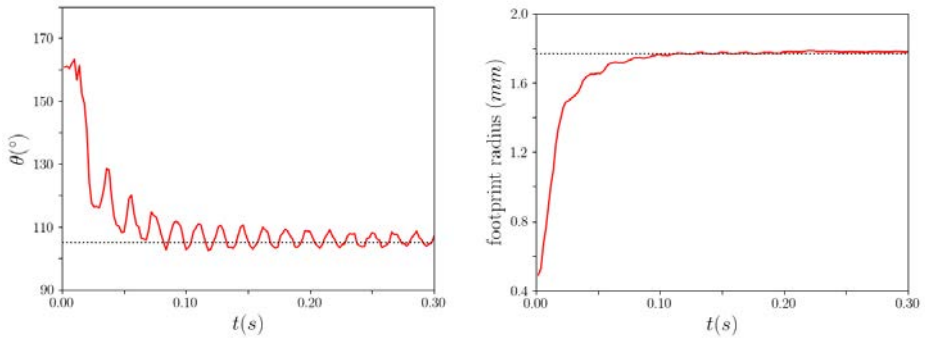

(a) (b)

Figure 11: Time-evolution of (a) the contact–angle and (b) the footprint radius of a droplet spreading with $Bo = 0.48$ and $\theta_Y = 105°$. The solid red line and the dotted line correspond to the numerical result and the theoretical prediction $(\theta_Y, r_{Y,g})$, respectively.

The above-presented results show that the present numerical model can successfully capture the configuration of a spreading droplet consistently with the theoretical predictions.

3.2. Validation against experimental data

Next, the proposed numerical method is validated by simulating the spreading of a liquid (squalane) droplet on a solid (silicone wafer) substrate and comparing the obtained numerical results with the experimental data reported in [26]. In this test, besides the time-evolution of the configuration of the droplet at the near-equilibrium stage, the initial stage of the droplet spreading (in which inertia also plays an important role) is taken into account. Therefore, this test allows for the in-depth validation of the proposed numerical method.

Squalane has a viscosity of $\mu_1 = 3.14 \times 10^{-2} Pa.s$, density $\rho_1 = 810 kg/m^3$, and the liquid-air surface tension $\gamma = 3.11 \times 10^{-2} N/m$. The squalane droplet in contact with the surrounding air and the silicone wafer substrate creates an equilibrium contact angle of 38.8°. Same computational domain as the one used in section 3.1 is chosen (see Fig. 6), while the initial radius and contact-angle of the droplet are set to $R_0 = 0.9mm$ and $\theta_0 = 180°$, respectively. Here, ζ is set to $0.7Pa.s$ in order to correspond to the value calculated in [26] by performing a data fitting based on the linear Petrov model. The Navier-slip

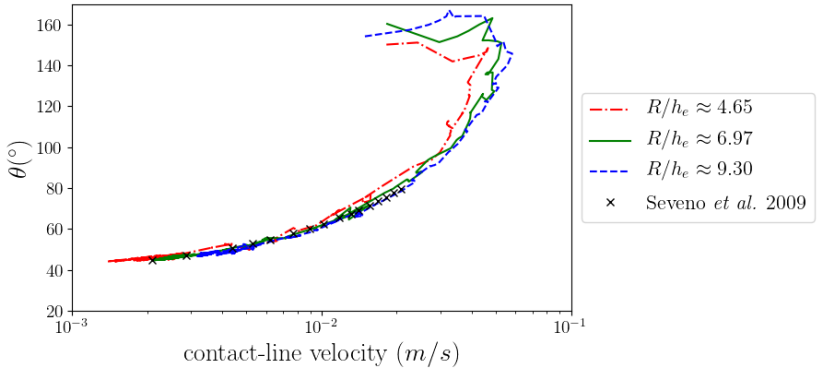

Figure 12: Contact-angle as a function of the velocity of the contact-line; comparison of the experiment [26] with the numerical data obtained for structured meshes of different resolutions.

coefficient of $\beta = 10^3 Pa.s/m$ is chosen so to provide the best match with the experimentally obtained contact velocity-angle relation as shown in Fig. 12. It is observed that the experimental data can perfectly be reproduced by the implemented model for the moving contact-line. Numerical data are obtained by performing simulations on three different structured meshes of tetrahedral elements with $R_0/h_e \approx 4.65$, 6.97, and 9.30. Varying the mesh resolution has a negligible effect on the contact velocity-angle relation.

In Fig. 13, the experimentally obtained time-evolution of the contact-angle is compared to the numerical value for different mesh resolutions. Numerical results are in a good agreement with the experimental data. Mesh-convergence of the solution is confirmed by comparing the results obtained for $R_0/h_e \approx 6.97$, and 9.30. The mesh-convergence is further shown in Fig. 14 for the footprint radius of the droplet during the spreading.

In an attempt to compare the radius of the droplet with data reported in [26], correlation $R = r/\cos(\theta - \pi/2)$ is applied to the numerical data. This correlation, based on the assumption that the spreading droplet has a spherical-cap shape, is valid in the current test-case only during the final stage of the spreading, for which $\theta < 70^\circ$ [26]. Figure 15 illustrates the reproduced radius of the droplet for different mesh resolutions in comparison with the experimental data.

Upon validation of the proposed method, in the following, the perfor-

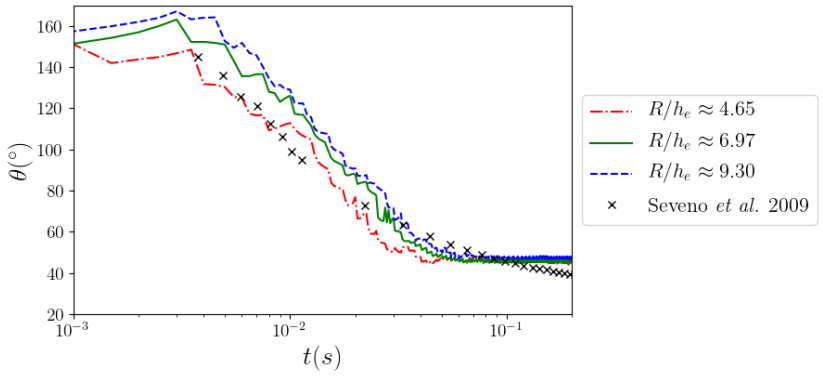

Figure 13: Time evolution of the contact-angle; comparison of the experiment [26] with the numerical data obtained for structured meshes of different resolutions.

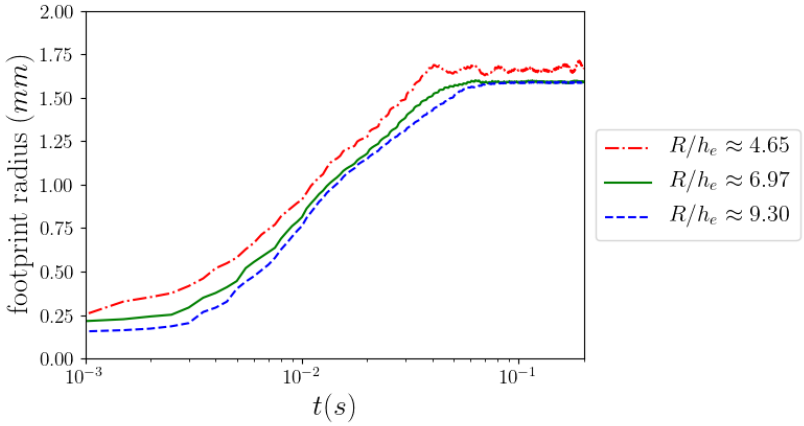

Figure 14: Time evolution of the footprint radius; comparison of data obtained for structured meshes of different resolutions.

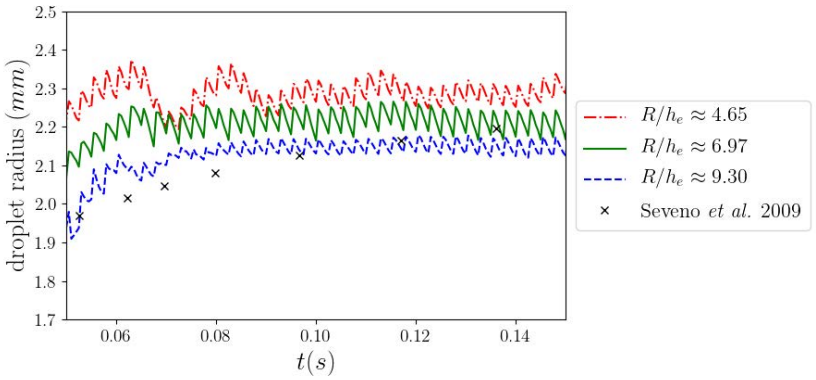

Figure 15: Radius of the droplet; comparison of the data presented in [26] with the numerical data obtained for structured meshes of different resolutions.

mance of the method is investigated for the same test is simulated on an unstructured mesh. The initial radius to (average) element size ratio of $R_0/h_e \approx 9$ is set for the elements located on the solid surface, *i.e.* $\Omega^e \cap \Omega_s \neq \varnothing$, while the mesh resolution is significantly coarser for internal elements with $R_0/h_e \approx 4.5$. Keeping parameters β and ζ unchanged, the numerically obtained contact velocity-angle relation is shown in Fig. 16. Despite a slight deviation, the result is completely satisfactory. The time-evolution of the contact-angle obtained for the unstructured mesh is shown in Fig. 17. The result obtained on the unstructured mesh shows a slight increase in the high-frequency oscillations comparing to that of the structured mesh during the middle stage of the droplet spreading. In order to explore the pressure field, the computational domain is evenly divided and the pressure contours are plotted on the division plane in Fig. 18. The results obtained on structured and unstructured meshes exhibit a good match. The isometric (three-dimensional) and side view of the droplet-air interface is presented in Fig. 19 at different instances. These are obtained by plotting the zero level-set ($\phi = 0$) iso-surfaces obtained for the unstructured mesh. As seen in Figs. 19(g) and 19(h), the deviation from the spherical-cap shape is evident for the initial stage of the spreading.

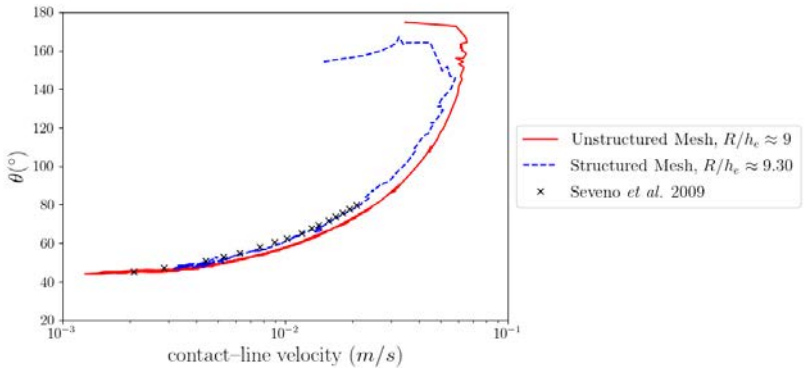

Figure 16: Contact-angle as a function of the velocity of the contact-line; comparison between the experimental data [26] and the numerical results obtained for the structured and the unstructured meshes.

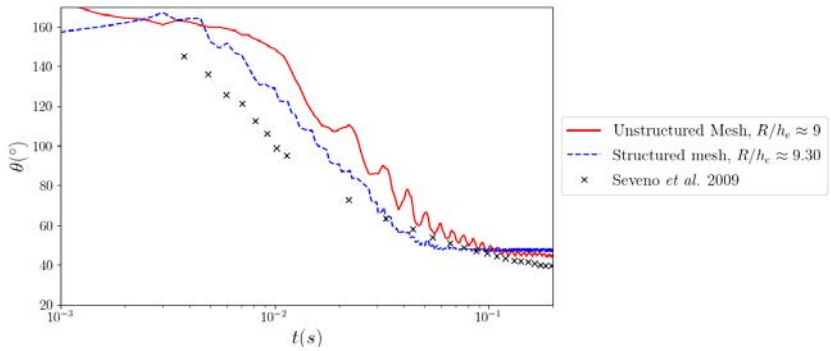

Figure 17: Time evolution of the contact-angle; comparison between the experimental data [26] and the numerical results obtained for the structured and the unstructured meshes.

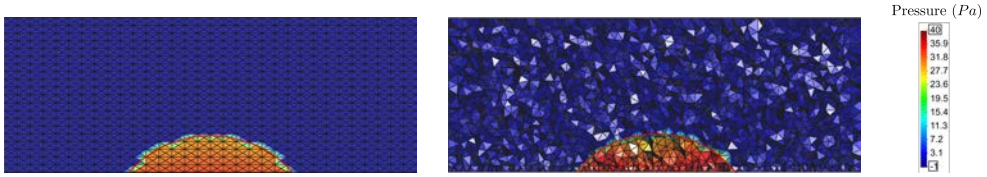

(a) (b)

Figure 18: Pressure contours obtained at $t = 0.1s$ for (a) structured and (b) unstructured meshes.

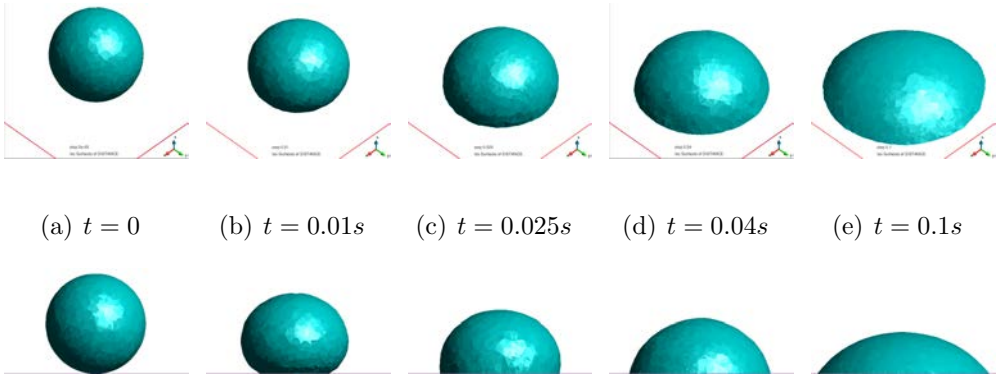

(a) $t = 0$ (b) $t = 0.01s$ (c) $t = 0.025s$ (d) $t = 0.04s$ (e) $t = 0.1s$

(f) $t = 0$ (g) $t = 0.01s$ (h) $t = 0.025s$ (i) a (j) $t = 0.1s$

Figure 19: Evolution of the liquid-air interface of the squalane droplet spreading on silicone wafer.

3.3. Droplet trapped in conical pores

In order to assess the capability of the proposed method in a more complex case, in the following the numerical method is applied to the evolution of a droplet trapped inside conical pores. The settings of this test-case preclude the straight-forward application of the conventional schemes, which are basically developed for structured meshes.

The schematic of the configuration of the pore with the initially spherical droplet of radius $R_0 = 0.9mm$ in tangential contact with the cone is shown in Fig. 20. Physical parameters are set according to data reported in section 3.2 for the squalane droplet on the silicone wafer substrate. Here, the simulations are performed for two conical pores of $\alpha = 30°$ and $60°$ with $H = 5.5mm$ and $4mm$, respectively. The computational domain is discretized with tetrahedral elements of size $R_0/h_e \approx 14.3$ adjacent to the solid surface and $R_0/h_e \approx 9$ inside the domain.

The evolution of the trapped droplet is shown in Fig. 21 for $\alpha = 30°$. Starting from a perfectly spherical shape, concave interfaces are gradually established due to $\theta_Y < \pi/2$. As shown in Fig. 22, this leads to a reduced (negative) pressure inside the droplet at equilibrium. Figures 22 and 23 present the pressure contours inside the computational domain obtained at different time-instances for $\alpha = 30°$ and $60°$, respectively. It is evident that by evolving the interface from a convex to a concave shape, pressure inside

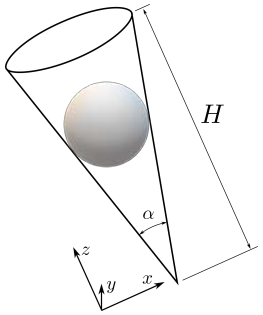

Figure 20: Schematic of the initial configuration of the droplet trapped in a conical pore.

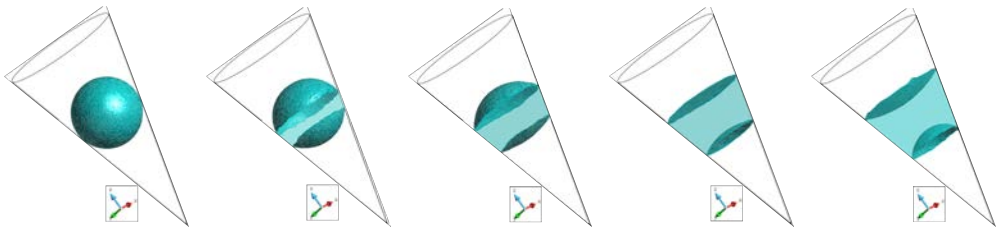

(a) Initial state (b) $t = 0.005s$ (c) $t = 0.01s$ (d) $t = 0.02s$ (e) $t = 0.08s$

Figure 21: Evolution of the liquid-air interface of the droplet trapped inside a conical pore with $\alpha = 30°$.

the droplet varies from the maximum to the minimum value. The average value of the numerically obtained terminal contact-angle is $\theta_{eq} \approx 43.3^\circ$ for $\alpha = 30^\circ$, and $\theta_{eq} \approx 43.9^\circ$ for $\alpha = 60^\circ$; this is consistent with $\theta_Y = 38.8^\circ$ set as an input parameter for simulations.

The present set of test-cases required, on average, three to four iterations to reach pressure and velocity convergence in each time-step, while the linear solver fulfilled the maximum tolerance condition in about 50 iterations.

4. Summary and Conclusion

In order to develop a level-set/enriched finite element method with the capability of treating dynamics of the moving contact-line, a systematic and physically consistent methodology was proposed; the role of the molecular–kinetic theory and the hydrodynamic theory in the numerical modeling were elaborated along with the necessary customization of the boundary conditions including the contact–line dynamics. By applying the proposed method to the spreading of a droplet, an acceptable mesh-convergence was observed. The results were also compared for both the structured and unstructured meshes and a good agreement was revealed. Furthermore, the straightforward employment of the proposed method to simulate a droplet trapped in a (closed) conical pore, suggests the applicability of the developed numerical tool for pore-scale multi-phase flows. It must be noted that in this work no mesh-refinement strategy was utilized to locally increase the resolution close to the droplet interface.

One of the interesting features of the present method was that in order to obtain physically meaningful results, the contact-line dissipation coefficient was set according to the corresponding parameter that was obtained by fitting the linear Petrov's model into the experimental data. This alleviates the ambiguity associated with the setting of this parameter in the approaches rely on the generalized Navier-slip condition. However, further investigation with a wider range of liquid/solid materials is necessary to further support this affirmation, which would be the topic of a separate research.

Generally, during the initial stage of the droplet spreading, inertial effects are rather significant and therefore, the validity of the simplified model used in the present work to resolve the sub-elemental hydrodynamics becomes dubious. Therefore, in order to increase the accuracy while capturing the spreading with a finite inertia, a more sophisticated hydrodynamic model

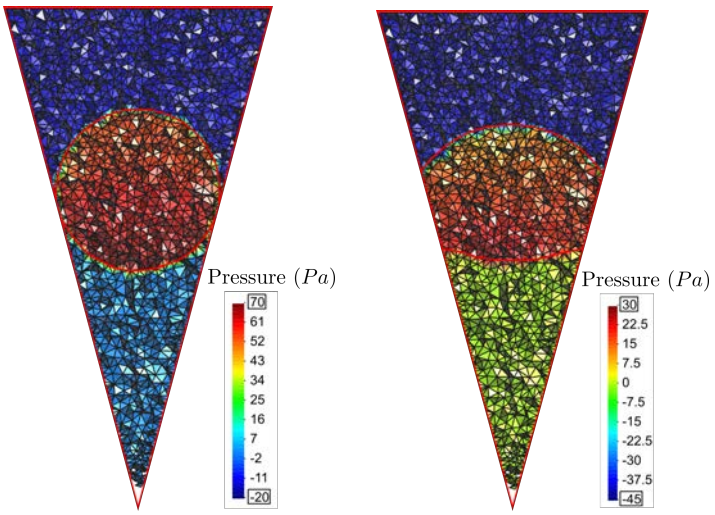

(a) $t = 0.001s$ (b) $t = 0.01s$

(c) $t = 0.02s$ (d) $t = 0.2s$

Figure 22: Pressure contours for $\alpha = 30°$. At $t = 0.2s$, the system has almost reached its equilibrium configuration.

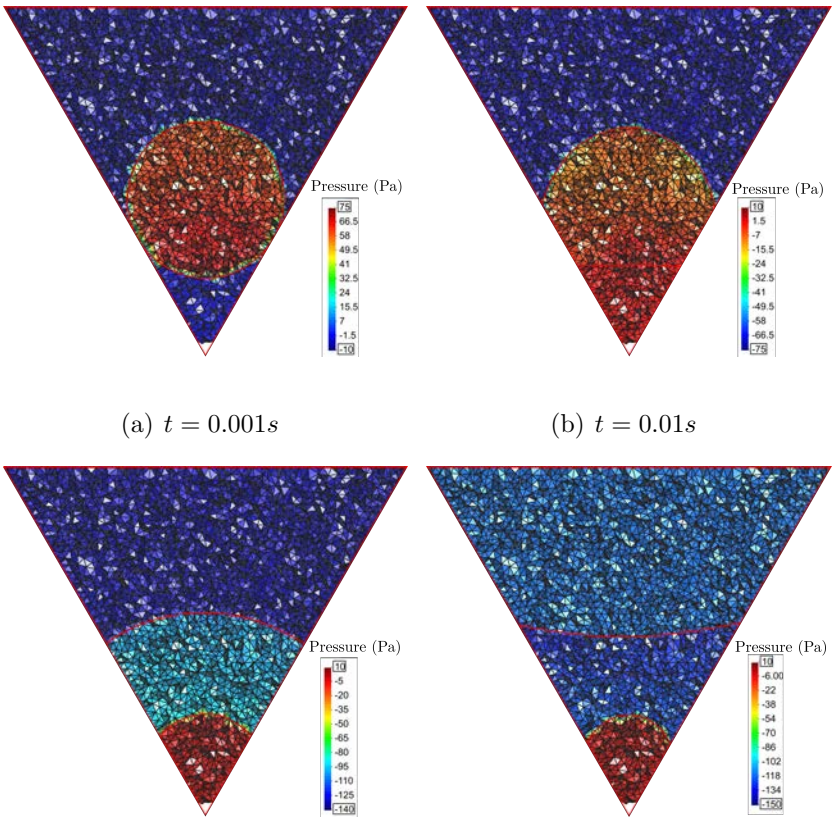

(a) $t = 0.001s$ (b) $t = 0.01s$

(c) $t = 0.02s$ (d) $t = 0.14s$

Figure 23: Pressure contours for $\alpha = 60°$. At $t = 0.14s$, the system has almost reached its equilibrium configuration.

that also incorporates the terms appearing at finite Reynolds number can be acquired. This is a subject for future developments.

In order to improve the coupling between the momentum equation and the evolving interface that is represented by the level-set function, in this work the level-set convection equation is split in time as shown in Algorithm 1. Numerical simulations showed that such splitting could positively affect the accuracy of the method and alleviate the need for an excessive diffusive level-set smoothing to regularize the interface. Nevertheless, further investigations are needed to quantify this improvement.

5. Acknowledgment

This work was performed within the framework of AMADEUS project ("Advanced Multi-scAle moDEling of coupled mass transport for improving water management in fUel cellS", reference number PGC2018-101655-B-I00) supported by the *Ministerio de Ciencia, Innovacion e Universidades* of Spain. The authors also acknowledge financial support of the mentioned Ministry via the "Severo Ochoa Programme" for Centres of Excellence in R&D (referece: CEX2018-000797-S) given to the International Centre for Numerical Methods in Engineering (CIMNE).

Conflict of interest

The authors declare that they have no conflict of interest.

References

[1] D. Bonn, J. Eggers, J. Indekeu, J. Meunier, E. Rolley, Wetting and spreading, Reviews of Modern Physics 81 (2009) 739–805. URL: https://link.aps.org/doi/10.1103/RevModPhys.81.739. doi:10.1103/RevModPhys.81.739, publisher: American Physical Society.

[2] C. N. Baroud, H. Willaime, Multiphase flows in microfluidics, Comptes Rendus Physique 5 (2004) 547–555. URL: http://www.sciencedirect.com/science/article/pii/S1631070504000854. doi:10.1016/j.crhy.2004.04.006.

[3] L. Shui, J. C. T. Eijkel, A. van den Berg, Multiphase flow in microfluidic systems – Control and applications of droplets and interfaces, Advances in Colloid and Interface Science 133 (2007) 35–49. URL: http://www.sciencedirect.com/science/article/pii/S0001868607000590. doi:10.1016/j.cis.2007.03.001.

[4] K. A. Culligan, D. Wildenschild, B. S. B. Christensen, W. G. Gray, M. L. Rivers, Pore-scale characteristics of multiphase flow in porous media: A comparison of air–water and oil–water experiments, Advances in Water Resources 29 (2006) 227–238. URL: http://www.sciencedirect.com/science/article/pii/S030917080500120X. doi:10.1016/j.advwatres.2005.03.021.

[5] K. E. Thompson, Pore-scale modeling of fluid transport in disordered fibrous materials, AIChE Journal 48 (2002) 1369–1389. URL: http://aiche.onlinelibrary.wiley.com/doi/abs/10.1002/aic.690480703. doi:10.1002/aic.690480703, _eprint: https://onlinelibrary.wiley.com/doi/pdf/10.1002/aic.690480703.

[6] X. Zhu, P. Sui, N. Djilali, Three-dimensional numerical simulations of water droplet dynamics in a PEMFC gas channel, Journal of Power Sources 181 (2008) 101–115. URL: https://linkinghub.elsevier.com/retrieve/pii/S0378775308004989. doi:10.1016/j.jpowsour.2008.03.005.

[7] M. Andersson, S. B. Beale, M. Espinoza, Z. Wu, W. Lehnert, A review of cell-scale multiphase flow modeling, including water management, in polymer electrolyte fuel cells, Applied Energy 180 (2016) 757–778. URL: http://www.sciencedirect.com/science/article/pii/S0306261916310972. doi:10.1016/j.apenergy.2016.08.010.

[8] A. Z. Weber, R. L. Borup, R. M. Darling, P. K. Das, T. J. Dursch, W. Gu, D. Harvey, A. Kusoglu, S. Litster, M. M. Mench, R. Mukundan, J. P. Owejan, J. G. Pharoah, M. Secanell, I. V. Zenyuk, A Critical Review of Modeling Transport Phenomena in Polymer-Electrolyte Fuel Cells, Journal of The Electrochemical Society 161 (2014) F1254–F1299. URL: https://iopscience.iop.org/article/10.1149/2.0751412jes. doi:10.1149/2.0751412jes.

[9] A. Jarauta, P. Ryzhakov, Challenges in Computational Modeling of Two-Phase Transport in Polymer Electrolyte Fuel Cells Flow Channels: A Review, Archives of Computational Methods in Engineering 25 (2018) 1027–1057. URL: http://link.springer.com/10.1007/s11831-017-9243-2. doi:10.1007/s11831-017-9243-2.

[10] J. H. Snoeijer, B. Andreotti, Moving Contact Lines: Scales, Regimes, and Dynamical Transitions, Annual Review of Fluid Mechanics 45 (2013) 269–292. URL: http://www.annualreviews.org/doi/10.1146/annurev-fluid-011212-140734. doi:10.1146/annurev-fluid-011212-140734.

[11] Y. D. Shikhmurzaev, Moving contact lines and dynamic contact angles: a 'litmus test' for mathematical models, accomplishments and new challenges, The European Physical Journal Special Topics 229 (2020) 1945–1977. URL: https://doi.org/10.1140/epjst/e2020-900236-8. doi:10.1140/epjst/e2020-900236-8.

[12] C. Huh, L. E. Scriven, Hydrodynamic model of steady movement of a solid/liquid/fluid contact line, Journal of colloid and interface science 35 (1971) 85–101. Publisher: Elsevier.

[13] E. B. Dussan V., S. H. Davis, On the motion of a fluid-fluid interface along a solid surface, Journal of Fluid Mechanics 65 (1974) 71–95. URL: https://www.cambridge.org/core/product/identifier/S0022112074001261/type/journal_article. doi:10.1017/S0022112074001261.

[14] L. M. Hocking, A moving fluid interface. Part 2. The removal of the force singularity by a slip flow, Journal of Fluid Mechanics 79 (1977) 209–229. URL: https://www.cambridge.org/core/product/identifier/S0022112077000123/type/journal_article. doi:10.1017/S0022112077000123.

[15] L. M. Hocking, A. D. Rivers, The spreading of a drop by capillary action, Journal of Fluid Mechanics 121 (1982) 425. URL: http://www.journals.cambridge.org/abstract_S0022112082001979. doi:10.1017/S0022112082001979.

[16] P. A. Thompson, M. O. Robbins, Simulations of contact-line motion: slip and the dynamic contact angle, Physical Review Letters 63 (1989) 766. Publisher: APS.

[17] T. Qian, X.-P. Wang, P. Sheng, Power-Law Slip Profile of the Moving Contact Line in Two-Phase Immiscible Flows, Physical Review Letters 93 (2004) 094501. URL: https://link.aps.org/doi/10.1103/PhysRevLett.93.094501. doi:10.1103/PhysRevLett.93.094501, publisher: American Physical Society.

[18] T. Qian, X.-P. Wang, P. Sheng, Molecular hydrodynamics of the moving contact line in two-phase immiscible flows, arXiv preprint cond-mat/0510403 (2005).

[19] R. G. Cox, The dynamics of the spreading of liquids on a solid surface. Part 1. Viscous flow, Journal of Fluid Mechanics 168 (1986) 169. URL: http://www.journals.cambridge.org/abstract_S0022112086000332. doi:10.1017/S0022112086000332.

[20] P. Zhang, K. Mohseni, Theoretical model of a finite force at the moving contact line, International Journal of Multiphase Flow 132 (2020) 103398. URL: http://www.sciencedirect.com/science/article/pii/S0301932220305073. doi:10.1016/j.ijmultiphaseflow.2020.103398.

[21] T. D. Blake, J. M. Haynes, Kinetics of liquidliquid displacement, Journal of Colloid and Interface Science 30 (1969) 421–423. URL: http://www.sciencedirect.com/science/article/pii/0021979769904111. doi:10.1016/0021-9797(69)90411-1.

[22] T. D. Blake, A. Clarke, J. De Coninck, M. J. de Ruijter, Contact angle relaxation during droplet spreading: comparison between molecular kinetic theory and molecular dynamics, Langmuir 13 (1997) 2164–2166. URL: https://doi.org/10.1021/la962004g. doi:10.1021/la962004g, publisher: American Chemical Society.

[23] M. J. de Ruijter, T. D. Blake, J. De Coninck, Dynamic Wetting Studied by Molecular Modeling Simulations of Droplet Spreading, Langmuir 15 (1999) 7836–7847. URL: https://doi.org/10.1021/la9901711. doi:10.1021/la9901711, publisher: American Chemical Society.

[24] J. G. Petrov, J. Ralston, M. Schneemilch, R. A. Hayes, Dynamics of Partial Wetting and Dewetting in Well-Defined Systems, The Journal of Physical Chemistry B 107 (2003) 1634–1645. URL: https://doi.org/10.1021/jp026723h. doi:10.1021/jp026723h, publisher: American Chemical Society.

[25] T. D. Blake, The physics of moving wetting lines, Journal of Colloid and Interface Science 299 (2006) 1–13. URL: https://linkinghub.elsevier.com/retrieve/pii/S0021979706002463. doi:10.1016/j.jcis.2006.03.051.

[26] D. Seveno, A. Vaillant, R. Rioboo, H. Adao, J. Conti, J. De Coninck, Dynamics of wetting revisited, Langmuir 25 (2009) 13034–13044. Publisher: ACS Publications.

[27] M. J. de Ruijter, J. De Coninck, T. D. Blake, A. Clarke, A. Rankin, Contact Angle Relaxation during the Spreading of Partially Wetting Drops, Langmuir 13 (1997) 7293–7298. URL: https://doi.org/10.1021/la970825v. doi:10.1021/la970825v, publisher: American Chemical Society.

[28] S. R. Ranabothu, C. Karnezis, L. L. Dai, Dynamic wetting: Hydrodynamic or molecular-kinetic?, Journal of Colloid and Interface Science 288 (2005) 213–221. URL: http://www.sciencedirect.com/science/article/pii/S0021979705002316. doi:10.1016/j.jcis.2005.02.074.

[29] A. Mohammad Karim, S. H. Davis, H. P. Kavehpour, Forced versus Spontaneous Spreading of Liquids, Langmuir 32 (2016) 10153–10158. URL: https://doi.org/10.1021/acs.langmuir.6b00747. doi:10.1021/acs.langmuir.6b00747, publisher: American Chemical Society.

[30] W. Ren, D. Hu, W. E, Continuum models for the contact line problem, Physics of Fluids 22 (2010) 102103. URL: https://aip-scitation-org.recursos.biblioteca.upc.edu/doi/full/10.1063/1.3501317. doi:10.1063/1.3501317, publisher: American Institute of Physics.

[31] P. Petrov, I. Petrov, A combined molecular-hydrodynamic approach to wetting kinetics, Langmuir 8 (1992) 1762–1767. Publisher: ACS Publications.

[32] F. Brochard-Wyart, P. G. de Gennes, Dynamics of partial wetting, Advances in Colloid and Interface Science 39 (1992) 1–11. URL: http://www.sciencedirect.com/science/article/pii/000186869280052Y. doi:10.1016/0001-8686(92)80052-Y.

[33] M. J. de Ruijter, J. De Coninck, G. Oshanin, Droplet Spreading: Partial Wetting Regime Revisited, Langmuir 15 (1999) 2209–2216. URL: https://doi.org/10.1021/la971301y. doi:10.1021/la971301y, publisher: American Chemical Society.

[34] M. J. de Ruijter, M. Charlot, M. Voué, J. De Coninck, Experimental Evidence of Several Time Scales in Drop Spreading, Langmuir 16 (2000) 2363–2368. URL: https://doi.org/10.1021/la990769t. doi:10.1021/la990769t, publisher: American Chemical Society.

[35] C. M. Phan, A. V. Nguyen, G. M. Evans, Combining hydrodynamics and molecular kinetics to predict dewetting between a small bubble and a solid surface, Journal of Colloid and Interface Science 296 (2006) 669–676. URL: http://www.sciencedirect.com/science/article/pii/S0021979705010076. doi:10.1016/j.jcis.2005.09.062.

[36] J.-C. Fernández-Toledano, T. D. Blake, J. De Coninck, Taking a closer look: A molecular-dynamics investigation of microscopic and apparent dynamic contact angles, Journal of Colloid and Interface Science 587 (2021) 311–323. URL: https://www.sciencedirect.com/science/article/pii/S0021979720316672. doi:10.1016/j.jcis.2020.12.013.

[37] T. Qian, X.-P. Wang, P. Sheng, Molecular scale contact line hydrodynamics of immiscible flows, Physical Review E 68 (2003) 016306. Publisher: APS.

[38] T. Qian, X.-P. Wang, P. Sheng, A variational approach to moving contact line hydrodynamics, Journal of Fluid Mechanics 564 (2006) 333. URL: http://www.journals.cambridge.org/abstract_S0022112006001935. doi:10.1017/S0022112006001935.

[39] W. Ren, W. E, Boundary conditions for the moving contact line problem, Physics of fluids 19 (2007) 022101. Publisher: American Institute of Physics.

[40] X. Xu, Y. Di, H. Yu, Sharp-interface limits of a phase-field model with a generalized Navier slip boundary condition for moving contact lines, Journal of Fluid Mechanics 849 (2018) 805–833. URL: https://www.cambridge.org/core/product/identifier/S0022112018004287/type/journal_article. doi:10.1017/jfm.2018.428.

[41] W. Ren, E. Weinan, Derivation of continuum models for the moving contact line problem based on thermodynamic principles, Communications in Mathematical Sciences 9 (2011) 597–606. URL: http://www.intlpress.com/site/pub/pages/journals/items/cms/content/vols/0009/0002/a013/. doi:10.4310/CMS.2011.v9.n2.a13.

[42] S. Manservisi, R. Scardovelli, A variational approach to the contact angle dynamics of spreading droplets, Computers & Fluids 38 (2009) 406–424. Publisher: Elsevier.

[43] S. Guo, M. Gao, X. Xiong, Y. J. Wang, X. Wang, P. Sheng, P. Tong, Direct Measurement of Friction of a Fluctuating Contact Line, Physical Review Letters 111 (2013) 026101. URL: https://link.aps.org/doi/10.1103/PhysRevLett.111.026101. doi:10.1103/PhysRevLett.111.026101, publisher: American Physical Society.

[44] Y. Yamamoto, T. Ito, T. Wakimoto, K. Katoh, Numerical simulations of spontaneous capillary rises with very low capillary numbers using a front-tracking method combined with generalized Navier boundary condition, International Journal of Multiphase Flow 51 (2013) 22–32. Publisher: Elsevier.

[45] J. Zhang, P. Yue, A level-set method for moving contact lines with contact angle hysteresis, Journal of Computational Physics (2020) 109636. Publisher: Elsevier.

[46] E. Mahrous, A. Jarauta, T. Chan, P. Ryzhakov, A. Z. Weber, R. V. Roy, M. Secanell, A particle finite element-based model for droplet spreading

analysis, Physics of Fluids 32 (2020) 042106. Publisher: AIP Publishing LLC.

[47] S. Zahedi, K. Gustavsson, G. Kreiss, A conservative level set method for contact line dynamics, Journal of Computational Physics 228 (2009) 6361–6375. Publisher: Elsevier.

[48] D. Jacqmin, Contact-line dynamics of a diffuse fluid interface, Journal of Fluid Mechanics 402 (2000) 57–88. URL: https://www.cambridge.org/core/product/identifier/S0022112099006874/type/journal_article. doi:10.1017/S0022112099006874.

[49] P. Yue, J. J. Feng, Wall energy relaxation in the Cahn–Hilliard model for moving contact lines, Physics of Fluids 23 (2011) 012106. URL: https://aip-scitation-org.recursos.biblioteca.upc.edu/doi/full/10.1063/1.3541806. doi:10.1063/1.3541806, publisher: American Institute of Physics.

[50] Y. Sui, H. Ding, P. D. Spelt, Numerical Simulations of Flows with Moving Contact Lines, Annual Review of Fluid Mechanics 46 (2014) 97–119. URL: https://doi.org/10.1146/annurev-fluid-010313-141338. doi:10.1146/annurev-fluid-010313-141338, _eprint: https://doi.org/10.1146/annurev-fluid-010313-141338.

[51] O. Weinstein, L. Pismen, Scale dependence of contact line computations, Mathematical Modelling of Natural Phenomena 3 (2008) 98–107. Publisher: EDP Sciences.

[52] F. Schönfeld, S. Hardt, Dynamic contact angles in CFD simulations, Computers & Fluids 38 (2009) 757–764. URL: http://www.sciencedirect.com/science/article/pii/S0045793008001916. doi:10.1016/j.compfluid.2008.05.007.

[53] J.-B. Dupont, D. Legendre, Numerical simulation of static and sliding drop with contact angle hysteresis, Journal of Computational Physics 229 (2010) 2453–2478. Publisher: Elsevier.

[54] Y. Sui, P. D. Spelt, An efficient computational model for macroscale simulations of moving contact lines, Journal of Computational Physics 242 (2013) 37–52. Publisher: Elsevier.

[55] S. Afkhami, S. Zaleski, M. Bussmann, A mesh-dependent model for applying dynamic contact angles to VOF simulations, Journal of Computational Physics 228 (2009) 5370–5389. Publisher: Elsevier.

[56] Y. Yamamoto, K. Tokieda, T. Wakimoto, T. Ito, K. Katoh, Modeling of the dynamic wetting behavior in a capillary tube considering the macroscopic–microscopic contact angle relation and generalized Navier boundary condition, International journal of multiphase flow 59 (2014) 106–112. Publisher: Elsevier.

[57] J. Luo, X. Y. Hu, N. A. Adams, Curvature boundary condition for a moving contact line, Journal of Computational Physics 310 (2016) 329–341. URL: http://www.sciencedirect.com/science/article/pii/S0021999116000322. doi:10.1016/j.jcp.2016.01.024.

[58] S. O. Unverdi, G. Tryggvason, A front-tracking method for viscous, incompressible, multi-fluid flows, Journal of computational physics 100 (1992) 25–37. Publisher: Elsevier.

[59] Y.-C. Chang, T. Hou, B. Merriman, S. Osher, A level set formulation of Eulerian interface capturing methods for incompressible fluid flows, Journal of computational Physics 124 (1996) 449–464. Publisher: Elsevier.

[60] M. Sussman, S. Uto, A computational study of the spreading of oil underneath a sheet of ice, CAM Report 114 (1998) 146–159.

[61] J. U. Brackbill, D. B. Kothe, C. Zemach, A continuum method for modeling surface tension, Journal of computational physics 100 (1992) 335–354. Publisher: Elsevier.

[62] J.-J. Xu, W. Ren, A level-set method for two-phase flows with moving contact line and insoluble surfactant, Journal of Computational Physics 263 (2014) 71–90. URL: https://linkinghub.elsevier.com/retrieve/pii/S0021999114000394. doi:10.1016/j.jcp.2014.01.012.

[63] A. Jarauta, P. Ryzhakov, M. Secanell, P. R. Waghmare, J. Pons-Prats, Numerical study of droplet dynamics in a polymer electrolyte fuel cell gas channel using an embedded Eulerian-Lagrangian approach, Journal of Power Sources 323 (2016)

201–212. URL: https://linkinghub.elsevier.com/retrieve/pii/S0378775316305687. doi:10.1016/j.jpowsour.2016.05.030.

[64] P. B. Ryzhakov, A. Jarauta, M. Secanell, J. Pons-Prats, On the application of the PFEM to droplet dynamics modeling in fuel cells, Computational Particle Mechanics 4 (2017) 285–295. URL: http://link.springer.com/10.1007/s40571-016-0112-9. doi:10.1007/s40571-016-0112-9.

[65] M. R. Hashemi, P. B. Ryzhakov, R. Rossi, An enriched finite element/level-set method for simulating two-phase incompressible fluid flows with surface tension, Computer Methods in Applied Mechanics and Engineering 370 (2020) 113277. URL: http://www.sciencedirect.com/science/article/pii/S004578252030462X. doi:10.1016/j.cma.2020.113277.

[66] G. C. Buscaglia, R. F. Ausas, Variational formulations for surface tension, capillarity and wetting, Computer Methods in Applied Mechanics and Engineering 200 (2011) 3011–3025. Publisher: Elsevier.

[67] R. G. Cox, Inertial and viscous effects on dynamic contact angles, Journal of Fluid Mechanics 357 (1998) 249–278. URL: http://www.cambridge.org/core/journals/journal-of-fluid-mechanics/article/inertial-and-viscous-effects-on-dynamic-contact-angles/02C101E9C7C2119FCC2EEE58BDF14C1F. doi:10.1017/S0022112097008112, publisher: Cambridge University Press.

[68] M. Wörner, X. Cai, H. Alla, P. Yue, A semi-analytical method to estimate the effective slip length of spreading spherical-cap shaped droplets using Cox theory, Fluid Dynamics Research 50 (2018) 035501. URL: https://doi.org/10.1088%2F1873-7005%2Faaaef6. doi:10.1088/1873-7005/aaaef6, publisher: IOP Publishing.

[69] Y. D. Shikhmurzaev, Spreading of drops on solid surfaces in a quasi-static regime, Physics of Fluids 9 (1997) 266–275. URL: https://aip.scitation.org/doi/abs/10.1063/1.869147. doi:10.1063/1.869147, publisher: American Institute of Physics.

[70] E. B. Dussan, On the Spreading of Liquids on Solid Surfaces: Static and Dynamic Contact Lines, Annual Review of Fluid Mechanics 11 (1979) 371–400. URL: http://www.annualreviews.org/doi/10.1146/annurev.fl.11.010179.002103. doi:10.1146/annurev.fl.11.010179.002103.

[71] T. Young, III. An essay on the cohesion of fluids, Philosophical Transactions of the Royal Society of London 95 (1805) 65–87. URL: https://royalsocietypublishing-org.recursos.biblioteca.upc.edu/doi/abs/10.1098/rstl.1805.0005. doi:10.1098/rstl.1805.0005, publisher: Royal Society.

[72] D. Seveno, T. D. Blake, J. De Coninck, Young's Equation at the Nanoscale, Physical Review Letters 111 (2013) 096101. URL: https://link.aps.org/doi/10.1103/PhysRevLett.111.096101. doi:10.1103/PhysRevLett.111.096101, publisher: American Physical Society.

[73] L. M. Pismen, Some singular errors near the contact line singularity, and ways to resolve both, The European Physical Journal Special Topics 197 (2011) 33. URL: https://doi.org/10.1140/epjst/e2011-01433-0. doi:10.1140/epjst/e2011-01433-0.

[74] D. N. Sibley, N. Savva, S. Kalliadasis, Slip or not slip? A methodical examination of the interface formation model using two-dimensional droplet spreading on a horizontal planar substrate as a prototype system, Physics of Fluids 24 (2012) 082105. URL: https://aip.scitation.org/doi/abs/10.1063/1.4742895. doi:10.1063/1.4742895, publisher: American Institute of Physics.

[75] R. Zorrilla, A. Larese, R. Rossi, A modified Finite Element formulation for the imposition of the slip boundary condition over embedded volumeless geometries, Computer Methods in Applied Mechanics and Engineering 353 (2019) 123–157. Publisher: Elsevier.

[76] Y. Wei, E. Rame, L. M. Walker, S. Garoff, Dynamic wetting with viscous Newtonian and non-Newtonian fluids, Journal of Physics: Condensed Matter 21 (2009) 464126. URL: https://doi.org/10.1088%2F0953-8984%2F21%2F46%2F464126. doi:10.1088/0953-8984/21/46/464126, publisher: IOP Publishing.

[77] L. Chen, J. Yu, H. Wang, Convex Nanobending at a Moving Contact Line: The Missing Mesoscopic Link in Dynamic Wetting, ACS Nano 8 (2014) 11493–11498. URL: https://doi.org/10.1021/nn5046486. doi:10.1021/nn5046486, publisher: American Chemical Society.

[78] R. Codina, S. Badia, J. Baiges, J. Principe, Variational multiscale methods in computational fluid dynamics, in: Encyclopedia of Computational Mechanics Second Edition, Wiley Online Library, 2018, pp. 1–28.

[79] M. Sussman, P. Smereka, S. Osher, A level set approach for computing solutions to incompressible two-phase flow, Journal of Computational physics 114 (1994) 146–159. Publisher: Elsevier.

[80] R. Codina, A discontinuity-capturing crosswind-dissipation for the finite element solution of the convection-diffusion equation, Computer Methods in Applied Mechanics and Engineering 110 (1993) 325–342. URL: http://www.sciencedirect.com/science/article/pii/004578259390213H. doi:10.1016/0045-7825(93)90213-H.

[81] M. F. Trujillo, L. Anumolu, D. Ryddner, The distortion of the level set gradient under advection, Journal of Computational Physics 334 (2017) 81–101. Publisher: Elsevier.

[82] S. Groß, V. Reichelt, A. Reusken, A finite element based level set method for two-phase incompressible flows, Computing and visualization in science 9 (2006) 239–257. Publisher: Springer.

[83] C. Min, On reinitializing level set functions, Journal of computational physics 229 (2010) 2764–2772. Publisher: Elsevier.

[84] G. Della Rocca, G. Blanquart, Level set reinitialization at a contact line, Journal of Computational Physics 265 (2014) 34–49. Publisher: Elsevier.

[85] R. N. Elias, M. A. Martins, A. L. Coutinho, Simple finite element-based computation of distance functions in unstructured grids, International journal for numerical methods in engineering 72 (2007) 1095–1110. Publisher: Wiley Online Library.

[86] A.-K. Tornberg, B. Engquist, A finite element based level-set method for multiphase flow applications, Computing and Visualization in Science 3 (2000) 93–101. Publisher: Springer.

[87] P. Dadvand, R. Rossi, E. Oñate, An Object-oriented Environment for Developing Finite Element Codes for Multi-disciplinary Applications, Archives of Computational Methods in Engineering 17 (2010) 253–297. URL: http://link.springer.com/10.1007/s11831-010-9045-2. doi:10.1007/s11831-010-9045-2.

[88] D. Demidov, AMGCL: an Efficient, Flexible, and Extensible Algebraic Multigrid Implementation, Lobachevskii Journal of Mathematics 40 (2019) 535–546. Publisher: Springer.

[89] H. Lamb, Hydrodynamics, University Press, 1924.

Chapter 4

Droplet Dynamics in Gas Channel: Contact–angle Hysteresis

4.1 Introduction

One of the essential requirements for the realistic modeling of the water transport in the gas–channel of the PEM fuel cells is the inclusion of the contact–angle hysteresis phenomenon associated with the dynamics of the water droplet in contact with the (hydrophobic) outer face of the gas diffusion (fibrous) media. In this chapter, the introduced pressure–enriched finite element/level–set framework is further developed by incorporating a modeling approach for capturing the contact–angle hysteresis phenomenon. Additionally, a momentum correction formula is proposed to prevent the instabilities that occur as a result of mass conservation corrections introduced in rather long–time simulations. Here, the validation tests involve the dynamics of a water droplet on the outer surface of a gas diffusion layer (used in commercial PEM fuel cells). This chapter is compiled within the following publication.

4.2 Article data

Title: Towards Droplet Dynamics Simulation in Polymer Electrolyte Membrane Fuel Cells: Three-Dimensional Numerical Modeling of Confined Water Droplets with Dynamic Contact Angle and Hysteresis
Authors: M.R. Hashemi, P.B. Ryzhakov and R. Rossi

Journal: Physics of Fluids, *in press*
Accepted: November 2021

Towards Droplet Dynamics Simulation in Polymer Electrolyte Membrane Fuel Cells: Three–Dimensional Numerical Modeling of Confined Water Droplets with Dynamic Contact Angle and Hysteresis

Mohammad R. Hashemi,[1,2] Pavel B. Ryzhakov,[1,2] and Riccardo Rossi[1,2]

[1)] *Centre Internacional de Mètodes Numèrics en Enginyeria (CIMNE), 08034 Barcelona, Spain.*

[2)] *Universitat Politècnica de Catalunya (UPC), 08034 Barcelona, Spain.*

(*Electronic mail: mhashemi@cimne.upc.edu)

(Dated: 18 November 2021)

This work focuses on three-dimensional simulation of the dynamics of droplets with contact–angle hysteresis. In order to consistently model the dynamics of the contact–line, a combination of the linear molecular kinetic theory and the hydrodynamic theory is implemented in the present numerical method. Without presetting the contact–line and/or the contact–angle, such simulations are generally prone to irregularities at the contact–line, which are mainly due to the imposition of the pinning and unpinning mechanisms associated with the hysteresis phenomenon. An effective treatment for this issue is proposed based on a simple procedure for calculating the nodal contact–angle within the framework of enriched finite element/level set method. The resulting method also benefits from a manipulated momentum conservation equation that incorporates the effect of the liquid mass conservation correction, which is essentially important for simulations with a rather long (physical) run–time. In this paper, the proposed numerical model is validated against the previously published experimental data addressing the configuration of a water droplet on a tilted rough hydrophobic surface. In this test, the effect of the the contact–line pinning as the underlying mechanism for droplet hysteresis phenomenon is also studied. The model is further employed to simulate a liquid droplet confined in a channel in the presence of air flow.

I. INTRODUCTION

Polymer electrolyte membrane (PEM) fuel cells (also known as proton exchange membrane fuel cells) are powerful modern energy conversion devices, known for their high efficiency and ambient-friendliness[1]. Despite the promising potential of PEM fuel cells to become one of the main sources of clean energy for transportation purposes[2], their usage is still hindered by their durability[3]. Water management[4] is among the challenging issues that directly affect the performance and durability of PEM fuel cells[5]. Efficient water management requires the evacuation of the water droplets that breakthrough the outer face of the gas diffusion layer (GDL) into the gas channel (GC). This evacuation is mediated by the air flowing in the GC at the cathode. Particular attention is paid to the prediction of the droplet detachment conditions, which, in turn, lead to insights regarding the efficiency of water evacuation for a given operation regime.

In this context, the analysis of the dynamics of water droplets confined in the GC is of main importance[6], which requires the incorporation of the complex wettability characteristics of the outer face of the GDL[7,8]. In such analyses, besides the experimental investigations and deliberate measurements and/or visualizations, numerical modelling can be acquired as a viable means to provide fundamental understanding of the phenomena.

For the numerical analysis of droplet dynamics in GC, one of the major requirements is to incorporate a dynamic (non–static) contact–angle[9,10] along with the prerequisites of the hysteresis phenomenon[11]. The latter is of particular importance due to the physicochemical properties of the fibrous substrate formed by the face of GDL[12]. Once the equilibrium condition at the three-phase contact–line is disturbed, unbalanced interfacial forces provide a tendency towards a new equilibrium leading to either wetting or dewetting process. The dynamic behavior the contact–angle[13] during these complex processes cannot be characterized by the Young's relation [14,15] anymore, as the mentioned law is limited to the definition of the static equilibrium contact–angle. It should be noted that modeling of the droplet dynamics on solid substrates has a vast range of applications from spray cooling[16,17] to fundamental biological phenomena[18].

The main approaches for the modeling of the contact–line dynamics are the molecular–kinetic[19,20] and hydrodynamic[21,22] theories with former focusing on the dissipation at the inter–molecular length–scale and latter treating the movement of the contact–line at the continuum–level. Nevertheless, recent studies[23,24] have revealed that the improved results are obtained when using a combination[25] of these two approaches.

One of the major complexities in the droplet spreading modeling is the contact–angle hysteresis phenomenon[26,27]. Hysteresis is associated with the pinning of the contact–line[28] and characterized by receding and advancing contact–angles[29], which are linked to the dewetting and wetting processes, respectively. This phenomenon is basically caused by the chemical properties[30], or more accurately by the heterogeneity[31,32] in the properties of the solid substrate that comes into contact with the gas and liquid phases. Surface roughness and its micro–structure are also among determining factors that cause dramatic variations in the contact–angle hysteresis[33–35].

Recent advances in the numerical modeling of multi–phase flows allowed to establish a reliable basis for the numerical simulation of the transport of water droplets in GC[10,11,36,37]. The numerical approaches in this context can be classified within the main categories of the phase–field models and the sharp–interface capturing techniques. The framework of the phase–field models provides a means to capture the dynamics of the contact–line without prior imposition of any specific dynamic contact–angle model[38]. Nevertheless, the phase–field models require an extreme mesh refinement in the vicinity of the liquid-gas interface, which leads to prohibitively high computational costs in three–dimensional simulations. The most used interface–capturing techniques on the other hand are the volume of fluid (VOF)[39] and the level–set method[40]. While the VOF method perfectly preserves the mass conservation, it lacks a systematic and efficient mechanism for reproduction of the geometric data associated with the liquid–gas interface. Unlike VOF, the level–set method circumvents the complexities associated with the calculation of the necessary geometric data, though it needs additional treatment for mass conservation preservation[41–43]. Besides these Eulerian approaches, a Lagrangian framework can also be acquired in this field[44,45]. However, the employment of such a Lagrangian approach in three-dimensional cases would lead to a prohibitively high computational cost.

Authors have recently introduced enriched finite element / level–set method[46,47] that creates a framework for a sharp (zero–thickness) interface treatment, which is a key for efficient simulation of droplet dynamics. Moreover, this method allows for the direct implementation of experimentally admitted dynamic contact–line models. In the present work, the method is further developed by incorporating a consistent treatment of the contact–angle hysteresis phenomenon. The current numerical method models the dynamic contact–angle by a combination of the molecular–kinetic and the hydrodynamic theories. Additionally, in this paper, a simple mass conservation improvement technique is introduced and the effect of the corresponding correction term on the momentum conservation equation is incorporated.

In the following, first, the governing equations and the hysteresis modeling technique are briefly discussed. The level–set method, the corresponding contact–angle calculation, and the (liquid) mass conservation treatment technique are described afterwards. Next, the incorporation of the mass conservation correction into the momentum conservation equation, and consequently, the variational formulation are derived. At the end of section II, a summary of the proposed numerical algorithm is provided. In section III, first, the impact of incorporating the mass conservation correction term into the momentum equation is shown. Afterwards, the proposed method is validated and applied to the tests involving the dynamics of a water droplet on the outer surface of a GDL with an emphasis on the hysteresis phenomenon. The essential importance of imposing a pinning mechanism for obtaining realistic results is analyzed in these tests.

II. NUMERICAL METHOD

A. Governing Equations

The gas-liquid system under consideration involves air and water. The flow of each homogeneous phase Ω_i, $i \in l, g$ of this system can be described by momentum

$$\rho\left(\frac{\partial \mathbf{u}}{\partial t} + \mathbf{u}\cdot\nabla\mathbf{u}\right) = \rho\mathbf{b} - \nabla p + \mu\nabla^2\mathbf{u} \quad \text{in}\,\Omega_i, \tag{1}$$

and mass

$$\nabla\cdot\mathbf{u} = 0 \quad \text{in}\,\Omega_i, \tag{2}$$

conservation equations, which are derived for incompressible Newtonian fluids. In the above equations, $\mathbf{u}$ is velocity, p is pressure, and $\mathbf{b} = -g\mathbf{e}_z$ denotes the body force, with ρ and μ being density and dynamic viscosity of the fluid phase, respectively.

Governing equations (1-2) are subject to the initial as well as the Dirichlet and Neumann boundary conditions, which read

$$\mathbf{u}(\mathbf{x},0) = \mathbf{u}_0 \quad \text{in}\,\Omega, \tag{3}$$

$$\mathbf{u}(\mathbf{x},t) = \mathbf{u}_D \quad \text{on}\,\partial\Omega_D, \tag{4}$$

and

$$\mathbf{T}(\mathbf{x},t) = \mathbf{T}_N \quad \text{on}\,\partial\Omega_N, \tag{5}$$

respectively, where $\mathbf{T}$ denotes the traction vector.

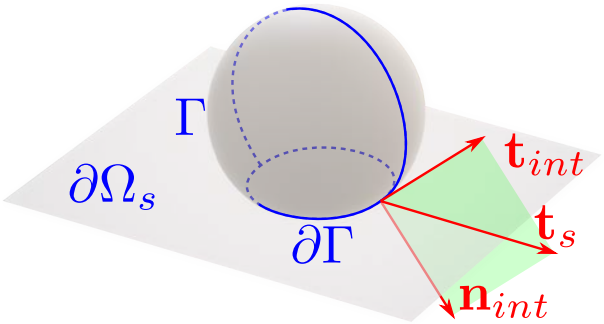

FIG. 1. Schematic of a droplet lying on a solid substrate. Unit vectors $\mathbf{t}_{int}$, $\mathbf{t}_s$, and $\mathbf{n}_{int}$ are all in the same plane, which is perpendicular to $\partial\Omega_s$. Contact–angle is the supplementary of the angle between unit vectors $\mathbf{t}_{int}$ and $\mathbf{t}_s$.

The liquid–gas interface (see Fig. 1), $\Gamma = (\Omega_l \cap \Omega_g)$, partially determines the boundary of each homogeneous phase and is subject to the following conditions

$$[\![\mathbf{T}(\mathbf{x},t)]\!] = -\gamma\kappa\mathbf{n}_{int} \quad \text{on}\,\Gamma, \tag{6}$$

and

$$[\![\mathbf{u}(\mathbf{x},t)]\!] = 0 \quad \text{on}\,\Gamma, \tag{7}$$

where γ and κ are the surface tension coefficient and the local curvature of the interface, respectively. In these equations, $\mathbf{T}$ represents the traction vector, $\mathbf{n}$ is the outward normal vector, and $[\![\cdot]\!]$ denotes the jump operator with respect to $\partial\Omega$. For a Newtonian fluid, the traction vector is calculated as

$$\mathbf{T} = \left[-p\mathbb{I} + \mu\left(\nabla\mathbf{u} + \nabla\mathbf{u}^T\right)\right]\cdot\mathbf{n}. \tag{8}$$

In case the interface is located at the solid substrate (see Fig. 1), the equilibrium condition[48] dictates that the liquid–gas surface tension must be balanced by liquid–solid (γ_{ls}) and gas–solid (γ_{gs}) interfacial tensions at the contact–line, $\partial\Gamma = (\partial\Omega_s \cap \Gamma)$. This gives the Young's relation[14,49]

$$\gamma\cos(\theta_Y) + \gamma_{ls} = \gamma_{gs}. \tag{9}$$

with θ_Y denoting the equilibrium contact angle. Once the equilibrium is disturbed, a model for incorporating the unbalanced interfacial forces (that are rendered to the Young stress) is required[50],

$$\tau_Y = \gamma[\cos(\theta_Y) - \cos(\theta)], \tag{10}$$

which is a function of the dynamic contact–angle, θ. In this work, the (simplified) linear molecular kinetic theory[13]

$$\tau_Y = \zeta u_{slip} \quad \text{on } \partial\Gamma, \tag{11}$$

with constant coefficient of friction ζ is used to model the dynamics of the contact–line. Here, $u_{slip} = \mathbf{t}_s \cdot \mathbf{u}$ is the local slip velocity of the contact–line. Taking into account nanometric (physical) length–scale and l_{micro} associated with the dynamic contact–angle, one can use the hydrodynamic theory[21], to correlate numerically captured contact–angle θ^{num} to microscopic θ as

$$\theta^3 = (\theta^{num})^3 - 9\frac{\mu u_{slip}}{\gamma}\ln(\frac{h_e}{l_{micro}}), \tag{12}$$

where h_e denote the length–scale associated with the resolution of the computational mesh (see[47] for more details). It must be noted that fixing parameters ζ and l_{micro} needs deliberately designed experiments[13].

Another complexity associated with the modeling of the moving contact–line is the stress singularity occurring in the vicinity of the contact–line if one tries to treat the solid substrate as a no–slip boundary[51]. The good practice to resolve this issue is to substitute the no–slip condition on the solid substrate with the Navier–slip condition formulated as[52]

$$\mathbf{n}_s \cdot \mathbf{u} = 0 \quad \text{on } \partial\Omega_s, \tag{13}$$

and

$$(\mathbb{I} - \mathbf{n}_s \otimes \mathbf{n}_s) \cdot \mathbf{T} = -\beta \mathbf{u} \quad \text{on } \partial\Omega_s, \tag{14}$$

with $\mathbb{I}$ and $\mathbf{n}_s$ being the identity tensor and the vector normal to the solid substrate, respectively.

B. Hysteresis

In the numerical modeling, the hysteresis phenomenon is generally rendered into the contact–line pinning conditions:

$$\text{contact–line is } \begin{cases} \text{free for wetting} & \text{if } \theta \geq \theta_A \\ \text{pinned} & \text{if } \theta_R < \theta < \theta_A \\ \text{free for dewetting} & \text{if } \theta \leq \theta_R \end{cases} \tag{15}$$

Here, θ_A and θ_R are the static advancing and the static receding contact–angles that characterize the pinning threshold[53]. Therefore, the (static) contact–angle hysteresis is calculated as $\Delta\theta_{static} =$

$\theta_A - \theta_R$[29]. In order to prevent confusion, it should be noted that in this work, θ_a and θ_r (with lower–case subscripts) denote the maximum and the minimum contact–angles, respectively. In this way, the instantaneous contact–angle hysteresis can be measured as $\Delta\theta = \theta_a - \theta_r$.

Besides implementing the pinning condition (15), in order to make the whole formulation consistent with the physical interpretation of hysteresis phenomenon[40], the equilibrium contact–angle, θ_Y, that appears in the definition of the unbalanced Young stress (10) is also set according to

$$\theta_Y = \begin{cases} \theta_A & \text{if wetting} \\ \theta & \text{if pinned} \\ \theta_R & \text{if dewetting} \end{cases} \tag{16}$$

This guarantees that while pinned, the contact–line has no tendency for movement. It is necessary to highlight that checking the liquid spreading direction, *i.e.* being in the wetting or dewetting regime, is of high importance for the physically justified incorporation of the pinning mechanism via conditions (15) and (16).

C. Level–set Method

The level–set method[54] is a robust interface capturing approach based on the convection of the continuous signed distance function, ϕ, according to

$$\frac{\partial \phi}{\partial t} + \mathbf{u} \cdot \nabla \phi = 0 \quad \text{in}\, \Omega. \tag{17}$$

The theoretical definition of ϕ reads

$$\phi(\mathbf{x},t) = \begin{cases} -d & \text{if}\, \mathbf{x} \in \Omega_l \\ 0 & \text{if}\, \mathbf{x} \in \Gamma \\ d & \text{if}\, \mathbf{x} \in \Omega_g \end{cases} \tag{18}$$

with d being the distance $\mathbf{x}$ from the interface, or equivalently, $\|\nabla \phi\| = 1$. Using level–set function ϕ, the wetting and dewetting can easily be formulated in the vicinity of the contact–line as

$$\frac{\partial \phi(\mathbf{x},t)}{\partial t} = \begin{cases} < 0 & \text{if wetting} \\ > 0 & \text{if dewetting} \end{cases} \tag{19}$$

During the evolution of the interface, there is a high chance of the occurrence of irregularities in level–set function ϕ that are re-presentable as a deviation from the true distance function (i.e.

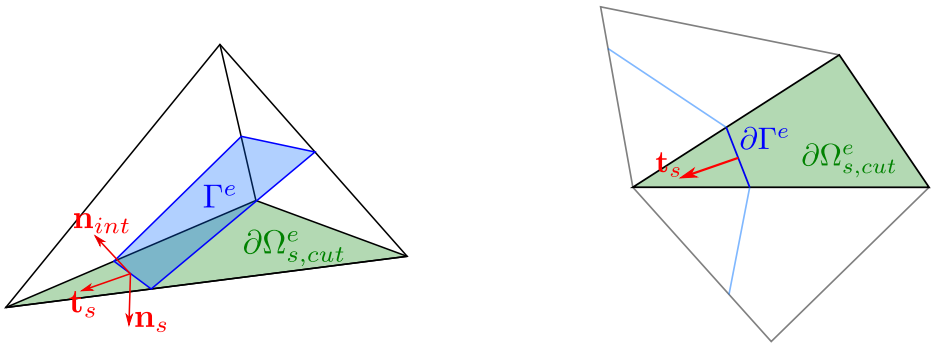

(a) (b)

FIG. 2. Schematics of (a) A cut element, Ω^e_{cut}, and (b) the corresponding contact–line, $\partial\Gamma^e$.

$\|\nabla\phi\| \neq 1$) and/or noise in the reproduced interface[46]. In order to address these irregularities, distance re-initialization[55] and level–set smoothing[47] techniques are utilized in the present method. The descretization of Eq. (17) is done using the streamline–upwind Petrov–Galerkin (SUPG) approach with the addition of the cross–wind stabilization term[56].

1. *Contact–angle Calculation*

Figure 2 illustrates a cut element located on the solid substrate and the associated unit vectors, $\mathbf{n}_{int}$, $\mathbf{n}_s$, and $\mathbf{t}_s$. Based on the definition of the level–set function, the normal vector to the interface can be calculated as

$$\mathbf{n}_{int} = \frac{\nabla\phi}{\|\nabla\phi\|}$$

In this way, the numerical contact–angle corresponding to the cut element is obtained as

$$\theta_e^{num} = \pi - \cos^{-1}\left(\mathbf{n}_s \cdot \frac{\nabla\phi}{\|\nabla\phi\|}\right). \tag{20}$$

The tangent to the substrate (normal to the contact–line) is also simply calculable as

$$\mathbf{t}_s = \frac{1}{\sin(\theta_e^{num})}\left[\mathbf{n}_s \times (\mathbf{n}_s \times \mathbf{n}_{int})\right].$$

In order to prevent inadequate imposition of the pinning condition, it is necessary to obtain regularly distributed contact–angle values. In the present work, the pinning condition (15) is selected based on the nodal value of the contact–angle, calculated as

$$\theta_I^{num} = \frac{1}{\left|\mathscr{E}_I^{cl}\right|}\sum_{e\in\mathscr{E}_I^{cl}} \theta_e^{num}, \tag{21}$$

where $\left|\mathscr{E}_I^{cl}\right|$ denotes the size of $\mathscr{E}_I^{cl}$, which is the set of elements that are cut by the contact–line and share node I. As long as a node is pinned according to condition (15), the corresponding value of level–set function ϕ is fixed and treated as a known value during the assembly of the system of equations obtained by discretization of Eq. (17).

2. *Mass Conservation Correction*

As shown in the literature[57], the level–set method does not guarantee the conservation of the mass of the fluid phases. Although (adaptive) mesh refinement[58] and higher–order methods[42] can be utilized to prevent any mass loss, a simple and efficient approach to compensate for this adverse artifact is a global correction to the level-set field. This can be defined as

$$\phi_{corr} = \phi + \frac{\int_{\Omega,liq} d\Omega - \mathscr{V}_{liq,0}}{\int_\Gamma d\Gamma}, \tag{22}$$

where ϕ_{corr} denotes the corrected level-set field and $V_{liq,0}$ is the initial volume of the liquid phase including the net liquid inflow. The volume correction term can equivalently be represented in term of pseudo-velocity

$$u'_{int} = -\frac{1}{dt}\frac{\int_{\Omega,liq} d\Omega - \mathscr{V}_{liq,0}}{\int_\Gamma d\Gamma}. \tag{23}$$

Nonetheless, employing a volume correction technique requires correcting the momentum conservation equation accordingly. Without loss of generality, consider a case with volume loss; the pseudo–velocity is positive and consequently, the mass correction procedure increases the momentum of the liquid phase while the gas momentum is decreased. In this work, the associated momentum transfer is formulated and incorporated into the momentum conservation equation as follows.

D. Variational Formulation

Considering an arbitrary fluid domain (Ω), the rate of the total momentum reads

$$\frac{D}{Dt}\int_\Omega \rho\mathbf{u} d\Omega = \int_\Omega \frac{\partial}{\partial t}(\rho\mathbf{u}) d\Omega + \int_{\partial\Omega}(\rho\mathbf{u})\,\mathbf{u}\cdot\mathbf{n} d(\partial\Omega). \tag{24}$$

Supposing that the boundary of the the arbitrary domain ($\partial\Omega$) partially coincides with the liquid-gas interface (Γ), one has

$$\frac{D}{Dt}\int_\Omega \rho\mathbf{u} d\Omega = \int_\Omega \frac{\partial}{\partial t}(\rho\mathbf{u}) d\Omega + \int_{\partial\Omega\setminus\Gamma}(\rho\mathbf{u})\,\mathbf{u}\cdot\mathbf{n} d(\partial\Omega) + \int_\Gamma (\rho\mathbf{u})\,\mathbf{u}_\Gamma\cdot\mathbf{n} d\Gamma, \tag{25}$$

where $\mathbf{u}_\Gamma = \mathbf{u} + u'_{int}\mathbf{n}$ is the effective (imposed) velocity of the interface, which takes into account both the computed velocity and the contribution of the correction calculated in Eq. (23). This gives

$$\frac{D}{Dt}\int_\Omega \rho\mathbf{u}d\Omega = \int_\Omega \frac{\partial}{\partial t}(\rho\mathbf{u})\,d\Omega + \int_{\partial\Omega}(\rho\mathbf{u})\,\mathbf{u}\cdot\mathbf{n}d(\partial\Omega) + \int_\Gamma (\rho\mathbf{u})\,u'_{int}d\Gamma, \tag{26}$$

or equivalently

$$\frac{D}{Dt}\int_\Omega \rho\mathbf{u}d\Omega = \int_\Omega \left[\frac{\partial}{\partial t}(\rho\mathbf{u}) + \nabla\cdot(\rho\mathbf{u})\right] d\Omega + \int_\Gamma (\rho\mathbf{u})\,u'_{int}d\Gamma. \tag{27}$$

Incorporating the second term on the right-hand-side of Eq. (27), which is associated with the mass conservation correction, and implementing the surface tension condition at the liquid–gas interface (8), the molecular kinetic theory along the contact–line (11), the Navier–slip condition on the solid substrate (14), and Neumann boundary condition (5), the variational form of the momentum conservation equation becomes

$$\begin{aligned}
&\int_\Omega \rho\left(\frac{\partial\mathbf{u}}{\partial t} + \mathbf{u}\cdot\nabla\mathbf{u}\right)\cdot\mathbf{w}d\Omega + \int_\Gamma \rho u'_{int}\mathbf{u}\cdot\mathbf{w}d\Gamma = \int_\Omega \rho\mathbf{b}\cdot\mathbf{w}d\Omega \\
&+ \int_\Omega p\nabla\cdot\mathbf{w}d\Omega - \int_\Omega \mu\left(\nabla\mathbf{u} + \nabla\mathbf{u}^T\right):\nabla\mathbf{w}d\Omega \\
&+ \int_{\partial\Omega_N}\mathbf{T}_N\cdot\mathbf{w}d(\partial\Omega) - \int_{\partial\Omega_s}\beta\mathbf{u}\cdot\mathbf{w}d(\partial\Omega) - \int_\Gamma \gamma\kappa\mathbf{n}_{int}\cdot\mathbf{w}d\Gamma \\
&+ \int_{\partial\Gamma}\left[(\gamma\mathbf{t}_{int} - \zeta\mathbf{u})\cdot\mathbf{t}_s + \gamma_{gs} - \gamma_{ls}\right]\mathbf{t}_s\cdot\mathbf{w}d(\partial\Gamma).
\end{aligned} \tag{28}$$

In the present work, the test function, $\mathbf{w}$, is chosen from the finite element space. All elements cut by the interface undergo a domain splitting process, which facilitates the accurate calculation of the integrals presented in Eq. (28) and circumvents the need for implementing a regularized delta function. The jump in the pressure field is treated utilizing a pressure–enriched finite element space[46] and the algebraic sub-grid scale technique[59] is used to stabilize the method. For the sake of brevity in this paper, only the new aspects of the present numerical model are discussed, while the detailed description of the enriched finite element framework developed by the authors[46,47] is omitted.

Before moving on and focus on the hysteresis phenomenon, it is worth to analyse the effect of the proposed momentum correction term in a simple test–case, in which an ellipsoidal liquid droplet with its surface being defined as

$$\left(\frac{x-x_c}{a}\right)^2 + \left(\frac{y-y_c}{b}\right)^2 + \left(\frac{x-z_c}{c}\right)^2 = 1,$$

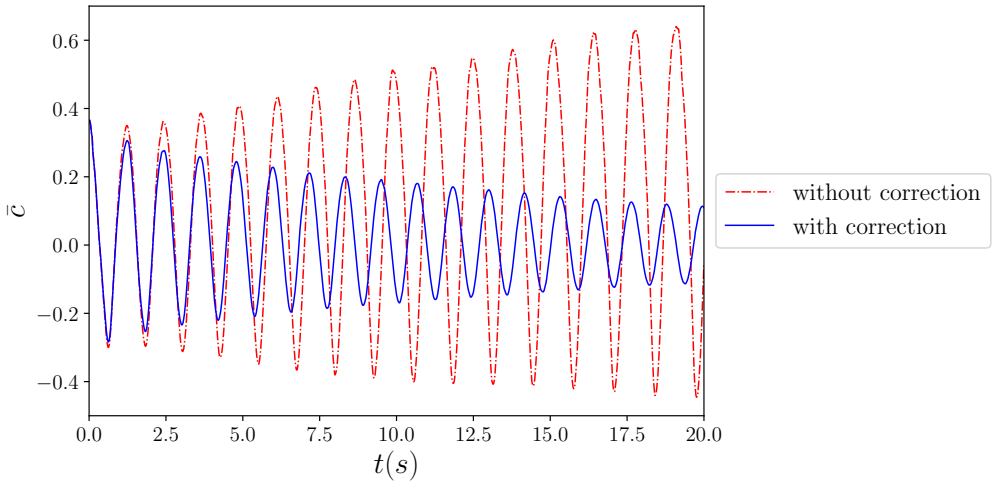

FIG. 3. Time evolution of the amplitude of the oscillating droplet with and without incorporating the momentum correction term.

is confined inside a $1 \times 1 \times 1m^3$ box. Setting $a = b = 0.25m$, $c = 0.4m$, and $x_c = y_c = z_c = 0.5m$, the droplet oscillates until reaching an equilibrium spherical shape with radius $a_{eq} = \sqrt[3]{abc}$. Considering the comparatively large length-scales and consequently, the small curvature, in order to accelerate the droplet deformation, a rather large surface tension of $\gamma = 100N/m$ is used in this test–case along with $\rho_l = 1000kg/m^3$, $\rho_g = 1kg/m^3$, $\mu_l = 1Pa.s$, and $\mu_g = 0.01Pa.s$.

Figure 3 presents the time–evolution of the amplitude of the droplet oscillations along z–axis ($\bar{c}$) that is normalized by a_{eq} for both the corrected and uncorrected formulations. It is evident that without the proposed correction to the momentum equation, the amplitude of the oscillation is growing, contrary to the basic physical expectations. Such behaviour is a cause of numerical instability specially after rather long simulation run–times that obligates significant level–set correction to preserve the mass continuity. It should be noted that in order to highlight the effectiveness of the proposed correction, in the present test–case, the parameters are chosen in a way that the pseudo–velocity associated with the mass conservation correction and consequently, the correction term on the right-hand-side of Eq. (26), be significant. For this test, the Reynolds number is $Re \sim O(10^2)$.

E. Computational Algorithm

In this work, the linearized momentum conservation is implicitly solved together with the mass conservation equation. The computational domain is discretized using linear tetrahedral elements.

Algorithm 1: Time–marching

$n = 1$;

$t = 0$;

while $t <$ *run-time* **do**

- **calculate** nodal contact–angle according to Eq. (21);
- **impose** fixing/unfixing ϕ according to Eq. (15);
- **solve** Eq. (17) for ϕ for the first ***half*** time-step with $\mathbf{u}_n$;
- **reinitialize** ϕ;
- **calculate** curvature as $\kappa = \nabla \cdot (\nabla\phi / \|\nabla\phi\|)$;
- **for** *all elements e* **do**
  - **if** $e \cap \Gamma \neq \varnothing$ **then**
    - **do** element splitting;
    - **impose** pinning condition according to Eq. (16);
    - **calculate** θ according to Eq. (12);
  - **create** elemental system of equations according to Eq. (28);
- **do** assembling the Linear System of Equations (LSE);
- **solve** LSE for $[\mathbf{u}, p]$;
- **solve** Eq. (17) for ϕ for the second ***half*** time-step and the updated $\mathbf{u}$;
- **update** $n = n + 1$;
- **update** $t = n\Delta t$;

TABLE I. Summary of the proposed method.

The convergence of the velocity and pressure fields is obtained by assuring a relative tolerance of 10^{-5}. All the linear systems of equations are solved using the GMRES ($m = 40$) with a convergence tolerance of 10^{-6}. All the implementations are done within KRATOS Multiphysics code[60]. AMGCL library[61] is utilized for solving the linear system of equation. In Table I, the main steps of the proposed numerical method are outlined.

III. RESULTS

In the following, the main test–cases are presented, which are dedicated to the hysteresis phenomenon. Unless otherwise mentioned, the liquid and gas properties correspond to those of water and air, respectively; $\rho_l = 1000 kg/m^3$, $\mu_l = 0.001 Pa.s$, $\rho_g = 1 kg/m^3$, $\mu_g = 0.00001 Pa.s$, and $\gamma = 0.072 N/m$. Gravity is set to $g = 9.81 m/s^2$ in all test–cases.

Computational consistency requires Navier–slip parameter β to be much larger than μ/h_e; in this work, $\beta = 1000 Pa.s/m$ passes this criteria for all the meshes. The parameter of the molecular-kinetic model and the microscopic length–scale are set to $\zeta = 0.5 Pa.s$ and $l_{micro} = 10^{-9} m$, respectively. These values are within the measured range of the two parameters. Nevertheless, since for the test–cases solved in the present work, an emphasis is given to the pinning (underlying the hysteresis phenomenon) rather than the dynamics of the contact–line, these three parameters have a minor effect on the results. In other words, changing these parameters only affects the dynamics of the droplet spreading on the solid substrate wherever the contact–line is unpinned, while the (final) equilibrium configuration of the droplet is unaffected.

In all cases considered below, the receding and advancing static contact angles of $\theta_R = 115^\circ$ and $\theta_A = 149^\circ$ are considered, respectively. These correspond to experimentally measured values for a water droplet on the outer surface of a typical commercial GDL of a fuel cell[8]. It should be noted that for cases with static contact-angle hysteresis, one cannot provide any equilibrium contact–angle. The contact-angle is subject to variations due to the movement of the contact-line as well as the droplet deformation, which can be active even for a fully pinned droplet. The external forces, e.g. gravity and/or the drag of the air–flow, and droplet inertial oscillations lead to the deformation of partially or fully pinned droplets in the following tests. Not incorporating any prescribed contact–angle, the proposed numerical method is capable of capturing such dynamic behavior. In the present work, all tests are performed in three dimensions and two-dimensional images of the droplets correspond to cross-sections of the three-dimensional domain made at its horizontal plane-of-symmetry if not mentioned otherwise.

A. Water Droplet on Tilted Solid Substrate

First, a test consisting of a water droplet released on top of a (tilted) solid substrate in the presence of gravity is considered. The corresponding schematic is shown in Fig. 4. The ultimate

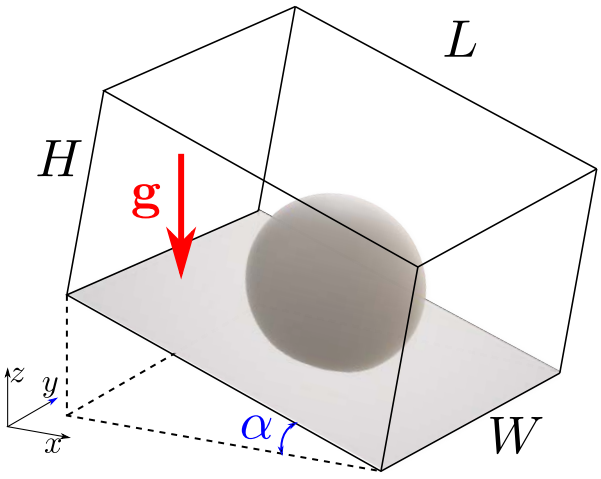

FIG. 4. Schematic of the liquid droplet on a tilted solid substrate.

configuration of the droplet is basically characterized by the hysteresis phenomenon. This test has been widely used as a benchmark for analyzing the hysteresis[8,62–65]. The main aim here is to validate the proposed method and further study the effect of the pinning/unpinning mechanism on the droplet configuration. In this sense, besides the comparison with the experimental data (reported in[8]), this section also includes the results of the (same) test–cases re–simulated without the explicit imposition of the pinning condition (15).

In this section, the volume of the droplet is set to $10\mu L$ and the time–step is $\Delta t = 10^{-5}s$ for all cases. Figure 5 shows the initial (spherical-cap) configuration of the water droplet. For this configuration, one obtains the volume of the droplet as

$$\mathscr{V}_{liq} = \int_0^{\theta_0} \pi R_0^3 \sin^3(\theta) d\theta = \frac{\pi R_0^3}{3}\left[2 - 3\cos(\theta_0) + \cos^3(\theta_0)\right].$$

Once the liquid volume is set, the initial radius (R_0) and vertical offset $Z_0 = R_0 \sin(\theta_0 - 90^\circ)$ are calculated. It is important to note that the numerical results with $\theta_0 < 180^\circ$ can be compared to the experimental results with $\theta_0 = 180^\circ$ only if $\theta_0 > \theta_{avd}$. For the present test–case, the initial contact–angle is set to $\theta_0 = 155^\circ$.

It must be noted that an important physical phenomenon here is the occurrence of oscillations, which are rooted in the concurrent effect of inertia and surface tension[8,66,67]. In order to prevent strong droplet oscillations in this section, first, the gravity is linearly increased from zero to $g = 9.81 m/s^2$ with a slope of g/τ_r while the tilting angle is kept zero. Then, the tilting angle is increased from zero to α following a linear trend with the slope of $\pi/(18\tau_r)$. In this test, the relaxation time is set to $\tau_r = 0.01s$. In the actual experiments, similar precautions are followed by

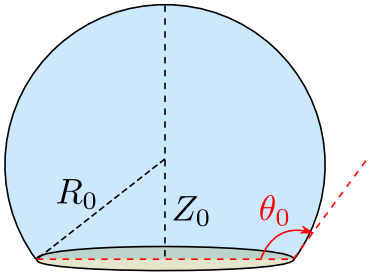

FIG. 5. Schematic of the initial configuration of the liquid droplet.

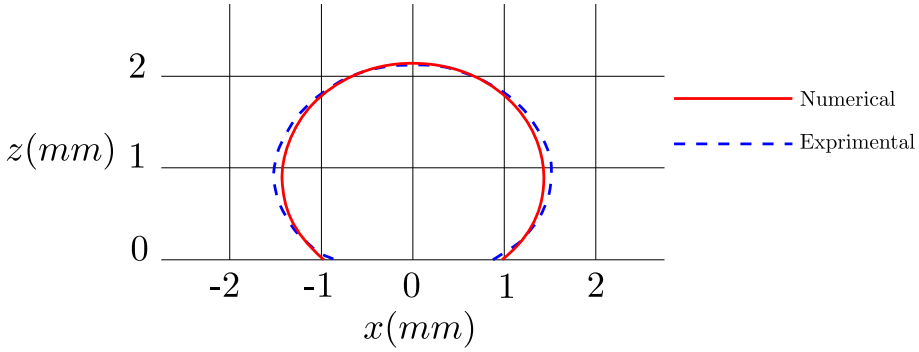

FIG. 6. Comparison of the numerical result with the experimental result reported in[8] for zero tilting angle.

slowly releasing the droplet from the injection tip and gradually inclining the solid plane.

In this section, the computational mesh corresponding to $R_0/h \approx 11.0$ is composed of $\sim 350K$ elements and $\sim 75K$ nodes leading to $\sim 300K$ degrees–of–freedom. We shall consider this mesh as "standard" and it will be used by default in the simulations. In case of using a different mesh resolution, it will be explicitly specified. Using this setup, for each test–case, reaching the physical time of $t = 0.1s$ (or equivalently 10^4 time–steps for the present case) in the simulation requires almost 80 hours of run–time on 4 cores of a PC equipped with an Intel® Core™ i7-4770 processor. In this sense, the prohibitive computational cost associated with very long simulation times, impedes the use of an extremely large relaxation time.

Figure 6 illustrates the numerically obtained interface of the droplet on the xz–plane for the zero–tilting ($\alpha = 0$) case in comparison with the experimental result reported in[8]. The results are in a good agreement. The difference between the simulated footprint radius and its experimental value is $\sim 10\%$.

In order to check the effect of mesh resolution, the same test was also simulated on a coarser and a finer mesh with $R_0/h \approx 8.3$ and $R_0/h \approx 13.8$, respectively. In order to verify the mesh–

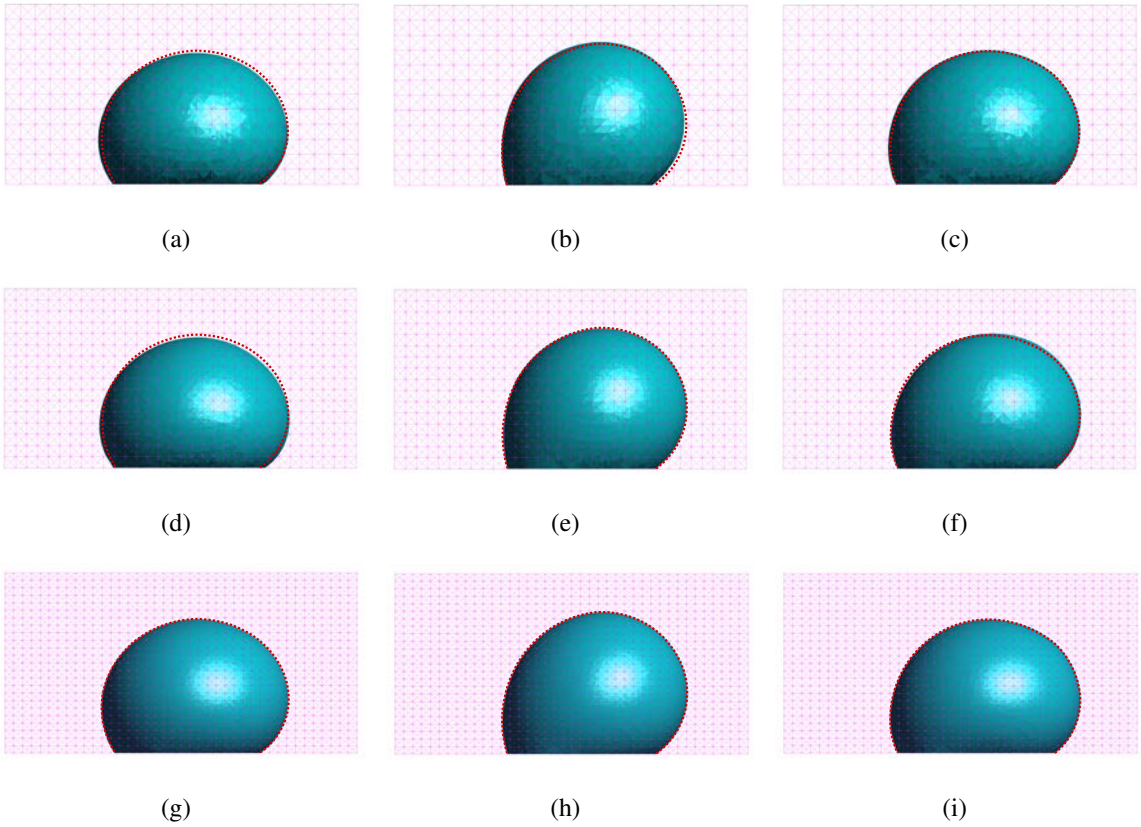

FIG. 7. Comparison of the configuration of the droplet obtained at (a,d,g) $t = 0.035s$, (b,e,h) $t = 0.045s$, and (c,f,i) $t = 0.055s$. In the first row, (a,b,c) the results are shown for the coarsest mesh size, $R_0/h \approx 8.3$. The second and third rows correspond to the mesh sizes of $R_0/h \approx 11.0$ and 13.8, respectively. The dotted–lines are fitted to the droplet configurations obtained for the finest mesh and replicated on the other figures for the sake of comparison.

independence for a more rigorous test–case, here, the tilting angle is set to $\alpha = 30^\circ$. Therefore, in this test, once the magnitude of the gravity reaches $9.81 m/s^2$, the tilting angle is dynamically increasing from zero up to 30 degrees. The resulting droplet configurations are presented in Fig. 7 at three different instances in time. In this figure, the generated computational meshes are also illustrated. It is important to mention that in this test, droplet is continuously deforming under the effects of a dynamic gravitational force, surface tension, and the inertia. The excellent match between the results obtained for different mesh resolutions is evident in Fig. 7. Thus, the rest of the simulations are all performed with $R_0/h \approx 11.0$.

Upon increasing the tilting angle, θ_a increases and θ_r decreases until the pinning threshold (determined by θ_A and θ_R) is surpassed and consequently, the droplet is detached. In Fig. 8, the

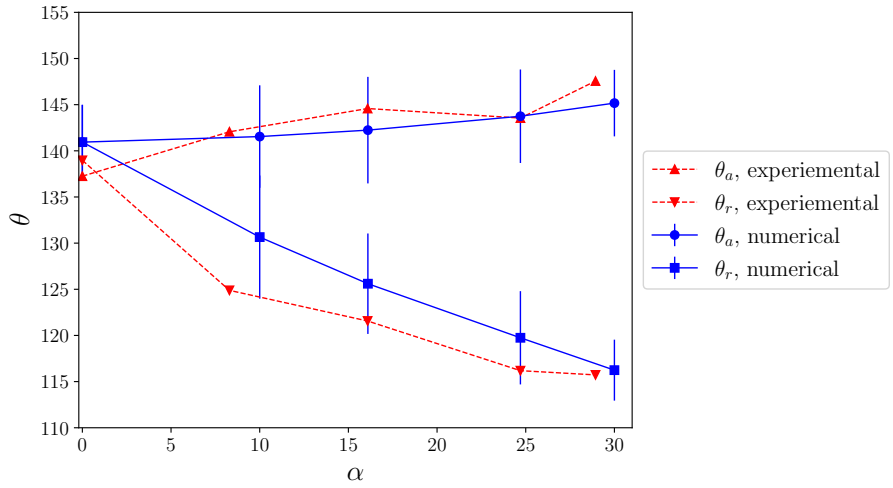

FIG. 8. Comparison of the numerical results with the experimental results reported in[8] for different tilting angles.

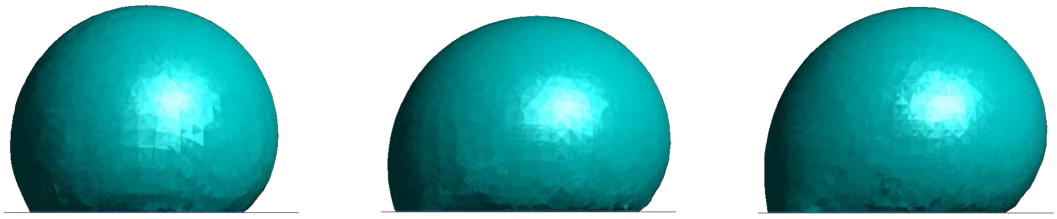

(a) (b) (c)

FIG. 9. Droplet configuration obtained with pinning mechanism for different tilting angles, (a) $\alpha = 10°$, (c) $\alpha = 30°$, and (c) $\alpha = 50°$.

instantaneous contact–angle hysteresis (in terms of θ_a and θ_r) of a pinned droplet attached to a tilted solid substrate is compared with the experimental data[8]. The error bars in Fig. 8 show the standard deviation of the result associated with the averaging of the advancing and the receding contact–angles. The agreement between the numerical and experimental results is observed in Fig. 8. The side view of the droplet and the configuration of its contact–line are presented in Figs. 9 and 10, respectively. These figures also include the result for $\alpha = 50°$, for which the droplet detachment occurred. The presented results correspond to the instances when the droplet has nearly reached a terminal shape. Nonetheless, droplet oscillations are present, leading to slight deformations in–time.

Next, it is worth to investigate the same test–case without explicit imposition of the contact–

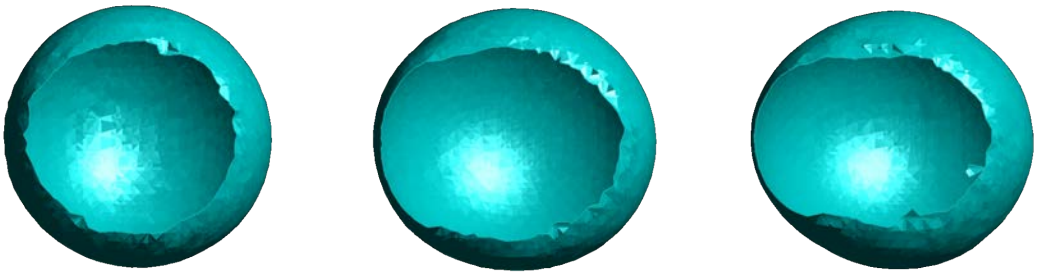

(a) (b) (c)

FIG. 10. The configuration of the contact–line obtained with pinning mechanism for different tilting angles, (a) $\alpha = 10^\circ$, (b) $\alpha = 30^\circ$, and (c) $\alpha = 50^\circ$.

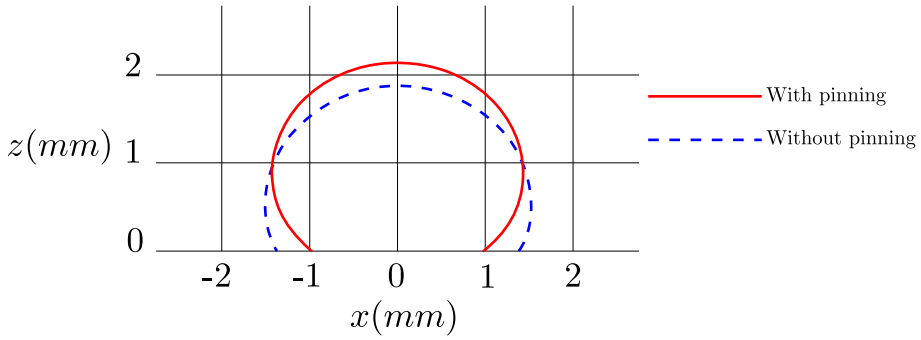

FIG. 11. Comparison of the numerical results with and without imposing the pinning mechanism.

line pinning/unpinning threshold. The present methodology allows for performing such simulations directly by setting $\theta_A = \theta_R = \theta_{eq}$. In the presence of static contact–angle hysteresis, the corresponding droplet adhesion (pinning) force is proportional to $\gamma|\cos(\theta_R) - \cos(\theta_A)|$[45,68]. Consequently, and taking into account that in the absence of the static contact–angle hysteresis, the net surface force acting on the contact–line is measured as $\gamma\cos(\theta_{eq})$, the corresponding equilibrium contact–angle can be estimated as

$$\theta_{eq} = \cos^{-1}\left(\frac{1}{2}\left[\cos(115^\circ) + \cos(149^\circ)\right]\right) \approx 129.8^\circ.$$

As expected and shown in Fig. 11, without a pinning mechanism, the droplet is spread more. Without a pinning mechanism, the instantaneous contact–angle hysteresis, $\Delta\theta = \theta_a - \theta_r$, is also significantly smaller as seen in Fig. 12 compared to Fig. 9. In the absence of a pinning mechanism, the frictional effect on the solid substrate is responsible for the manifestation of the (dynamic) contact–line hysteresis. The corresponding configurations of the contact–line are also presented

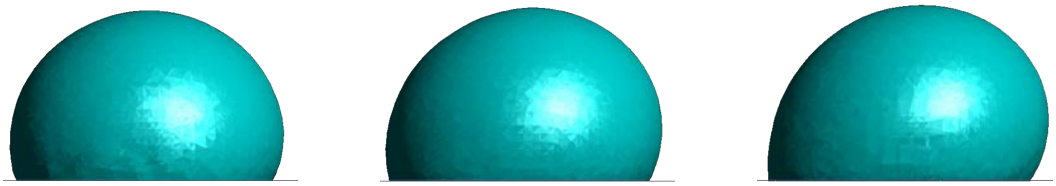

(a) (b) (c)

FIG. 12. The configuration of the contact–line obtained without pinning mechanism for different tilting angles, (a) $\alpha = 10^\circ$, (b) $\alpha = 30^\circ$, and (c) $\alpha = 50^\circ$.

(a) (b) (c)

FIG. 13. The configuration of the contact–line obtained without pinning mechanism for different tilting angles, (a) $\alpha = 10^\circ$, (b) $\alpha = 30^\circ$, and (c) $\alpha = 50^\circ$.

in Fig. 13.

B. Water Droplet Exposed to the Airflow in a Gas Channel

In the following tests, the computational domain is similar to the one schematically shown in Fig. 4, however, without tilting ($\alpha = 0$). The domain sizes are $L = 800\mu m$, $W = 300\mu m$, and $H = 200\mu m$. Here, a water droplet of $R_0 = 107\mu m$ is positioned on the solid substrate with the initial contact–angle of $\theta_0 = 90^\circ$ and is subject to an air–flow. The inlet boundary condition is defined by applying fixed prescribed velocity of

$$u = \begin{cases} \frac{u_0}{2}\left[1 - \cos\left(\frac{\pi}{0.001}t\right)\right] & \text{if } t \leq 0.001s \\ u_0 & \text{if } t > 0.001s \end{cases}$$

in x–direction, and at the outlet, a constant (zero) pressure boundary condition is imposed. The rather large relaxation time of $0.001s$ provides the droplet enough time to obtain contact–angles

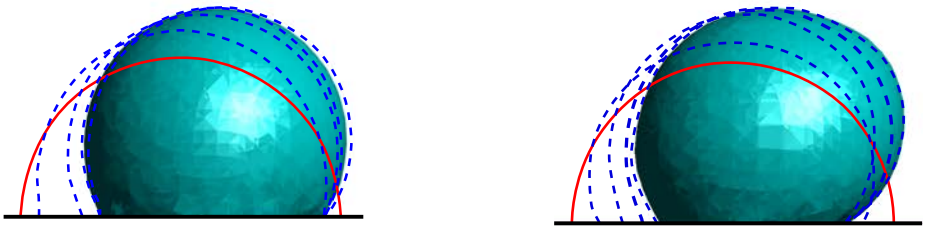

(a) (b)

FIG. 14. Evolution of the interface of the droplet subject to air–flow with (a) $u_0 = 2m/s$ and (b) $u_0 = 6m/s$. The outline of the evolving interface is shown with dashed–line, while the solid–line corresponds to the initial configuration of the droplet.

significantly larger than 90° according to the hydrophobicity of the substrate, before the imposition of the maximum velocity. Moreover, the droplet is initially $1.5H$ away from the inlet in order to minimize the effect of spatially uniform velocity set at the boundary of the domain. Here, the time–step is set to $\Delta t = 10^{-6}s$ and the computational domain is discretized by $\sim 250K$ elements.

Figure 14 shows the evolution of the droplet until reaching its terminal configuration for cases with $u_0 = 2m/s$ and $u_0 = 6m/s$. The corresponding Reynolds numbers are $Re = 55$ and 166, based on the hydraulic diameter of the channel and air properties. It is observed that by increasing the air–flow velocity, the contact–line sweeps a larger distance both at the receding and advancing fronts of the droplet. As expected, the larger drag force also leads to a significant increase in θ_a. This is further presented in Table II, which provides the contact–angle hysteresis, along with θ_a and θ_r, for the equilibrium configuration of the droplet. Besides the increase in θ_a, by increasing the velocity of the air–flow, a slight increase in θ_r is also observed. The rate of the change in θ_a dramatically increases by approaching the threshold of droplet detachment, which is $u_0 = 6m/s$ in this case.

TABLE II. Contact–angle hysteresis obtained for different u_0.

u_0	$\theta_a(^\circ)$	$\theta_r(^\circ)$	$\Delta\theta(^\circ)$
$2m/s$	135.6 ± 1.5	124.4 ± 1.5	11.2 ± 2.1
$4m/s$	139.3 ± 2.2	128.0 ± 1.1	11.3 ± 2.5
$5m/s$	140.8 ± 1.6	128.5 ± 2.2	12.3 ± 2.8
$6m/s$	150.0 ± 1.8	131.3 ± 1.3	18.7 ± 2.2

It is important to mention that hysteresis must be observed as a three–dimensional phenomenon and droplet detachment cannot be judged by taking into account only the contact–angles at the advancing and receding fronts. This indicates that using 2D approximations may lead to erroneous conclusions regarding the prediction of droplet detachment, since the lateral parts of the droplet might well be pinned, while the angle in the vicinity of triple–points (2D counterpart of the contact line) on the axis–of–symmetry exceed the threshold. This can clearly be seen for example in the above test–case with $u_0 = 6m/s$, where although the advancing contact–angle has already reached θ_A, still the major part of the contact–line is pinned and consequently the droplet retains its location.

Velocity vectors on a vertical and a horizontal cross–section are shown in Fig. 15 for $u_0 = 6m/s$. The onset of a wake adjacent to the droplet in the downstream is detectable in Fig. 15(a). By further increasing the inlet velocity, such complex features of the air–flow become more significant and therefore, in order to adequately capture the physical phenomena, a more refined computational mesh and/or special numerical treatments that are generally categorized within the context of turbulent flow modeling are required.

IV. CONCLUSION

A level–set/enriched finite element method that have been developed by the authors, was further advanced in this work by including the pinning mechanism along with other "ingredients" necessary for successful modeling of the hysteresis phenomenon. A modification to the momentum equation was proposed to incorporate the effect of the mass-conservation correction and its performance was analyzed in the simple test of a freely oscillating droplet. The present numerical model was validated for a benchmark involving a water droplet placed on a tilted plane. It was also shown that if the pinning is absent, a dynamic contact–angle hysteresis is still observable due to the frictional forces acting at the surface of the solid substrate. This however, is much smaller than the experimentally detected static contact–angle hysteresis occurring in the presence of pinning.

The numerical model was also employed to simulate a water droplet confined in a channel and exposed to an air–flow with Reynolds numbers ranging from $Re \sim 50$ to 150. It is necessary to mention that for these tests, it was hardly possible to capture all the features of the air–flow on a rather coarse computational mesh that was employed. These features become more important as the Reynolds number increases. For capturing such effects, a significantly finer mesh resolution

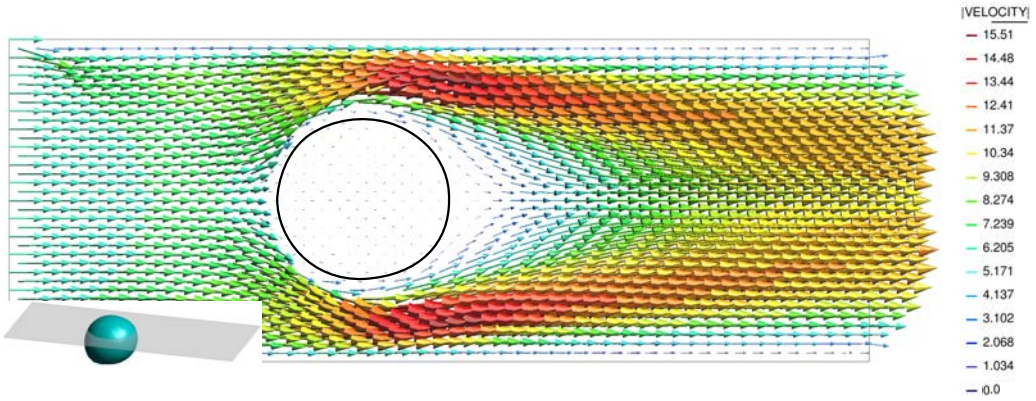

(a)

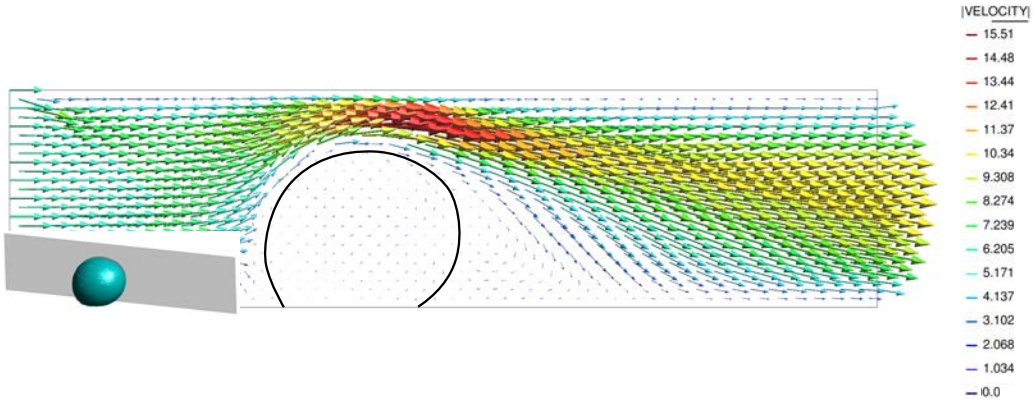

(b)

FIG. 15. Velocity vectors around the droplet subject to air–flow with $u_0 = 6m/s$. Cross–sectional views perpendicular to (a) y–axis and (b) z–axis.

and consequently, prohibitively higher computational costs are needed for the accurate simulation of the time–evolution of the droplet configuration at larger Reynolds numbers.

Overall, the simulations performed indicate that the proposed approach (three-dimensional enriched finite element/level set method) is capable of providing important insights regarding behavior of droplets contacting solid substrates accounting for dynamic contact line with hysteresis. Moreover, reproducing the interfacial discontinuity in a sharp way allows employing relatively coarse meshes that facilitate performing 3D simulations in reasonable execution time.

ACKNOWLEDGMENT

This work was performed within the framework of AMADEUS project ("Advanced Multi-scAle moDEling of coupled mass transport for improving water management in fUel cellS", reference number PGC2018-101655-B-I00) supported by the *Ministerio de Ciencia, Innovacion e Universidades* of Spain. The authors acknowledge financial support of the mentioned Ministry via the “Severo Ochoa Programme" for Centres of Excellence in R&D (referece: CEX2018-000797-S) given to the International Centre for Numerical Methods in Engineering (CIMNE). The authors also acknowledge PRACE for awarding us access to MareNostrum hosted by Barcelona Supercomputing Center, Spain (project reference: 2010PA5560).

CONFLICT OF INTEREST

The authors declare that they have no conflict of interest.

DATA AVAILABILITY STATEMENT

The data that support the findings of this study are available from the corresponding author upon reasonable request.

REFERENCES

[1]F. Barbir, *PEM Fuel Cells: Theory and Practice* (Academic Press, 2012) google-Books-ID: elO7n4Z6uLoC.

[2]M. Contestabile, “Analysis of the market for diesel PEM fuel cell auxiliary power units onboard long-haul trucks and of its implications for the large-scale adoption of PEM FCs,” Energy Policy The socio-economic transition towards a hydrogen economy - findings from European research, with regular papers, **38**, 5320–5334 (2010).

[3]T. Fletcher, R. Thring, and M. Watkinson, “An Energy Management Strategy to concurrently optimise fuel consumption & PEM fuel cell lifetime in a hybrid vehicle,” International Journal of Hydrogen Energy **41**, 21503–21515 (2016).

[4]P. C. Okonkwo and C. Otor, "A review of gas diffusion layer properties and water management in proton exchange membrane fuel cell system," International Journal of Energy Research **45**, 3780–3800 (2021), _eprint: https://onlinelibrary.wiley.com/doi/pdf/10.1002/er.6227.

[5]M. Grimm, M. Hellmann, H. Kemmer, and S. Kabelac, "Water Management of PEM Fuel Cell Systems Based on the Humidity Distribution in the Anode Gas Channels," Fuel Cells **20**, 477–486 (2020), _eprint: https://onlinelibrary.wiley.com/doi/pdf/10.1002/fuce.202000070.

[6]T. C. Wu and N. Djilali, "Experimental investigation of water droplet emergence in a model polymer electrolyte membrane fuel cell microchannel," Journal of Power Sources **208**, 248–256 (2012).

[7]X. Zhu, P. C. Sui, and N. Djilali, "Three-dimensional numerical simulations of water droplet dynamics in a PEMFC gas channel," Journal of Power Sources SPECIAL SECTION Selected papers from the 1st POLISH FORUM ON FUEL CELLS AND HYDROGEN, **181**, 101–115 (2008).

[8]A. Jarauta, P. Ryzhakov, M. Secanell, P. R. Waghmare, and J. Pons-Prats, "Numerical study of droplet dynamics in a polymer electrolyte fuel cell gas channel using an embedded Eulerian-Lagrangian approach," Journal of Power Sources **323**, 201–212 (2016).

[9]A. Theodorakakos, T. Ous, M. Gavaises, J. M. Nouri, N. Nikolopoulos, and H. Yanagihara, "Dynamics of water droplets detached from porous surfaces of relevance to PEM fuel cells," Journal of Colloid and Interface Science **300**, 673–687 (2006).

[10]M. Andersson, V. Vukčević, S. Zhang, Y. Qi, H. Jasak, S. B. Beale, and W. Lehnert, "Modeling of droplet detachment using dynamic contact angles in polymer electrolyte fuel cell gas channels," International Journal of Hydrogen Energy **44**, 11088–11096 (2019).

[11]X. Zhang and Y. Qin, "Contact angle hysteresis of a water droplet on a hydrophobic fuel cell surface," Journal of Colloid and Interface Science **545**, 231–241 (2019).

[12]E. Gauthier, T. Hellstern, I. G. Kevrekidis, and J. Benziger, "Drop Detachment and Motion on Fuel Cell Electrode Materials," ACS Applied Materials & Interfaces **4**, 761–771 (2012), publisher: American Chemical Society.

[13]D. Seveno, A. Vaillant, R. Rioboo, H. Adao, J. Conti, and J. De Coninck, "Dynamics of wetting revisited," Langmuir **25**, 13034–13044 (2009), publisher: ACS Publications.

[14]T. Young, "III. An essay on the cohesion of fluids," Philosophical Transactions of the Royal Society of London **95**, 65–87 (1805), publisher: Royal Society.

[15]A. Hamraoui, K. Thuresson, T. Nylander, and V. Yaminsky, "Can a Dynamic Contact Angle Be Understood in Terms of a Friction Coefficient?" Journal of Colloid and Interface Science **226**, 199–204 (2000).

[16]W. Qi and P. B. Weisensee, "Dynamic wetting and heat transfer during droplet impact on bi-phobic wettability-patterned surfaces," Physics of Fluids **32**, 067110 (2020), publisher: American Institute of Physics.

[17]M. Kumar, R. Bhardwaj, and K. C. Sahu, "Coalescence dynamics of a droplet on a sessile droplet," Physics of Fluids **32**, 012104 (2020), publisher: American Institute of Physics.

[18]R. Bhardwaj and A. Agrawal, "Likelihood of survival of coronavirus in a respiratory droplet deposited on a solid surface," Physics of Fluids **32**, 061704 (2020), publisher: American Institute of Physics.

[19]T. D. Blake and J. M. Haynes, "Kinetics of liquidliquid displacement," Journal of Colloid and Interface Science **30**, 421–423 (1969).

[20]L. Zhao and J. Cheng, "Analyzing the Molecular Kinetics of Water Spreading on Hydrophobic Surfaces via Molecular Dynamics Simulation," Scientific Reports **7**, 10880 (2017).

[21]R. G. Cox, "The dynamics of the spreading of liquids on a solid surface. Part 1. Viscous flow," Journal of Fluid Mechanics **168**, 169 (1986).

[22]J.-H. Kim, H. P. Kavehpour, and J. P. Rothstein, "Dynamic contact angle measurements on superhydrophobic surfaces," Physics of Fluids **27**, 032107 (2015), publisher: American Institute of Physics.

[23]J.-C. Fernández-Toledano, T. D. Blake, and J. De Coninck, "Taking a closer look: A molecular-dynamics investigation of microscopic and apparent dynamic contact angles," Journal of Colloid and Interface Science **587**, 311–323 (2021).

[24]A. M. Karim, K. Fujii, and H. P. Kavehpour, "Contact line dynamics of gravity driven spreading of liquids," Fluid Dynamics Research **53**, 035503 (2021), publisher: IOP Publishing.

[25]P. Petrov and I. Petrov, "A combined molecular-hydrodynamic approach to wetting kinetics," Langmuir **8**, 1762–1767 (1992), publisher: ACS Publications.

[26]H. B. Eral, D. J. C. M. 't Mannetje, and J. M. Oh, "Contact angle hysteresis: a review of fundamentals and applications," Colloid and Polymer Science **291**, 247–260 (2013).

[27]Q. Liu, J. Yu, and H. Wang, "The role of the substrate roughness in contact angle hysteresis and dynamic deviation," International Journal of Heat and Mass Transfer **148**, 118985 (2020).

[28]P. G. de Gennes, "Wetting: statics and dynamics," Reviews of Modern Physics **57**, 827–863 (1985).

[29]L. Gao and T. J. McCarthy, "Contact Angle Hysteresis Explained," Langmuir **22**, 6234–6237 (2006), publisher: American Chemical Society.

[30]C. W. Extrand and Y. Kumagai, "Liquid Drops on an Inclined Plane: The Relation between Contact Angles, Drop Shape, and Retentive Force," Journal of Colloid and Interface Science **170**, 515–521 (1995).

[31]S. Brandon, A. Wachs, and A. Marmur, "Simulated Contact Angle Hysteresis of a Three-Dimensional Drop on a Chemically Heterogeneous Surface: A Numerical Example," Journal of Colloid and Interface Science **191**, 110–116 (1997).

[32]M. Hatipogullari, C. Wylock, M. Pradas, S. Kalliadasis, and P. Colinet, "Contact angle hysteresis in a microchannel: Statics," Physical Review Fluids **4**, 044008 (2019), publisher: American Physical Society.

[33]D. Quéré, "Wetting and Roughness," Annual Review of Materials Research **38**, 71–99 (2008), _eprint: https://doi.org/10.1146/annurev.matsci.38.060407.132434.

[34]S. Qiao, Q. Li, and X.-Q. Feng, "Sliding friction and contact angle hysteresis of droplets on microhole-structured surfaces," The European Physical Journal E **41**, 25 (2018).

[35]Y. Di, J. Qiu, G. Wang, H. Wang, L. Lan, and B. Zheng, "Exploring Contact Angle Hysteresis Behavior of Droplets on the Surface Microstructure," Langmuir **37**, 7078–7086 (2021), publisher: American Chemical Society.

[36]H.-Y. Kim, S. Jeon, M. Song, and K. Kim, "Numerical simulations of water droplet dynamics in hydrogen fuel cell gas channel," Journal of Power Sources **246**, 679–695 (2014).

[37]J. Yang, X. Ma, L. Fei, X. Zhang, K. H. Luo, and S. Shuai, "Effects of hysteresis window on contact angle hysteresis behaviour at large Bond number," Journal of Colloid and Interface Science **566**, 327–337 (2020).

[38]P. Yue, "Thermodynamically consistent phase-field modelling of contact angle hysteresis," Journal of Fluid Mechanics **899** (2020), 10.1017/jfm.2020.465, publisher: Cambridge University Press.

[39]C. Fang, C. Hidrovo, F.-m. Wang, J. Eaton, and K. Goodson, "3-D numerical simulation of contact angle hysteresis for microscale two phase flow," International Journal of Multiphase Flow **34**, 690–705 (2008), publisher: Elsevier.

[40]J. Zhang and P. Yue, "A level-set method for moving contact lines with contact angle hysteresis," Journal of Computational Physics , 109636 (2020), publisher: Elsevier.

[41]Y. F. Yap, J. C. Chai, T. N. Wong, K. C. Toh, and H. Y. Zhang, "A Global Mass Correction Scheme for the Level-Set Method," Numerical Heat Transfer, Part B: Fundamentals **50**, 455–472 (2006), publisher: Taylor & Francis _eprint: https://doi.org/10.1080/10407790600646958.

[42]Z. Solomenko, P. D. M. Spelt, L. Ó Náraigh, and P. Alix, "Mass conservation and reduction of parasitic interfacial waves in level-set methods for the numerical simulation of two-phase flows: A comparative study," International Journal of Multiphase Flow **95**, 235–256 (2017).

[43]Z. Ge, J.-C. Loiseau, O. Tammisola, and L. Brandt, "An efficient mass-preserving interface-correction level set/ghost fluid method for droplet suspensions under depletion forces," Journal of Computational Physics **353**, 435–459 (2018).

[44]E. Mahrous, A. Jarauta, T. Chan, P. Ryzhakov, A. Z. Weber, R. V. Roy, and M. Secanell, "A particle finite element-based model for droplet spreading analysis," Physics of Fluids **32**, 042106 (2020), publisher: AIP Publishing LLC.

[45]E. Mahrous, R. V. Roy, A. Jarauta, and M. Secanell, "A two-dimensional numerical model for the sliding motion of liquid drops by the particle finite element method," Physics of Fluids **33**, 032117 (2021), publisher: American Institute of Physics.

[46]M. R. Hashemi, P. B. Ryzhakov, and R. Rossi, "An enriched finite element/level-set method for simulating two-phase incompressible fluid flows with surface tension," Computer Methods in Applied Mechanics and Engineering **370**, 113277 (2020).

[47]M. R. Hashemi, P. B. Ryzhakov, and R. Rossi, "Three dimensional modeling of liquid droplet spreading on solid surface: An enriched finite element/level-set approach," Journal of Computational Physics **442**, 110480 (2021).

[48]E. B. Dussan, "On the Spreading of Liquids on Solid Surfaces: Static and Dynamic Contact Lines," Annual Review of Fluid Mechanics **11**, 371–400 (1979).

[49]D. Seveno, T. D. Blake, and J. De Coninck, "Young's Equation at the Nanoscale," Physical Review Letters **111**, 096101 (2013), publisher: American Physical Society.

[50]F. Brochard-Wyart and P. G. de Gennes, "Dynamics of partial wetting," Advances in Colloid and Interface Science **39**, 1–11 (1992).

[51]L. M. Pismen, "Some singular errors near the contact line singularity, and ways to resolve both," The European Physical Journal Special Topics **197**, 33 (2011).

[52]W. Ren and W. E, "Boundary conditions for the moving contact line problem," Physics of fluids **19**, 022101 (2007), publisher: American Institute of Physics.

[53]V. Starov, "Static contact angle hysteresis on smooth, homogeneous solid substrates," Colloid and Polymer Science **291**, 261–270 (2013).

[54]M. Sussman, P. Smereka, and S. Osher, "A level set approach for computing solutions to incompressible two-phase flow," Journal of Computational physics **114**, 146–159 (1994), publisher: Elsevier.

[55]R. N. Elias, M. A. Martins, and A. L. Coutinho, "Simple finite element-based computation of distance functions in unstructured grids," International journal for numerical methods in engineering **72**, 1095–1110 (2007), publisher: Wiley Online Library.

[56]R. Codina, "A discontinuity-capturing crosswind-dissipation for the finite element solution of the convection-diffusion equation," Computer Methods in Applied Mechanics and Engineering **110**, 325–342 (1993).

[57]M. Sussman and E. G. Puckett, "A Coupled Level Set and Volume-of-Fluid Method for Computing 3D and Axisymmetric Incompressible Two-Phase Flows," Journal of Computational Physics **162**, 301–337 (2000).

[58]R. Nourgaliev, S. Wiri, N. Dinh, and T. Theofanous, "Adaptive Strategies for Mass Conservation in Level Set Treatment," in *17th AIAA Computational Fluid Dynamics Conference* (American Institute of Aeronautics and Astronautics) _eprint: https://arc.aiaa.org/doi/pdf/10.2514/6.2005-5348.

[59]R. Codina, S. Badia, J. Baiges, and J. Principe, "Variational multiscale methods in computational fluid dynamics," in *Encyclopedia of Computational Mechanics Second Edition* (Wiley Online Library, 2018) pp. 1–28.

[60]P. Dadvand, R. Rossi, and E. Oñate, "An Object-oriented Environment for Developing Finite Element Codes for Multi-disciplinary Applications," Archives of Computational Methods in Engineering **17**, 253–297 (2010).

[61]D. Demidov, "AMGCL —A C++ library for efficient solution of large sparse linear systems," Software Impacts **6**, 100037 (2020).

[62]D. Quéré, M.-J. Azzopardi, and L. Delattre, "Drops at Rest on a Tilted Plane," Langmuir **14**, 2213–2216 (1998), publisher: American Chemical Society.

[63]N. L. Grand, A. Daerr, and L. Limat, "Shape and motion of drops sliding down an inclined plane," Journal of Fluid Mechanics **541**, 293–315 (2005), publisher: Cambridge University

Press.

[64]J. Hyväluoma, A. Koponen, P. Raiskinmäki, and J. Timonen, "Droplets on inclined rough surfaces," The European Physical Journal E **23**, 289–293 (2007).

[65]Y. H. Yeong, A. Milionis, E. Loth, and I. S. Bayer, "Microscopic Receding Contact Line Dynamics on Pillar and Irregular Superhydrophobic Surfaces," Scientific Reports **5**, 8384 (2015), bandiera_abtest: a Cc_license_type: cc_by Cg_type: Nature Research Journals Number: 1 Primary_atype: Research Publisher: Nature Publishing Group Subject_term: Nanoparticles;Surface assembly Subject_term_id: nanoparticles;surface-assembly.

[66]A. J. B. Milne and A. Amirfazli, "Drop Shedding by Shear Flow for Hydrophilic to Superhydrophobic Surfaces," Langmuir **25**, 14155–14164 (2009), publisher: American Chemical Society.

[67]S. Burgmann, M. Dues, B. Barwari, J. Steinbock, L. Büttner, J. Czarske, and U. Janoske, "Flow measurements in the wake of an adhering and oscillating droplet using laser-Doppler velocity profile sensor," Experiments in Fluids **62**, 47 (2021).

[68]G. Yang, X. Chu, V. Vaikuntanathan, S. Wang, J. Wu, B. Weigand, and A. Terzis, "Droplet mobilization at the walls of a microfluidic channel," Physics of Fluids **32**, 012004 (2020), publisher: American Institute of Physics.

Chapter 5

Conclusion

Here, first, the main achievements of the present work are outlined. The second part is further dedicated to the shortcomings of the present numerical approach and possible strategies to resolve them.

5.1 Achievements

In the present work, a computational method was proposed for simulating (liquid–gas) two–phase flow transport problem. This method was based on a pressure enriched finite element technique to solve the Navier–Stokes equation incorporating the interfacial effects, *i.e.* surface tension and contact–line dynamics. Benefiting from a static condensation, the introduced enriched finite element space accurately captures both the weak and the strong pressure discontinuities without increasing the number of the degrees–of–freedom of the global system of equations. In the proposed computational method, the evolution of the phase boundaries was captured using the level–set method. In this work, the crucial aspects of the developed numerical model were addressed, including the (small–cut) stabilization, mass conservation correction, and level–set noise reduction.

In order to consistently treat the movement of the contact–line, the molecular kinetic theory was implemented along with the customized (Navier–slip) boundary condition on the solid substrate. The hydrodynamic theory was further utilized to incorporate the sub–elemental (numerically unresolved) variation in the contact–angle. The developed numerical method was further developed by incorporation of the contact–line hysteresis via implementing a pinning mechanism that conditionally depends on the

wetting/dewetting direction of the movement of the contact–line.

Besides the main contributions, as parts of the present project, an accurate method was also developed to solve the level–set convection equation (presented in Appendix A).

The presented numerical model can readily be applied to simulate the transport of liquid water in different parts of a fuel cell. However, due to extremely high computational costs, the so–called "direct numerical simulation" (DNS, which was employed in this work) of the water transport in GDL was not performed here. This can be done by improving the parallelization of the implemented model with the aim of exploiting the computational power of HPC facilities for performing DNS of sample GDLs.

The capabilities and robustness of the proposed method were proved by solving various benchmarks and test–cases involving droplet dynamics in contact with solid substrates. This work provides the a framework for the numerical simulation of the liquid-gas transport in microfluidic application. However, one can improve its robustness by addressing the following aspects of the method.

5.2 Future research lines

In the present work, the contact–line dynamics was captured by combining the linear molecular kinetic model with the hydrodynamic theory and a Navier–slip condition was imposed on the solid substrate to circumvent the stress singularity. Since the d level–set/enriched–FEM framework is suitable for treating different contact–angle/contact–line velocity relations, it is worth to analyse the results using the nonlinear form of the molecular kinetic theory, specially for initial stages of the droplet spreading. On the other hand, there are some, not thoroughly tested, extensions to the hydrodynamic theory [20, 28, 118, 152], for example, incorporating finite inertia and removing its limitation to the small capillary numbers. One significant contribution would be the incorporation and analysis of such formulations.

In the context of two–phase flow with finite surface tension, experiences have shown that the utilization of a time–marching scheme of Strang splitting type can lead to significant improvements in the accuracy of the method. Nevertheless, proposing an efficient and robust scheme for (second–order) splitting of the contributions of the Navier–Stokes and the level–set convection equations requires further theoretical analyses and numerical investigations.

As in many other CFD applications, adaptive mesh–refinement is a means to improve

the efficiency of the present two–phase flow solver. It is majorly important in cases deal with the necking and separation of the droplets; a highly refined mesh is necessary to resolve the topological changes in the phase interface. Nevertheless, the use of non–uniform meshes arises complexities that need further treatments.

One of the main drawbacks of the DNS approach is its demand for highly intensive computations. For example, the computational costs associated with the pore–scale simulation of water transport in a sample portion of a diffusion media is prohibitively high. Although one can run a few simulations of this kind on HPC facilities, reaching the number of test–cases that are necessary for the interpretation of the fundamental physical phenomena is hardly possible. In this sense, considering the recent advances in "data–driven" approaches in CFD applications, it is worth to step up the efforts in searching for viable algorithms that suit the (transient nature of) droplet dynamic simulations.

Appendix A

Non–Oscillatory BFECC Algorithm for Level–set Equation

A.1 Introduction

In this Appendix, a monotonicity–preserving technique is introduced based on the idea comprised by the so–called "back and forth error compensation correction" (BFECC) method [36] to dramatically improve the accuracy of the level–set convection solvers (generally, any reversible transport equation). The effectiveness of the proposed technique is revealed for three different classes of the stabilized solvers; the SUPG method along with the cross–wind stabilization [23], an explicit algebraically stabilized finite element method, and the unconditionally stable semi–Lagrangian approach [109]. This technique is elaborated in the following, *under review* manuscript.

A.2 Article data

Title: An Enhanced Non–Oscillatory BFECC Algorithm for Finite Element Solution of Advective Transport Problems
Authors: M.R. Hashemi, R. Rossi and P.B. Ryzhakov
under review

An Enhanced Non–Oscillatory BFECC Algorithm for Finite Element Solution of Advective Transport Problems

Mohammad R. Hashemi[a,b,*], Riccardo Rossi[a,b], Pavel B. Ryzhakov[a,b]

[a] *Universitat Politècnica de Catalunya (UPC), 08034 Barcelona, Spain*
[b] *Centre Internacional de Mètodes Numèrics en Enginyeria (CIMNE), 08034 Barcelona, Spain*

Abstract

In this paper, the so-called "back and forth error compensation correction (BFECC)" methodology is utilized to improve the solvers developed for the advection equation. Strict obedience to the so-called "discrete maximum principle" is enforced by incorporating a gradient–based limiter into the BFECC algorithm. The accuracy of the BFECC algorithm in capturing the steep–fronts in hyperbolic scalar–transport problems is improved by introducing a controlled anti–diffusivity. This is achieved at the cost of performing an additional backward sub–solution–step and modifying the formulation of the error compensation accordingly. The performance of the proposed methodology is assessed by solving a series of benchmarks utilizing different combinations of the BFECC algorithms and the underlying numerical schemes. Results are presented for both the structured and unstructured meshes.

Keywords: Convection–dominated transport, BFECC, Limiter, Monotonicity preservation, Discrete maximum principle

*Corresponding author.
Email addresses: mhashemi@cimne.upc.edu (Mohammad R. Hashemi), rrossi@cimne.upc.edu (Riccardo Rossi), pryzhakov@cimne.upc.edu (Pavel B. Ryzhakov)

1. Introduction

In a wide range of fluid dynamic applications, an elemental step in the numerical simulations is to solve advective, or more generally, convection–dominated transport problems (for example see [1, 2, 3]). In this context, the main challenge addressed by the researchers presently is to accurately capture the steep fronts while suppressing the spurious oscillations. In other words, the numerical method should preserve the monotonicity property [4] of the problem while ensuring sufficient spatial accuracy [5]. This challenging requirement has made the numerical solution of convection–dominated transport problems an active topic for decades, and adopting the continuous finite element method, a vast variety of the approaches have so–far been developed [6, 7, 8, 9, 10].

Stemming from the streamline–upwind/Petrov–Galerkin (SUPG) method [11], a series of methods were developed by introducing a residual–based stabilization term [6]. Although stable for rather smooth cases, SUPG–like methods are not monotonicity–preserving and therefore, suffer from spurious oscillations in the vicinity of a steep gradient [12, 13]. This causes the development of the so–called "spurious oscillations at layers diminishing (SOLD)" techniques [14], which need an extremely careful choice of parameters to provide a satisfactory result [15].

Taking into account that the mathematical description of the monotonicity–preservation can be rendered into the discrete maximum principle (DMP) [13], the necessary requirement for obtaining a non–oscillatory solution is that the solver embodies DMP. Successful methods have been developed based on introducing an artificial diffusion adjusted so that DMP is satisfied [16, 17, 8, 18]. The class of algebraic flux correction schemes [19, 1, 20, 21, 22, 23] is also developed by enforcing DMP at the level of the algebraic system of equations. Consistently with Godunov's statement [24], in order to retain both the spatial accuracy and monotonicity, almost all these methods rely on a nonlinear discretized equation, which in most cases, necessitates an iterative solution procedure.

As an alternative to such iterative methods, the back and forth error compensation correction (BFECC) algorithm creates a framework for improving the solution of any time–reversible problem [25] [26]; applying BFECC to a first–order underlying scheme, a second–order numerical method is obtained [27]. The BFECC algorithm is based on three sub–solution–steps; first, advancing in–time using a first–order scheme, then, retreating in–time

using the same scheme to evaluate the error, and finally, advancing the compensated field in–time using the same scheme. In this sense, if an explicit underlying scheme is used, the resulting method is fully explicit (with a fixed number of sub–steps). Assuming that the underlying scheme holds DMP, and considering the evaluated error as an anti–diffusivity term, BFECC can be categorized along with the predictor–corrector algorithms of the kind described in [28]. However, despite its great potential, there are only a few attempts to utilize, analyze, and enhance the BFECC algorithm. This is mainly due to the fact that the conventional (unlimited) BFECC algorithm deteriorates the capability of the underlying numerical scheme in terms of the prevention of the spurious oscillations. In order to circumvent this issue, limited BFECC algorithms were proposed; Selle *et al.* [27] proposed to detect and enforce the local bounds of the final solution following the characteristic line of the advection equation. General application of such limiter is not computationally justifiable unless the semi–Lagrangian CIR scheme [29] is used. In an alternative approach, Hu *et al.* [30] introduced a limiter based on the detection of the over/under–shoots in the final solution, which requires two additional sub–solution–steps that significantly increases the computational cost of the method.

Knowing that the BFECC algorithm violates DMP at the error compensation step, a shock detector (limiter) can be employed to retain the monotonicity–preserving property of the solver if the underlying scheme, itself, embodies DMP. In this way, no additional sub–solution–step is required and consequently, the efficiency of the BFECC algorithm is not affected. In the present work, a gradient–based [31] continuous nodal limiter [32] is incorporated to the BFECC algorithm, recovering the DMP of the resulting scheme. In addition to the methods based on the conventional BFECC, a modified algorithm is proposed permitting more accurate capturing of the steep fronts. This modified algorithm also results in a superior performance in the smooth cases. In order to highlight the versatility of the proposed BFECC algorithm, it is applied to DMP–preserving Eulerian and semi–Lagrangian underlying schemes.

In the following sections, first, the scalar transport equation and the low–order over–diffusive monotonicity–preserving solver are described. Then, the BFECC algorithms and the incorporation of the gradient–based limiter are discussed. In section 4, an enhanced underlying scheme is briefly presented that partially compensates for the extra–diffusivity of the low–order underlying scheme. In the final section of the present paper, numerical tests are

presented addressing the one– and two–dimensional advection problems on structured and unstructured meshes.

2. Scalar Transport Equation

2.1. Continuum Formulation

As a frequently encountered example of hyperbolic problems, the conservation of scalar field $u(\mathbf{x}, t)$ is addressed in this work. This problem is governed by a time–reversible partial differential equation [27] formulated as

$$\frac{\partial u}{\partial t} + \nabla \cdot (\mathbf{v}u) = 0 \qquad \text{in } \Omega. \tag{1}$$

Assuming that velocity field $\mathbf{v}(\mathbf{x}, t)$ retains the incompressibility condition, $\nabla \cdot \mathbf{v} = 0$, Eq. (1) can be rewritten in advective form [33].

$$\frac{\partial u}{\partial t} + \mathbf{v} \cdot \nabla u = 0 \qquad \text{in } \Omega, \tag{2}$$

This equation is subject to the initial condition,

$$u(\mathbf{x}, 0) = u_0(\mathbf{x}) \qquad \text{in } \Omega, \tag{3}$$

and Dirichlet boundary condition

$$u = u_D \qquad \text{on } \partial\Omega_D, \tag{4}$$

providing that there is an inward flux at $\partial\Omega_D$, *i.e.* $\mathbf{v} \cdot \mathbf{n} < 0$ with $\mathbf{n}$ denoting the outward normal to boundary $\partial\Omega$.

2.2. Galerkin Discretization

Using test–function $q \in \mathcal{L}_2(\Omega)$, Eq. (2) leads to the problem of finding u that satisfies

$$\int_\Omega q \left(\frac{\partial u}{\partial t} + \mathbf{v} \cdot \nabla u \right) = 0 \qquad \forall q. \tag{5}$$

The finite element solution to this problem is obtained by discretizing the computational domain into a set of elements, $\mathcal{E}$, and choosing both the test–function and the trial–function in the finite element space. In this way, u is approximated as $u_h = \sum_{\mathcal{N}^e} u_i \phi_i^e(\mathbf{x})$ and $q_h \in \phi_i; i \in \mathcal{N}^e \setminus \mathcal{N}_D$ within element e. Here, ϕ_i denotes the shape function associated with node i, and $\mathcal{N}^e$

and $\mathcal{N}_D$ are the sets of nodes associated with e and the Dirichlet boundary condition, respectively. By doing the substitutions, the discrete form of the problem reads

$$\mathcal{A}_{e\in\mathcal{E}}\left(\mathbb{M}_C^e\frac{d\mathbf{U}^e}{dt}+\mathbb{C}^e\mathbf{U}^e\right)=0, \tag{6}$$

where $\mathbf{U}^e$ is the vector of nodal unknowns u_i with $i \in \mathcal{N}^e \setminus \mathcal{N}_D$. Here, operator $\mathcal{A}$ represents the assembly of the elemental system of equations, and $\mathcal{E}$ denotes the set of the elements in the computational domain. The entities of the elemental consistent mass and convection matrices are calculated as

$$m_{ij}^e=\int_{\Omega^e}\phi_i\phi_j d\Omega, \qquad i\in\mathcal{N}^e\setminus\mathcal{N}_D, \text{ and } j\in\mathcal{N}^e, \tag{7}$$

and

$$c_{ij}^e=\int_{\Omega^e}\phi_i\mathbf{v}\cdot\nabla\phi_j d\Omega, \qquad i\in\mathcal{N}^e\setminus\mathcal{N}_D, \text{ and } j\in\mathcal{N}^e, \tag{8}$$

respectively. Assembling the contributions of all the elements, the global linear system of equations is obtained as

$$\mathbb{M}_C\frac{d\mathbf{U}}{dt}+\mathbb{C}\mathbf{U}=0. \tag{9}$$

Without loss of generality, the finite element space is constructed by shape functions of simplex elements in this work.

2.3. Stabilization

It is widely known that in its pure form (i.e. without introducing any diffucion), Eq. (9) is subject to severe numerical instabilities [12]. Starting from Eq. (6), an established practice [34, 21, 35] to achieve a stabilized numerical scheme is to substitute the consistent mass matrix with lumped mass matrix $\mathbb{M}_L^e$ and introduce artificial numerical diffusion $\mathbf{D}^e$, which gives

$$\mathcal{A}_{e\in\mathcal{E}}\left(\mathbb{M}_L^e\frac{d\mathbf{U}^e}{dt}+\mathbb{C}^e\mathbf{U}^e+\mathbf{D}^e\right)=0. \tag{10}$$

The entities of $\mathbb{M}_L^e$ are obtained as

$$m_{L,ij}^e=\begin{cases} m_i^e=\int_{\Omega^e}\phi_i d\Omega & \textbf{if} \quad i=j \\ 0 & \textbf{if} \quad i\neq j \end{cases} \tag{11}$$

The numerical diffusion term can be calculated as

$$\mathbf{D}^e = \nu^e \left(\mathbb{M}_L^e - \mathbb{M}_C^e\right) \mathbf{U}^e, \tag{12}$$

to formulate the global system of equations as

$$\mathbb{M}_L \frac{d\mathbf{U}}{dt} = \mathbb{L}\mathbf{U}, \tag{13}$$

with $\mathbb{L}^e = \nu^e \left(\mathbb{M}_C^e - \mathbb{M}_L^e\right) - \mathbb{C}^e$. Equivalently, one can write

$$m_i \frac{du_i}{dt} = \sum_j l_{ij} u_j, \tag{14}$$

with $m_i = \sum_{e \in \mathcal{E}_i} m_i^e$ (for linear elements), where $\mathcal{E}_i$ denotes the set of elements that share node i. It is easy to show that, as a requirement for conservation, $\sum_j l_{ij} = 0$; therefore, the sufficient condition to abide with DMP and positivity of the result [28, 21] is

$$l_{ij} \geq 0, \quad i \neq j. \tag{15}$$

This is the key to attain a stabilized monotonicity-preserving *low–order* scheme [19, 1], and subsequently, prevent the spurious overshoots and undershoots in the result. Providing this condition, coefficient ν can be calculated for each element as

$$\nu^e = \max\left(\frac{c_{ij}^e}{m_{ij}^e}, 0\right) \qquad \forall i, j \in \mathcal{N}^e. \tag{16}$$

The resulting scheme is known to be non–oscillatory but strongly over–diffusive [35]. It must be noted that one can reduce the artificial diffusivity by calculating ν according to the DMP at the level of the assembled global system of equation. Nonetheless, the excessive diffusion of the stabilized scheme must be alleviated in order to obtain an accurate method. One possibility consists in applying the the so-called "back and forth error compensation and correction (BFECC)" algorithm that is described below.

3. Back and Forth Error Compensation and Correction

The basic idea of the BFECC algorithm is to estimate and compensate for the error associated with any numerical underlying scheme utilized for

solving a reversible differential equation [27]; this is done by reversing the solution of the numerical scheme and comparing the result with the starting state, which requires consecutive application of the underlying scheme in the forward and backward directions. For solving Eq. (2), the BFECC algorithm, as first proposed in [26], can be summarized in four steps:

1. starting from $u_n(\mathbf{x})$ and solving Eq. (2) forward in time to obtain $u^*_{n+1}(\mathbf{x})$.
2. starting from $u^*_{n+1}(\mathbf{x})$ and solving Eq. (2) backward in time (by reversing velocity vector $\mathbf{v}$) to obtain $u^*_n(\mathbf{x})$.
3. estimating the error as $e(\mathbf{x}) = [u^*_n(\mathbf{x}) - u_n(\mathbf{x})]/2$ and do the compensation as $\tilde{u}_n(\mathbf{x}) = u_n(\mathbf{x}) - e(\mathbf{x})$.
4. starting from $\tilde{u}_n(\mathbf{x})$ and solving Eq. (2) forward in time to obtain $u_{n+1}(\mathbf{x})$.

Here, subscript n denotes the solution at time $t = n\Delta t$. It should be note that a variable time–step (Δt) can be used according to the requirement (CFL–like condition) of the underlying numerical scheme.

If the numerical scheme acquired to solve Eq. (2) can be formulated as

$$\mathbb{M}\frac{d\mathbf{U}}{dt} = \mathbb{L}\mathbf{U}, \tag{17}$$

employing the backward Euler scheme in time, the application of the BFECC algorithm reads

$$\left(\frac{1}{\Delta t}\mathbb{M} - \mathbb{L}_F\right)\mathbf{U}^*_{n+1} = \frac{1}{\Delta t}\mathbb{M}\mathbf{U}_n, \tag{18}$$

$$\left(\frac{1}{\Delta t}\mathbb{M} - \mathbb{L}_B\right)\mathbf{U}^*_{n} = \frac{1}{\Delta t}\mathbb{M}\mathbf{U}^*_{n+1}, \tag{19}$$

$$\mathbf{E} = \frac{1}{2}\left(\mathbf{U}^*_n - \mathbf{U}_n\right) = \frac{\Delta t}{2}\mathbb{M}^{-1}\left(\mathbb{L}_F\mathbf{U}^*_{n+1} + \mathbb{L}_B\mathbf{U}^*_n\right), \tag{20}$$

and finally,

$$\begin{aligned}\left(\frac{1}{\Delta t}\mathbb{M} - \mathbb{L}_F\right)\mathbf{U}_{n+1} &= \frac{1}{\Delta t}\mathbb{M}\tilde{\mathbf{U}}_n \\ &= \frac{1}{\Delta t}\mathbb{M}\mathbf{U}_n - \frac{1}{2}\left(\mathbb{L}_F\mathbf{U}^*_{n+1} + \mathbb{L}_B\mathbf{U}*_n\right).\end{aligned} \tag{21}$$

Subscripts F and B, respectively, denote the forward and the backward advection of u. Here, it is assumed that velocity field $\mathbf{v}(\mathbf{x}, t)$ is given and

therefore, matrices $\mathbb{L}_F$ and $\mathbb{L}_B$ are constructed for mid–time–step velocity $\mathbf{v}_{n+1/2} = (\mathbf{v}_{n+1} + \mathbf{v}_n)/2$.

For the simple one-dimensional case described in the following section, it is easy to show that

$$\mathbb{C}^e = \frac{1}{2}\left(\mathbb{L}_B^e - \mathbb{L}_F^e\right). \tag{22}$$

Therefore, the last term on the right–hand–side of Eq. (21) can be interpreted as an anti-diffusive term, which is introduced by application of the BFECC algorithm. This term partially compensates for numerical diffusion $\mathbf{D}$. This property of the BFECC algorithm leads to the dismissal of condition (15) and undermines the stability of the method by making it prone to spurious over–/undershoots in the result. The occurrence of such oscillations has been mentioned in the literature and was tackled by limiting the results [27, 30]. In the following, this issue will be further discussed for a simple one-dimensional case.

3.1. Analysis of One-Dimensional Case

For the one-dimensional case with linear elements of length h, the elemental matrices associated with the algebraically stabilized scheme described in Section 2.3 are

$$\mathbb{M}_C^e = \begin{bmatrix} \frac{h}{3} & \frac{h}{6} \\ \frac{h}{6} & \frac{h}{3} \end{bmatrix}, \tag{23}$$

$$\mathbb{M}_L^e = \begin{bmatrix} \frac{h}{2} & 0 \\ 0 & \frac{h}{2} \end{bmatrix}, \tag{24}$$

$$\mathbb{C}^e = \begin{bmatrix} -\frac{v}{2} & \frac{v}{2} \\ -\frac{v}{2} & \frac{v}{2} \end{bmatrix}, \tag{25}$$

$$\mathbb{L}_F^e = \begin{bmatrix} 0 & 0 \\ v & -v \end{bmatrix}, \tag{26}$$

and

$$\mathbb{L}_B^e = \begin{bmatrix} -v & v \\ 0 & 0 \end{bmatrix}. \tag{27}$$

Upon assembling these matrices to obtain the global linear system of equations, one has

$$\frac{du_i}{dt} + \frac{v\left(u_i - u_{i-1}\right)}{h} = 0, \tag{28}$$

which is equivalent to the first–order upwind scheme. In this simple case, jth element is formed by nodes j and $j+1$.

Considering the forward Euler scheme for more simplicity, and applying the BFECC algorithm, the resulting method reads

$$\begin{aligned} u_{n+1,i} = u_{n,i} + \frac{1}{2}\big[&\left(\lambda^3-\lambda^2\right)u_{n,i-2} + \left(-3\lambda^3+4\lambda^2+\lambda\right)u_{n,i-1} \\ &+ \left(3\lambda^3-5\lambda^2\right)u_{n,i} + \left(-\lambda^3+2\lambda^2-\lambda\right)u_{n,i+1}\big], \end{aligned} \tag{29}$$

where $\lambda = v\Delta t/h$ denotes the Courant–Friedrichs–Levy (CFL) number. While the sum of the coefficients of nodal u on the right–hand–side of Eq. (29) is zero, condition (15) is not fulfilled and hence, DMP is not guaranteed. This explains the oscillatory results of the BFECC algorithm in the vicinity of steep fronts [30], regardless of the underlying scheme used for solving Eq. (2). In Section 3.3, this issue is resolved by introducing a limited BFECC algorithm with the monotonicity–preserving property.

3.1.1. Truncation Error

The exact solution of Eq. (2) in one-dimension requires that

$$\begin{aligned} u(x,t+\Delta t) = u(x-\delta,t) = u(x,t) - \delta\frac{\partial u(x,t)}{\partial x} + \frac{1}{2}\delta^2\frac{\partial^2 u(x,t)}{\partial x^2} \\ - \frac{1}{6}\delta^3\frac{\partial^3 u(x,t)}{\partial x^3} + O(\delta^4), \end{aligned} \tag{30}$$

with $\delta = v\Delta t$. It is possible to perform the Taylor expansion for the discretized equations as well; the Galerkin scheme (9) can be expanded as

$$u_{n+1,i} = u_{n,i} - \delta\frac{u_{n,i+1}-u_{n,i-1}}{2h} = u_{n,i} - \delta\left(\frac{\partial u}{\partial x} + \frac{h^2}{6}\frac{\partial^3 u}{\partial x^3} + O(h^3)\right). \tag{31}$$

It must be noted that here, for the sake of simplicity, the mass matrix is considered to be lumped. Comparing Eqs. (30) and (31), the associated truncation error is

$$Tr_i = u(x_i,t_n+\Delta t) - u_{n+1,i} = \frac{\delta^2}{2}\frac{\partial^2 u}{\partial x^2} + \frac{\delta^3}{6}\left(\frac{h^2}{\delta^2}-1\right)\frac{\partial^3 u}{\partial x^3} + O(\delta^4). \tag{32}$$

Similarly, for the stabilized *low–order* underlying scheme (28) one obtains

$$Tr_i = \frac{\delta^2}{2}\left(1-\frac{h}{\delta}\right)\frac{\partial^2 u}{\partial x^2} + O(\delta^3). \tag{33}$$

Here, it is assumed that CFL number λ and consequently h/δ are set as constants. In this sense, factorizing δ appears to be logical.

Applying the same procedure to Eq. (29), for the BFECC algorithm using the stabilized *low–order* underlying scheme (28), one has

$$u_{n+1,i} = u_{n,i} - \delta\frac{\partial\phi}{\partial x} + \frac{\delta^2}{2}\frac{\partial^2\phi}{\partial x^2} - \delta^3\left(\frac{1}{2} + \frac{h}{2\delta} + \frac{h^2}{6\delta^2}\right)\frac{\partial^3\phi}{\partial x^3} + O(\delta^4). \tag{34}$$

The associated truncation error reads

$$Tr_i = \delta^3\left(\frac{1}{3} + \frac{h}{2\delta} + \frac{h^2}{6\delta^2}\right)\frac{\partial^3\phi}{\partial x^3} + O(\delta^4). \tag{35}$$

The truncation error shows a one–order improvement comparing to Eq. (33). It is evident that keeping the CFL number constant, element–size h and time–step Δt (or equivalently δ) are interchangeable.

It is worth noting that the positive coefficient of $\partial^2 u/\partial x^2$ in Eq. (32) shows the anti-diffusive (with severe spatial oscillations) characteristic of the Galerkin scheme. On the other hand, for $\lambda < 1$, the negative coefficient of the leading term in Eq. (33) reveals the diffusive nature of the stabilized *low–order* scheme, which is worsen by reducing the CFL number. Nonetheless, the absence of this leading term in Eq. (35), discloses the ability of the BFECC algorithm to compensate for the excessive diffusion of the solver. This section is closed by further proving the ability of the BFECC algorithm in removing the anti-diffusivity imposed by the Galerkin scheme; applying the BFECC algorithm to Eq. (31), one obtains

$$\begin{aligned} u_{n+1,i} = u_{n,i} + \frac{1}{16}\big[&\lambda^3 u_{n,i-3} + 2\lambda^2 u_{n,i-2} + \left(-3\lambda^3 + 8\lambda\right)u_{n,i-1} \\ &-4\lambda^2 u_{n,i} + \left(3\lambda^3 - 8\lambda\right)u_{n,i+1} + 2\lambda^2 u_{n,i+2} - \lambda^3 u_{n,i+3}\big], \end{aligned} \tag{36}$$

and consequently have

$$u_{n+1,i} = u_{n,i} - \delta\frac{\partial u}{\partial x} + \frac{\delta^2}{2}\frac{\partial^2 u}{\partial x^2} + \delta^3\left(\frac{1}{4} - \frac{h^2}{12\delta^2}\right)\frac{\partial^3 u}{\partial x^3} + O(\delta^4). \tag{37}$$

Therefore, the associated truncation error is

$$Tr_i = \delta^3\left(-\frac{5}{12} + \frac{h^2}{12\delta^2}\right)\frac{\partial^3 u}{\partial x^3} + O(\delta^4). \tag{38}$$

The absence of $\partial^2 u/\partial x^2$ in Eq (38) asserts the compensation for the anti–diffusivity detected in Eq. (32).

3.2. Modified Algorithm

In order to obtain further improvement, the BFECC algorithm can be modified as outlined in the following steps;

1. starting from $u_n(\mathbf{x})$ and solving Eq. (2) forward in time to obtain $u^*_{n+1}(\mathbf{x})$.
2. starting from $[u_n(\mathbf{x}) + u^*_{n+1}(\mathbf{x})]/2$ and solving Eq. (2) *half–way* $(\Delta t/2)$ backward in time (by reversing velocity vector $\mathbf{v}$) to obtain $u^*_n(\mathbf{x})$.
3. estimating the error as $e(\mathbf{x}) = u^*_n(\mathbf{x}) - u_n(\mathbf{x})$ and do the compensation as $\tilde{u}_n(\mathbf{x}) = u_n(\mathbf{x}) - e(\mathbf{x})$.
4. starting from $\tilde{u}_n(\mathbf{x})$ and solving Eq. (2) forward in time to obtain $u_{n+1}(\mathbf{x})$.

As done before for the conventional BFECC algorithm by employing the backward Euler scheme in time, the application of this modified BFECC algorithm to the scheme presented in Eq. (17) reads

$$\left(\frac{1}{\Delta t}\mathbb{M} - \mathbb{L}_F\right)\mathbf{U}^*_{n+1} = \frac{1}{\Delta t}\mathbb{M}\mathbf{U}_n, \tag{39}$$

as the first step, and

$$\left(\frac{2}{\Delta t}\mathbb{M} - \mathbb{L}_B\right)\mathbf{U}^*_{n} = \frac{1}{\Delta t}\mathbb{M}\left(\mathbf{U}^*_{n+1} + \mathbf{U}_n\right), \tag{40}$$

as the second step. Adding Eqs. (39) and (40), one obtains

$$\frac{2}{\Delta t}\mathbb{M}\mathbf{U}^*_n = \mathbb{L}_B\mathbf{U}^*_n + \mathbb{L}_F\mathbf{U}^*_{n+1} + \frac{2}{\Delta t}\mathbb{M}\mathbf{U}_n, \tag{41}$$

from which the third step of the modified BFECC algorithm leads to

$$\mathbf{E} = \mathbf{U}^*_n - \mathbf{U}_n = \frac{\Delta t}{2}\mathbb{M}^{-1}\left(\mathbb{L}_F\mathbf{U}^*_{n+1} + \mathbb{L}_B\mathbf{U}^*_n\right), \tag{42}$$

that is the same as the error calculated in Eq. (20) for the conventional BFECC algorithm. Therefore, it is readily seen that both the conventional and the modified BFECC algorithms are equivalent if applied to a solver formulated as Eq. (17) and discretized in time using the backward Euler scheme. Nevertheless, if an explicit (*e.g.* forward Euler) scheme is used, this modified algorithm is not equivalent to the conventional BFECC algorithm. In the following, it is shown that besides the conventional BFECC algorithm, the introduced modified BFECC algorithm can be acquired to add a controlled anti-diffusivity to the solution.

3.2.1. One-Dimensional Case

Similar to Section 3.1, application of the modified BFECC algorithm to the stabilized *low–order* scheme (28) with the forward Euler time discretization leads to

$$u_{n+1,i} = u_{n,i} + \frac{1}{4}\left[\left(\lambda^3 - 2\lambda^2\right) u_{n,i-2} + \left(-3\lambda^3 + 7\lambda^2 + 2\lambda\right) u_{n,i-1} + \left(3\lambda^3 - 8\lambda^2\right) u_{n,i} + \left(-\lambda^3 + 3\lambda^2 - 2\lambda\right) u_{n,i+1}\right]. \tag{43}$$

This leads to

$$u_{n+1,i} = u_{n,i} - \delta\frac{\partial u}{\partial x} + \frac{\delta^2}{4}\frac{\partial^2 u}{\partial x^2} - \delta^3\left(\frac{1}{4} + \frac{h}{2\delta} + \frac{h^2}{6\delta^2}\right)\frac{\partial^3 u}{\partial x^3} + O(\delta^4), \tag{44}$$

from which, the truncation error is calculated as

$$Tr_i = \frac{\delta^2}{4}\frac{\partial^2 u}{\partial x^2} + \delta^3\left(\frac{1}{6} + \frac{h}{2\delta} + \frac{h^2}{6\delta^2}\right)\frac{\partial^3 u}{\partial x^3} + O(\delta^4). \tag{45}$$

Equation (45) clearly shows that the modified BFECC algorithm adds half the amount of the anti-diffusivity of the Galerkin scheme (see Eq. 32). Moreover, the modified algorithm neither improves nor impairs the order of the solver unlike the conventional BFECC algorithm which is proved to provide enhancement upon application to the first–order solvers. Nonetheless, in Section 3.4, a combined algorithm is introduced that benefits from the advantages of both the conventional and the modified BFECC algorithms.

3.3. Nodal Limiter

As discussed above, the maximum principle and the positivity are no more guaranteed upon the application of (either the conventional or modified) BFECC algorithm. Therefor, in order to circumvent the associated instability issues in the present work, a continuous nodal limiter is utilized to control the application of the BFECC algorithm; the idea is to fully apply the error compensation according to the BFECC algorithm wherever the convected field is smooth while ignoring the correction in the vicinity of local extrema. In this way, upon the application of limiter function α, the third step of (either the standard or modified) BFECC algorithm reads $\tilde{u}_n(\mathbf{x}) = u_n(\mathbf{x}) - \alpha(\mathbf{x})e(\mathbf{x})$. It is worth mentioning that while DMP and the positivity condition are guaranteed for the solver underlying the forth-step of the BFECC algorithm, preserving the monotonicity for $\tilde{u}_n$ is the sufficient

condition for the BFECC algorithm to satisfy these essential requirements. Here, the continuity of the limiter function allows the partial application of the BFECC algorithm by quantifying the smoothness of the convected field.

The limiter utilized in the present work was originally proposed in [32] and further utilized in [18] to control over the artificial diffusion associated with the stabilization term introduced to a convection–diffusion equation. Later on, addressing its shortcoming for asymmetric meshes [31], a more general version of this limiter was introduced as [35]

$$\alpha_i = 1 - \left[\frac{\left| \sum_{j \in \mathcal{N}_i \setminus i} \beta_{ij} \left(u_i - u_j \right) \right|}{\sum_{j \in \mathcal{N}_i \setminus i} \beta_{ij} \left| u_i - u_j \right| + \varepsilon} \right]^{\zeta}, \tag{46}$$

where $\alpha_i = \alpha(\mathbf{x}_i)$ and $\mathcal{N}_i$ denotes the set of nodes, which share an edge with node i. In Eq. (46), $\varepsilon \sim O(10^{-15})$ is an extremely small constant that is introduced to prevent division by zero in cases of flat u, and power ζ characterizes the spatial variation of α by determining the acuteness of its decay rate nearby the location of a non-smooth convected field. In the present work, $\zeta = 2$ is set for limiting the BFECC algorithm. Coefficient β_{ij} is calculated based on the procedure introduced by Kuzmin *et al.* [35] in order to maintain the linearity–preservation in cases of an asymmetric mesh.

3.4. Combined Algorithm

The outstanding characteristic of the conventional BFECC algorithm in enhancing the order of accuracy of the method begin to fade away as the limiter decreases from unity; this is an inevitable cost to preserve the monotonicity. The more acute the local change in the gradient is, the smaller the limiter becomes. On the other hand, the nodal limiter (46) can be employed as a shock detector [18], and consequently, a measure for determining the nodes that are subject to relatively large numerical diffusion. The basic idea here is to acquire the limited amount of anti-diffusivity introduced by the modified BFECC algorithm (see Eq. (45) and the discussion afterwards) to partially compensate for excessive numerical diffusion.

In this manner, the combined BFECC algorithm is proposed as

1. starting from $u_n(\mathbf{x})$ and solving Eq. (2) forward in time to obtain $u^*_{n+1}(\mathbf{x})$.
2. doing the backward steps:

2.1 starting from $u^*_{n+1}(\mathbf{x})$ and solving Eq. (2) backward in time to obtain $u^*_n(\mathbf{x})$.

2.2 starting from $[u_n(\mathbf{x}) + u^*_{n+1}(\mathbf{x})]/2$ and solving Eq. (2) half-way $(\Delta t/2)$ backward in time to obtain $u^{**}_n(\mathbf{x})$.

3. do the compensation as $\tilde{u}_n(\mathbf{x}) = u_n(\mathbf{x}) - e(\mathbf{x})$ with error depending on α:

$$e(\mathbf{x}) = \begin{cases} [u^*_n(\mathbf{x}) - u_n(\mathbf{x})]/2 & \textbf{if} \quad \alpha(\mathbf{x}) > \alpha_{th} \\ u^{**}_n(\mathbf{x}) - u_n(\mathbf{x}) & \textbf{if} \quad \alpha(\mathbf{x}) \leq \alpha_{th} \end{cases} \tag{47}$$

4. starting from $\tilde{u}_n(\mathbf{x})$ and solving Eq. (2) forward in time to obtain $u_{n+1}(\mathbf{x})$.

In this algorithm, α_{th} denotes the threshold, below which the conventional BFECC algorithm is substituted by the modified BFECC algorithm. Numerical tests show that the most desirable results can be obtained by $\alpha_{th} \approx 0.9$.

4. Enhanced Scheme

In this section, a methodology is described that allows limiting the extra diffusivity of the stabilized *low–order* underlying scheme (10). The resulting scheme is called as the "*enhanced* scheme" throughout this paper. The improvement of the *low–order* stabilized scheme (10) is based on rolling back the stabilization procedure in the smooth area in order to minimize the artificial diffusion. In the meantime, the formulation remains intact in the vicinity of local extrema in order to hold DMP. Similar to the introduced limited BFECC algorithm, limiter α plays the key role in this formulation enhancement procedure.

Rewriting Eq. (10) and expanding the artificial diffusion term, $\mathbf{D}^e$, one has

$$\mathcal{A}_{e\in\mathcal{E}} \left(\mathbb{M}^e_L \frac{d\mathbf{U}^e}{dt} + \mathbb{C}^e \mathbf{U}^e + \nu^e \left(\mathbb{M}^e_L - \mathbb{M}^e_C \right) \mathbf{U}^e \right) = 0. \tag{48}$$

Towards the minimization of the numerical diffusion, one can take two distinguished steps; bringing back the consistent mass–matrix and compensating for the artificial diffusion term. Incorporating the limiter, these two steps read

$$\mathcal{A}_{e\in\mathcal{E}} \left\{ [\alpha^e \mathbb{M}^e_C + (1-\alpha^e)\mathbb{M}^e_L] \frac{d\mathbf{U}^e}{dt} + \mathbb{C}^e \mathbf{U}^e + \nu^e \left(\mathbb{M}^e_L - \mathbb{M}^e_C \right) \mathbf{U}^e - \alpha^e \hat{\mathbf{D}}^e \right\} = 0, \tag{49}$$

where $\hat{\mathbf{D}}^e$ is an approximation of $\mathbf{D}^e$. For a simplex element, it can be shown that [35]

$$m_i^e u_i - \sum_{j \in \mathcal{N}^e} m_{ij}^e u_j = (1+d) \int_{\Omega^e} \phi_i (u_h - \bar{u}^e) d\Omega, \tag{50}$$

where d denotes the number of dimensions ($d = 2$ in 2D) and elemental average $\bar{u}^e$ is calculated as

$$\bar{u}^e = \frac{\int_{\Omega^e} u_h d\Omega}{\int_{\Omega^e} d\Omega}. \tag{51}$$

Introducing $u_h(\mathbf{x}) \approx \bar{u}^e + \mathbf{g}^e \cdot (\mathbf{x} - \bar{\mathbf{x}}^e)$ into Eq. (50), the entities of $\hat{\mathbf{D}}^e$ are calculated as

$$\hat{d}_i^e = \nu^e (1+d) \int_{\Omega^e} \phi_i \mathbf{g}^e \cdot (\mathbf{x} - \bar{\mathbf{x}}^e) d\Omega, \tag{52}$$

In this work, $\mathbf{g}^e$ is calculated as the elemental average of nodal gradients $\mathbf{g}_i$, which are obtained using lumped–mass projection of ∇u as

$$\mathbf{g}_i = \frac{1}{m_i} \int_{\Omega} \phi_i \sum_{j \in \mathcal{N}} \nabla \phi_j u_j d\Omega. \tag{53}$$

The elemental limiter is then the minimum of the associated nodal ones, *i.e.*

$$\alpha^e = \min_{i \in \mathcal{N}^e} \alpha_i^e. \tag{54}$$

In the computation of Eq. (54), α_i^e is calculated using Eq. (46) with $\zeta = 4$. It must be noted that the presented scheme can be considered as an explicit variant of the method proposed by Kuzmin *et al.* [35], which has similarities in essence with the formulation introduced in [36]. It is also worth noting that for $\alpha^e \to 1$, Eq. (49) tends to the Galerkin scheme and therefore, a strong anti-diffusivity is expected. In Appendix B, the implementation of this *enhanced* scheme is further described. In the numerical tests, it is shown how the application of the proposed limited BFECC algorithm further improves the results by eliminating the extra anti–diffusivity of this underlying *enhanced* scheme.

5. Results

In this section, the performance of the proposed combined BFECC algorithm is investigated in three test–cases; in the first set of tests, different

BFECC algorithms are applied to the *low–order* and *enhanced* underlying schemes and employed for the one–dimensional advection of both a non–smooth square–wave and a smooth sine–wave. The second test–case is the solid–body rotation of a notched cylinder, smooth hump and a cone [33], which is a well-established benchmark in this context. Here, the versatility of the proposed BFECC methodology is further analyzed by its application to the unconditionally stable (semi–Lagrangian) CIR scheme [29, 27] (see Appendix A) and the SUPG scheme (with the cross–wind stabilization [12]). In the last test–case, the oblique in–flow of a scalar field is simulated in order to study the effect of the combined BFECC algorithm on the cross–stream and the stream–wise diffusion of the solver.

In the following, all the simulations are performed using the forward Euler scheme for discretizing the governing equations in time. Moreover, for the application of the combined BFECC algorithm, the switch between the algorithms is done according to the threshold of $\alpha_{th} = 0.9$ and 0.95 for the Eulerian schemes and the semi–Lagrangian approach, respectively. For these test-cases, L^1– and L^2–norm of the error are approximated as [28, 31]

$$E_1 = \sum_{i \in \mathcal{N}} m_i \left| u(\mathbf{x}_i) - u_i \right|, \tag{55}$$

and

$$E_2 = \sqrt{\sum_{i \in \mathcal{N}} m_i \left[u(\mathbf{x}_i) - u_i \right]^2}, \tag{56}$$

respectively.

5.1. One Dimensional Advection

The test–cases addressed in this section consist of the one–dimensional[1] advection of a square–wave with an initially discontinuous field and a sine–wave, which corresponds to an initially smooth field; the associated initial conditions are defined, respectively, by

$$u_0(x) = \begin{cases} 1 & \textbf{if} \quad 0.1 \geq x \leq 0.31 \\ 0 & \textbf{else} \end{cases} \tag{57}$$

[1]It must be highlighted that the results are obtained on a two–dimensional mesh as shown in Fig. 1.

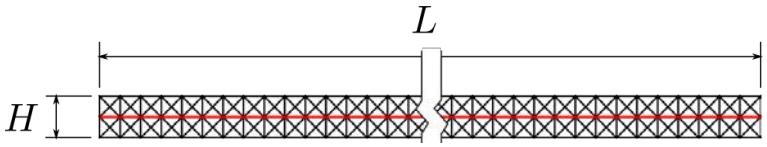

Figure 1: Semi–1D mesh for advection of the square wave. Results are presented for the nodes lie on the center–line marked by a red solid line.

and

$$u_0(x) = \begin{cases} \frac{1}{2} - \frac{1}{2}\sin\left(10(x-0.1) + \frac{\pi}{2}\right) & \textbf{if} \quad 0.1 \geq x \leq 0.3 \\ 0 & \textbf{else} \end{cases} \tag{58}$$

The former case is a well–established test for the assessment of the performance of the numerical methods [19, 37] in the presence of a severe non-smoothness in the field. On the other hand, the sine–wave test is designed to reveal the ability of the numerical approach to minimize the unwanted side–effects of the compensatory anti–diffusivity. These test–cases are simulated on the semi–1D mesh shown in Fig. 1 with $L = 1$, $H = 0.02$, and $\mathbf{v} = \mathbf{e}_x$, where $\mathbf{e}_x$ is the unit vector in the x–direction. The associated mesh–size is calculated as $h = 1/DOF_{cl}$[2], where DOF_{cl} denotes the number of degrees–of–freedom along the center–line of the domain shown in Fig. 1.

5.1.1. Low–order Stabilized Eulerian Scheme

The first scheme to analyze in combination with the proposed limited BFECC algorithm is the stabilized *low–order* scheme described in section 2.3. Here, the time–step is set to $dt = 0.004$ and $DOF_{cl} = 100$, which give $CFL = dt|\mathbf{v}|/h = 0.4$. The final ($t = 0.5$) distribution of u along the center–line is illustrated for the non–smooth and the smooth wave in Figs. 2 and 3, respectively. As expected, without the application of an error compensation algorithm, the stabilized *low–order* scheme is too diffusive and consequently, leads to an undesirable solution in both cases; making a compensation for the extra diffusivity, the conventional BFECC algorithm dramatically improves the result. By further adding an extra anti–diffusion to the solution of the advection equation, the modified BFECC scheme provides a better result than the conventional BFECC algorithm in the non–smooth case. However,

[2]It must be noted that due to the symmetry of the mesh (shown in Fig. 1), the effective mesh–size is smaller than $1/DOF_{cl}$.

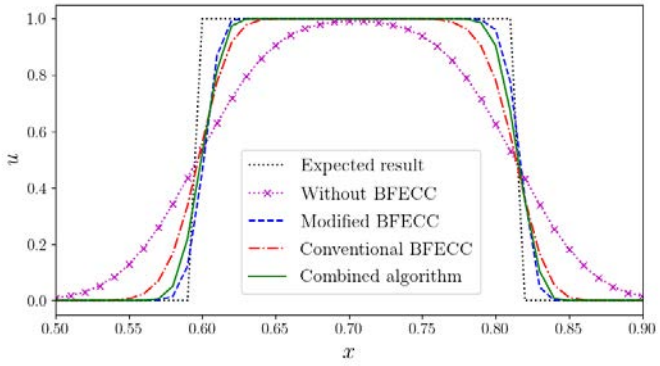

Figure 2: Advection of a square–wave using different BFECC algorithms combined with the stabilized *low–order* underlying scheme.

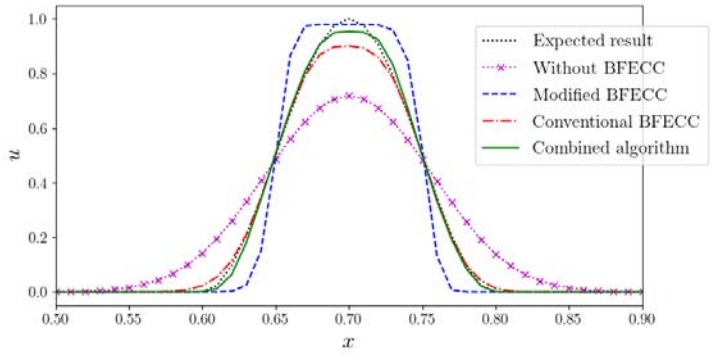

Figure 3: Advection of a sine–wave with $dt = 0.004$ and $\theta = 0$.

Table 1: Error associated with the advection of a square–wave using different BFECC algorithms combined with the stabilized *low–order* underlying scheme.

Algorithm	E_1	E_2
Without BFECC	1.301×10^{-3}	1.951×10^{-2}
Modified BFECC	2.995×10^{-4}	1.036×10^{-2}
Conventional BFECC	5.497×10^{-4}	1.260×10^{-2}
Combined algorithm	3.726×10^{-4}	1.076×10^{-2}

Table 2: Error associated with the advection of a sine–wave using different BFECC algorithms combined with the stabilized *low–order* underlying scheme.

Algorithm	E_1	E_2
Without BFECC	7.349×10^{-4}	1.117×10^{-2}
Modified BFECC	4.127×10^{-4}	8.293×10^{-3}
Conventional BFECC	1.015×10^{-4}	2.370×10^{-3}
Combined algorithm	6.947×10^{-5}	1.388×10^{-3}

this extra anti-diffusion disturbs the solution for the smooth case. On the other hand, the combined BFECC algorithm although increases the computational cost by 30%, leads to a result that closely follows that of the modified BFECC algorithm in the non-smooth case while does not disturb the solution in the smooth case. Figure 3 clearly shows the great advantage of using the combined BFECC algorithm for the advection of the smooth–wave; comparing to the conventional BFECC algorithm, the proposed BFECC algorithm provides a more accurate solution in the smooth case. A more critical assessment of the performance of different BFECC algorithms is possible by comparing L^1– and L^2–norm of the associated errors as presented in Tables 1 and 2.

So far, the results were reported for a single mesh with $DOF_{cl} = 100$. Here, the sine–wave test–case is further solved for $DOF_{cl} = 50$, 200, and 400, in order to assess the effect of different BFECC algorithms on the convergence of the solver, which is measured by the so–called "experimental order of convergence (EOC)" defined as [33, 38]

$$EOC = \frac{\log(\frac{E(h_2)}{E(h_1)})}{\log(\frac{h_2}{h_1})}, \tag{59}$$

where $E(h)$ is the error associated with mesh–size h. The EOC values are presented for the stabilized *low–order* scheme with and without the proposed

Table 3: Convergence of the results of the advection of a sine–wave obtained using the stabilized *low–order* underlying scheme with and without the proposed combined BFECC algorithm for $dt = 0.001$.

	Without BFECC				**Combined BFECC algorithm**			
Mesh–size	E_1	EOC_1	E_2	EOC_2	E_1	EOC_1	E_2	EOC_2
1/50	0.0016		0.022		0.0014		0.021	
1/100	0.0011	0.55	0.016	0.46	0.00062	1.16	0.010	1.06
1/200	0.00062	0.83	0.0096	0.74	0.00013	2.22	0.0023	2.17
1/400	0.00024	1.40	0.0038	1.32	0.000019	2.80	0.00035	2.72

combined BFECC algorithm in Table 3. These set of data are obtained by setting the time–step to $dt = 0.001$.

It is clearly observed that in addition to the dramatic decrease in the magnitude of the error, the proposed combined BFECC algorithm improves the mesh–convergence; by applying the proposed algorithm, EOC is almost doubled. In the following, the same tests are administered for the alternative underlying scheme discussed in the present work, *i.e.* the *enhanced* method.

5.1.2. Enhanced Scheme

Following the results presented for the *low–order* scheme, in this section, different BFECC algorithms are combined with the *enhanced* scheme (described in section 4) and applied to the same one–dimensional test–cases. Considering that this enhanced underlying scheme is more sensitive to the time–step than the *low–order* scheme, here, $dt = 0.001$ is set for $DOF_{cl} = 100$. Results are presented in Figs. 4 and 5 for the non–smooth and the smooth test–cases, respectively.

Benefiting from limited corrective terms, it is expected that the *enhanced* scheme provides more accurate solutions without violating the positivity as well as the maximum principle; it is clearly seen by comparing the results presented in Fig. 4 with those presented in Figs. 2 for the non–smooth case. Nonetheless, for the smooth case, the application of the proposed combined BFECC algorithm to the stabilized *low–order* scheme provides a comparably accurate result (see Figs. 3 and 5).

Here, one should highlight the potential of the BFECC algorithm to adjust the extra anti–diffusivity together with its capability to compensate for the extra diffusivity of the schemes developed for the convection–dominated problems; it is evident in Fig. 5 that by applying either the conventional or the proposed combined BFECC algorithm, the anti–diffusivity of the *enhance*

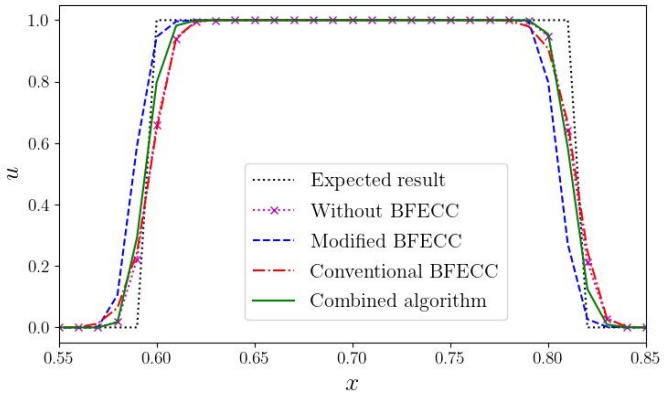

Figure 4: Advection of a square–wave with improved stabilized scheme, $dt = 0.001$, and $\theta = 0$.

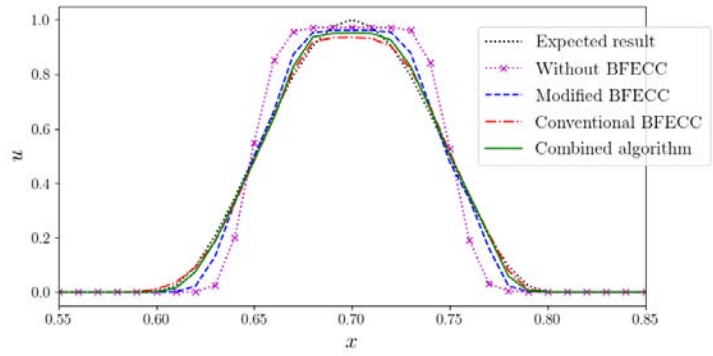

Figure 5: Advection of a sine–wave with improved stabilized scheme, $dt = 0.001$, and $\theta = 0$.

Table 4: Error associated with the advection of a square–wave using different BFECC algorithms combined with the *enhanced* underlying scheme.

Algorithm	E_1	E_2
Without BFECC	2.729×10^{-4}	8.750×10^{-3}
Modified BFECC	3.502×10^{-4}	1.378×10^{-2}
Conventional BFECC	3.106×10^{-4}	9.223×10^{-3}
Combined algorithm	2.405×10^{-4}	8.598×10^{-3}

Table 5: Error associated with the advection of a sine–wave using different BFECC algorithms combined with the *enhanced* underlying scheme.

Algorithm	E_1	E_2
Without BFECC	3.658×10^{-4}	7.153×10^{-3}
Modified BFECC	1.390×10^{-4}	2.769×10^{-3}
Conventional BFECC	7.812×10^{-5}	1.536×10^{-3}
Combined algorithm	7.587×10^{-5}	1.446×10^{-3}

scheme is finely adjusted minimizing the associated error in the smooth case. In Tables 4 and 5, L^1– and L^2–norm of the error are presented for different approaches developed based on the *enhanced* scheme and applied to the one–dimensional advection of the square–wave and the sine–wave, respectively.

Similar to what is observed for the *low–order* scheme, the proposed combined BFECC algorithm shows an overall outperformance in the non–smooth and smooth cases; it improves the method in the non–smooth case while provides a slightly more accurate result than the conventional BFECC algorithm in the smooth case.

5.2. Solid–Body Rotation

In this section, the counter–clockwise rotation of a slotted disk,

$$u_0(x,y) = \begin{cases} 1 & \textbf{if} \begin{cases} \sqrt{(x-0.5)^2+(y-0.75)^2} \leq 0.15 \quad \textbf{and} \\ |x-0.5| \geq 0.025 \quad \textbf{or} \quad y \geq 0.85 \end{cases} \\ 0 & \textbf{else} \end{cases} \tag{60}$$

a non–smooth (sharp) cone,

$$u_0(x,y) = \begin{cases} 1 - \frac{\sqrt{(x-0.5)^2+(y-0.25)^2}}{0.15} & \textbf{if} \quad \sqrt{(x-0.5)^2+(y-0.25)^2} \leq 0.15 \\ 0 & \textbf{else} \end{cases} \tag{61}$$

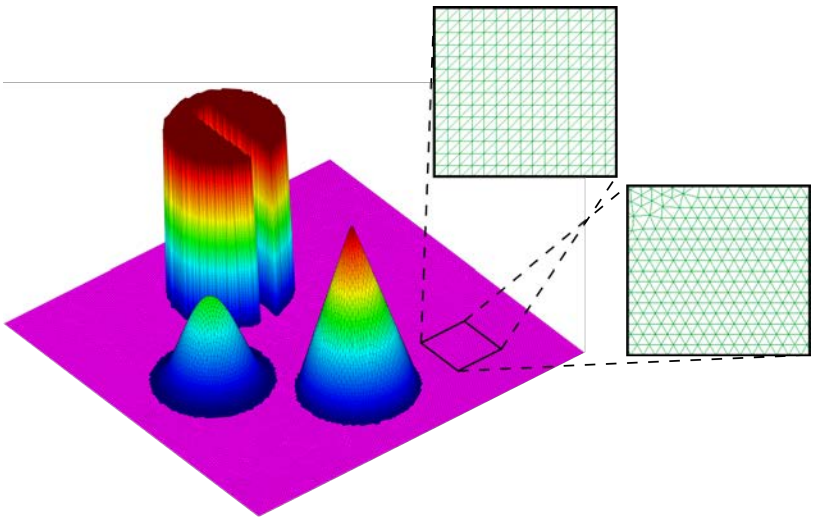

Figure 6: Initial configuration of the solid–body rotation test–case. Structured and unstructured meshes are shown.

and a smooth hump,

$$u_0(x,y) = \begin{cases} \frac{1}{4} + \frac{1}{4}\cos\left(\frac{\pi\sqrt{(x-0.25)^2+(y-0.5)^2}}{0.15}\right) & \textbf{if} \quad \sqrt{(x-0.25)^2+(y-0.5)^2} \leq 0.15 \\ 0 & \textbf{else} \end{cases} \tag{62}$$

is simulated with $\mathbf{v}(x,y) = (0.5-y, x-0.5)$, in a square 1×1–domain centered at $(x,y) = (0.5, 0.5)$. The initial condition, u_0, is shown in Fig. 6. As first proposed in [33], this test has become a benchmark for the assessment of the performance of the numerical methods developed for convection–dominated problems [28, 38, 39, 40]. Here, the time–step is set to $dt = 0.001$ unless otherwise mentioned, and the computational domain is discretized using both a structured mesh with 129^2 nodes and an unstructured mesh with the average mesh–size of $h = 1/128$ (see Fig. 6). In this section, all the results are presented after one complete rotation at $t = 6.28$.

Figures 7 shows the results of the stabilized *low–order* and *enhanced* schemes with and without the proposed combined BFECC algorithm that are obtained using the structured mesh. Here, the result of the CIR underlying scheme is also included for the sake of its comparison with the *low–order* scheme. Without the BFECC algorithm, the *low–order* scheme (as well as the CIR scheme) brings about a highly diffused u–field and therefore, the

corresponding results are not shown here. It is clearly seen that all the numerical schemes abide with the positivity and the maximum principle by keeping $0 \geq u \leq 1.0$. For a better assessment of the performance of the acquired numerical schemes, the results obtained using the *enhanced* scheme with and without the proposed combined BFECC algorithm on the unstructured mesh are also presented in Fig. 8. The slightly more accurate solution on the unstructured mesh is due to its slightly larger number of mesh–nodes comparing to the structured mesh.

In Figs. 9 and 10, the same set of results are presented as the contours of u at $t = 6.28$. The L^1–norm of the corresponding errors is also reported in these figures. It is observable that, in an overall view, the semi–Lagrangian approach slightly outperforms the *low–order* Eulerian scheme while by applying these two schemes along with the BFECC algorithm, the symmetry of the slotted disk is disturbed after one complete rotation. In case of the *enhanced* scheme, the application of the proposed BFECC algorithm yields a considerable improvement in the advection of the slotted-disk.

In order to bring the effect of the proposed combined BFECC algorithm into sharp focus, the result of the *enhanced* scheme with and without the application of this algorithm are shown in Figs. 11 and 12 along different cut–lines passing through the domain. These figures correspond to the unstructured mesh. In addition to the better representation of the slotted disk, the proposed BFECC algorithm remarkably improves the results for the advection of the smooth hump and the linear body of the cone, which is brought about by its capability to adjust the (anti–)diffusivity of the numerical schemes. In other words, using the presented *enhanced* scheme, due to an excessive anti–diffusivity, the result is subject to a difficulty denoted as "*terracing*" [21] that is majorly cured by utilizing the BFECC algorithm.

At the end of this section, it is worth to briefly investigate the performance of the proposed BFECC algorithm in combination with the SUPG-CWS scheme. Results are presented in Figs. 13 and 14 as the surface of $z = u(x, y)$ and contours of $u(x, y)$, respectively. Upon the application of the proposed BFECC algorithm, the result of the SUPG-CWS scheme is dramatically improved. Therefore, the proposed BFECC can also be considered as a viable means to improve the class of SUPG–like methods.

5.3. Oblique Inflow

This section aims at the investigation of the effect of the proposed BFECC algorithm on reducing the stream–wise as well as the cross-stream diffusion

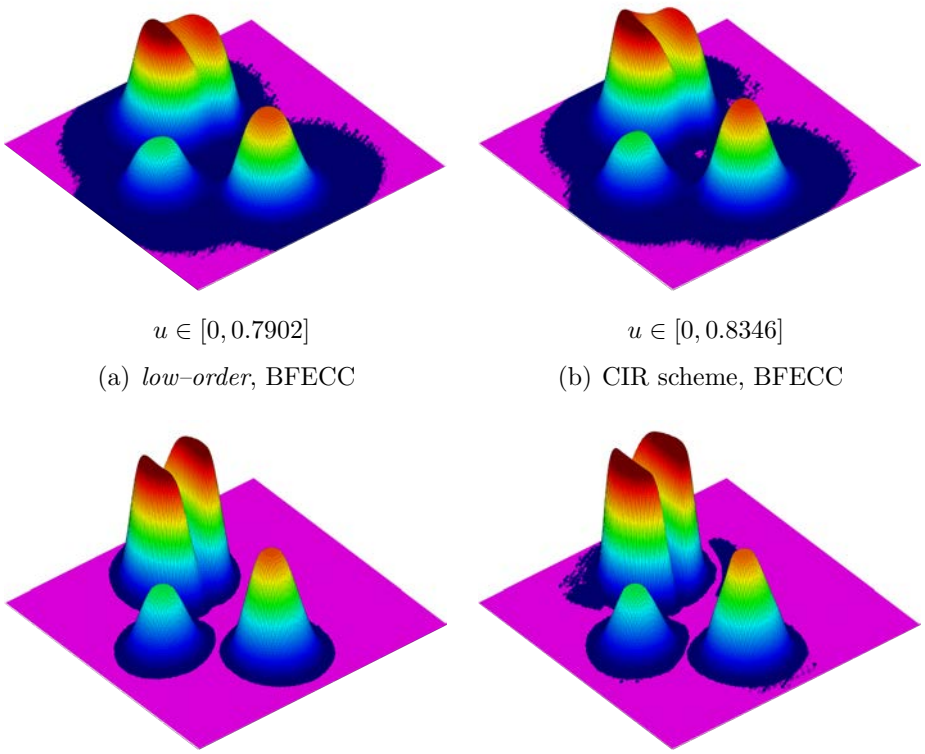

$u \in [0, 0.7902]$

(a) *low–order*, BFECC

$u \in [0, 0.8346]$

(b) CIR scheme, BFECC

$u \in [0, 0.9914]$

(c) *enhanced* scheme, no BFECC

$u \in [0, 1.0]$

(d) *enhanced* scheme, BFECC

Figure 7: Solid–body rotation at $t = 6.28$. Results are obtained using different schemes on the structured mesh and presented as surface $z = u(x, y)$; (a) and (b) correspond to the *low–order* Eulerian scheme and the semi–Lagrangian underlying scheme with the application of the proposed combined BFECC algorithm, respectively. The results of the *enhanced* scheme without and with the combined BFECC algorithm are shown in (c) and (d), respectively.

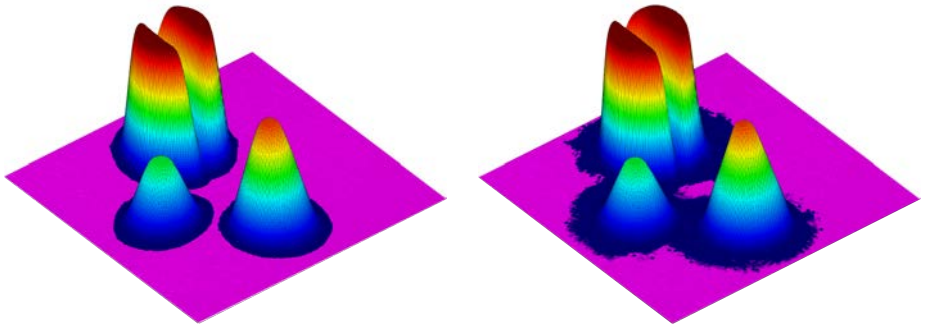

$u \in [0, 1.0001]$ $u \in [0, 0.9995]$

(a) Without BFECC (b) Combined BFECC

Figure 8: Solid–body rotation at $t = 6.28$. Results are obtained for the unstructured mesh and presented as surface $z = u(x, y)$; (a) and (b) correspond to the *enhanced* underlying scheme without and with the combined BFECC algorithm, respectively.

during the transport of a sharp layer. To this end, Eq. (2) is solved in a square 1×1–domain with constant velocity $\mathbf{v} = -0.8\mathbf{e}_x - 0.6\mathbf{e}_y$, $dt = 0.001$, and Dirichlet boundary condition

$$u_D(x, y) = \begin{cases} 1 & \textbf{if} \quad x \geq 0.8 \, \textbf{and} \, y = 1 \\ 0 & \textbf{else} \end{cases} \tag{63}$$

imposed on the inflow ($x = 1$ and $y = 1$) boundaries of the domain. Here, the time–step is set to $dt = 0.001$ and the results are obtained using the *enhanced* scheme with and without the proposed combined BFECC algorithm on the 129^2 structured mesh as shown in Fig. 15.

Figures 16 and 17 present the results along a perpendicular to the stream and a parallel to the stream cut–line, respectively. It is clearly observable that the proposed combined BFECC algorithm effectively reduces the cross–stream diffusivity while it improves the capturing of the theoretically sharp stream–wise front. The L^1–norm of the error is $E_1 = 0.0203$ for the *enhanced* scheme without the BFECC algorithm. Upon the application of the proposed combined BFECC algorithm, the error is reduced to $E_1 = 0.0158$.

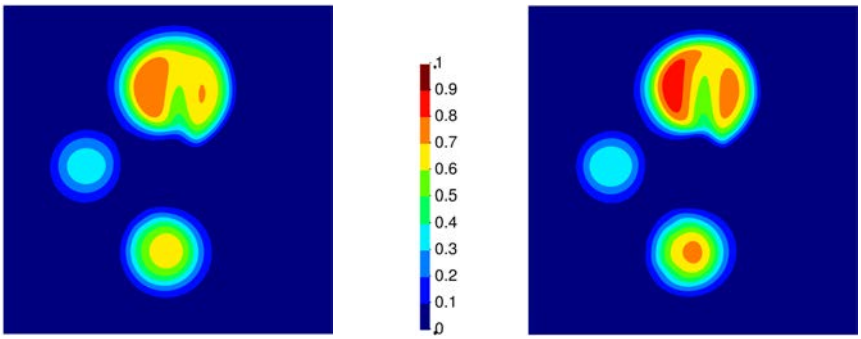

$E_1 = 5.22 \times 10^{-2}$ u $E_1 = 4.80 \times 10^{-2}$

(a) *low–order*, BFECC (c) CIR scheme, BFECC

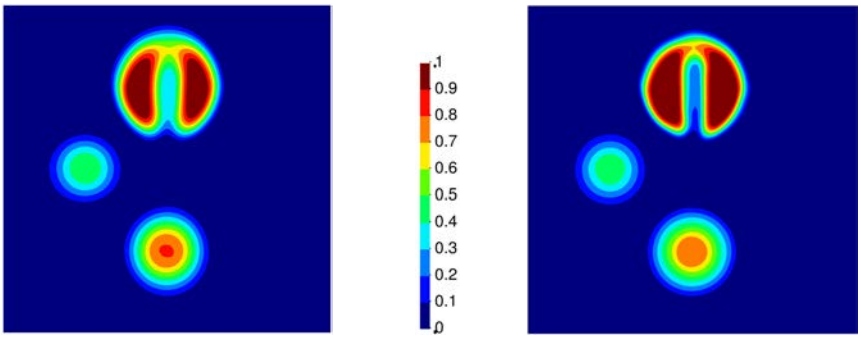

$E_1 = 2.80 \times 10^{-2}$ u $E_1 = 1.97 \times 10^{-2}$

(d) *enhanced* scheme, no BFECC (f) *enhanced* scheme, BFECC

Figure 9: Solid–body rotation at $t = 6.28$. Results are obtained using different schemes on the structured mesh and presented as contours of $u(x, y)$; (a) and (b) correspond to the *low–order* Eulerian scheme and the semi–Lagrangian approach with the underlying scheme of the proposed combined BFECC algorithm, respectively. The results of the *enhanced* scheme without and with the combined BFECC algorithm are shown in (c) and (d), respectively.

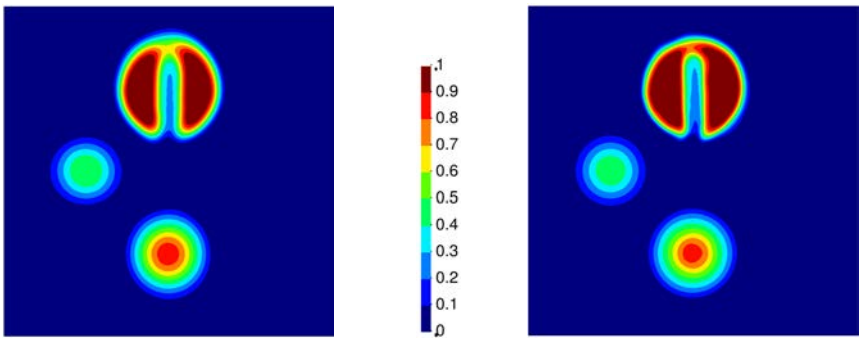

$E_1 = 2.33 \times 10^{-2}$ u $E_1 = 1.78 \times 10^{-2}$

(a) Without BFECC (c) Combined BFECC

Figure 10: Solid–body rotation at $t = 6.28$. Results are obtained for the unstructured mesh and presented as contours of $u(x, y)$; (a) and (b) correspond to the *enhanced* underlying scheme without and with the combined BFECC algorithm, respectively.

6. Conclusion

This work constituted a methodology to substantially improve the accuracy of the numerical solution of the advection equation by adjusting the diffusivity of the numerical schemes; this was achieved by enhancing the back and forth error compensation and correction (BFECC) algorithm. It was shown how a gradient–based limiter can be used to retain the monotonicity of the numerical method obtained as a combination of the BFECC algorithm and an originally monotonicity–preserving scheme. The proposed algorithm was combined with different stabilized schemes and the resulting solvers were applied to a series of advection test–cases. It was revealed that while the proposed algorithm possesses the capability of the conventional BFECC algorithm for adjusting both the extra diffusivity and anti–diffusivity of the underlying numerical scheme, it provides a considerable improvement to the result in the vicinity of the local extrema. In addition to a strong reduction in the error, it was proved that the proposed algorithm substantially increases the rate of mesh–convergence; it was almost doubled upon the application of the presented BFECC algorithm to a *low–order* scheme. In all cases, the compliance of the results with the positivity and maximum principle was observed.

All the results presented in this work were obtained utilizing an explicit

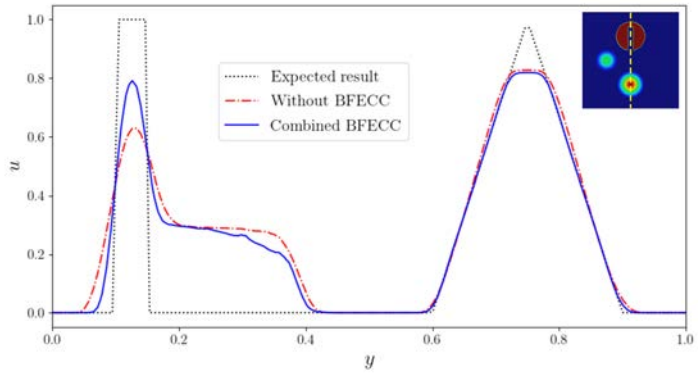

(a) $x = 0.5$

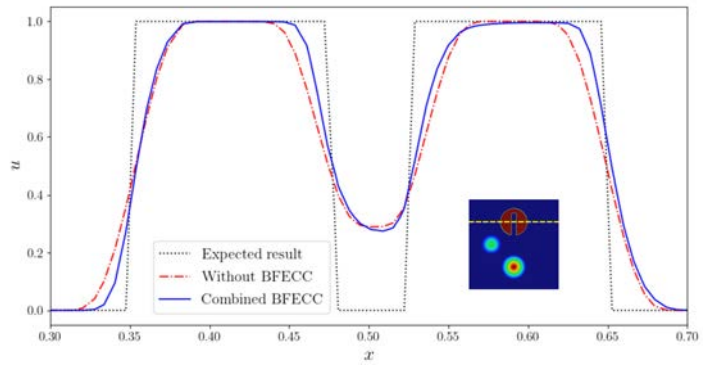

(b) $y = 0.75$

Figure 11: Solid–body rotation at $t = 6.28$. Results are obtained using the *enhanced* underlying scheme on the unstructured mesh and presented for the nodes lie on (a) $x = 0.5$ and (b) $y = 0.75$ cut–lines.

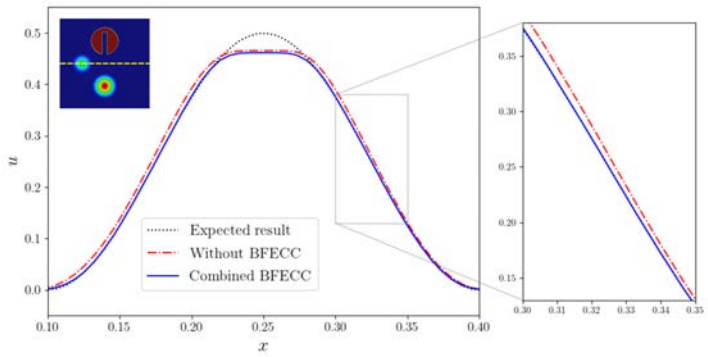

(a) $y = 0.5$

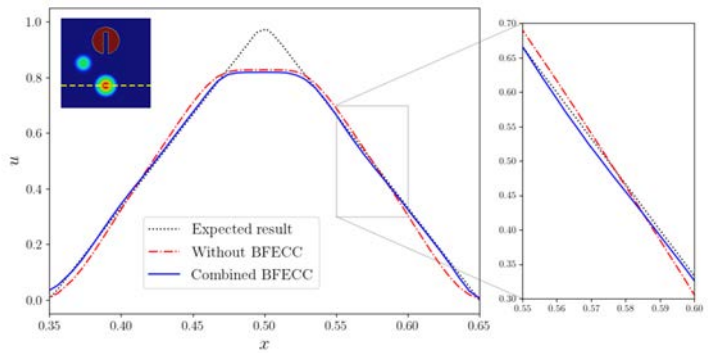

(b) $y = 0.25$

Figure 12: Solid–body rotation at $t = 6.28$. Results are obtained using the *enhanced* underlying scheme on the unstructured mesh and presented for the nodes lie on (a) $x = 0.5$ and (b) $y = 0.75$ cut–lines.

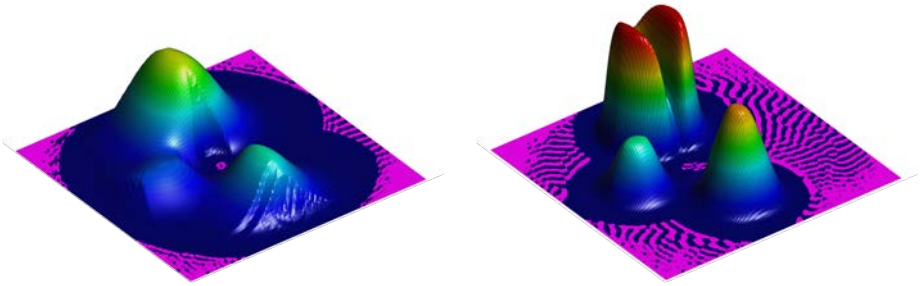

$u \in [-6.6 \times 10^{-6}, 0.6267]$ $u \in [-1.1 \times 10^{-5}, 0.9307]$

(a) Without BFECC (b) Combined BFECC

Figure 13: Solid–body rotation at $t = 6.28$. Results are obtained for the structured mesh and presented as surface $z = u(x, y)$; (a) and (b) correspond to the SUPG-CWS underlying scheme without and with the combined BFECC algorithm, respectively.

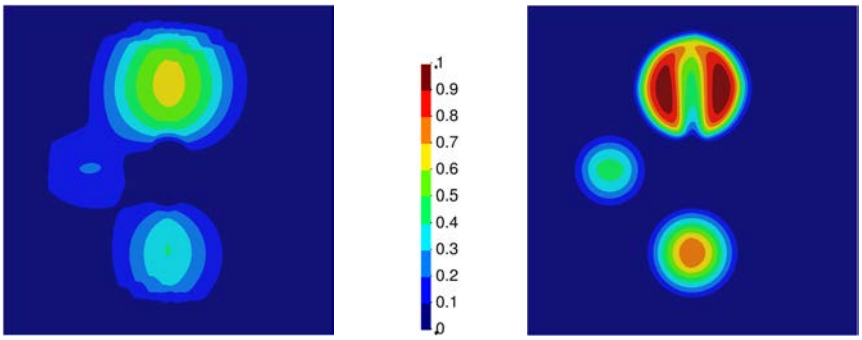

$E_1 = 8.22 \times 10^{-2}$ u $E_1 = 2.94 \times 10^{-2}$

(a) Without BFECC (c) Combined BFECC

Figure 14: Solid–body rotation at $t = 6.28$. Results are obtained for the structured mesh and presented as contours of $u(x, y)$; (a) and (b) correspond to the SUPG-CWS underlying scheme without and with the combined BFECC algorithm, respectively.

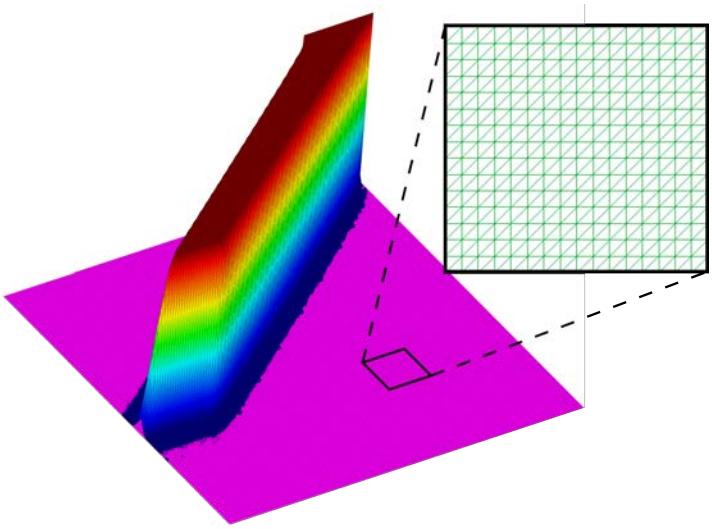

Figure 15: Oblique inflow at $t = 1$, simulated using the *enhanced* underlying scheme with the proposed combined BFECC algorithm. The result is presented as surface $z = u(x, y)$.

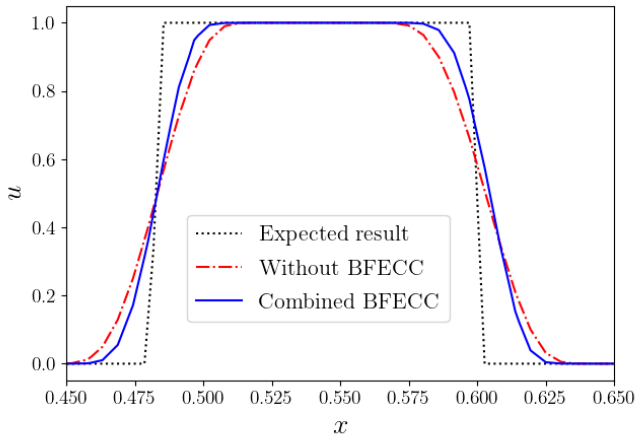

Figure 16: Oblique inflow at $t = 1$, simulated using the *enhanced* underlying scheme with and without the proposed combined BFECC algorithm. Results are presented along a cut–line perpendicular to the stream ($y = 1 - 4x/3$).

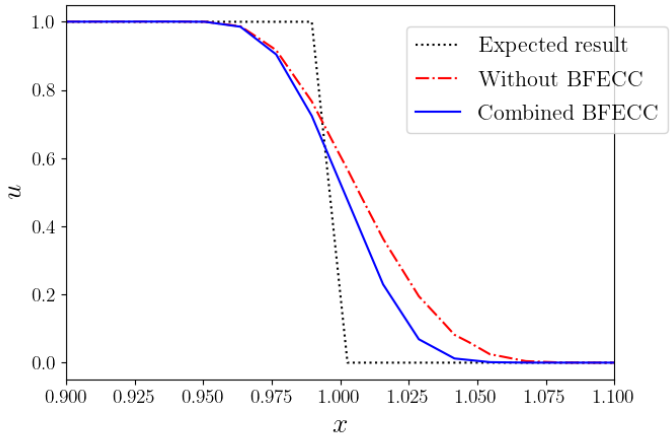

Figure 17: Oblique inflow at $t = 1$, simulated using the *enhanced* underlying scheme with the BFECC algorithm. Results are presented along a cut–line parallel to the stream ($y = 0.325 + 3x/4$).

scheme (forward Euler discretization in time). Considering that the coefficient of unknowns incorporated only a combination of the consistent and the lumped mass matrix, the associated computational effort was rather low. Moreover, at each time–step, the proposed algorithm requires a fixed number of (four) sub–steps to estimate the error and do the correction. Therefore, in case the contribution of the consistent mass matrix is neglected, a fully explicit method would be obtained. Taking into account that by applying the proposed BFECC algorithm to the presented enhanced Eulerian scheme, the resulting error in the benchmark problem was comparable to that of the state–of–the–art numerical methods, this work provided an alternative to the nonlinear approaches developed to address convection–dominated transport problems. It must be noted that the application of the proposed algorithm is not limited to the underlying schemes presented in this work; in a wider view point, this algorithm can also be customized to be applied to numerical techniques other than the finite element method.

7. Acknowledgment

This work was performed within the framework of AMADEUS project (”Advanced Multi-scAle moDEling of coupled mass transport for improv-

ing water management in fUel cellS", reference number PGC2018-101655-B-I00) supported by the *Ministerio de Ciencia, Innovacion e Universidades* of Spain. The authors also acknowledge financial support of the mentioned Ministry via the "Severo Ochoa Programme" for Centres of Excellence in R&D (referece: CEX2018-000797-S) given to the International Centre for Numerical Methods in Engineering (CIMNE).

Conflict of interest

The authors declare that they have no conflict of interest.

Appendix A. Semi–Lagrangian Approach

The unconditionally stable CIR scheme [41, 42, 29, 27], which is named after Courant, Isaacson, and Rees [43], depicts the constructive idea of the semi–Lagrangian approach for solving hyperbolic differential equations; the solution at $(\mathbf{x}, t)$ is obtained by following the corresponding characteristic line to reach $(\mathbf{x}', t - \Delta t)$ in the spatial–temporal space [44].

For Eq. (2) the CIR scheme reads

$$u(\mathbf{x}, t) = u(\mathbf{x} - \Delta t \mathbf{v}, t - \Delta t). \tag{A.1}$$

This scheme is temporally and spatially first–order [27]; nevertheless, it can be further enhanced to obtain a second–order solver [42] by acquiring non-linear interpolation schemes, which is beyond the scope of the present work. It should be noted that this scheme relies on the spatial search within the computational domain and consequently, in cases that the characteristic line points to the outside of the domain, the implementation of the solution algorithm is not straightforward. This issue specifically occurs in the vicinity of the inlet and curved boundaries.

Appendix B. Comment on Enhanced Scheme Implementation

The *enhanced* scheme is based on the implementation of Eq. (49) that by using the forward Euler time discretization, reads

$$\frac{1}{dt}\mathbb{M}\mathbf{U}_{n+1} = \left(\frac{1}{dt}\mathbb{M} + \mathbb{C} + \mathbb{D}\right)\mathbf{U}_n - \mathbf{F}_n = 0, \tag{B.1}$$

where the elemental contributions are assembled as

$$\mathbb{M} = \mathcal{A}_{e\in\mathcal{E}} \left(\alpha^e \mathbb{M}_C^e + (1-\alpha^e)\mathbb{M}_L^e\right), \tag{B.2}$$

$$\mathbb{D} = \mathcal{A}_{e\in\mathcal{E}} \left(\nu^e \left[\mathbb{M}_L^e - \mathbb{M}_C^e\right]\right), \tag{B.3}$$

and

$$\mathbf{F} = \mathcal{A}_{e\in\mathcal{E}} \left(\alpha^e \hat{\mathbf{D}}^e\right). \tag{B.4}$$

In combination of the BFECC algorithm, Eq. B.1 is solved in forward and backward convection steps, *i.e.* first, second, and fourth step of the algorithms described in this paper.

References

[1] D. Kuzmin, S. Turek, High-resolution FEM-TVD schemes based on a fully multidimensional flux limiter, Journal of Computational Physics 198 (2004) 131–158. URL: http://www.sciencedirect.com/science/article/pii/S0021999104000221. doi:10.1016/j.jcp.2004.01.015.

[2] V. Le Chenadec, H. Pitsch, A monotonicity preserving conservative sharp interface flow solver for high density ratio two-phase flows, Journal of Computational Physics 249 (2013) 185–203. URL: http://www.sciencedirect.com/science/article/pii/S0021999113002921. doi:10.1016/j.jcp.2013.04.027.

[3] C.-T. Ha, J. H. Lee, A modified monotonicity-preserving high-order scheme with application to computation of multi-phase flows, Computers & Fluids 197 (2020) 104345. URL: https://www.sciencedirect.com/science/article/pii/S0045793019303044. doi:10.1016/j.compfluid.2019.104345.

[4] V. S. Borisov, On Discrete Maximum Principles for Linear Equation Systems and Monotonicity of Difference Schemes, SIAM Journal on Matrix Analysis and Applications 24 (2003) 1110–1135. URL: https://epubs-siam-org.recursos.biblioteca.upc.edu/doi/abs/10.1137/S0895479802409687. doi:10.1137/S0895479802409687, publisher: Society for Industrial and Applied Mathematics.

[5] J.-L. Guermond, M. Nazarov, B. Popov, Y. Yang, A Second-Order Maximum Principle Preserving Lagrange Finite Element Technique for Nonlinear Scalar Conservation Equations, SIAM Journal on Numerical Analysis 52 (2014) 2163–2182. URL: https://epubs.siam.org/doi/10.1137/130950240. doi:10.1137/130950240, publisher: Society for Industrial and Applied Mathematics.

[6] R. Codina, Comparison of some finite element methods for solving the diffusion-convection-reaction equation, Computer Methods in Applied Mechanics and Engineering 156 (1998) 185–210. URL: http://www.sciencedirect.com/science/article/pii/S0045782597002065. doi:10.1016/S0045-7825(97)00206-5.

[7] V. John, E. Schmeyer, Finite element methods for time-dependent convection–diffusion–reaction equations with small diffusion, Computer Methods in Applied Mechanics and Engineering 198 (2008) 475–494. URL: http://www.sciencedirect.com/science/article/pii/S0045782508003150. doi:10.1016/j.cma.2008.08.016.

[8] S. Badia, A. Hierro, On Monotonicity-Preserving Stabilized Finite Element Approximations of Transport Problems, SIAM Journal on Scientific Computing 36 (2014) A2673–A2697. URL: https://epubs.siam.org/doi/10.1137/130927206. doi:10.1137/130927206, publisher: Society for Industrial and Applied Mathematics.

[9] D. Kuzmin, Monolithic convex limiting for continuous finite element discretizations of hyperbolic conservation laws, Computer Methods in Applied Mechanics and Engineering 361 (2020) 112804. URL: http://www.sciencedirect.com/science/article/pii/S0045782519306966. doi:10.1016/j.cma.2019.112804.

[10] J. Bonilla, S. Badia, Monotonicity-preserving finite element schemes with adaptive mesh refinement for hyperbolic problems, Journal of Computational Physics 416 (2020) 109522. URL: https://www.sciencedirect.com/science/article/pii/S0021999120302965. doi:10.1016/j.jcp.2020.109522.

[11] A. N. Brooks, T. J. R. Hughes, Streamline upwind/Petrov-Galerkin formulations for convection dominated flows with particular emphasis on the incompressible Navier-Stokes equations, Computer

655 Methods in Applied Mechanics and Engineering 32 (1982) 199–
656 259. URL: https://www.sciencedirect.com/science/article/pii/
657 0045782582900718. doi:10.1016/0045-7825(82)90071-8.

658 [12] R. Codina, A discontinuity-capturing crosswind-dissipation for the
659 finite element solution of the convection-diffusion equation, Com-
660 puter Methods in Applied Mechanics and Engineering 110 (1993) 325–
661 342. URL: http://www.sciencedirect.com/science/article/pii/
662 004578259390213H. doi:10.1016/0045-7825(93)90213-H.

663 [13] E. Burman, A. Ern, Nonlinear diffusion and discrete maximum principle
664 for stabilized Galerkin approximations of the convection–diffusion-
665 reaction equation, Computer Methods in Applied Mechanics
666 and Engineering 191 (2002) 3833–3855. URL: https://www.
667 sciencedirect.com/science/article/pii/S0045782502003183.
668 doi:10.1016/S0045-7825(02)00318-3.

669 [14] V. John, P. Knobloch, On spurious oscillations at layers diminishing
670 (SOLD) methods for convection–diffusion equations: Part I – A re-
671 view, Computer Methods in Applied Mechanics and Engineering 196
672 (2007) 2197–2215. URL: https://www.sciencedirect.com/science/
673 article/pii/S0045782506003926. doi:10.1016/j.cma.2006.11.013.

674 [15] V. John, P. Knobloch, On spurious oscillations at lay-
675 ers diminishing (SOLD) methods for convection–diffusion equa-
676 tions: Part II – Analysis for P1 and Q1 finite elements,
677 Computer Methods in Applied Mechanics and Engineering 197
678 (2008) 1997–2014. URL: https://www.sciencedirect.com/science/
679 article/pii/S0045782508000182. doi:10.1016/j.cma.2007.12.019.

680 [16] E. Burman, On nonlinear artificial viscosity, discrete maxi-
681 mum principle and hyperbolic conservation laws, BIT Numerical
682 Mathematics 47 (2007) 715–733. URL: https://doi.org/10.1007/
683 s10543-007-0147-7. doi:10.1007/s10543-007-0147-7.

684 [17] J.-L. Guermond, M. Nazarov, A maximum-principle preserving C0
685 finite element method for scalar conservation equations, Computer
686 Methods in Applied Mechanics and Engineering 272 (2014) 198–
687 213. URL: http://www.sciencedirect.com/science/article/pii/
688 S0045782514000024. doi:10.1016/j.cma.2013.12.015.

[18] S. Badia, J. Bonilla, Monotonicity-preserving finite element schemes based on differentiable nonlinear stabilization, Computer Methods in Applied Mechanics and Engineering 313 (2017) 133–158. URL: http://www.sciencedirect.com/science/article/pii/S0045782516306405. doi:10.1016/j.cma.2016.09.035.

[19] D. Kuzmin, S. Turek, Flux Correction Tools for Finite Elements, Journal of Computational Physics 175 (2002) 525–558. URL: http://www.sciencedirect.com/science/article/pii/S0021999101969554. doi:10.1006/jcph.2001.6955.

[20] D. Kuzmin, Algebraic Flux Correction I, in: D. Kuzmin, R. Löhner, S. Turek (Eds.), Flux-Corrected Transport: Principles, Algorithms, and Applications, Scientific Computation, Springer Netherlands, Dordrecht, 2012, pp. 145–192. URL: https://doi.org/10.1007/978-94-007-4038-9_6. doi:10.1007/978-94-007-4038-9_6.

[21] D. Kuzmin, R. Löhner, S. Turek, Flux-corrected transport: principles, algorithms, and applications, Springer, 2012.

[22] G. R. Barrenechea, V. John, P. Knobloch, Analysis of Algebraic Flux Correction Schemes, SIAM Journal on Numerical Analysis 54 (2016) 2427–2451. URL: https://epubs.siam.org/doi/abs/10.1137/15M1018216. doi:10.1137/15M1018216, publisher: Society for Industrial and Applied Mathematics.

[23] G. R. Barrenechea, V. John, P. Knobloch, R. Rankin, A unified analysis of algebraic flux correction schemes for convection–diffusion equations, SeMA Journal 75 (2018) 655–685. URL: https://doi.org/10.1007/s40324-018-0160-6. doi:10.1007/s40324-018-0160-6.

[24] S. Godunov, I. Bohachevsky, Finite difference method for numerical computation of discontinuous solutions of the equations of fluid dynamics, Matematičeskij sbornik 89 (1959) 271–306.

[25] L. Hu, Numerical algorithms based on the back and forth error compensation and correction, Ph.D. thesis, 2014. URL: https://smartech.gatech.edu/handle/1853/54839, accepted: 2016-05-27T13:08:58Z Publisher: Georgia Institute of Technology.

[26] T. F. Dupont, Y. Liu, Back and forth error compensation and correction methods for removing errors induced by uneven gradients of the level set function, Journal of Computational Physics 190 (2003) 311–324. Publisher: Elsevier.

[27] A. Selle, R. Fedkiw, B. Kim, Y. Liu, J. Rossignac, An Unconditionally Stable MacCormack Method, Journal of Scientific Computing 35 (2008) 350–371. URL: https://doi.org/10.1007/s10915-007-9166-4. doi:10.1007/s10915-007-9166-4.

[28] D. Kuzmin, Explicit and implicit FEM-FCT algorithms with flux linearization, Journal of Computational Physics 228 (2009) 2517–2534. URL: http://www.sciencedirect.com/science/article/pii/S0021999108006475. doi:10.1016/j.jcp.2008.12.011.

[29] T. F. Dupont, Y. Liu, Back and forth error compensation and correction methods for semi-Lagrangian schemes with application to level set interface computations, Mathematics of Computation (2007) 647–668. Publisher: JSTOR.

[30] L. Hu, Y. Li, Y. Liu, A limiting strategy for the back and forth error compensation and correction method for solving advection equations, Mathematics of Computation 85 (2016) 1263–1280. URL: https://www.ams.org/mcom/2016-85-299/S0025-5718-2016-03026-4/. doi:10.1090/mcom/3026.

[31] D. Kuzmin, J. N. Shadid, Gradient-based nodal limiters for artificial diffusion operators in finite element schemes for transport equations, International Journal for Numerical Methods in Fluids 84 (2017) 675–695. URL: http://onlinelibrary.wiley.com/doi/abs/10.1002/fld.4365. doi:10.1002/fld.4365, _eprint: https://onlinelibrary.wiley.com/doi/pdf/10.1002/fld.4365.

[32] G. R. Barrenechea, E. Burman, F. Karakatsani, Edge-based nonlinear diffusion for finite element approximations of convection–diffusion equations and its relation to algebraic flux-correction schemes, Numerische Mathematik 135 (2017) 521–545. URL: https://doi.org/10.1007/s00211-016-0808-z. doi:10.1007/s00211-016-0808-z.

[33] R. J. LeVeque, High-Resolution Conservative Algorithms for Advection in Incompressible Flow, SIAM Journal on Numerical Analysis 33 (1996) 627–665. URL: https://epubs-siam-org.recursos.biblioteca.upc.edu/doi/abs/10.1137/0733033. doi:10.1137/0733033, publisher: Society for Industrial and Applied Mathematics.

[34] J. Donea, A. Huerta, Finite element methods for flow problems, John Wiley & Sons, 2003.

[35] D. Kuzmin, S. Basting, J. N. Shadid, Linearity-preserving monotone local projection stabilization schemes for continuous finite elements, Computer Methods in Applied Mechanics and Engineering 322 (2017) 23–41. URL: http://www.sciencedirect.com/science/article/pii/S0045782516302262. doi:10.1016/j.cma.2017.04.030.

[36] V. John, S. Kaya, W. Layton, A two-level variational multiscale method for convection-dominated convection–diffusion equations, Computer Methods in Applied Mechanics and Engineering 195 (2006) 4594–4603. URL: https://www.sciencedirect.com/science/article/pii/S0045782505004457. doi:10.1016/j.cma.2005.10.006.

[37] D. Kuzmin, On the design of general-purpose flux limiters for finite element schemes. I. Scalar convection, Journal of Computational Physics 219 (2006) 513–531. URL: http://www.sciencedirect.com/science/article/pii/S0021999106001902. doi:10.1016/j.jcp.2006.03.034.

[38] C. Lohmann, D. Kuzmin, J. N. Shadid, S. Mabuza, Flux-corrected transport algorithms for continuous Galerkin methods based on high order Bernstein finite elements, Journal of Computational Physics 344 (2017) 151–186. URL: http://www.sciencedirect.com/science/article/pii/S0021999117303388. doi:10.1016/j.jcp.2017.04.059.

[39] J. Bonilla, S. Badia, Maximum-principle preserving space–time isogeometric analysis, Computer Methods in Applied Mechanics and Engineering 354 (2019) 422–440. URL: https://www.sciencedirect.com/science/article/pii/S0045782519303123. doi:10.1016/j.cma.2019.05.042.

[40] D. Kuzmin, M. Quezada de Luna, Subcell flux limiting for high-order Bernstein finite element discretizations of scalar hyperbolic conservation laws, Journal of Computational Physics 411 (2020) 109411. URL: http://www.sciencedirect.com/science/article/pii/S0021999120301856. doi:10.1016/j.jcp.2020.109411.

[41] J. Strain, A Fast Modular Semi-Lagrangian Method for Moving Interfaces, Journal of Computational Physics 161 (2000) 512–536. URL: https://www.sciencedirect.com/science/article/pii/S0021999100965082. doi:10.1006/jcph.2000.6508.

[42] C. Min, F. Gibou, A second order accurate projection method for the incompressible Navier–Stokes equations on non-graded adaptive grids, Journal of Computational Physics 219 (2006) 912–929. URL: https://www.sciencedirect.com/science/article/pii/S0021999106003366. doi:10.1016/j.jcp.2006.07.019.

[43] R. Courant, E. Isaacson, M. Rees, On the solution of nonlinear hyperbolic differential equations by finite differences, Communications on Pure and Applied Mathematics 5 (1952) 243–255. URL: http://onlinelibrary.wiley.com/doi/abs/10.1002/cpa.3160050303. doi:https://doi.org/10.1002/cpa.3160050303, _eprint: https://onlinelibrary.wiley.com/doi/pdf/10.1002/cpa.3160050303.

[44] J. Strain, Semi-Lagrangian Methods for Level Set Equations, Journal of Computational Physics 151 (1999) 498–533. URL: http://www.sciencedirect.com/science/article/pii/S0021999199961946. doi:10.1006/jcph.1999.6194.

Bibliography

[1] M. O. Abu-Al-Saud, S. Popinet, and H. A. Tchelepi. A conservative and well-balanced surface tension model. *Journal of Computational Physics*, 371:896–913, 2018. Publisher: Elsevier.

[2] S. Afkhami, S. Zaleski, and M. Bussmann. A mesh-dependent model for applying dynamic contact angles to VOF simulations. *Journal of Computational Physics*, 228(15):5370–5389, 2009. Publisher: Elsevier.

[3] N. Akhtar and P. Kerkhof. Dynamic behavior of liquid water transport in a tapered channel of a proton exchange membrane fuel cell cathode. *International Journal of Hydrogen Energy*, 36(4):3076–3086, Feb. 2011.

[4] M. Andersson, S. B. Beale, M. Espinoza, Z. Wu, and W. Lehnert. A review of cell-scale multiphase flow modeling, including water management, in polymer electrolyte fuel cells. *Applied Energy*, 180:757–778, Oct. 2016.

[5] M. Andersson, V. Vukcevic, S. Zhang, Y. Qi, H. Jasak, S. B. Beale, and W. Lehnert. Modeling of droplet detachment using dynamic contact angles in polymer electrolyte fuel cell gas channels. *International Journal of Hydrogen Energy*, 44(21):11088–11096, Apr. 2019.

[6] R. F. Ausas, G. C. Buscaglia, and S. R. Idelsohn. A new enrichment space for the treatment of discontinuous pressures in multi-fluid flows. *International Journal for Numerical Methods in Fluids*, 70(7):829–850, 2012. Publisher: Wiley Online Library.

[7] R. F. Ausas, F. S. Sousa, and G. C. Buscaglia. An improved finite element space for discontinuous pressures. *Computer Methods in Applied Mechanics and Engineering*, 199(17-20):1019–1031, 2010. Publisher: Elsevier.

[8] F. Barbir. *PEM Fuel Cells: Theory and Practice*. Academic Press, Oct. 2012. Google-Books-ID: elO7n4Z6uLoC.

[9] C. N. Baroud and H. Willaime. Multiphase flows in microfluidics. *Comptes Rendus Physique*, 5(5):547–555, June 2004.

[10] T. D. Blake. The physics of moving wetting lines. *Journal of Colloid and Interface Science*, 299(1):1–13, July 2006.

[11] T. D. Blake, A. Clarke, J. De Coninck, and M. J. de Ruijter. Contact angle relaxation during droplet spreading: comparison between molecular kinetic theory and molecular dynamics. *Langmuir*, 13(7):2164–2166, Apr. 1997. Publisher: American Chemical Society.

[12] T. D. Blake and J. M. Haynes. Kinetics of liquidliquid displacement. *Journal of Colloid and Interface Science*, 30(3):421–423, July 1969.

[13] D. Bonn, J. Eggers, J. Indekeu, J. Meunier, and E. Rolley. Wetting and spreading. *Reviews of Modern Physics*, 81(2):739–805, May 2009. Publisher: American Physical Society.

[14] J. U. Brackbill, D. B. Kothe, and C. Zemach. A continuum method for modeling surface tension. *Journal of computational physics*, 100(2):335–354, 1992. Publisher: Elsevier.

[15] S. Brandon, A. Wachs, and A. Marmur. Simulated Contact Angle Hysteresis of a Three-Dimensional Drop on a Chemically Heterogeneous Surface: A Numerical Example. *Journal of Colloid and Interface Science*, 191(1):110–116, July 1997.

[16] F. Brochard-Wyart and P. G. de Gennes. Dynamics of partial wetting. *Advances in Colloid and Interface Science*, 39:1–11, Apr. 1992.

[17] J. Bruchon, Y. Liu, and N. Moulin. Finite element setting for fluid flow simulations with natural enforcement of the triple junction equilibrium. *Computers & Fluids*, 171:103–121, 2018. Publisher: Elsevier.

[18] G. C. Buscaglia and R. F. Ausas. Variational formulations for surface tension, capillarity and wetting. *Computer Methods in Applied Mechanics and Engineering*, 200(45-46):3011–3025, 2011. Publisher: Elsevier.

[19] F. C. Cetinbas, R. K. Ahluwalia, A. D. Shum, and I. V. Zenyuk. Direct Simulations of Pore-Scale Water Transport through Diffusion Media. *Journal of The Electrochemical Society*, 166(7):F3001–F3008, 2019.

[20] T. S. Chan, C. Kamal, J. H. Snoeijer, J. E. Sprittles, and J. Eggers. Cox–Voinov theory with slip. *Journal of Fluid Mechanics*, 900, Oct. 2020. Publisher: Cambridge University Press.

[21] Y.-C. Chang, T. Hou, B. Merriman, and S. Osher. A level set formulation of Eulerian interface capturing methods for incompressible fluid flows. *Journal of computational Physics*, 124(2):449–464, 1996. Publisher: Elsevier.

[22] J. Chessa and T. Belytschko. An enriched finite element method and level sets for axisymmetric two-phase flow with surface tension. *International Journal for Numerical Methods in Engineering*, 58(13):2041–2064, 2003. Publisher: Wiley Online Library.

[23] R. Codina. A discontinuity-capturing crosswind-dissipation for the finite element solution of the convection-diffusion equation. *Computer Methods in Applied Mechanics and Engineering*, 110(3):325–342, Dec. 1993.

[24] R. Codina, S. Badia, J. Baiges, and J. Principe. Variational multiscale methods in computational fluid dynamics. In *Encyclopedia of Computational Mechanics Second Edition*, pages 1–28. Wiley Online Library, 2018.

[25] M. Contestabile. Analysis of the market for diesel PEM fuel cell auxiliary power units onboard long-haul trucks and of its implications for the large-scale adoption of PEM FCs. *Energy Policy*, 38(10):5320–5334, Oct. 2010.

[26] A. Coppola-Owen and R. Codina. Improving Eulerian two-phase flow finite element approximation with discontinuous gradient pressure shape functions. *International journal for numerical methods in fluids*, 49(12):1287–1304, 2005. Publisher: Wiley Online Library.

[27] R. G. Cox. The dynamics of the spreading of liquids on a solid surface. Part 1. Viscous flow. *Journal of Fluid Mechanics*, 168(-1):169, July 1986.

[28] R. G. Cox. Inertial and viscous effects on dynamic contact angles. *Journal of Fluid Mechanics*, 357:249–278, Feb. 1998. Publisher: Cambridge University Press.

[29] K. A. Culligan, D. Wildenschild, B. S. B. Christensen, W. G. Gray, and M. L. Rivers. Pore-scale characteristics of multiphase flow in porous media: A comparison of air–water and oil–water experiments. *Advances in Water Resources*, 29(2):227–238, Feb. 2006.

[30] P. G. de Gennes. Wetting: statics and dynamics. *Reviews of Modern Physics*, 57(3):827–863, July 1985.

[31] M. J. de Ruijter, T. D. Blake, and J. De Coninck. Dynamic Wetting Studied by Molecular Modeling Simulations of Droplet Spreading. *Langmuir*, 15(22):7836–7847, Oct. 1999. Publisher: American Chemical Society.

[32] M. J. de Ruijter, M. Charlot, M. Voue, and J. De Coninck. Experimental Evidence of Several Time Scales in Drop Spreading. *Langmuir*, 16(5):2363–2368, Mar. 2000. Publisher: American Chemical Society.

[33] M. J. de Ruijter, J. De Coninck, T. D. Blake, A. Clarke, and A. Rankin. Contact Angle Relaxation during the Spreading of Partially Wetting Drops. *Langmuir*, 13(26):7293–7298, Dec. 1997. Publisher: American Chemical Society.

[34] M. J. de Ruijter, J. De Coninck, and G. Oshanin. Droplet Spreading: Partial Wetting Regime Revisited. *Langmuir*, 15(6):2209–2216, Mar. 1999. Publisher: American Chemical Society.

[35] J.-B. Dupont and D. Legendre. Numerical simulation of static and sliding drop with contact angle hysteresis. *Journal of Computational Physics*, 229(7):2453–2478, 2010. Publisher: Elsevier.

[36] T. F. Dupont and Y. Liu. Back and forth error compensation and correction methods for removing errors induced by uneven gradients of the level set function. *Journal of Computational Physics*, 190(1):311–324, 2003. Publisher: Elsevier.

[37] E. B. Dussan V. and S. H. Davis. On the motion of a fluid-fluid interface along a solid surface. *Journal of Fluid Mechanics*, 65(1):71–95, Aug. 1974.

[38] H. B. Eral, D. J. C. M. Mannetje, and J. M. Oh. Contact angle hysteresis: a review of fundamentals and applications. *Colloid and Polymer Science*, 291(2):247–260, Feb. 2013.

[39] C. W. Extrand and Y. Kumagai. Liquid Drops on an Inclined Plane: The Relation between Contact Angles, Drop Shape, and Retentive Force. *Journal of Colloid and Interface Science*, 170(2):515–521, Mar. 1995.

[40] G. Falcucci, E. Jannelli, S. Ubertini, and S. Succi. Direct numerical evidence of stress-induced cavitation. *Journal of Fluid Mechanics*, 728:362–375, Aug. 2013.

[41] C. Fang, C. Hidrovo, F.-m. Wang, J. Eaton, and K. Goodson. 3-D numerical simulation of contact angle hysteresis for microscale two phase flow. *International Journal of Multiphase Flow*, 34(7):690–705, 2008. Publisher: Elsevier.

[42] J.-C. Fernandez-Toledano, T. D. Blake, and J. De Coninck. Taking a closer look: A molecular-dynamics investigation of microscopic and apparent dynamic contact angles. *Journal of Colloid and Interface Science*, 587:311–323, Apr. 2021.

[43] R. B. Ferreira, D. Falcao, V. Oliveira, and A. Pinto. Numerical simulations of two-phase flow in an anode gas channel of a proton exchange membrane fuel cell. *Energy*, 82:619–628, Mar. 2015.

[44] T. Fletcher, R. Thring, and M. Watkinson. An Energy Management Strategy to concurrently optimise fuel consumption & PEM fuel cell lifetime in a hybrid vehicle. *International Journal of Hydrogen Energy*, 41(46):21503–21515, Dec. 2016.

[45] M. M. Francois, S. J. Cummins, E. D. Dendy, D. B. Kothe, J. M. Sicilian, and M. W. Williams. A balanced-force algorithm for continuous and sharp interfacial surface tension models within a volume tracking framework. *Journal of Computational Physics*, 213(1):141–173, 2006. Publisher: Elsevier.

[46] S. Ganesan, G. Matthies, and L. Tobiska. On spurious velocities in incompressible flow problems with interfaces. *Computer Methods in Applied Mechanics and Engineering*, 196(7):1193–1202, 2007. Publisher: Elsevier.

[47] L. Gao and T. J. McCarthy. Contact Angle Hysteresis Explained. *Langmuir*, 22(14):6234–6237, July 2006. Publisher: American Chemical Society.

[48] E. Gauthier, T. Hellstern, I. G. Kevrekidis, and J. Benziger. Drop Detachment and Motion on Fuel Cell Electrode Materials. *ACS Applied Materials & Interfaces*, 4(2):761–771, Feb. 2012. Publisher: American Chemical Society.

[49] Z. Ge, J.-C. Loiseau, O. Tammisola, and L. Brandt. An efficient mass-preserving interface-correction level set/ghost fluid method for droplet suspensions under depletion forces. *Journal of Computational Physics*, 353:435–459, Jan. 2018.

[50] D. Gerlach, G. Tomar, G. Biswas, and F. Durst. Comparison of volume-of-fluid methods for surface tension-dominant two-phase flows. *International Journal of Heat and Mass Transfer*, 49(3-4):740–754, Feb. 2006.

[51] J. Gostick, M. Aghighi, J. Hinebaugh, T. Tranter, M. A. Hoeh, H. Day, B. Spellacy, M. H. Sharqawy, A. Bazylak, A. Burns, W. Lehnert, and A. Putz. OpenPNM: A Pore Network Modeling Package. *Computing in Science Engineering*, 18(4):60–74, July 2016. Conference Name: Computing in Science Engineering.

[52] J. T. Gostick, M. A. Ioannidis, M. W. Fowler, and M. D. Pritzker. Pore network modeling of fibrous gas diffusion layers for polymer electrolyte membrane fuel cells. *Journal of Power Sources*, 173(1):277–290, Nov. 2007.

[53] M. Grimm, M. Hellmann, H. Kemmer, and S. Kabelac. Water Management of PEM Fuel Cell Systems Based on the Humidity Distribution in the Anode Gas Channels. *Fuel Cells*, 20(4):477–486, 2020. _eprint: https://onlinelibrary.wiley.com/doi/pdf/10.1002/fuce.202000070.

[54] S. Gross and A. Reusken. An extended pressure finite element space for two-phase incompressible flows with surface tension. *Journal of Computational Physics*, 224(1):40–58, May 2007.

[55] S. Guo, M. Gao, X. Xiong, Y. J. Wang, X. Wang, P. Sheng, and P. Tong. Direct Measurement of Friction of a Fluctuating Contact Line. *Physical Review Letters*, 111(2):026101, July 2013. Publisher: American Physical Society.

[56] A. Hamraoui, K. Thuresson, T. Nylander, and V. Yaminsky. Can a Dynamic Contact Angle Be Understood in Terms of a Friction Coefficient? *Journal of Colloid and Interface Science*, 226(2):199–204, June 2000.

[57] P. Hansbo, M. G. Larson, and S. Zahedi. A cut finite element method for a Stokes interface problem. *Applied Numerical Mathematics*, 85:90–114, 2014. Publisher: Elsevier.

[58] M. R. Hashemi, P. B. Ryzhakov, and R. Rossi. An enriched finite element/level-set method for simulating two-phase incompressible fluid flows with surface tension. *Computer Methods in Applied Mechanics and Engineering*, 370:113277, Oct. 2020.

[59] M. Hatipogullari, C. Wylock, M. Pradas, S. Kalliadasis, and P. Colinet. Contact angle hysteresis in a microchannel: Statics. *Physical Review Fluids*, 4(4):044008, Apr. 2019. Publisher: American Physical Society.

[60] C. Hirt and B. Nichols. Volume of fluid (VOF) method for the dynamics of free boundaries. *Journal of Computational Physics*, 39(1):201–225, Jan. 1981.

[61] L. M. Hocking. A moving fluid interface. Part 2. The removal of the force singularity by a slip flow. *Journal of Fluid Mechanics*, 79(2):209–229, Feb. 1977.

[62] L. M. Hocking and A. D. Rivers. The spreading of a drop by capillary action. *Journal of Fluid Mechanics*, 121(-1):425, Aug. 1982.

[63] C. Huh and L. E. Scriven. Hydrodynamic model of steady movement of a solid/liquid/fluid contact line. *Journal of colloid and interface science*, 35(1):85–101, 1971. Publisher: Elsevier.

[64] S. R. Idelsohn, J. M. Gimenez, J. Marti, and N. M. Nigro. Elemental enriched spaces for the treatment of weak and strong discontinuous fields. *Computer Methods in Applied Mechanics and Engineering*, 313:535–559, 2017. Publisher: Elsevier.

[65] D. Jacqmin. Calculation of Two–Phase Navier–Stokes Flows Using Phase–Field Modeling. *Journal of Computational Physics*, 155(1):96–127, Oct. 1999.

[66] D. Jacqmin. Contact-line dynamics of a diffuse fluid interface. *Journal of Fluid Mechanics*, 402:57–88, Jan. 2000.

[67] A. Jarauta and P. Ryzhakov. Challenges in Computational Modeling of Two-Phase Transport in Polymer Electrolyte Fuel Cells Flow Channels: A Review. *Archives of Computational Methods in Engineering*, 25(4):1027–1057, Nov. 2018.

[68] A. Jarauta, P. Ryzhakov, J. Pons-Prats, and M. Secanell. An implicit surface tension model for the analysis of droplet dynamics. *Journal of Computational Physics*, 374:1196–1218, Dec. 2018.

[69] A. Jarauta, P. Ryzhakov, M. Secanell, P. R. Waghmare, and J. Pons-Prats. Numerical study of droplet dynamics in a polymer electrolyte fuel cell gas channel using an embedded Eulerian-Lagrangian approach. *Journal of Power Sources*, 323:201–212, Aug. 2016.

[70] M. Kang, R. P. Fedkiw, and X.-D. Liu. A Boundary Condition Capturing Method for Multiphase Incompressible Flow. *Journal of Scientific Computing*, 15(3):323–360, Sept. 2000.

[71] A. M. Karim, K. Fujii, and H. P. Kavehpour. Contact line dynamics of gravity driven spreading of liquids. *Fluid Dynamics Research*, 53(3):035503, May 2021. Publisher: IOP Publishing.

[72] H.-Y. Kim, S. Jeon, M. Song, and K. Kim. Numerical simulations of water droplet dynamics in hydrogen fuel cell gas channel. *Journal of Power Sources*, 246:679–695, Jan. 2014.

[73] J.-H. Kim, H. P. Kavehpour, and J. P. Rothstein. Dynamic contact angle measurements on superhydrophobic surfaces. *Physics of Fluids*, 27(3):032107, Mar. 2015. Publisher: American Institute of Physics.

[74] E. C. Kumbur, K. V. Sharp, and M. M. Mench. Liquid droplet behavior and instability in a polymer electrolyte fuel cell flow channel. *Journal of Power Sources*, 161(1):333–345, Oct. 2006.

[75] H. Liu, S. Krishnan, S. Marella, and H. Udaykumar. Sharp interface Cartesian grid method II: A technique for simulating droplet interactions with surfaces of arbitrary shape. *Journal of Computational Physics*, 210(1):32–54, Nov. 2005.

[76] J. Luo, X. Y. Hu, and N. A. Adams. Curvature boundary condition for a moving contact line. *Journal of Computational Physics*, 310:329–341, Apr. 2016.

[77] E. Mahrous, A. Jarauta, T. Chan, P. Ryzhakov, A. Z. Weber, R. V. Roy, and M. Secanell. A particle finite element-based model for droplet spreading analysis. *Physics of Fluids*, 32(4):042106, 2020. Publisher: AIP Publishing LLC.

[78] S. Manservisi and R. Scardovelli. A variational approach to the contact angle dynamics of spreading droplets. *Computers & Fluids*, 38(2):406–424, 2009. Publisher: Elsevier.

[79] J.-M. Martinez, X. Chesneau, and B. Zeghmati. A new curvature technique calculation for surface tension contribution in PLIC-VOF method. *Computational Mechanics*, 37(2):182–193, Jan. 2006.

[80] M. d. Mier-Torrecilla, S. Idelsohn, and E. OÃśate. Advances in the simulation of multi-fluid flows with the particle finite element method. Application to bubble dynamics. *International journal for numerical methods in fluids*, 67(11):1516–1539, 2011. Publisher: Wiley Online Library.

[81] P. Minev, T. Chen, and K. Nandakumar. A finite element technique for multi-fluid incompressible flow using Eulerian grids. *Journal of Computational Physics*, 187(1):255–273, 2003. Publisher: Elsevier.

[82] A. Mohammad Karim, S. H. Davis, and H. P. Kavehpour. Forced versus Spontaneous Spreading of Liquids. *Langmuir*, 32(40):10153–10158, Oct. 2016. Publisher: American Chemical Society.

[83] A. Mukherjee and S. G. Kandlikar. A Numerical Analysis of Growing Water Droplet inside an Air Supply Channel of a PEM Fuel Cell. In *Fluids Engineering*, pages 131–136, Chicago, Illinois, USA, Jan. 2006. ASMEDC.

[84] P. P. Mukherjee, C.-Y. Wang, and Q. Kang. Mesoscopic modeling of two-phase behavior and flooding phenomena in polymer electrolyte fuel cells. *Electrochimica Acta*, 54(27):6861–6875, Nov. 2009.

[85] J. H. Nam, K.-J. Lee, G.-S. Hwang, C.-J. Kim, and M. Kaviany. Microporous layer for water morphology control in PEMFC. *International Journal of Heat and Mass Transfer*, 52(11-12):2779–2791, May 2009.

[86] R. O'hayre, S.-W. Cha, W. Colella, and F. B. Prinz. *Fuel cell fundamentals*. John Wiley & Sons, 2016.

[87] P. C. Okonkwo and C. Otor. A review of gas diffusion layer properties and water management in proton exchange membrane fuel cell system. *International Journal of Energy Research*, 45(3):3780–3800, 2021. _eprint: https://onlinelibrary.wiley.com/doi/pdf/10.1002/er.6227.

[88] H. Patel, S. Das, J. Kuipers, J. Padding, and E. Peters. A coupled Volume of Fluid and Immersed Boundary Method for simulating 3D multiphase flows with contact line dynamics in complex geometries. *Chemical Engineering Science*, 166:28–41, July 2017.

[89] J. G. Petrov, J. Ralston, M. Schneemilch, and R. A. Hayes. Dynamics of Partial Wetting and Dewetting in Well-Defined Systems. *The Journal of Physical Chemistry B*, 107(7):1634–1645, Feb. 2003. Publisher: American Chemical Society.

[90] P. Petrov and I. Petrov. A combined molecular-hydrodynamic approach to wetting kinetics. *Langmuir*, 8(7):1762–1767, 1992. Publisher: ACS Publications.

[91] A. Pfrang. Fuel cell testing Degradation of fuel cells and its impact on fuel cell applications. *GIT Laboratory Journal Europe*, 13(3-4):42–44, 2009.

[92] C. M. Phan, A. V. Nguyen, and G. M. Evans. Combining hydrodynamics and molecular kinetics to predict dewetting between a small bubble and a solid surface. *Journal of Colloid and Interface Science*, 296(2):669–676, Apr. 2006.

[93] S. Popinet. An accurate adaptive solver for surface-tension-driven interfacial flows. *Journal of Computational Physics*, 228(16):5838–5866, 2009. Publisher: Elsevier.

[94] S. Popinet and S. Zaleski. A front-tracking algorithm for accurate representation of surface tension. *International Journal for Numerical Methods in Fluids*, 30(6):775–793, 1999. Publisher: Wiley Online Library.

[95] T. Qian, X.-P. Wang, and P. Sheng. Molecular scale contact line hydrodynamics of immiscible flows. *Physical Review E*, 68(1):016306, 2003. Publisher: APS.

[96] T. Qian, X.-P. Wang, and P. Sheng. Power-Law Slip Profile of the Moving Contact Line in Two-Phase Immiscible Flows. *Physical Review Letters*, 93(9):094501, Aug. 2004. Publisher: American Physical Society.

[97] T. Qian, X.-P. Wang, and P. Sheng. Molecular hydrodynamics of the moving contact line in two-phase immiscible flows. *arXiv preprint cond-mat/0510403*, 2005.

[98] T. Qian, X.-P. Wang, and P. Sheng. A variational approach to moving contact line hydrodynamics. *Journal of Fluid Mechanics*, 564:333, Oct. 2006.

[99] D. Quere. Wetting and Roughness. *Annual Review of Materials Research*, 38(1):71–99, 2008. _eprint: https://doi.org/10.1146/annurev.matsci.38.060407.132434.

[100] A. Rabbani and M. Babaei. Hybrid pore-network and lattice-Boltzmann permeability modelling accelerated by machine learning. *Advances in Water Resources*, 126:116–128, Apr. 2019.

[101] S. R. Ranabothu, C. Karnezis, and L. L. Dai. Dynamic wetting: Hydrodynamic or molecular-kinetic? *Journal of Colloid and Interface Science*, 288(1):213–221, Aug. 2005.

[102] W. Ren and W. E. Boundary conditions for the moving contact line problem. *Physics of fluids*, 19(2):022101, 2007. Publisher: American Institute of Physics.

[103] W. Ren, D. Hu, and W. E. Continuum models for the contact line problem. *Physics of Fluids*, 22(10):102103, Oct. 2010. Publisher: American Institute of Physics.

[104] W. Ren and E. Weinan. Derivation of continuum models for the moving contact line problem based on thermodynamic principles. *Communications in Mathematical Sciences*, 9(2):597–606, 2011.

[105] P. B. Ryzhakov and A. Jarauta. An embedded approach for immiscible multi-fluid problems: An embedded approach for immiscible multi-fluid problems. *International Journal for Numerical Methods in Fluids*, 81(6):357–376, June 2016.

[106] P. B. Ryzhakov, A. Jarauta, M. Secanell, and J. Pons-Prats. On the application of the PFEM to droplet dynamics modeling in fuel cells. *Computational Particle Mechanics*, 4(3):285–295, July 2017.

[107] E. Samiei, M. Shams, and R. Ebrahimi. A novel numerical scheme for the investigation of surface tension effects on growth and collapse stages of cavitation bubbles. *European Journal of Mechanics - B/Fluids*, 30(1):41–50, Jan. 2011.

[108] F. Schonfeld and S. Hardt. Dynamic contact angles in CFD simulations. *Computers & Fluids*, 38(4):757–764, Apr. 2009.

[109] A. Selle, R. Fedkiw, B. Kim, Y. Liu, and J. Rossignac. An Unconditionally Stable MacCormack Method. *Journal of Scientific Computing*, 35(2):350–371, June 2008.

[110] D. Seveno, A. Vaillant, R. Rioboo, H. Adao, J. Conti, and J. De Coninck. Dynamics of wetting revisited. *Langmuir*, 25(22):13034–13044, 2009. Publisher: ACS Publications.

[111] Y. D. Shikhmurzaev. Singularities at the moving contact line. Mathematical, physical and computational aspects. *Physica D: Nonlinear Phenomena*, 217(2):121–133, 2006. Publisher: Elsevier.

[112] Y. D. Shikhmurzaev. Moving contact lines and dynamic contact angles: a "litmus test" for mathematical models, accomplishments and new challenges. *The European Physical Journal Special Topics*, 229(10):1945–1977, Sept. 2020.

[113] L. Shui, J. C. T. Eijkel, and A. van den Berg. Multiphase flow in microfluidic systems - control and applications of droplets and interfaces. *Advances in Colloid and Interface Science*, 133(1):35–49, May 2007.

[114] P. K. Sinha and C.-Y. Wang. Pore-network modeling of liquid water transport in gas diffusion layer of a polymer electrolyte fuel cell. *Electrochimica Acta*, 52(28):7936–7945, Nov. 2007.

[115] J. H. Snoeijer and B. Andreotti. Moving Contact Lines: Scales, Regimes, and Dynamical Transitions. *Annual Review of Fluid Mechanics*, 45(1):269–292, Jan. 2013.

[116] Z. Solomenko, P. D. M. Spelt, L. O Naraigh, and P. Alix. Mass conservation and reduction of parasitic interfacial waves in level-set methods for the numerical simulation of two-phase flows: A comparative study. *International Journal of Multiphase Flow*, 95:235–256, Oct. 2017.

[117] Y. Sui, H. Ding, and P. D. Spelt. Numerical Simulations of Flows with Moving Contact Lines. *Annual Review of Fluid Mechanics*, 46(1):97–119, 2014. _eprint: https://doi.org/10.1146/annurev-fluid-010313-141338.

[118] Y. Sui and P. D. Spelt. An efficient computational model for macroscale simulations of moving contact lines. *Journal of Computational Physics*, 242:37–52, 2013. Publisher: Elsevier.

[119] X. Sun, Y. Hasegawa, H. Kohno, Z. Jiao, K. Hayakawa, K. Okita, and N. Shikazono. Calculation of contact angles at triple phase boundary in solid oxide fuel cell

anode using the level set method. *Materials Characterization*, 96:100–107, Oct. 2014.

[120] P. Suresh and S. Jayanti. Effect of air flow on liquid water transport through a hydrophobic gas diffusion layer of a polymer electrolyte membrane fuel cell. *International Journal of Hydrogen Energy*, 35(13):6872–6886, July 2010.

[121] M. Sussman. A second order coupled level set and volume-of-fluid method for computing growth and collapse of vapor bubbles. *Journal of Computational Physics*, 187(1):110–136, May 2003.

[122] M. Sussman and E. G. Puckett. A Coupled Level Set and Volume-of-Fluid Method for Computing 3D and Axisymmetric Incompressible Two-Phase Flows. *Journal of Computational Physics*, 162(2):301–337, Aug. 2000.

[123] M. Sussman, P. Smereka, and S. Osher. A level set approach for computing solutions to incompressible two-phase flow. *Journal of Computational physics*, 114(1):146–159, 1994. Publisher: Elsevier.

[124] M. Sussman, K. M. Smith, M. Y. Hussaini, M. Ohta, and R. Zhi-Wei. A sharp interface method for incompressible two-phase flows. *Journal of computational physics*, 221(2):469–505, 2007. Publisher: Elsevier.

[125] M. Sussman and S. Uto. A computational study of the spreading of oil underneath a sheet of ice. *CAM Report*, 114:146–159, 1998.

[126] V. Talimi, Y. Muzychka, and S. Kocabiyik. Numerical simulation of the pressure drop and heat transfer of two phase slug flows in microtubes using moving frame of reference technique. *International Journal of Heat and Mass Transfer*, 55(23-24):6463–6472, Nov. 2012.

[127] T. E. Tezduyar. Interface-tracking and interface-capturing techniques for finite element computation of moving boundaries and interfaces. *Computer Methods in Applied Mechanics and Engineering*, 195(23-24):2983–3000, Apr. 2006.

[128] A. Theodorakakos, T. Ous, M. Gavaises, J. M. Nouri, N. Nikolopoulos, and H. Yanagihara. Dynamics of water droplets detached from porous surfaces of relevance to PEM fuel cells. *Journal of Colloid and Interface Science*, 300(2):673–687, Aug. 2006.

[129] K. E. Thompson. Pore-scale modeling of fluid transport in disordered fibrous materials. *AIChE Journal*, 48(7):1369–1389, 2002. _eprint: https://onlinelibrary.wiley.com/doi/pdf/10.1002/aic.690480703.

[130] P. A. Thompson and M. O. Robbins. Simulations of contact-line motion: slip and the dynamic contact angle. *Physical Review Letters*, 63(7):766, 1989. Publisher: APS.

[131] A.-K. Tornberg and B. Engquist. A finite element based level-set method for multiphase flow applications. *Computing and Visualization in Science*, 3(1-2):93–101, 2000. Publisher: Springer.

[132] Z. Tukovic and H. Jasak. A moving mesh finite volume interface tracking method for surface tension dominated interfacial fluid flow. *Computers & Fluids*, 55:70–84, Feb. 2012.

[133] S. O. Unverdi and G. Tryggvason. A front-tracking method for viscous, incompressible, multi-fluid flows. *Journal of computational physics*, 100(1):25–37, 1992. Publisher: Elsevier.

[134] J. Vollmer, R. Mencl, and H. Mueller. Improved laplacian smoothing of noisy surface meshes. In *Computer graphics forum*, volume 18, pages 131–138, 1999. Issue: 3.

[135] A. Z. Weber, R. L. Borup, R. M. Darling, P. K. Das, T. J. Dursch, W. Gu, D. Harvey, A. Kusoglu, S. Litster, M. M. Mench, R. Mukundan, J. P. Owejan, J. G. Pharoah, M. Secanell, and I. V. Zenyuk. A Critical Review of Modeling Transport Phenomena in Polymer-Electrolyte Fuel Cells. *Journal of The Electrochemical Society*, 161(12):F1254–F1299, 2014.

[136] O. Weinstein and L. Pismen. Scale dependence of contact line computations. *Mathematical Modelling of Natural Phenomena*, 3(1):98–107, 2008. Publisher: EDP Sciences.

[137] M. Worner. Numerical modeling of multiphase flows in microfluidics and micro process engineering: a review of methods and applications. *Microfluidics and Nanofluidics*, 12(6):841–886, May 2012.

[138] M. Worner, X. Cai, H. Alla, and P. Yue. A semi-analytical method to estimate the effective slip length of spreading spherical-cap shaped droplets using Cox theory. *Fluid Dynamics Research*, 50(3):035501, Mar. 2018. Publisher: IOP Publishing.

[139] T. C. Wu and N. Djilali. Experimental investigation of water droplet emergence in a model polymer electrolyte membrane fuel cell microchannel. *Journal of Power Sources*, 208:248–256, June 2012.

[140] B. Xie, P. Jin, Y. Du, and S. Liao. A consistent and balanced-force model for incompressible multiphase flows on polyhedral unstructured grids. *International Journal of Multiphase Flow*, 122:103125, 2020. Publisher: Elsevier.

[141] J.-J. Xu and W. Ren. A level-set method for two-phase flows with moving contact line and insoluble surfactant. *Journal of Computational Physics*, 263:71–90, Apr. 2014.

[142] X. Xu, Y. Di, and H. Yu. Sharp-interface limits of a phase-field model with a generalized Navier slip boundary condition for moving contact lines. *Journal of Fluid Mechanics*, 849:805–833, Aug. 2018.

[143] Y. Yamamoto, T. Ito, T. Wakimoto, and K. Katoh. Numerical simulations of spontaneous capillary rises with very low capillary numbers using a front-tracking method combined with generalized Navier boundary condition. *International Journal of Multiphase Flow*, 51:22–32, 2013. Publisher: Elsevier.

[144] Y. Yamamoto, K. Tokieda, T. Wakimoto, T. Ito, and K. Katoh. Modeling of the dynamic wetting behavior in a capillary tube considering the macroscopicâĂŞmicroscopic contact angle relation and generalized Navier boundary condition. *International journal of multiphase flow*, 59:106–112, 2014. Publisher: Elsevier.

[145] J. Yang, X. Ma, L. Fei, X. Zhang, K. H. Luo, and S. Shuai. Effects of hysteresis window on contact angle hysteresis behaviour at large Bond number. *Journal of Colloid and Interface Science*, 566:327–337, Apr. 2020.

[146] Y. F. Yap, J. C. Chai, T. N. Wong, K. C. Toh, and H. Y. Zhang. A Global Mass Correction Scheme for the Level-Set Method. *Numerical Heat Transfer, Part B: Fundamentals*, 50(5):455–472, Nov. 2006. Publisher: Taylor & Francis _eprint: https://doi.org/10.1080/10407790600646958.

[147] T. Young. III. An essay on the cohesion of fluids. *Philosophical Transactions of the Royal Society of London*, 95:65–87, Jan. 1805. Publisher: Royal Society.

[148] P. Yue. Thermodynamically consistent phase-field modelling of contact angle hysteresis. *Journal of Fluid Mechanics*, 899, Sept. 2020. Publisher: Cambridge University Press.

[149] P. Yue and J. J. Feng. Wall energy relaxation in the CahnâĂŞHilliard model for moving contact lines. *Physics of Fluids*, 23(1):012106, Jan. 2011. Publisher: American Institute of Physics.

[150] S. Zahedi, K. Gustavsson, and G. Kreiss. A conservative level set method for contact line dynamics. *Journal of Computational Physics*, 228(17):6361–6375, 2009. Publisher: Elsevier.

[151] J. Zhang and P. Yue. A level-set method for moving contact lines with contact angle hysteresis. *Journal of Computational Physics*, page 109636, 2020. Publisher: Elsevier.

[152] P. Zhang and K. Mohseni. Theoretical model of a finite force at the moving contact line. *International Journal of Multiphase Flow*, 132:103398, Nov. 2020.

[153] X. Zhang and Y. Qin. Contact angle hysteresis of a water droplet on a hydrophobic fuel cell surface. *Journal of Colloid and Interface Science*, 545:231–241, June 2019.

[154] J. Zhao, F. Qin, D. Derome, and J. Carmeliet. Simulation of quasi-static drainage displacement in porous media on pore-scale: Coupling lattice Boltzmann method and pore network model. *Journal of Hydrology*, 588:125080, Sept. 2020.

[155] L. Zhao and J. Cheng. Analyzing the Molecular Kinetics of Water Spreading on Hydrophobic Surfaces via Molecular Dynamics Simulation. *Scientific Reports*, 7(1):10880, Dec. 2017.

[156] X. Zhu, P. C. Sui, and N. Djilali. Three-dimensional numerical simulations of water droplet dynamics in a PEMFC gas channel. *Journal of Power Sources*, 181(1):101–115, June 2008.